Doctoral Dissertation

Novel bonding process using surface-modified microscale Cu particles for high-temperature electronic packaging

Xiangdong Liu

May 2017

Graduate School of Engineering,
Osaka University,

Supervisor

Assoc. Prof. Hiroshi Nishikawa, Ph. D.

Joining and Welding Research Institute

Osaka University

Doctoral Committee

Assoc. Prof. Hiroshi Nishikawa, Ph. D.

Joining and Welding Research Institute

Osaka University

Prof. Michihiko Ike , Ph. D.

Division of Sustainable Energy and Environmental Engineering, Graduate school of Engineering

Osaka University

Prof. Akio Hirose, Ph. D.

Division of Materials and Manufacturing Science, Graduate school of Engineering

Osaka University

Prof. Soshu Kirihara, Ph. D.

Joining and Welding Research Institute

Osaka University

To my parents

Contents

CHAPTER 2

CHAPTER 3

List of figures

List of tables

Chapter 1
Research background

1.1 New generation high-temperature power device based on wide bandgap semiconductors

1.1.1 Current power device

Nowadays, nearly 40% of the worldwide energy is consumed as electric energy. Modern human society is increasing dependent upon electrical application for industry, transportation and live, which is continuously driving great advances in power generation, storage, distribution and management technologies [1]. These significant advancements should owe to improvements in the performance of power electronic systems that regulate the electricity flow in its generation–storage–distribution cycle. Solid-state power semiconductor devices have been recognized as the heart of all electric power systems, and it is estimated that at least 50% of the electricity used in the world is controlled by power devices [2]. For decades, researchers have worked relentlessly to improve semiconductor materials, processing, fabrication and packaging, and these efforts have contributed to the successful evolution of a variety of advanced power devices available today.

Bipolar power thyristors that can control operation between blocking states and on-states by using a third terminal were first developed in the 1950s [3, 4]. Starting with a modest current of 100

A and several hundreds volts in the 1950s, the current and voltage rating has been scaled to approach 5000 A and 8000 V respectively for a single device. Such devices are used in power distribution systems such as high-voltage direct current (HVDC) transmission networks.

In the 1970s, first silicon power metallic oxide semiconductor field effect transistor (MOSFET) was created as a new class of devices for power switching applications as well [5]. Their excellent switching speed opened new applications operating in the 10–50 kHz frequency domain. Today, these silicon-based power MOSFETs have exhibited extensive use in high frequency applications with relatively low operating voltages (below 200 V), and it is expected that power MOSFETs will remain dominant for low-voltage high-frequency applications in future.

In the 1980s, the merger of MOS and bipolar physics led to a successful innovation, a new class of device, named insulated gate bipolar transistor (IGBT) was created [6]. Due to the high power density, simple interface, and ruggedness, the IGBT structure is now the predominant power switch technology for medium and high power applications [7, 8]. In Fig 1.1, various applications of power devices are shown under various operating frequency and power level. On the high power end of the

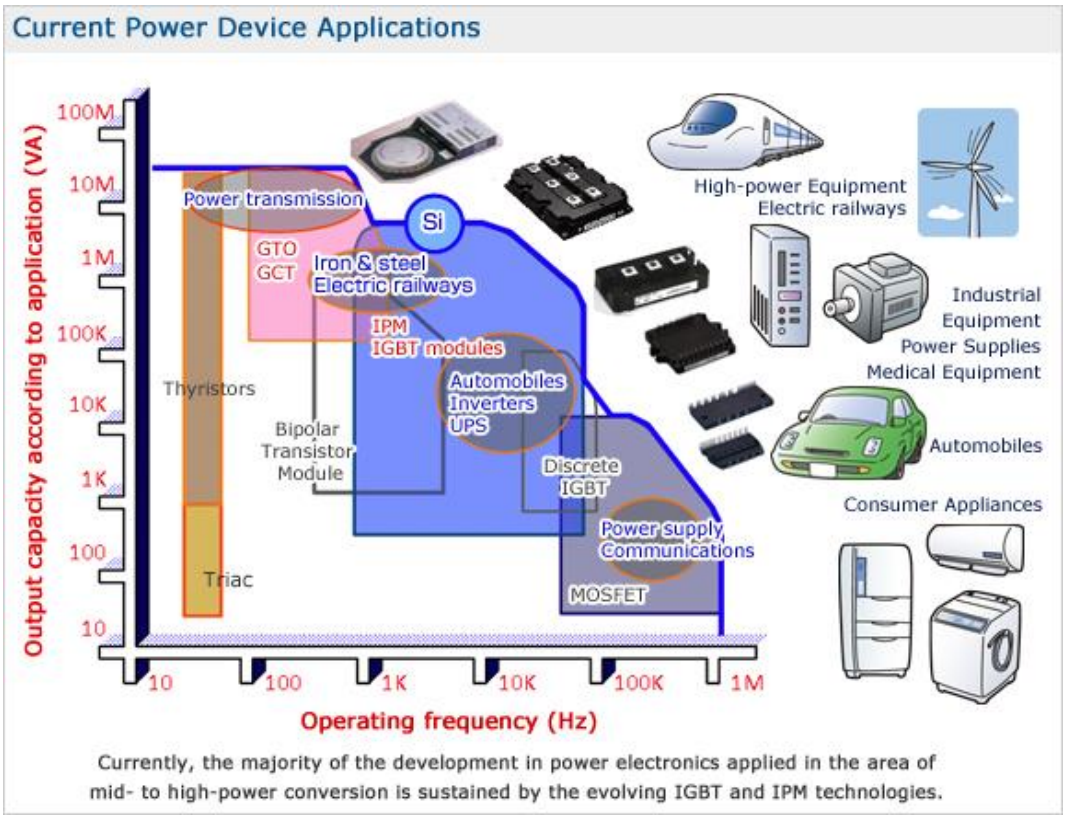

Figure 1.1 Various applications for power devices (courtesy of Mitsubishi Electric Corporation).

chart, thyristors are available that can individually handle over 10 MW with a low frequency by a single device. These devices are suitable for the HVDC power transmission. For the broad range of systems that require medium voltage and current (up to 3 KV and 1 KA) with a middle frequency such as power module in hybrid electrical vehicle, the IGBT has been found to be the optimum solution. When the required current and voltage are low (up to 1 KV and 100 A) and frequency is high (up to 1MHz), the use of discrete power MOSFETs with appropriate control ICs is more effective for the applications such as switch mode power supplies and automotive electronics. Therefore, there is no single device structure that can satisfy all the applications, and plenty of room still exists for further innovations [2, 8].

1.1.2 Wide band gap semiconductor for power device

Many industries require power devices that can operate reliably at high temperatures, such as the aircraft [10], automotive [8, 9], space exploration [11], deep oil/gas extraction [12] and etc. Traditionally, engineers had to rely on thermal management system when designing electronics that must operate outside of normal temperature ranges. However, these thermal management methods also introduce additional issues in term of longer wires, extra connectors, and cooling systems that add undesired weight and volume to the device, as well as increased risk for failure [13]. Moreover, in some applications, cooling system could not be possible. Therefore, it may be more appealing for the power device to work at high temperature.

Currently, these devices are based on the very well established Silicon technology. However, many factors limit the use of silicon at high temperatures. First, due to a narrow bandgap of 1.12 eV, the silicon p-n junction will become intrinsic at high temperature (225 ℃ to 400 ℃ depending on doping levels). The intrinsic carrier concentration (n_i) is given by (1.1) [2]:

$$n_i = \sqrt{N_c N_v} \cdot e^{(-E_g/2kT)} \qquad (1.1)$$

where N_c is the effective density of states in the conduction band; N_v is the effective density of states in the valence band; E_g is bandgap energy; k is Boltzmann's constant; T is absolute temperature. The intrinsic carrier concentration increases with the rise of temperature. When the intrinsic carrier concentration is close to the doping concentration level, p-n junctions behave as resistors, rather than

diodes, and thereby transistors lose the switching characteristics.

Another problem is the rise of leakage current through a reverse-biased p-n junction as the temperature increases. The saturation current (I_o, the ideal reverse-bias current of the junction) is proportional to the square of the intrinsic carrier concentration [2]:

$$I_o \propto n_i^2 \propto T^3 e^{(E_{go}/kT)} \quad (1.2)$$

where E_{go} is the bandgap energy at T = 0 ℃. The leakage current approximately doubles for each 10 ℃ rise in junction temperature. Improved junction leakage currents increase power dissipation in the power device.

On the other hand, although trench isolation, silicon-on-insulator (SOI), and other improvement on the standard silicon process can decrease leakage current and enable the high-performance operation above 200 ℃, it cannot solve the fundamental limitations of Silicon and therefore device operation will be inherently limited to lower than 300 ℃ [14]. Consequently, a new generation of power devices based on "wide band gap" (WBG) semiconductor material that has a much larger

Table 1.1 Physical properties of Si and wide band gap semiconductors [17].

	Si	**3C-SiC**	**6H-SiC**	**4H-SiC**	**GaN**	**Diamond**
Band energy E_g (eV)	1.12	2.3	2.9	3.2	3.39	5.6
Electron mobility μ_n ($cm^2V^{-1}s^{-1}$)	1450	1000	415	950	2000	4000
Hole mobility μ_p ($cm^2V^{-1}s^{-1}$)	450	45	90	115	350	3800
Critical electric field E_c (Vcm^{-1})	3×10^5	2×10^6	2.5×10^6	3×10^6	5×10^6	10^7
Saturation velocity v_{sat} (cms^{-1})	10^7	2.5×10^7	2×10^7	2×10^7	2×10^7	3×10^7
Thermal conductivity λ ($Wcm^{-1}K^{-1}$)	1.3	5	5	5	1.3	20
Dielectric constant ε_r	11.7	9.6	9.7	10	8.9	5.7

bandgap energy than silicon, show tremendous promise for the future [15], [16]. Some of the physical properties of Si and possible WBG semiconductor materials are listed in Table 1.1 [17] and Fig 1.2 [18]. The advantages of the wide-bandgap materials in Table 1.1, are a higher critical field, a higher saturation velocity, and a lower intrinsic carrier density (due to the higher bandgap).

These properties allows WBG power devices to have higher junction temperature, higher switching frequency, higher voltage and power capability, lower conduction drop, and better radiation hardness than Si power device. An example is shown in Fig. 1.3 [17]. The figure addresses the temperature limits in the blocking mode, but it provide a clear demonstration of the advantages of the wide-bandgap semiconductors in high-temperature operation. It is found that silicon devices rated above a few hundred volts cannot operate higher than 200 ℃. Moreover, an even lower junction temperature limitation (125 ℃) can be seen in high-voltage silicon components (6.5 kV IGBTs in this case). With wide-bandgap semiconductors, the operating area is much bigger, enable very high-voltage (up to 100 kV) devices operate at temperatures above 400 ℃ or more. Among the current WBG semiconductor candidates, Silicon Carbide (SiC) and Gallium Nitride (GaN) present the best balance between theoretical characteristics (high blocking voltage capability, high temperature operation, and high switching frequencies), real commercial availability of the starting material (wafers and epitaxial layers), and maturity of their technological processes [1]. Recently, SiC power devices were reported in many literatures, including high voltage and high temperature

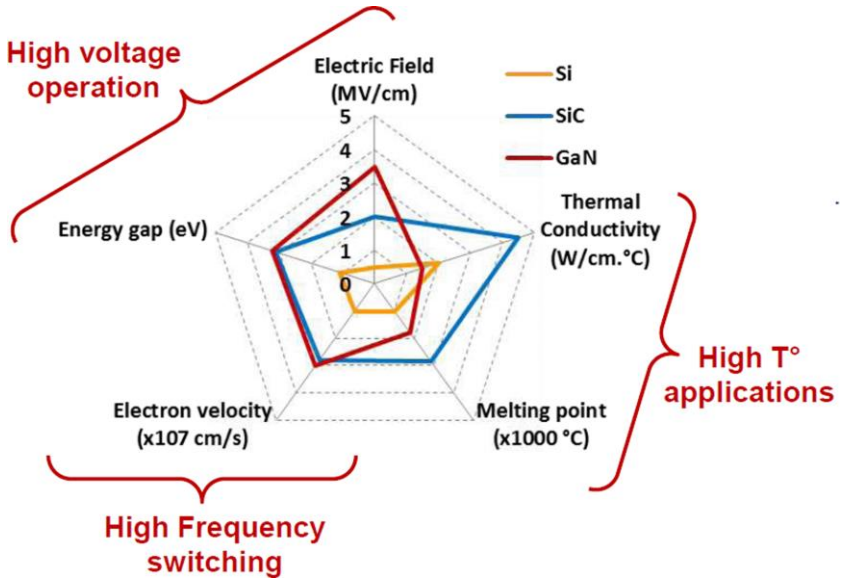

Figure 1.2 Some key material properties of WBG semiconductors candidates and Si [1].

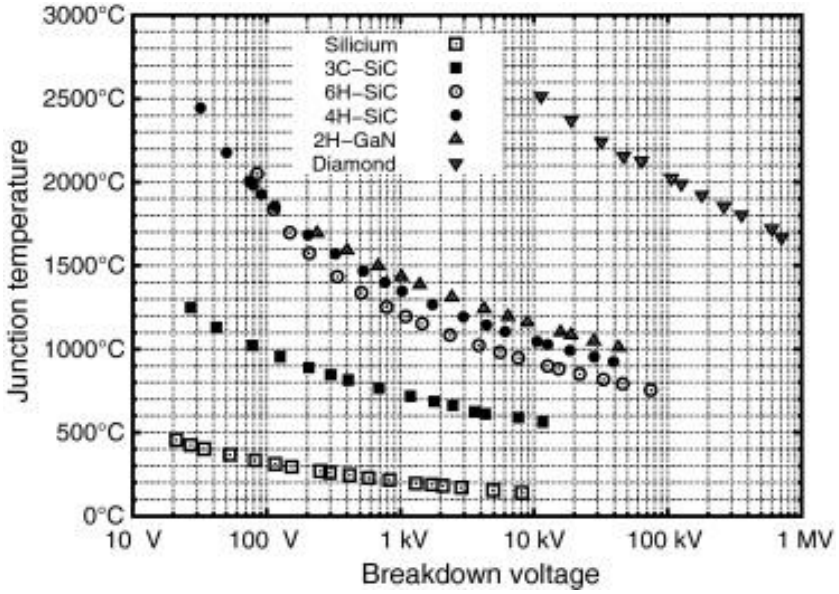

Figure 1.3 Thermal runaway limits for various semiconductors [17].

diodes, MOSFETs, IGBTs, and Thyristors. And those reported devices based on GaN include diodes, HEMTs and MOSFETs. What is more, some power devices made of silicon carbide have become commercially available recently. Schottky-barrier diodes can be bought from many suppliers (Infineon, Cree, ST Microelectronics), and controlled switches (Junction Field-effect Transistor, JEET) are available as engineering samples [17]. These novel devices represent a real breakthrough in power devices. Furthermore, the development of the packaging, drivers, and controllers in these novel power devices also require a great effort in research.

1.1.3 Integration and packaging of power device

To take full advantage of the high power density capabilities offered by WBG power devices, the advancement of packaging technologies is required. The materials used in the package and assemble must not only have an acceptable performance in specified high operation temperature range, but also operate reliably. Fig. 1.4 shows the conceptual structure of an IGBT module package and its essential components: the heat sink, the base plate, the substrate, the terminal lead, IGBT die, as well as the interconnections including wire bonding, die attach and substrate attach. It is typically at the interfaces within these components are connected together that failures occur as a result of the effects of thermal or power cycling, such as the fracture of die attach layer and substrate attach layer,

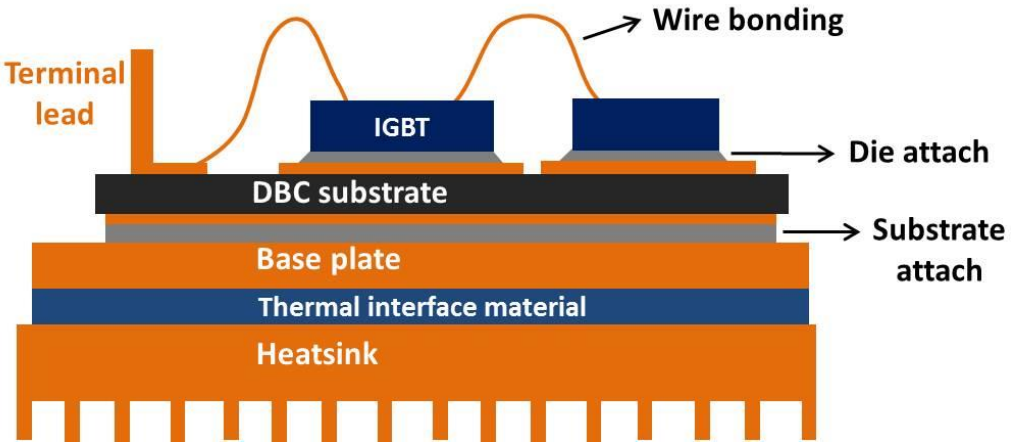

Figure 1.4 Schematic diagram of typical structure of IGBT power module [14].

lift-off or heel crack of wire bonding, as shown in Fig. 1.5 [19-22].

Die attach materials have a key role in the packaging of a power electronic module. The die attach materials require a variety of characteristics to guarantee that the device is a thermally efficient and mechanically reliable system. These characteristics include sufficient bonding between the die

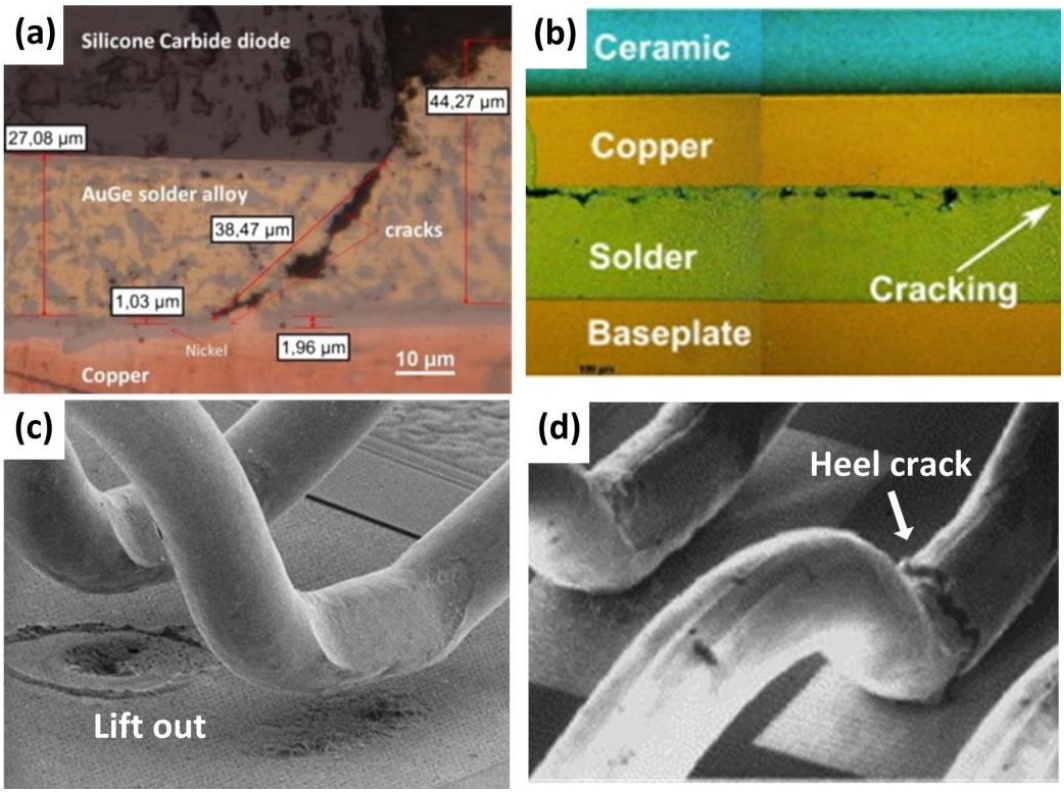

Figure 1.5 Typical failure locations under cyclic thermos-mechanical loading in IGBT module packaging: (a) die attach, (b) substrate attach, (c, d): wire bonding [19-22].

and the substrate so that cannot detach from the substrate, proper hardness to relief the thermal stress from the die and substrate, high thermal conductivity to dissipate heat generated by chip, suitable coefficient of thermal expansion (CTE) that matches with both substrate and die, an appropriate processing temperature and high stability at operating temperature. And it should exhibit excellent electrical conductivity [23]. On the other hand, die attach is also the most common failure location. Table 1.2 gives the thermal and mechanical properties of the common ceramic substrate, substrate metallization, semiconductor die, as well as die attach materials [23-26]. Differences in CTE between the substrate and the die could induce thermo-mechanical stresses and fatigue. Therefore, "soft" die attach materials is generally preferred because it relieves the thermo-mechanical stresses generated from mismatched coefficients of thermal expansion in the die attach layer. Besides, concentrated stresses at the die edge can lead to horizontal crack propagation and die lifting. Also, the problems of electromigration and interdiffusion are becoming serious with increasing temperature. Generally, the interdiffusion of different metals or the electromigration at the die bond pad could lead to failure of the interconnection.

Table 1.2 Thermal and mechanical properties of common packaging materials [23-26].

Component	Materials	Thermal conductivity ($Wcm^{-1}K^{-1}$)	Coefficient of thermal expansion (ppm/K)	Young module (GPa)
Semiconductor	Si	1.3	2.6	150
	SiC	5.0	3.8	410
	GaN	1.3	6.2	320
Die attach	Pb-5Sn	0.35	29	20
	Au-20Sn	0.57	16	68
	Nano-Ag	2.4	1.9	9
Metallization	Cu	4.0	16.5	110
	Al	2.05	17	68
Substrate	Al_2O_3	0.30	6.5	310
	AlN	2.0	4.5	310
	Si_3N_4	0.9	2.6	314

Moreover, in recent years, numerous studies and massive investments in high-temperature packaging materials have been triggered by the increasing demand for new-generation WBG power devices that can operate at a higher temperature than conventional Si-based devices. Especially, the high-temperature operation of WBG power devices requires a new die-attach process that can produce a reliable joint with a higher melting point, superior mechanical properties, and better thermal conductivity than conventional high-temperature solder alloys. Detailed information about the high temperature die attach materials will be discussed in *Section 1.2*.

1.2 Overview of die attach technology for high-temperature application

1.2.1 High-lead solders

The use of certain hazardous substances, including lead, in electrical and electronic equipment is forbidden by the restriction of hazardous substances (RoHS) directive passed in 2006. However, high-temperature solders (i.e. high-lead alloys containing 85 mass % or more) were exempted from the directive regardless of their application [27]. Pb-Sn alloys with a lead content of more than 85 mass %, namely high-lead solders are generally utilized in the die attachment, step soldering (attaching heat pins and lead sink), interconnections of passive devices, direct chip attachment, flip-chip packaging, and some board-level packaging for automotive, avionics , gas and oil, and space applications [28].

The microstructure of the high-lead solder composed of Sn phase dispersed on the matrix Pb phase, and no brittle intermetallic compound (IMC) is formed in the solder, as shown in Fig.1.6 [29]. The microstructure of high-lead solders is thermally stable and both the aging temperature and the aging durations do not have a great impact on the microstructure. It also possesses high ductility, high thermal shock reliability, and excellent fatigue resistance since high-lead solders are extremely soft. Moreover, the thermal conductivity of the high-lead solders is fairly good for dissipating heat even for the high power devices that generate high amounts of heat [30]. As a result, these advantages combined with lead being a low-cost metal make it an ideal option as die attach material for high-temperature electronic packaging applications.

However, in 2011, a recast of the RoHS directive (RoHS2) was passed to set deadlines for

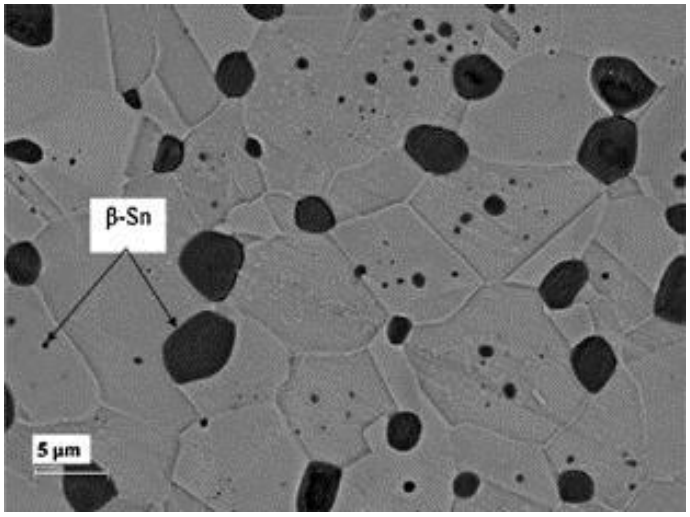

Figure 1.6 Microstructure of Pb-10Sn solder in the as-cast state [29].

eliminating the exempt applications such as high-lead solder alloys [31]. In addition, a decision for prolonging the current exemptions was also made. Particularly, for those product categories that were subject to the initial RoHS directive, the extended deadline for exempt applications was 5 years (2017). In Annex III of the RoHS2 directive, exemption applications were decided for lead alloy in high-melting temperature included:

- Exemption 7: ‘‘(a) Lead in high melting temperature type solders’’ (i.e. high-lead solder alloys that contain 85 % lead by weight or more).
- Exemption 14: ‘‘Lead in solders consisting of more than two elements for the connection between the pins and the package of microprocessors with a lead content of more than 80 % and less than 85 % by weight’’.
- Exemption 15: ‘‘Lead in solders to complete a viable electrical connection between semiconductor die and carrier within integrated circuit flip chip packages’’.

Since the high-lead solder alloy exemption in RoHS will expire for a large part of the electronic industry in 2017 if no technical reasons will be provided for further extension, the industry has to seek alternatives of high-lead solders. As a result, in order to establish suitable replacements to the high-lead solders for high-temperatur elelctornic packaging applications, considerable research effort has been made. The promising replacements include high-temperature lead-free solder alloys, transient liquid phase (TLP) bonding, and low-temperature Ag sintering technology. In the following

sections, we will show the currently available candidates for high-lead solder for high-temperature electronic packaging applications.

1.2.2 High-temperature lead-free solders

The current choice for high-temperature lead-free solders, typically designed to be used in the temperatures from 150 to 200 ℃, are derived from Au–Sn [32, 33], Au–Ge [34, 35], Zn–Al [36, 37], Zn–Sn [38], Bi–Ag [39] and Sn–Sb solders [40], as well as other binary or ternary systems. Some properties of these solders have been reported by many researchers, such as the microstructure, the melting and solidification behavior, interfacial compounds and reactions, mechanical performance and reliability. One of the basic criteria is having an appropriate melting range that allows for manufacture and packaging of the soldered components. This proper melting range has been defined by the industry as 270–350 ℃ to ensure efficient soldering process control [41]. Table 1.3 summarizes the some typical composition and solidus and liquidus temperatures of some high temperature lead-free alloy systems. Selection of the suitable solder alloy must guarantee that the

Table 1.3 Solidus and liquidus temperatures of high-temperature lead-free solders [42].

	Composition (wt.%)	**Solidus temperature (℃)**	**Liquidus temperature (℃)**
Au-Sn	Au-20Sn	280	280
	Au-95Sn	215-217	215-217
Au-Ge	Au-0.28 at.% Ge	360	360
Bi-Ag	Bi-2.5Ag	262.5	262.5
	Bi-10Ag	261.4	380.6
Zn-Al	Zn-6Al	381	381
	Zn-4Al-3Mg-3.2Ga	309	347
Zn-Sn	Zn-20Sn	198	383
	Zn-30Sn	198	374
	Zn-40Sn	198	365
Sn-Sb	Sn-5Sb	245	245

melting temperature (both the solidus and liquidus temperatures) is greatly higher than the operation temperature of soldered components. At the same time, the solder alloy also should have a sufficiently high solidus temperature in order to withstand peak temperatures of second level soldering. The suggested candidates of high-temperature lead-free solders remain some challenges [41]. A melting temperature of 240 ℃ limits the wide-scale applicability of Sn-Sb alloys in the high-temperature application. Zn-based alloys are brittle in nature, which may limit their operation in harsh operating environments. The high cost of gold alloys may prevent widespread usage. From a financial standpoint, gold-based lead-free solders are limited to niche markets, where cost is not one of the key issues. Also, gold-based solders are hard alloys and have high stiffness [41]. This results in the transfer of thermo-mechanical stresses and limits its application in semiconductor dies. Since Bi-based solders have low thermal conductivity, their use is limited in applications with high power dissipation. Additionally, Bi-based alloys have limited wettability on metallizations used in electronic products. Advantages and limitations of select high-temperature solders are listed in Table 1.4. To sum up, although high-temperature lead-free solders are being used, the drawbacks inhibit their wide adoption of in power electronic packaging, especially in the WGB power device.

Table 1.4 Advantages and disadvantages of alloys systems for high-temperature solder applications [42].

	Advantages	**Disadvantages**
Au-Sn	Fluxless, good creep resistance	Expensive, brittle Au–Sn IMCs
Au-Ge	Low elastic modulus, stable microstructure, high strength	Expensive, difficult to manufacture
Zn-Al	Low cost, easy to manufacture, no IMC formed under equilibrium	Highly corrosive, poor wetting
Zn-Sn	Low cost, no IMC formed at equilibrium, ductility improved compared to Zn–Al	Highly corrosive, low Solidus temperature
Sn-Sb	Good creep properties, stable microstructure	Toxic, low liquidus temperature
Bi-Ag	Acceptable melting point, affordable cost	Poor workability, low conductivity

1.2.3 Transient liquid phase bonding process

TLP bonding combines the characteristics of solid-phase diffusion bonding and liquid-phase soldering. The process relies on the partial melting of interlayer with low melting temperature and simultaneous reaction with parent metal. During the heating cycle, the low melting layer melts and intermetallic compound (IMC) phases are formed due to liquid/solid reaction. After that, the joint consists of the IMC with a high melting point, and thereby the remelting temperature of the system is increased [43, 44].

In particularly, the TLP bonding can be divided into four stages [43], interlayer preparation, melting, IMC formation and homogenization as described in Fig.1.7. Firstly, a thin interlayer metal with a low melting point is placed between two parent metals with high melting points. The interlayer material can be produced in the form of preforms of foils, by electroplating or by thin film deposition processes such as sputtering. In Stage 2, upon heating the entire system above the melting point of the interlayer metal, a liquid layer is formed at the interface. The liquid layer then wets the surfaces of the parent metal. It also dissolves a small amount of parent metal at the interface. The dissolution process causes the interface to widen. In Stage 3, the reaction between the liquid layer and the parent metal at the interface results in the formation of IMC with a high remelting temperature. At the same time, a diffusion of the parent metal to the IMC/liquid interface is performed, by which the IMC layer can continuously grow towards the liquid phase. The multiple layers of IMC with different composition form during this period. In Stage 4, after the liquid phase

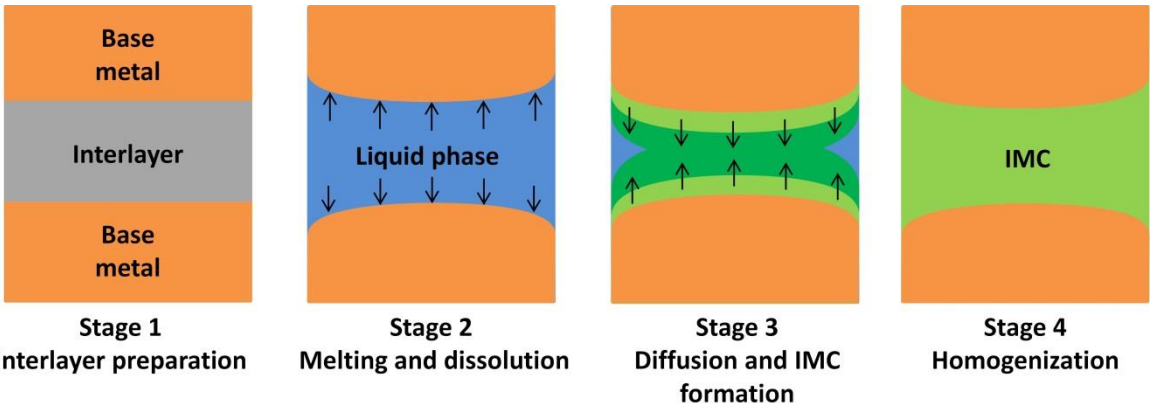

Figure 1.7 Schematic diagram of a TLP bonding process, including interlayer preparation, interlayer melting, IMC formation, and homogenization.

is completely consumed, a homogenization step is often deployed at a suitable heat treatment temperature. After the homogenization, a fully IMC joint with the thermodynamically favorable composition is finally achieved.

For the application of electronic packaging, TLP joint could easily be achieved below 300 ℃ by using metals with low-melting point metals like Sn and In as an interlayer. Recently, to improve the reliability of joints in the electronic systems operated at elevated temperatures, a number of TLP systems including Cu/Sn [45, 46], Ag/Sn [47], Ni/Sn [48], Cu/In [49, 50] and Au/In [51] have been studied. Table 1.5 shows several intermetallic systems such as Au/Sn, Cu/Sn, Au/In for TLP bonding. The Cu/Sn system exhibits the cheapest materials cost as well as the suitable bonding and remelt temperature. Moreover, the Cu-Sn system metallurgical reaction has been well studied over decades due to the wide use of Sn-based solder and Cu substrate in electronic packaging industry, Therefore, Cu/Sn system has been the most promising system for the TLP bonding used in the field of electronic packaging. Li et al. [46] reported the mechanism and kinetics of the interfacial reaction in Cu/Sn/Cu system during the TLP bonding process, in which the cross-sections of the Cu/Sn/Cu samples during the process was given, as shown in Fig.1.8. Bosco et al [52] reported the strength of the joints produced by the TLP bonding in Cu/Sn system, the TLP joint fully comprising the Cu-Sn IMCs exhibited higher strength, but lower toughness than pure Cu. Moreover, the fracture surface showed a combination of transgranular and intergranular fracture, indicating a brittle characteristic.

Table 1.5 Comparison of available ternary system for TLP bonding [50].

Materials	Bonding temperature (℃)	Remelt temperature (℃)	Relative Market price
Ni/Sn	300	400	Ni:1 Sn:0.8
Ag/Sn	250	600	Ag:63 Sn:0.8
Au/Sn	450	900	Au:2600 Sn:0.8
Cu/Sn	280	415	Cu:0.5 Sn:0.8
Au/In	200	495	Au:2600 In:37.5
Cu/In	200	667	Cu:0.5 In:37.5

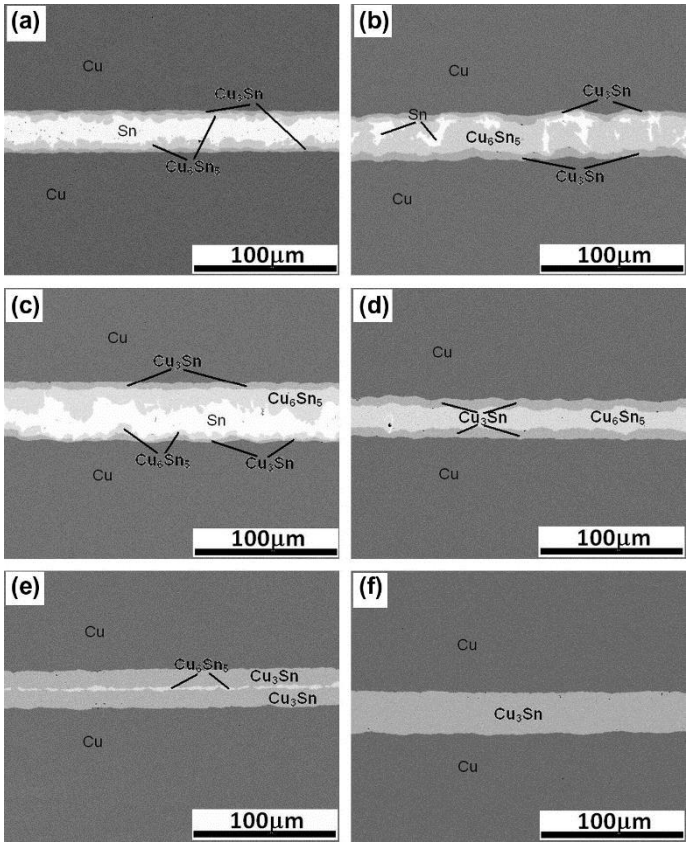

Figure 1.8 SEM images of cross-sections of Cu/Sn/Cu samples bonded at 340 ℃ for: (a) 10 min; (b) 40 min; (c) 60 min; (d) 90 min; (e) 240 min; and (f) 480 min [46].

In addition to the interlayer-based TLP bonding process, a powder-based TLP bonding process, or "TLP sintering process" has emerged because it is more compatible with the traditional soldering process [53-55]. During this TLP bonding process, Sn particles melt and react with Cu particles, forming Cu-Sn high-temperature IMC bond. In this sintering process, the complete consumption of low melt temperature Sn is also a critical issue; some Sn could remain in the bonding layer if processing time is insufficient, as shown in Fig. 1.9 (a) [55]. Lang et al. [53] reported the bond of SiC die with Si_3N_4 substrate using Cu/Sn powders TLP sintering process, in which a anneal process is needed to obtain the thermally stable microstructure. The cross-sectional microstructure of the as-bonded joint and the joint annealed at 300 ℃ for 500 h is give in Fig.1.9 (b). The TLP bonding process possesses several attractive attributes when considered as a die attach technology for high-temperature application. First, a completed TLP bond has similar composition to the interlayer, and therefore, mechanical, thermal, and electrical properties similar to that of the base material.

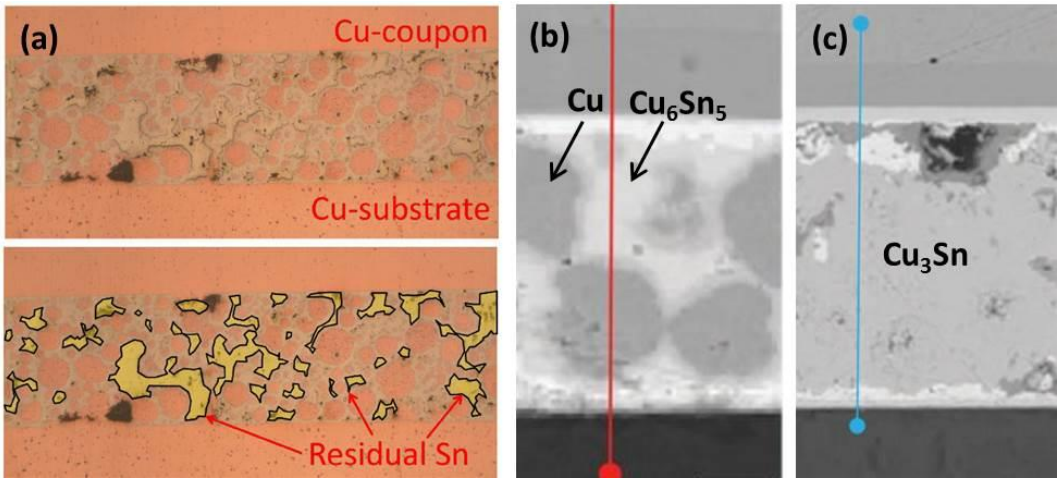

Figure 1.9 (a) Cross-section of a Cu-Sn powder-based TLP joint with insufficient sintering time. The joint consists of Cu particles and Cu_6Sn_5 IMCs, but dispersed pockets of residual Sn. Cross-section of (b) as-bonded Cu-Sn TLP sintering joint, consisting of Cu-particles and Cu_6Sn_5 IMC, (c) annealed Cu-Sn TLP sintering joint, which fully consists of Cu_3Sn IMC [53, 55].

Second, bonding can be processed at a low temperature, but the subsequent solidus temperature of the obtained IMC joint could be significantly higher than the bonding temperature. In addition, the materials cost of TLP bonding process is reasonable. However, current TLP bonding process also has some important drawbacks, and which could make it less suitable for the practical applications. These will be discussed in the *Section 1.3.1*.

1.2.4 Low-temperature Ag sintering process

Historically, sintering has been used for centuries for making ceramic tools. Today, it also finds its applications for the forming of metal or ceramic used in the aviation, aerospace, automobile and electronic industry etc. The reduction of the total surface energy is the driving force of sintering. The total surface energy of a powder compact is expressed as $\gamma \cdot A$, where γ is the specific surface (interface) energy and A is the total surface (interface) area of the compact [56]. The reduction of the total energy can be expressed as

$$\Delta(\gamma \cdot A) = \Delta\gamma \cdot A + \gamma \cdot \Delta A \quad (1.3)$$

Here, the change in surface energy ($\Delta\gamma$) is caused by densification and the change in interfacial area

(ΔA) is due to grain coarsening. For solid state sintering, $\Delta\gamma$ is related to the replacement of solid/vapor interfaces (surface) by solid/solid interfaces.

In the field of electronic packaging, Ag-sintering has been used as die attach technique for power device packaging. The increasing interest in Ag-sintering technique can be due to their several advantages, such as the character of low-temperature processing but high remelt temperature, as well as the superior mechanical, thermal and electrical properties compared with other lead-free alternatives. This trend is related to the increasing demand of WBG power devices, which require interconnecting materials to work at high junction temperatures of more than 200 ℃. In such a harsh operation environment, an Ag-sintered joint is one very ideal option.

The history of Ag sintering technique that is identified as a low-temperature joining technique can date back to the late 1980s [57-59]. It was developed by Siemens Microelectronics in 1987 to bond large area power thyristors on molybdenum substrates. The major challenge in Ag sintering technique is the reduction of sintering temperature. During Ag-sintering process, the densification rate of the sintering particles is related to driving force and the mass transport mechanism, which is thermally activated. As the thermally activated mass transport is low at low homologous temperature, the sintering driving force has to be significantly increased. One simple way is to apply the external pressure, the driving force can be increased, and at the same time, the sintering temperature is lowered. Hence, the initial Ag sintering pastes utilize microscale Ag flakes to produce pure Ag joints, and the joints were sintered at a temperature of 250 ℃ with a pressure of 10-40 MPa at a temperature of 250 ℃ [60]. The mechanism for this Ag-sintering lay under the category of ‘‘pressure-assisted sintering.’’

On the other hand, reducing the particle size can significantly increase the surface energy. The excess surface energy becomes the driving force for the sintering and results in the reduction of total interfacial energy. Thereby reducing the particle size from micron size to nanoscale can theoretically lower the sintering temperature. Therefore, Ag nanoparticle paste was developed in the mid of 2000s to reduce the applied pressure to lower than 5 MPa while remaining the processing temperature in the range of 200 ℃ to 300 ℃ [61, 62]. The lower of sintering pressure is due to the significant increase of effective specific surface area. Furthermore, in recent years, the nano-Ag sintering process without any assisted pressure process, namely pressureless Ag sintering has been reported by many

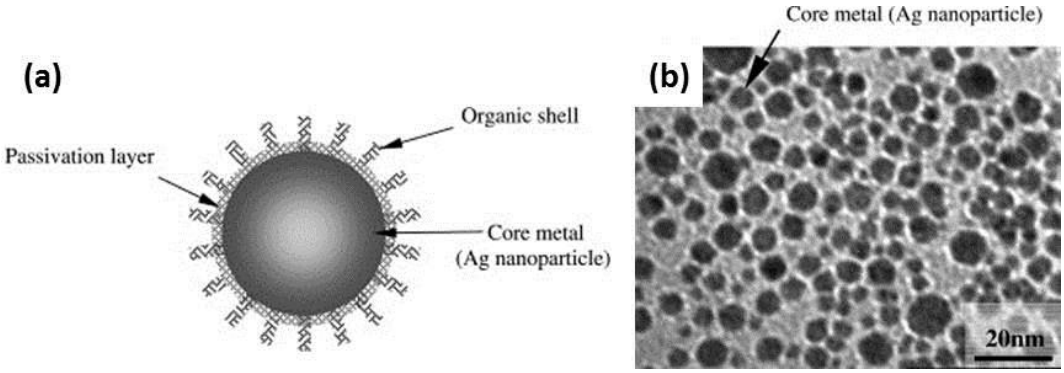

Figure 1.10 Ag metallo-organic nanoparticle: (a) schematic view of the core-shell structure and (b) transmission electron microscope (TEM) bright field (BF) image of Ag nanoparticles [62].

researchers [63-65].This pressureless sintering technique makes Ag sintering can be used on thin and brittle WBG chips, which has a risk of the passivation cracking under high sintering pressure. Some researchers have summarized the formulation of Ag paste, innovations in the process and equipment to form the Ag joint [66, 67]. Typical additives for the formulation of nano-Ag paste include dispersant, binder, and solvent. A typical feature of nanoparticle with a passivation layer is shown in Fig.1.10 (a). An image of nanoparticles obtained with transmission electron microscopy (TEM) is shown in Fig. 1.10 (b). During the sintering process, a preheating is generally needed for the volatilization of organic solvent. A schematic diagram of sintering behavior of Ag particles is shown in Fig.1.11. The variables that determine the microstructure and performance of the sintered Ag joint can be divided into two categories, material variables, and process variables, as shown in Table 1.6 [68]. The material variables usually influence the powder sinterability. The process variables are

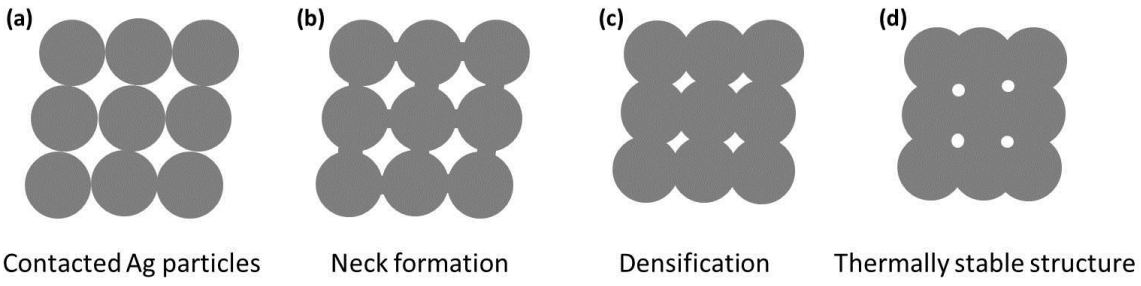

Figure 1.11 Schematic diagram of Ag nanoparticle sintering process: (a) initial contacted Ag particles, (b) neck formed between particles during initial stage of sintering, (c) densification process of sintered particles, (d) final densified structure

Table 1.6 Material and process variables of sintering

Material variables	**Powder:**	Shape, size, distribution, agglomeration, etc.
	Chemistry:	Impurity, solvent, etc.
Process variables		Temperature, time, pressure, atmosphere, heating and cooling rate, etc.

mostly the thermodynamic variables such as temperature, time, pressure etc., which greatly influence the quality of final sintered layer.

As for the reliability of the real Ag sintered die attachment, the current literature suggests that it has good high-temperature storage and thermal-fatigue properties if a proper porosity of the sintered microstructure is obtained, which should be sufficiently low to bear the fatigue failure and high enough for the stress relief [69-71]. Besides its density, Ag sintered joints also depend on a compatible substrate, a suitable substrate roughness, and a proper metallization or plating film to produce a robust Ag joint. To sum up, although the feasibility of the usage of Ag sintering as die attaching technique has been clearly demonstrated, the reliability of Ag-sintered joints are currently being studied for different electronics packaging types. [66, 67, 69-71]

1.3 Motivation of research

1.3.1 Issues associated with current bonding technology

In the view of practical application, there are five main aspects that can evaluate a die attach technology for power device packaging and they are: (1) Reliability; (2) Thermal conductivity; (3) Electrical conductivity; (4) Manufacturability and (5) Material cost. Within, the reliability, the thermal and electrical conductivity can be identified as performance factors. The manufacturability and the materials cost can be seen as production factors. The currently available die attach technology are assigned into three levels of “Good”, “Fair” or “Poor” on each of the above aspects, as listed in Table 1.7. In the follows, we will discuss the major issues associated with these die attach technologies. With the discussion, the necessity for developing a new die attach technology will be addressed.

Table 1.7 Comparison of various die attach technologies.

Technologies	Performance			Production	
	Reliability	Thermal	Electrical	Manufacturability	Materials cost
Solder reflow	Fair	Fair	Fair	Good	Optional
TLP bonding	Good	Fair	Fair	Poor	Good
Ag sintering	Good	Good	Good	Poor	Poor

Currently, the reflow process using high-lead content solders or high-temperature lead-free solders is still the most commonly used die attach technology. It is mainly because it has very excellent manufacturability, for example, the entire reflow process only lasts for several minutes and no external pressure is needed, which are very favorable to the large-scale production. On the other hand, the electrical and thermal conductivities of typical solder alloys are not as good as pure Ag metals. In addition, the solder alloys are complicated binary or trinary systems and the as-reflowed state of these solder alloys are generally not thermodynamically stable. At high temperature, over-growth of interfacial IMC, coarsening or phase separation of the microstructure may occur in the soldered joint which can cause joint failure eventually [41, 42]. What is more, the solder alloys exhibits significantly lower melt temperature than that of the TLP-based IMC joint or Ag-sintered joint, which basically eliminates the possibility of its applications in the extremely high temperature. Therefore, to some degree, the soldering technology can only be considered as a transitional technology for the die attachment of WBG power device.

Compared to the conventional high-temperature soldering process, the TLP bonding technique has an obvious advantage, namely “low-temperature formation but high-temperature remelt”. In other words, it can be identified as a low-temperature bonding process for high-temperature die attach. In addition to the high re-melting temperature, the IMC phase produced by the TLP bonding also exhibits high yield strength and high creep resistance, which enable a TLP joint to have a good high-temperature reliability. On the other hand, the IMC phase in the TLP joint exhibits moderate thermal and electrical conductivity, similar to pure Sn and Sn alloy but lower than pure Ag, as shown in Table 1.8 [72-74]. Table 1.8 also reveals that the IMCs have weak fracture toughness. Indeed, most of the IMC phases formed in a packaging are brittle than any of the high-temperature solder alloys,

and moreover, the Kirkendall voids may form at the bonding interface during the formation of IMC, which are generally deleterious to the cyclic loading capability of joint. In addition, compared with the short-time soldering process, the TLP process could be a time-consumed process and it is usually necessary to apply a further heat treatment to the bonded joint until the joint is ultimately homogenous, which seriously lower the manufacturability of TLP process. These critical issues are hindering the wide acceptance of TLP bonding as an alternative to high-temperature soldering.

Ag sintering is another low-temperature bonding process for high-temperature die attach. As mentioned before, the Ag sintered joint has a number of excellent performances, including high remelt temperature, good mechanical properties, and superior thermal and electrical conductivity. Hence, in the view of performance and reliability, Ag sintering may be the best choice among the current die attach technologies to address the critical issues of high-temperature operation of WBG power device. Another die attach materials, either high-temperature lead-free solder or IMC phase formed during TLP process have some inherent drawbacks, such as the low melt temperature of solder alloys and the poor thermal conductivity of IMC phase, which will limit the potential performance of the WBG power device. However, at present, some problems that could inhibit the large-scale application of low-temperature Ag sintering still exist, such as the use of nanoparticles,

Table 1.8 Physical properties of Ag, Cu, Sn, Sn3.5Ag solder and three common intermetallics in electronic packaging [72-74].

Material	Electrical Resistivity ($\mu\Omega$·cm)	Thermal conductivity (W/m Ҡ)	Fracture Toughness ($MPa/m^{1/2}$)
Ag	1.5	419	55
Cu	1.6	401	-
Sn	11.5	63.2	45
Sn3.5Ag alloy	12.3	78	-
Cu_3Sn	8.9	70.4	5.7
Cu_6Sn_5	17.5	34.1	2.8
Ni_3Sn_4	28.6	19.6	4.2

poor manufacturability, and high material cost.

Nanoparticle paste requires a high proportion of dispersants and other organic materials. Otherwise, the coalescence of nanoparticles will happen even at a room temperature. When such pastes are used to bond large surface areas, the organic materials tend to remain in the joint layer after heating, thus affecting the reliability of the joint. To avoid such problems, some researchers are working on the microscale Ag particle paste. Moreover, compared with the soldering process, Ag sintering needs much longer processing time and a certain amount of bonding pressure, thereby exhibiting a poor manufacturability. In order to realize the large-scale production of Ag sintering for die attach application, many power device companies, such as Infineon Technologies, ABB, and Semikron Elektronik, and have invested to design their own pressure-assisted sintering equipment in house. Some major equipment suppliers also have begun to develop generic pressure-assisted sintering equipment for Ag sintering [66]. The process of pressureless Ag sintering that only needs a similar procedure to the conventional epoxy-based die attaching also has obtained a great advancement in the recent years. These developments make it possible to improve the manufacturability of Ag sintering technology. However, the high material cost of Ag sintering seems a no solution problem, and which will inhibit its wide application as a die attach technology for power device packing.

1.3.2 Emerging of low-temperature Cu sintering technology

Among the available die attach materials, Cu exhibits the cheapest material cost, as shown in Table 1.5. And it exhibits similar physical properties to noble metal Ag, including good mechanical properties, superior electrical resistivity, and thermal conductivity, as shown in Table 1.8. Therefore, the Cu sintered joint is expected to have the competitive excellent performance to the Ag sintered joint, and in the past five years, researchers have begun to develop a low-temperature Cu sintering process as a high-temperature die attach technology for WBG power device packaging [75-78]. Ishizaki and Watanabe have reported the synthesis of Cu nanoparticles capped with fatty acids and amines from an insoluble salt, such as Cu carbonate and Cu hydroxide for the sintering bonding [75]. The mean diameter of the Cu nanoparticles was controlled from 93 to 13 nm as the alkyl carbon

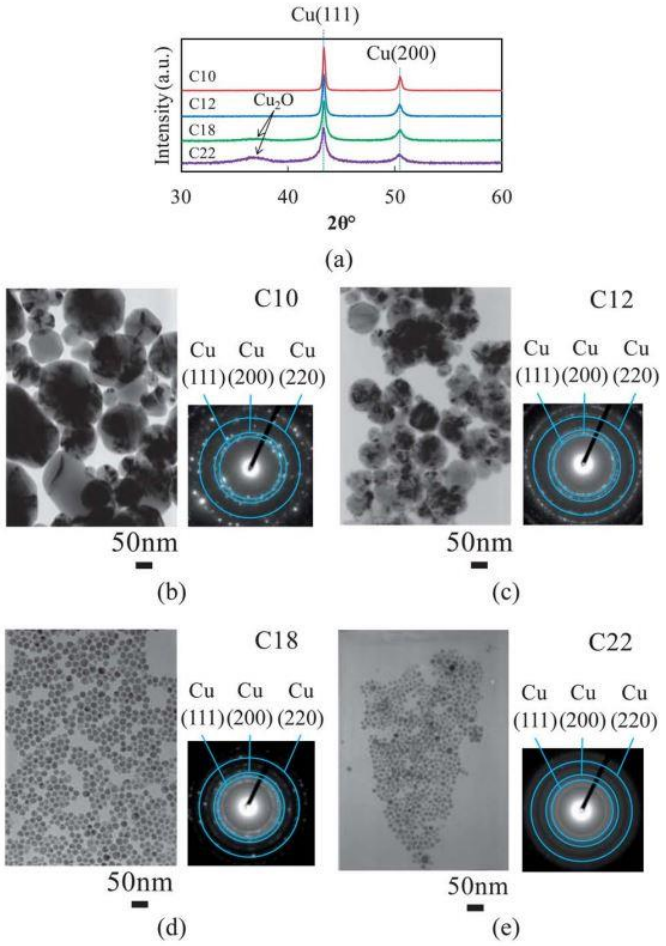

Figure 1.12 (a) XRD patterns and (b–e) TEM images of the Cu nanoparticles capped by fatty acid and fatty amine whose alkyl carbon number is from C10 to C22 [75].

number increased from C10 to C22, as shown in Fig 1.12. When the sintering was conducted at 300 ℃ in a hydrogen atmosphere, the shear strength of the Cu plates bonded by C12 and C18 Cu nanoparticles was higher than 30 MPa, the same level as for conventional high-temperature solders.

As the raw sintering materials, the major difference between Ag particles and Cu particles is their affinity to oxygen. The affinity of materials with oxygen can be evaluated using the Gibbs energy of formation of the corresponding oxides, which are summarized in the Ellingham diagram, as shown in Fig.1.13. The diagram suggests that the affinity of Cu is significantly higher than that of Ag, particularly, the oxidation of Cu can proceed spontaneously at any temperatures, whereas the oxidation of Ag hardly occurs above 150 ℃. Hence, the sintering of Ag particles can be performed in ambient air, however, a reducing atmosphere such as H_2 or formic acid vapor is generally needed in Cu sintering to avoid the formation of thin Cu oxides layer on the Cu particles because these oxides

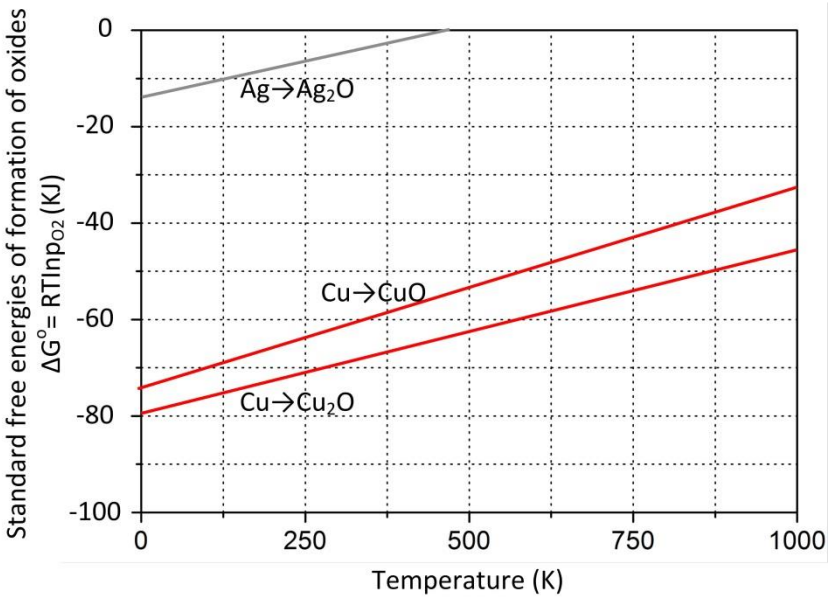

Figure 1.13 Ellingham Diagram for selected oxides [79].

layer will strongly inhibit the sintering behavior of Cu particles. Moreover, due to the strong affinity of Cu to oxygen, the Cu nanoparticles with a large specific surface area is very easily oxidized in air, thereby is significantly more difficult to synthesize and store than Ag nanoparticle. As shown in Fig. 1.12(a), the Cu_2O peak was observed in the C18 and C22 Cu nanoparticles, which has the smallest particle size in Ishizaki and Watanabe's study. On the other hand, microscale Cu particle is easy to manufacture, and whether by wet reaction process or atomizing process, it can be mass-produced. Moreover, the microscale Cu particles don't need some chemicals that are difficult to decompose, such as Polyvinyl Pyrrolidone (PVP), gelatin, and fatty acid, to prevent oxidation. Therefore it may be an unwise approach that reduces the size of Cu particle to nanoscale for increasing its sinterability, whereas, microscale Cu particle is more suitable as a sintering materials.

Another difference between Ag particles and Cu particles is that Cu particles could exhibit an inherent lower sinterability than that of Ag particles with the same particle size. In the view of the kinetic for Ag and Cu sintering, although their self-diffusion coefficients are expected to be similar based on their similarities in melting temperature and crystal structure, very wide ranges of self-diffusion coefficients have been reported in the literature for Ag 10^{-32}-10^{-9} m^2/s [80-84], and Cu 10^{-22}-10^{-16} m^2/s in the temperature range of 200 ℃ to 300 ℃ [84-87]. Moreover, Kim and etc. had reported a much faster surface diffusion of Ag than that of Cu at 220 ℃ based on the observation of

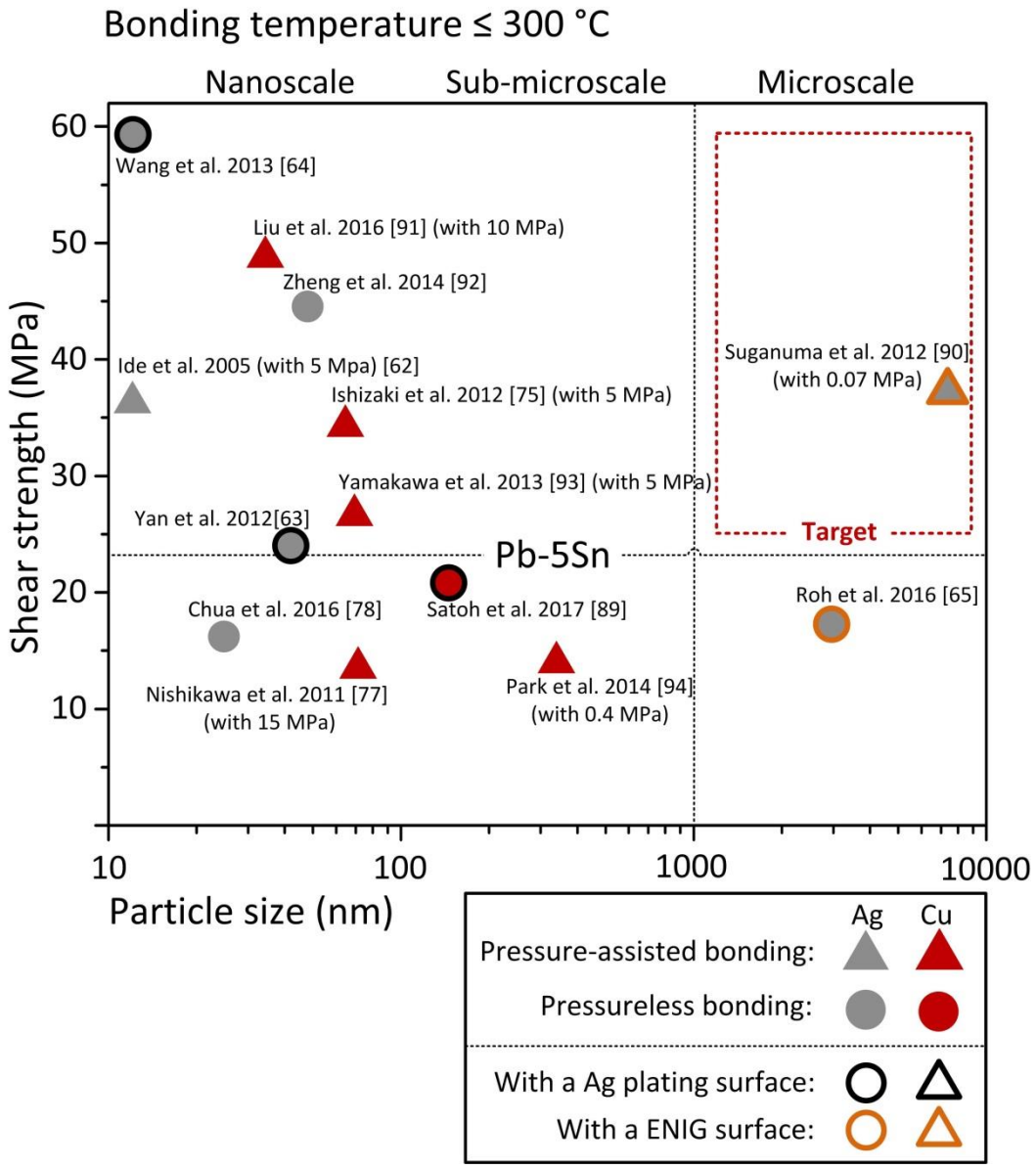

Figure 1.14 Shear strengths of joints bonded with different metallic particles in current studies. [62-65, 75, 78, 90-94]

the neck formation by surface self-diffusion [88]. In addition, Satoh and etc. also suggested that both the self-diffusion coefficient of Ag and the interdiffusion coefficient between Ag and Cu are greatly more than the self-coefficient of Cu in the temperature range of 200 ℃ to 300 ℃ [89]. Moreover, as shown in Fig. 1.14, researchers had reported that high-performance sintering joint can be produced by the pressureless sintering with Ag nanoparticle. In contrast, to fabricate a competitive Cu sintered joint, a high bonding pressure must be needed, even though the Cu nanoparticle sintering was performed in the reducing atmosphere for avoiding oxidation. Moreover, there has been some

researchers that reported sound Ag joints can be obtained by using low-pressure (<0.5 MPa) sintering or pressureless sintering of microscale Ag particles [65, 90], however, no publications can be found that reported the similar results with microscale Cu particles. Therefore, it is reasonable to deem that Cu particles perform a weaker bondability than Ag particles, and thus effective bonding with microscale Cu particles is very challenging.

1.4 Surface modification of microscale Cu particles

1.4.1 Theoretical basis

According to the discussion in *Chapter 1.3.2*, it can be concluded that, as a low cost and easy-to-manufacture metal particles, microscale Cu particles is suitable for the so-called low-temperature bonding process for high-temperature electronic packaging application, however, its low bondability is a hurdle that has to be crossed. With these in mind, we herein proposed a unique method, namely, surface modification to microscale Cu particles, in order to enhance the bondability of microscale Cu particles for achieving a high-performance joint. The target was shown in Fig. 1.14. In the following, we firstly discuss the theoretical basis the method of surface modification of microscale Cu particles, and then two different technical routes to achieve the surface modification are given.

As mentioned in *Section 1.2.4*, the driving force for sintering or bonding of particles is the reduction of the total interfacial energy and the reduction of the total energy can be expressed as

$$\Delta G = \Delta\left(\gamma \cdot A\right) = \Delta\gamma \cdot A + \gamma \cdot \Delta A \qquad (1.4)$$

In general, the size of microscale Cu particles for low-temperature bonding is in the range between 1 and 10 μm, and the total surface energy of the Cu particles is lower than 50 J/mole (surface energy of Cu is around 1-2 J/m^2 in the most literature [95-97]). This energy is inconsiderably small, compared with the energy change in oxide formation which is lower than -50 kJ/mole. So the desired bonded microstructure is difficult to achieve by the use of such a very small amount of energy, and it is necessary to enhance the driving force of the bonding. According to the equation 1, there are mainly three way to increase the driving force of bonding, including introducing additional free energy,

increasing the specific surface energy, and increasing the total surface area, as shown in equation 2-4. Within, increasing the total surface area is actually equal to reducing the particle size, and which has been beforehand abandoned. Therefore, we proposed a method, namely, surface modification to microscale Cu particles.

$$\Delta G_{new} = \Delta G_{additional} + \Delta(\gamma \cdot A) \quad (1.5)$$

$$\Delta G_{new} = \Delta(\gamma_{increased} \cdot A) \quad (1.6)$$

$$\Delta G_{new} = \Delta(\gamma \cdot A_{increased}) \quad (1.7)$$

In this study, a Sn surface coating on microscale Cu particle and a nanotextured surface formed on microscale Cu particle are suggested, respectively. It is expected that additional driving force for bonding can be introduced into the particle system by coated Sn on Cu particles, while the Cu nanotextured surface can significantly enhance the specific surface energy of pure Cu particles. In the follows, we will discuss the reason and the feasibility to these two surface modification methods.

1.4.2 Sn coating

Through coated Sn on Cu particles, a single-phase sintering system is changed to a binary-phase reactive system. And the spontaneous chemical reaction between Cu and Sn will happen during the bonding process, and which can help to facilitate the bonding. Below 350 ℃, there are two IMCs that formed by the reaction between Cu and Sn, and they are Cu_6Sn and Cu_3Sn [98]. The enthalpies of formation of Cu_6Sn and Cu_3Sn are shown in Table 1.9. It is clear that the formation energy of these IMCs is considerably larger than the total surface energy of microscale Cu particles in a single-phase

Table 1.9 Formation enthalpy of Cu_6Sn_5 and Cu_3Sn IMC in literatures.

Phase	Temperature (K)	Enthalpy of formation (kJ/mol)
Cu_6Sn_5 (η)	273 K	-7.03 [99]
	298 K	-6.1 [100]
Cu_3Sn (ε)	298 K	-8.2 [101]
	298 K	-7.82 [102]
	723 K	-7.81 [103]

system, therefore it is suggested that these great negative formation enthalpies can be regarded as an additional driving force of low-temperature bonding.

On the other hand, unlike the conventional TLP bonding process, the volume fraction of the IMCs phase formed in the joint can be controlled by adjusting the thickness of Sn coating, which can avoid the formation of fully IMC joint. In addition, electroless Sn plating on Cu is a well-matured technology, and therefore the feasibility of this surface modification method can be confirmed.

1.4.3 Cu nanotextured surface

In addition, to reduce the particle size, we also can improve the total surface energy in the bonding system by enhancing the surface energy of individual particles. One feasible method is to produce a nanotextured surface on the microscale Cu particles, by which the surface energy of those modified Cu particles will be significantly enhanced due to the nanoscale effect. With this in mind, we proposed an oxidation-reduction bonding process for producing a highly active nanotextured surface on microscale Cu particles. In-situ formation of Cu_2O nanoparticles took place on the surface of microscale Cu particles during the thermal oxidation process, followed by a transformation to Cu nanotextured surface during the consequent reduction process in the formic acid atmosphere. The detail of this process will be discussed in *Chapter 4*. Table1.10 summarized the main differences between two kinds of surface modification methods regarding the increased driving force for bonding, modification mode, and modification period.

Table 1.10 Comparison of two different surface modification methods

Method	Thermodynamic	Modification mode	Modification period
Sn surface coating	Negative formation enthalpies of IMC	Compositional	Pre-treatment
Cu nanotextured surface	Increased specific surface energy	Morphological	In-situ treatment

1.5 Purpose and scope of this study

The purpose of this study was to obtain a high-performance metallic joint based on low-temperature bonding using surface-modified microscale Cu particles for high-temperature electronic packaging application. Attempts were made to deal with the present challenges in Cu particle-based bonding technology. The dissertation presented two surface modification methods to improve the bondability of microscale Cu particles. It mainly covered the study of the process, mechanism, and thermal stability of transient liquid phase (TLP) bonding using Sn-coated Cu particles, solid-state bonding (SSB) using Sn-coated Cu particle, as well as oxidation-reduction bonding (ORB) using pure Cu particles, respectively.

In *Chapter 1*, the brief description on the background of wide-band-gap (WBG) semiconductor-based power device, immersing issues of WBG power device packaging and high-temperature die attach were given. And a purpose of low-temperature bonding process using surface-modified microscale Cu particles was also suggested.

In *Chapter 2*, the TLP bonding process using microscale Sn-coated Cu particles was suggested. Mainly, the microstructure, bonding strength, fracture mode, and high-temperature stability of the TLP bonding joint were clarified.

In *Chapter 3*, the processing and mechanism of the SSB process using microscale Sn-coated Cu particles was presented. The reliability of SSB joints under the high-temperature at 250 ℃ was also discussed.

In *Chapter 4*, the in-situ surface modification method of microscale Cu particles using an oxidation-reduction process was suggested. The surface morphological evolution of Cu particles during the thermal oxidation and subsequent reduction were clarified, and also the corresponding mechanism was discussed.

In *Chapter 5*, the oxidation-reduction process was introduced into the sintering bonding, and by which the ORB process was presented. The bonding properties of ORB process using microscale flake-shaped Cu particles were presented. Also, the thermal stability of the ORB joint was studied.

In Chapter 6, the effect of Cu particle sharp and substrate on the bonding properties of

pressureless ORB process was verified.

References

[1] J. Millan, P. Godignon, X. Perpina, A. Pérez-Tomás, and J. Rebollo, A survey of wide-bandgap power semiconductor devices. *IEEE trans. Power Electron.*, **29** (2014) 2155-2163.

[2] B. J. Baliga, *Fundamentals of power semiconductor devices*, Springer Science & Business Media, 2010.

[3] I.M. Mackintosh, The Electrical Characteristics of Silicon p–n–p–n Triodes, *Proceeding of the IRE*, **46** (1958) 1229-1235.

[4] R.W. Aldrich and N. Holonyak, Multiterminal p–n–p–n Switches, *Proceeding of the IRE*, **46** (1958) 1236-1239.

[5] D.A. Grant and J. Gowar, *Power MOSFETs: Theory and Applications*, Wiley, New York, 1989.

[6] B.J. Baliga, Enhancement and Depletion Mode Vertical Channel MOS-Gated Thyristors, *Electron. Lett*., **15** (1979) 645–647.

[7] T. M. Jahns and V. Blasko, Recent advances in power electronics technology for industrial and traction machine drives, *Proceedings of the IEEE*, **89** (2001) 963-975.

[8] B. K. Bose, Power electronics and motor drives recent progress and perspective, *IEEE Trans. Indus. Electron.*, **56** (2009) 581-588.

[9] R. W. Johnson, J. L. Evans, P. Jacobsen, J. R. Thompson, and M. Christopher, The changing automotive environment: high-temperature electronics. *IEEE Trans. Electron. Pack. Manuf.*, **27** (2004) 164-176.

[10] I.S. Mehdi, A.E. Brockschmidt, K.J. Karimi, *Proceedings of the High Temp. Electron. Conf. (HiTEC)*, 2006.

[11] R. F. Jurgens, High-temperature electronics applications in space exploration, *IEEE Trans. Indus. Electron.*, **2** (1982) 107-111.

[12] B.W. Ohme, M.R. Larson, J. Riekels, S. Schlesinger, K. Vignarajah, E.M. Nance, *Proceedings of the High Temp. Electron. Conf. (HiTEC)*, 2006.

[13] M. A. Huque, S. K. Islam, B. J. Blalock, C. Su, R. Vijayaraghavan, and L. M. Tolbert, Silicon-on-insulator based high-temperature electronics for automotive applications, *IEEE Int. Symp. Indus. Electron.*, (2008) 2538-2543.

[14] J. Watson, and G. Castro, A review of high-temperature electronics technology and applications, *J. Mater. Sci. Mater. Electron.*, **26** (2015) 9226-9235.

[15] P. G. Neudeck, R. S. Okojie, and L. Y. Chen, High-temperature electronics-a role for wide

bandgap semiconductors ?, *Proceedings of the IEEE,* **90** (2002) 1065-1076.

[16] M. N. Yoder, Wide bandgap semiconductor materials and devices, *IEEE Trans. Electron. Dev.*, **43** (1996) 1633-1636.

[17] C. Buttay, D. Planson, B. Allard, D. Bergogne, P. Bevilacqua, C. Joubert, M. Lazar, C. Martina, H. Morel, D. Tournier, and C. Raynaud, State of the art of high temperature power electronics, *Mater. Sci. Eng. B*, **176** (2011) 283-288.

[18] P. Roussel, SiC market and industry update, Int. SiC Power Electron. Appl. Workshop, 2011.

[19] W. Sabbah, S. Azzopardi, C. Buttay, R. Meuret, and E. Woirgard, Study of die attach technologies for high temperature power electronics: Silver sintering and gold–germanium alloy, *Microelectron. Reliab.*, **53** (2013) 1617-1621.

[20] M. A. Eleffendi, L. Yang, P. Agyakwa, and C. M. Johnson, Quantification of cracked area in thermal path of high-power multi-chip modules using transient thermal impedance measurement, *Microelectron. Reliab.*, **59** (2016) 73-83.

[21] E. Marcault, M. Breil, A. Bourennane, P. Tounsi, J. M. Dorkel, Study of mechanical stress impact on the I–V characteristics of a power VDMOS device using 2D FEM simulations, *Microelectron. Reliab.*, **52** (2012) 489-496.

[22] M. Ciappa, Selected failure mechanisms of modern power modules, *Microelectron. Reliab.*, **42** (2002) 653-667.

[23] L. Coppola, D. Huff, F. Wang, R. Burgos, and D. Boroyevich, Survey on high-temperature packaging materials for SiC-based power electronics modules, *IEEE Power Electron. Special. Conf.*, 2007 2234-2240

[24] T. McNutt, B. Passmore, J. Fraley, B. McPherson, R. Shaw, K. Olejniczak, A. Lostetter, High-Performance, Wide-Bandgap Power Electronics, *J. Electron. Mater.*, **43** (2014) 4552-4559.

[25] R. Thokala, J. Chaudhuri, Calculated elastic constants of wide band gap semiconductor thin films with a hexagonal crystal structure for stress problems, Thin Solid Films, **266** (1995) 189-191.

[26] K. Kim, W. R. Lambrecht, B. Segall, Elastic constants and related properties of tetrahedrally bonded BN, AlN, GaN, and InN, Phys. Rev. B, **53**(1996) 16310.

[27] Directive 2002/95/EC of the European Parliament and of the Council of 27 January 2003 on the restriction of the use of certain hazardous substances in electrical and electronic equipment, 2003,19–23,

[28] S. Menon, E. George, M. Osterman, M. Pecht, High lead solder (over 85%) solder in the electronics industry: RoHS exemptions and alternatives, *J. Mater. Sci. Mater. Electron.*, **26** (2015) 4021-4030.

[29] H. Schoeller, S. Bansal, A. Knobloch, D. Shaddock, J. Cho, Effect of alloying elements on

creep behavior of high Pb-based solders, *Mater. Sci. Eng. A*, **528** (2011) 1063–1070.

[30] M. Abtew, G. Selvaduray, Lead-free solders in microelectronics, *Mat. Sci. Eng. R*, **27** (2000) 95–141.

[31] European Commision, Recast of the RoHS directive.

[32] V. Chidambaram, J. Hattel, J. Hald, Design of lead-free candidate alloys for high-temperature soldering based on the Au–Sn system. *Mater. Des.*, **31** (2010) 4638-4645.

[33] Y. C. Liu, J. W. R. Teo, S. K. Tung, K. H. Lam, High-temperature creep and hardness of eutectic 80Au/20Sn solder. *J. Alloys Comp.*, **448** (2008) 340-343.

[34] V. Chidambaram, J. Hald, J. Hattel, Development of Au–Ge based candidate alloys as an alternative to high-lead content solders. *J. Alloys Comp.*, **490** (2010) 170-179.

[35] V. Chidambaram, H. B. Yeung, G. Shan, Reliability of Au-Ge and Au-Si eutectic solder alloys for high-temperature electronics, *J. Electron. Mater.*, **41**(2012) 2107-2117.

[36] Y. Takaku, L. Felicia, I. Ohnuma, R. Kainuma, K. Ishida, Interfacial reaction between Cu substrates and Zn-Al base high-temperature Pb-free solders, *J. Electron. Mater.*, **37** (2008) 314-323.

[37] N. Kang, H. S. Na, S. J. Kim, and C. Y. Kang, Alloy design of Zn–Al–Cu solder for ultra high temperatures, *J. Alloys Comp.*,**467** (2009) 246-250.

[38] S. Kim, K. S. Kim, S. S. Kim, and K. Suganuma, Interfacial reaction and die attach properties of Zn-Sn high-temperature solders, *J. Electron. Mater.*, **38** (2009) 266-272.

[39] J. M. Song, H. Y. Chuang, and Z. M. Wu, Interfacial reactions between Bi-Ag high-temperature solders and metallic substrates, *J. Electron. Mater.*, **35** (2006) 1041-1049.

[40] J. W. Jang, P. G. Kim, K. N. Tu, M. Lee, High-temperature lead-free Sn-Sb solders: Wetting reactions on Cu foils and phased in Cu–Cr thin films, *J. Mater. Res.*, **14**(1999) 3895-3900.

[41] V. Chidambaram, J. Hattel, J. Hald, High-temperature lead-free solder alternatives, *Microelectron. Eng.*, **88** (2011) 981-989.

[42] G. Zeng, S. McDonald, K. Nogita, Development of high-temperature solders: review, *Microelectron. Reliab.*, **52** (2012) 1306-1322.

[43] W. D. MacDonald, T. W. Eagar, Transient liquid phase bonding. *Annu. Rev. Mater. Sci.*, **22** (1992) 23-46.

[44] G. O. Cook, C. D. Sorensen, Overview of transient liquid phase and partial transient liquid phase bonding, *J. Mater. Sci.*, **46** (2011) 5305-5323.

[45] N. S.Bosco, F. W. Zok, Critical interlayer thickness for transient liquid phase bonding in the Cu-Sn system, *Acta Mater.*, **52** (2004) 2965-2972.

[46] J. F. Li, P. A. Agyakwa, C. M. Johnson, Interfacial reaction in Cu/Sn/Cu system during the

transient liquid phase soldering process, *Acta Mater.*, **59** (2011) 1198-1211.

[47] J. F. Li, P. A. Agyakwa, C. M. Johnson, Kinetics of Ag 3 Sn growth in Ag–Sn–Ag system during transient liquid phase soldering process, *Acta Mater.*, **58** (2010) 3429-3443.

[48] S. W. Yoon, M. D. Glover, K. Shiozaki, Nickel–tin transient liquid phase bonding toward high-temperature operational power electronics in electrified vehicles, *IEEE Trans. Power Electron.*, **28** (2013) 2448-2456.

[49] Y. C. Chen, C. C. Lee, Indium-copper multilayer composites for fluxless oxidation-free bonding, Thin Solid Films, **283** (1996) 243-246.

[50] J. B. Lee, H. Y. Hwang, M. W. Rhee, Reliability Investigation of Cu/In TLP Bonding, *J. Electron. Mater.*, **44** (2015), 435-441.

[51] B. J. Grummel, Z. J. Shen, H. A. Mustain, A. R. Hefner, Thermo-mechanical characterization of Au-In transient liquid phase bonding die-attach, *IEEE Trans. Compon. Pack. Manuf. Tech.*, **3** (2013) 716-723.

[52] N. S. Bosco, F. W. Zok, Strength of joints produced by transient liquid phase bonding in the Cu–Sn system, *Acta Mater.*, **53** (2005) 2019-2027.

[53] F. Lang, H. Yamaguchi, H. Nakagawa, H. Sato, Thermally stable bonding of SiC devices with ceramic substrates: Transient liquid phase sintering using Cu/Sn powders, *J. Electrochem. Soc.*, **160** (2013) 315-319.

[54] H. Greve, L. Y. Chen, I. Fox, F. P. McCluskey, Transient liquid phase sintered attach for power electronics, IEEE Electron. Compon. Technol. Conf., (2013) 435-440.

[55] H. Greve, S. A. Moeini, F. P. McCluskey, S. Joshi, Microstructural Evolution of Transient Liquid Phase Sinter Joints in High Temperature Environmental Conditions, IEEE Electron. Compon. Technol. Conferen., (2016) 2561-2568.

[56] S. J. L. Kang, *Sintering: densification, grain growth and microstructure*, Butterworth-Heinemann, 2004

[57] H. Schwarzbauer, Method of securing electronic components to a substrate, US4810672, Siemens, USA (1989).

[58] H. Schwarzbauer, Method and apparatus for fastening electronic components to substrates, US4903885, Siemens, USA (1990).

[59] H. Schwarzbauer, Apparatus for fastening electronic components to substrates, US5058796, Siemens, USA (1991).

[60] H. Schwarzbauer and R. Kuhnert, Novel large area joining technique for improved power device performance, *IEEE Trans. Ind. Appl.*, 1989.

[61] J. G. Bai, Z. Z. Zhang, J. N. Calata, G. Q. Lu, Low-temperature sintered nanoscale silver as a novel semiconductor device-metallized substrate interconnect material, IEEE Trans. Compon.

Pack. Technol., **29** (2006) 589-593.

[62] E. Ide, S. Angata, A. Hirose, K. F. Kobayashi, Metal–metal bonding process using Ag metallo-organic nanoparticles, *Acta Mater.*, **53** (2005) 2385-2393.

[63] J. Yan, G. Zou, A. P. Wu, J. Ren, J. Yan, A. Hu, Y. Zhou, Pressureless bonding process using Ag nanoparticle paste for flexible electronics packaging, *Scr. Mater.*, **66** (2012) 582-585.

[64] S. Wang, M. Li, H. Ji, C. Wang, Rapid pressureless low-temperature sintering of Ag nanoparticles for high-power density electronic packaging, *Scr. Mater.*, **69** (2013) 789-792.

[65] M. H. Roh, H. Nishikawa, S. Tsutsumi, N. Nishiwaki, K. Ito, K. Ishikawa, A. Katsuya, N. Kamada, M. Saito, Pressureless Bonding by Micro-Sized Silver Particle Paste for High-Temperature Electronic Packaging, *Mater. Trans.*, **57** (2016) 1209-1214.

[66] K. S. Siow, Are sintered silver joints ready for use as interconnect material in microelectronic packaging?, *J. Electron. Mater.*, **43** (2014) 947-961.

[67] K. S. Siow, Y. T. Lin, Identifying the Development State of Sintered Silver (Ag) as a Bonding Material in the Microelectronic Packaging Via a Patent Landscape Study, *J. Electron. Pack.*, **138** (2016), 020804.

[68] S. J. L. Kang, *Sintering: densification, grain growth and microstructure.* Butterworth-Heinemann, 2004.

[69] J. G. Bai, G. Q. Lu, Thermomechanical reliability of low-temperature sintered silver die attached SiC power device assembly, *IEEE Trans. Dev. Mater. Reliab.*, **6** (2006) 436-441.

[70] S. Sakamoto, T. Sugahara, K. Suganuma, Microstructural stability of Ag sinter joining in thermal cycling, *J. Mater. Sci. Mater. Electron.*, **24** (2013) 1332-1340.

[71] R. Khazaka, L. Mendizabal, D. Henry, Review on joint shear strength of nano-silver paste and its long-term high temperature reliability, *J. Electron. Mater.*, **43** (2014) 2459-2466.

[72] H. P. R. Frederikse, R. J. Fields, A. Feldman, Thermal and electrical properties of copper-tin and nickel-tin intermetallics, *J. Appl. Phys.*, **72** (1992) 2879-2882.

[73] G. Ghosh, Elastic properties, hardness, and indentation fracture toughness of intermetallics relevant to electronic packaging, *J. Mater. Res.*, **19** (2004) 1439-1454.

[74] C. C. Lee, P. J. Wang, J. S. Kim, Are intermetallics in solder joints really brittle?, *Proceedings of Electron. Compon. Technol. Conferen.*, (2007) 648-652.

[75] T. Ishizaki, R. Watanabe, A new one-pot method for the synthesis of Cu nanoparticles for low temperature bonding, *J. Mater. Chem.*, **22** (2012) 25198-25206.

[76] Y. Jianfeng, Z. Guisheng, H. Anming, Y. N. Zhou, Preparation of PVP coated Cu NPs and the application for low-temperature bonding, *J. Mater. Chem.*, **21** (2011) 15981-15986.

[77] H. Nishikawa, T. Hirano, T. Takemoto, N. Terada, Effects of joining conditions on joint strength of Cu/Cu joint using Cu nanoparticle paste, *Open Surf. Sci. J.*, **3** (2011) 60-64.

[78] T. Ishizaki, K. Akedo, T. Satoh, R. Watanabe, Pressure-free bonding of metallic plates with Ni affinity layers using Cu nanoparticles, *J. Electron. Mater.*, **43**(2014) 774-779.

[79] S. M. Howard, *Ellingham Diagrams: Standard Gibbs Energies of Formation for Oxides*, SD School of Mines and Technology, Rapid City, SD, 2006.

[80] R. Dannenberg, E. A. Stach, J. R. Groza, and B. J. Dresser, In-situ TEM observations of abnormal grain growth, coarsening, and substrate de-wetting in nanocrystalline Ag thin films, *Thin Solid Films*, **370** (2000) 54-62.

[81] U. Kurpick, G. Meister, and A. Goldmann, Diffusion of Ag on Cu (110) and Cu (111) studied by spatially resolved UV-photoemission, *Appl. Surf. Sci.*, **89** (1995) 383-392.

[82] G. E. Rhead, Surface self-diffusion of silver in various atmospheres, *Acta Metall.*, **13** (1965) 223-226.

[83] K. Yoshihara and K. Nii, The effect of oxygen potential on the surface self-diffusion coefficient of silver, *Trans. Jpn. Inst. Met.*, **20** (1979) 533-542.

[84] R. R. Hough, An investigation of the surface self-diffusion coefficients of pure copper and silver by the grain boundary grooving technique, *Scr. Metall.*, **4** (1970) 559-561.

[85] G. C. Kuczynski, Self-diffusion in sintering of metallic particles, *AIME TRANS.*, **185** (1949) 169-178.

[86] J. Y. Choi and P. G. Shewmon, Surface Diffusion of Gold and Copper on Copper, *AIME TRANS.*, **230** (1964) 123-132.

[87] N. A. Gjostein, Measurement of the surface self-diffusion coefficient of copper by the thermal grooving technique, *AIME TRANS.*, **221**(1961) 1039-1046.

[88] S. J. Kim, E. A. Stach, C. A. Handwerker, Fabrication of conductive interconnects by Ag migration in Cu–Ag core-shell nanoparticles, *Appl. Phys. Lett.*, **96** (2010) 144101.

[89] T. Satoh, T. Ishizaki, K. Akedo, Silver Adhesive Layer for Enhanced Pressure-Free Bonding Using Copper Nanoparticles, *J. Electron. Mater.*, **46** (2017) 1279-1286.

[90] K. Suganuma, S. Sakamoto, N. Kagami, D. Wakuda, K. S. Kim, M. Nogi, Low-temperature low-pressure die attach with hybrid silver particle paste, *Microelectron. Reliab.*, **52** (2012) 375-380.

[91] J. Liu, H. Chen, H. Ji, M. Li, Highly Conductive Cu–Cu Joint Formation by Low-Temperature Sintering of Formic Acid-Treated Cu Nanoparticles, *ACS Appl. Mater. Interf.*, **8** (2016) 33289-33298.

[92] H. Zheng, D. Berry, K. D. Ngo, G. Q. Lu, Chip-bonding on copper by pressureless sintering of nanosilver paste under controlled atmosphere, *IEEE Trans. Compon. Pack. Manuf. Technol.*, **4** (2014) 377-384.

[93] T. Yamakawa, T. Takemoto, M. Shimoda, H. Nishikawa, K. Shiokawa, N. Terada, Influence of

joining conditions on bonding strength of joints: efficacy of low-temperature bonding using Cu nanoparticle paste, *J. Electron. Mater.*, **42** (2013) 1260-1267.

[94] S. W. Park, R. Uwataki, S. Nagao, T. Sugahara, Y. Katoh, H. Ishino, K. Sugiura, K. Tsuruta K. Suganuma, Low-pressure sintering bonding with Cu and CuO flake paste for power devices. *Proceeding of IEEE Electron. Compon. Technol. Conf.*, (2014) 1179-1182.

[95] A. S. Skapski, A theory of surface tension of solids—I application to metals, *Acta Metal.*, **4** (1956) 576-582.

[96] W. R. Tyson, W. A. Miller, Surface free energies of solid metals: Estimation from liquid surface tension measurements, *Surf. Sci.*, **62** (1977) 267-276.

[97] V. K.Kumikov, K. B. Khokonov, On the measurement of surface free energy and surface tension of solid metals, *J. Appl. Phys.*, **54** (1983) 1346-1350.

[98] H. Okamoto, *Desk Handbook Phase Diagrams for Binary Alloys*, ASM International, Ohio, 2000.

[99] A. Gangulee, G.C. Das, M.B. Bever, An X-ray diffraction and calorimetric investigation of the compound Cu_6Sn_5, *Metall. Trans.* **4** (1973) 2063-2066.

[100] H. Flandorfer, U. Saeed, C. Luef, A. Sabbar, H. Ipser, Interfaces in lead-free solder alloys: Enthalpy of formation of binary Ag-Sn, Cu-Sn and Ni-Sn intermetallic compounds, *Thermochim. Acta*, **459** (2007) 34-39.

[101] J.B. Cohen, J.S.L.I. Leach, M.B. Bever, *JOM*, **6** (1954) 1257– 1258.

[102] O.J. Kleppa, Heat of formation of solid and liquid binary alloys of copper with cadmium, indium, tin and antimony at 450, *J. Phys. Chem.*, **60** (1956) 852–858.

[103] R. Hultgren, P.D. Desai, D.T. Hawkins, M. Gleiser, K.K. Kelley, *Selected Values of the Thermodynamic Properties of Binary Alloys*, ASM Metals Park, OH, USA, 1971.

Chapter 2
Transient liquid phase bonding using Sn-coated Cu particles

2.1 Introduction

When the Cu particles were coated by the Sn layer, the Cu-Sn metallurgical reaction was introduced into the bonding system. This metallurgical reaction has been well studied over decades [1-4]. According to the Cu-Sn binary phase diagram, as shown in Fig 2.1, it involves the formation of two kinds of intermetallic compound (IMC) below 350 ℃: Cu_6Sn_5 and Cu_3Sn. Many studies have been focused on the physical properties of Cu-Sn IMCs. It has been found they have a higher melting temperature, mechanical strength, and creep resistance than conventional Sn-based solders. Hence Cu-Sn IMCs are suitable as bonding materials for high-temperature electronic packaging. Indeed, Cu-Sn transient liquid phase (TLP) bonding, which can be processed at relatively low temperatures while resulting in higher remelt temperatures of Cu-Sn IMC joints, has been proven to be a possible solution to the high-temperature die attach application [6-8]. However, some common drawbacks of this process still remain. For example, the complete consumption of low-melting metals could be a time-consuming process. Moreover, an IMC joint is considered to show less ductility than a bulk

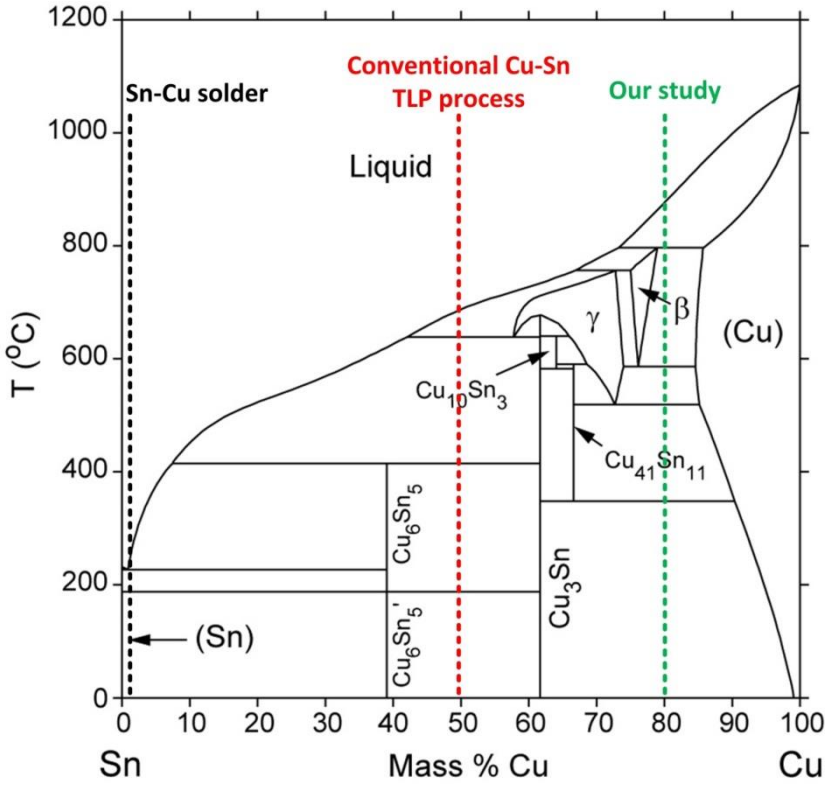

Figure 2.1 Cu-Sn binary phase diagram [5].

metallic joint obtained through conventional high-temperature soldering or Ag nanoparticles (NPs) sintering.

In this chapter, based on a microscale Sn-coated Cu particle, we presented a TLP bonding process and proposed that a thermally stable composite joint fully comprising a Cu_3Sn IMC with a dispersion of ductile Cu particles could be obtained after bonding at 300 ℃. Some unique feature of this TLP bonding process including obtained microstructure was presented. The influence of bonding condition on the mechanical property the TLP bonding joint was also studied. In addition, the high-temperature stability of the bonding joint, which is crucial for the high temperature reliability of the bonding joint, was also discussed.

2.2 Experimental

2.2.1 Fabrication of Sn-coated Cu particle

Microscale Cu particles were used as the starting material (1400Y, D50: 6.2 μm, Mitsui Mining

& Smelting Co. Ltd). The Sn-coated Cu particles, which is hereafter referred as Cu@Sn particles, were fabricated through electroless plating of Sn on Cu particles by Okuno Chemical Industries Co. Ltd. The Cu particles were firstly put into a dilute sulfuric acid (20 ml/L) to remove the native oxide layer and activate the surface of Cu particles. Then, after filtering and cleaning by deionized water, the Cu particles were added into the electroless Sn plating solution (Substar 5N-5, Okuno Chemical Industries Co. Ltd). The plating reaction was at 60 ℃ for 20 min with continuous stirring. After that,the Cu@Sn particles were filtered and cleaned by deionized water again. Finally, the particles were washed with ethanol, and then dried and ready for making paste. The cross-section view and X-ray diffraction (XRD) pattern of the Cu@Sn were shown in Fig. 2.2. The average diameter of the Cu particles was 6.2 μm and the average thickness of the Sn coating was less than 0.5 μm. The mole ratio of Cu to Sn in a Cu@Sn particle was more than 4:1, calculated using the following equation:

$$\frac{n_{Cu}}{n_{Sn}} = \frac{D_{Cu}^3 \rho_{Cu} M_{Sn}}{(D_{Cu@Sn}^3 - D_{Cu}^3)\rho_{Sn} M_{Cu}} \qquad (2.1)$$

where n, ρ, and M with subscripts representing Cu and Sn are the corresponding molar quantities, densities, and molar weights, respectively. D_{Cu} and $D_{Cu@Sn}$ are the mean diameters of Cu core particles and Cu@Sn particles, respectively. In the Fig. 2.2b, in addition to the diffraction peaks of Cu and Sn peaks, Cu_6Sn_5 (η) peak was also observed, indicating a slight Cu_6Sn_5 IMC has formed between Sn coating and Cu core during the electroless plating process.

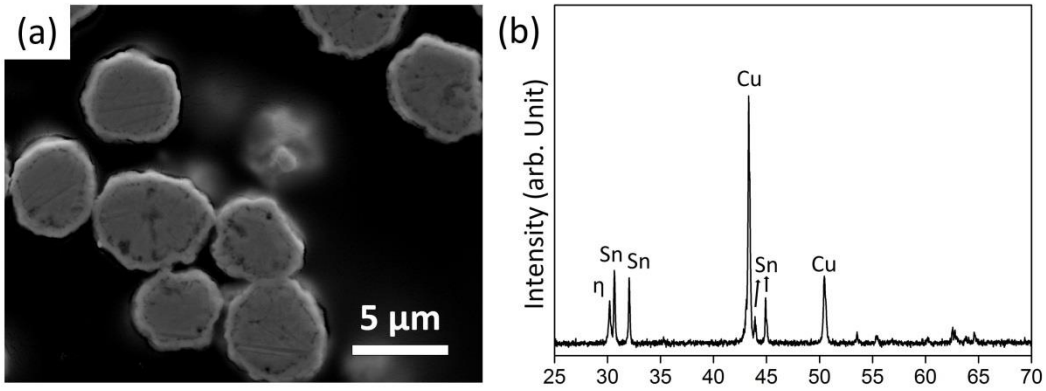

Figure 2.2 (a) SEM image of cross-section of Cu@Sn particles, (b) XRD profile of Cu@Sn particles.

2.2.2 Preparation of particle paste

Cu@Sn particle paste was prepared by adding a terpineol solvent (16 wt. %) to the Cu@Sn particles, as shown in Fig. 2.3a. Fig. 2.3b shows the thermogravimetric analysis (TGA) and the differential scanning calorimetry (DSC) traces for the paste during heating under N_2 (temperature increasing at 10.00 ℃ min -1), which revealed that the vaporization of the terpineol mostly occurred below 150 ℃. The DSC trace shows an obvious endothermic peak at approximately 230 ℃, indicating the melting of the Sn coating.

2.2.3 Transient liquid phase bonding process

Fig. 2.4a shows a schematic of the TLP bonding joint with Cu@Sn particle paste. A pure Cu disc was selected to fabricate the joint in this study. It is because direct bonding Cu (DBC) with Cu surface is the common used substrate for high-temperature die attach. Moreover, compared to the Ni- or Au-finished substrate, Cu substrate generally shows a modest bondability in current die attaching process, thus making it suitable as dummy substrate. Fig. 2.4b gives the typical heating profile of the bonding process. The prepared Cu-Cu joint specimens with the paste were first pre-heated at 130 ℃ for 5 min to evaporate the solvent, then heated continuously to the bonding temperature of 300 ℃ at 1 ℃/s, and bonded at 300 ℃ for different time. It should be noted that around 70 s was took when

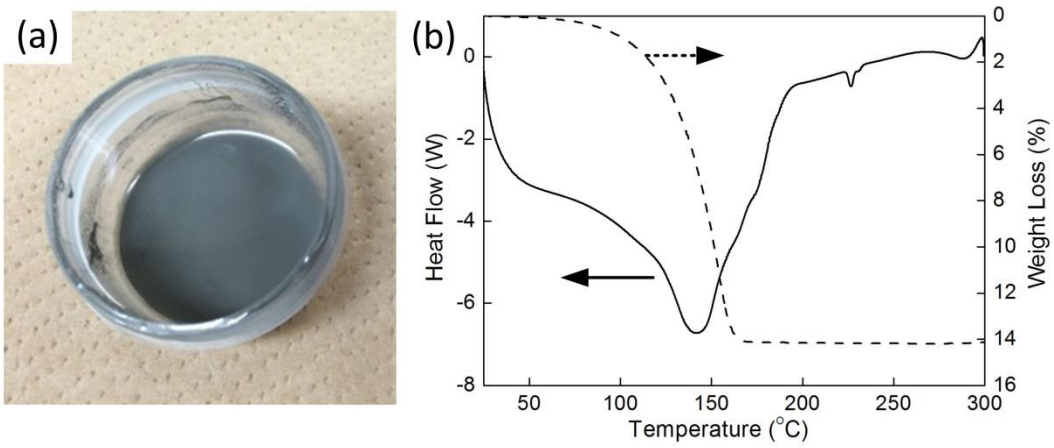

Figure 2.3 (a) Optical image of prepared Cu@Sn particle paste, (b) traces of TG and DSC for Cu@Sn particle paste during heating in N_2 (temperature increasing at 10 ℃ min^{-1}).

the temperature rose from the melt point of Sn to 300 ℃. The entire process was performed under a certain amount of applied pressure using a thermo-compression bonding system, as shown in Fig. 2.4c. A formic acid atmosphere was used in the entire bonding process to reduce the oxide layer on Sn coating. The removal of oxide layers on the coated Sn was attributed to the reducing reaction [9],

$$SnO + 2HCOOH(g) \rightarrow Sn(HCOO)_2 + H_2O(g) \quad (2.2)$$

$$SnO_2 + 2HCOOH(g) \rightarrow Sn(HCOO)_2 + H_2(g) + 2CO_2(g) \quad (2.3)$$

At temperatures higher than 150 ℃,

$$Sn(HCOO)_2 \rightarrow Sn + H_2(g) + 2CO_2(g) \quad (2.4)$$

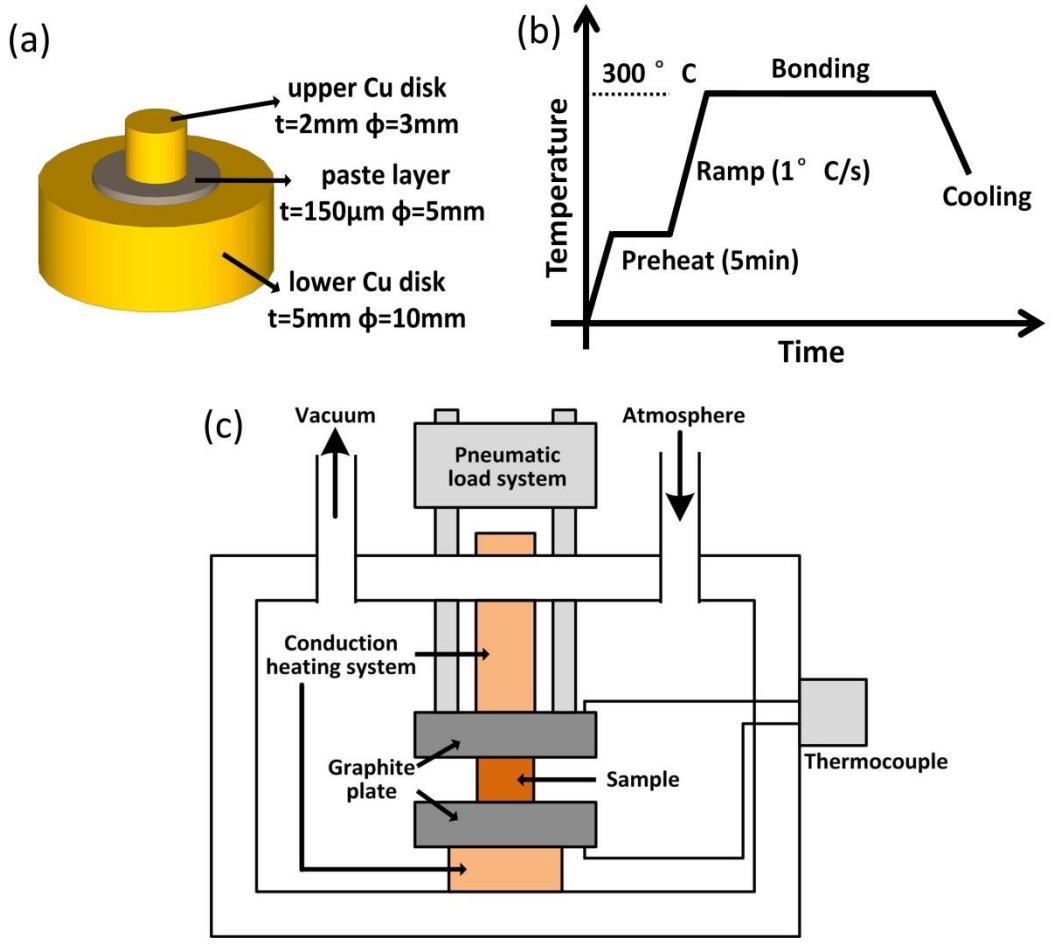

Figure 2.4 Illustration of TLP bonding process using Cu@Sn particle paste: (a) schematic diagram of Cu-Cu joint, (b) heating profile of bonding process, and (c) schematic diagram of large-area thermo-compression system used in the study.

In addition, thermal aging test of TLP bonding joint was conducted at 250 ℃ in the convection oven for the storage time up to 1000 h under an air atmosphere.

2.2.4 Characterization methods

The shear strength of the bonded joints was evaluated by using a shear tester (STR-1000, Rhesca) at head speed of 1mm/min, where the fly height was 200 μm from the bottom of the specimen. For each bonding condition, we tested three samples for collecting the shear strength data and calculated the average value. X-ray diffraction (XRD) analysis of was conducted by an X-ray diffractometer (Rigaku Ultima IV) using Cu-Kα radiation (λ = 1.5405 Å). The diffracted beam angle, 2θ was scanned in steps by 0.01 ° in the angular range from 20 to 80 °. The cross section microstructures and the fractured surfaces of the bonded joints were observed by a field emission scanning electron microscopy (FE-SEM, Hitachi SU-70). The composition of the microstructure and the fracture surface was measured with an electron probe microanalyzer (EPMA, JXA-8530F, JEOL).

2.3 Shear strength and microstructure of bonding joint

Fig. 2.5 shows the cross-sectional microstructure of joints after the TLP bonding at 300 ℃ for 30 s under a bonding pressure of 10 MPa. As shown in Fig 2.5b, a noticeable two-phase mixture microstructure was observed, which was shown by a gray color matrix with dark color embedded particles. Quantitative energy dispersive X-ray (EDX) point analysis showed that the atom ratio of Cu to Sn was near 3:1 in the light region of the TLP joints and that the dark particles uniformly distributed in the light region were Cu particles, which indicated that the bonding joints fully comprised the Cu-Sn IMC phase with a uniform dispersion of Cu particles. According to the Cu-Sn binary phase diagram, as shown in Fig. 2.1, this two-phase mixture microstructure achieves thermodynamic equilibrium below 350 ℃. In addition, although there are some small voids in the TLP joint, the microstructure of the TLP joint is very dense, which should be attributed to the form of liquid Sn during the bonding process. Fig. 2.6 gives the EMPA images and corresponding elemental mappings of a near-substrate region in the TLP joint, in which the two-phase composite microstructure is clear. The IMC matrix is dense and shows a very uniform composition in the entire

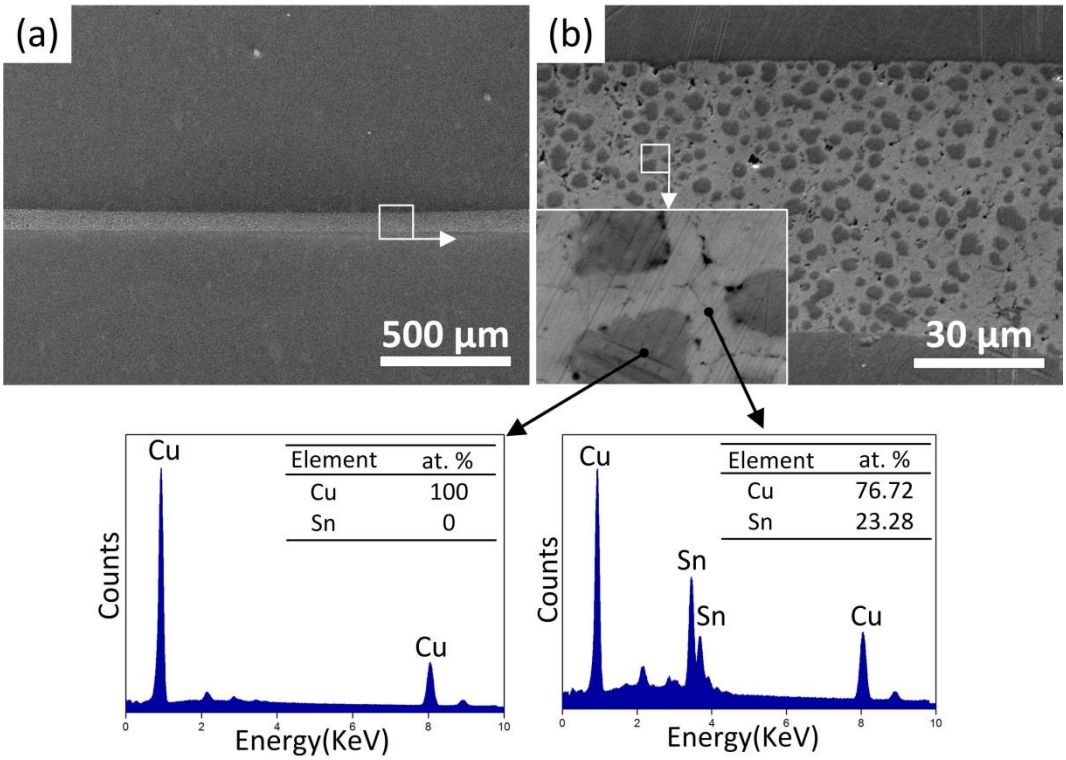

Figure 2.5 SEM images of TLP bonding joints after bonding at 300 ℃ for 30 s under a bonding pressure of 10 MPa and corresponding EDX spectra.

region, which means that the homogenization of the IMC phase has been completed. On the other hand, the embedded Cu particles shows a smaller size than the Cu core of the initial Cu@Sn particles, indicating a consumption of Cu by the Cu-Sn metallurgical reaction. In addition, it is found that some void formed in the Cu-Sn IMC matrix or at the interface between Cu-Sn IMC matrix and embedded Cu particles, and the mechanism of the formation of these voids will be discussed in the section 2.4. Fig. 2.7a shows the shear strength of TLP joints bonded with 30, 300, and 1200 s under the bonding pressure of 10 MPa. Under the bonding pressure of 10 MPa, the value for the shear strength reached 24.2 MPa with the bonding time of 30s, and it is higher than that of the joint using conventional Pb-5Sn high-temperature solder [10,11]. Moreover, it is found that the effect of bonding time on the shear strength is insignificant. The joint with the bonding time of 300 s shows an almost same shear strength to the joint bonded with 30 s. After a further increase of the bonding time to 1200 s, the shear strength of the joint was just slightly increased up to a value of 27.5 MPa. In addition, the shear strength of the joint bonded in N_2 is also given in the Figure. The joint bonded for 1200 s under a

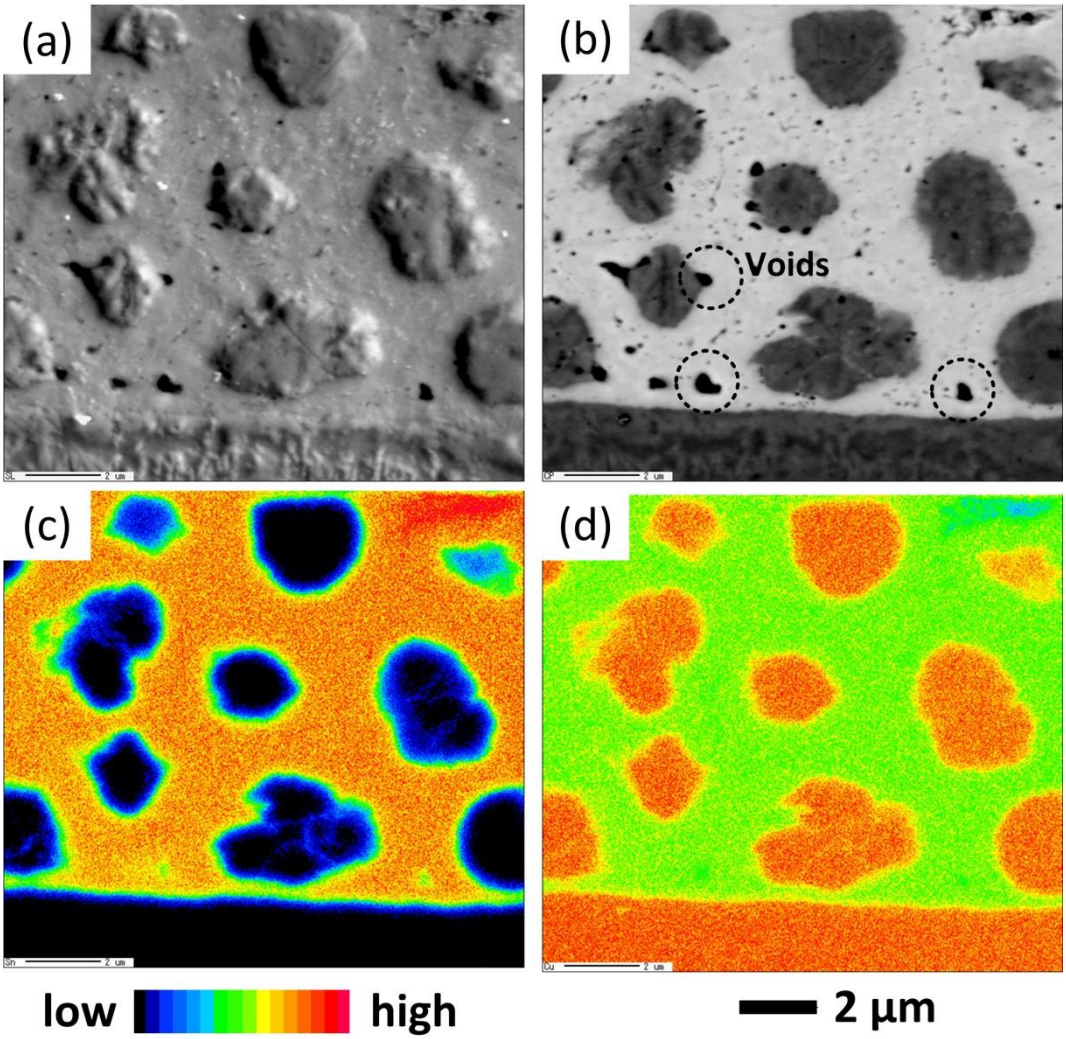

Figure 2.6 (a) SEM image and (b) backscattered electron (BSE) image of near-substrate region in TLP joint bonded with 30 s under a bonding pressure of 10 MPa. (c) and (d) is the corresponding EMPA elemental mapping of Sn and Cu, respectively.

pressure of 10MPa only exhibited a negligible strength lower than 3 MPa, indicating that the formic acid gas atmosphere is needed to obtain an effective bonding. Fig. 2.7b shows the shear strength of TLP joints bonded for 30 s under the bonding pressure of 5, 10, and 20 MPa,respectively. It can be seen the bonding pressure had a great influence on the shear strength of the TLP joint. With the same bonding time of 30 s, the shear strength was obviously increased with the increase of the bonding pressure.

The microstructures of the TLP joints bonded with different conditions are given in Fig. 2.8. In Fig. 2.8ab, the joints were bonded at 300 ℃ under a bonding pressure of 10 MPa for 30 s and 1200 s,

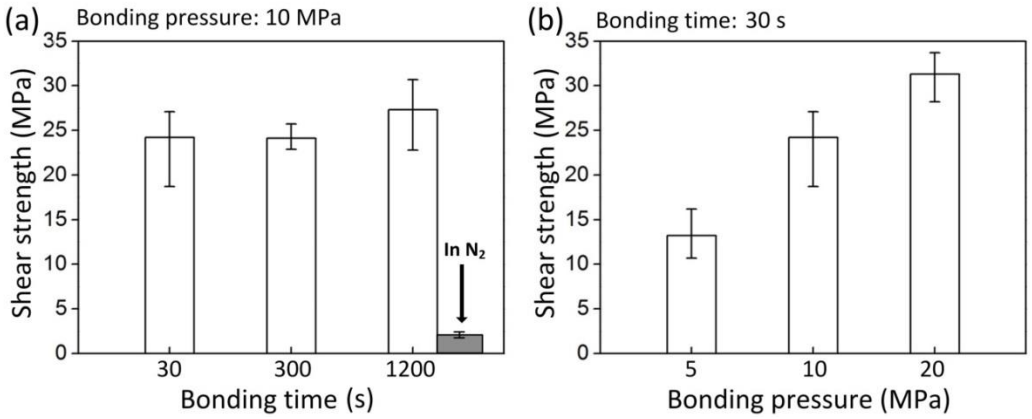

Figure 2.7 (a) Shear strength of joints: (a) after bonding with a pressure of 10 MPa for 30, 300, 1200 s, respectively, and (b) after bonding for 30 s with a pressure of 5, 10, 20 MPa, respectively.

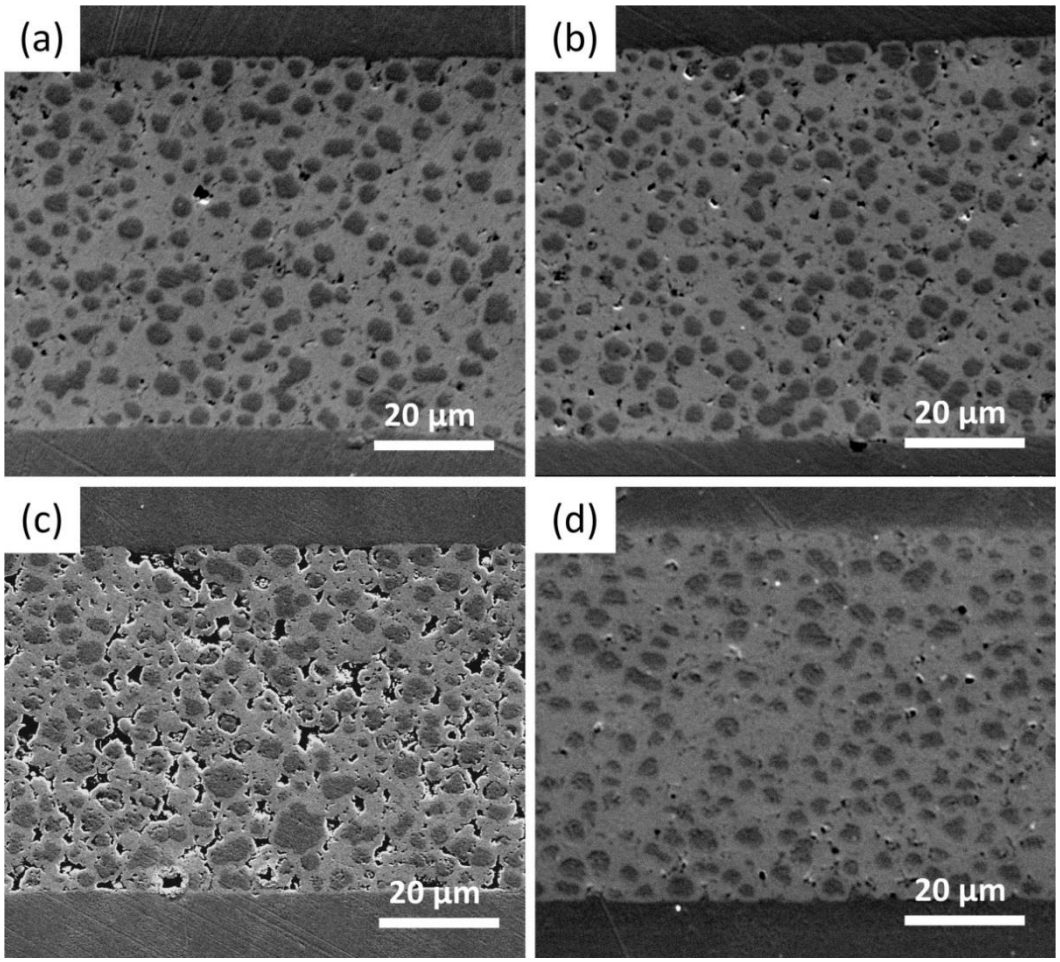

Figure 2.8 SEM images of TLP bonding joints: (a) after bonding at 300 ℃ for 30 s under a bonding pressure of 10 MPa, (b) after bonding at 300 ℃ for 1200 s under a bonding pressure of 10 MPa, (c) after bonding at 300 ℃ for 30 s under a bonding pressure of 5 MPa, (d) after bonding at 300 ℃ for 30 s under a bonding pressure of 20 MPa.

respectively. Both joints exhibited the similar noticeable two-phase mixture microstructure, and also, the density of both joints showed little different. It demonstrates that the most densification process in the TLP joint had finished after the bonding for 30 s, consistent with the result of joint strengths in Fig 2.7a. On the other hand, Fig. 2.8cd show the microstructure of the TLP joint boned at 300 ℃ for 30 s under the bonding pressure of 5 MPa and 20 MPa, respectively. Many obvious cracks and pores can be observed in the bonding layer of the joint bonded with 5 MPa, and which should attribute to the poor joint strength lower than 15 MPa, as shown in Fig. 2.7b. In contrast, the joint bonded with 20 MPa (Fig. 2.7d) exhibited a similar dense bonding layer with the joint bonded with 10 MPa (Fig. 2.7a). It is believed that high bonding pressure induced dense microstructure, and thus leading to a sound bonding strength. In addition, although the joint bonded with 20 MPa exhibited the highest shear strength, the bonding pressure of 10 MPa was enough to form the dense bonding microstructure and to obtain the sound joint. Therefore, 10 MPa is selected as the standard bonding pressure in my study.

2.4 Phase transform and bonding mechanism

XRD analysis of Cu@Sn particles after heating was conducted to understand the phase evolution of the joints during the TLP bonding, as shown in Fig. 2.9. The Cu@Sn particle samples were first heated under the same process conditions of TLP bonding except for the bonding pressure, then cooled to the room temperature to analyze. After the particles were heated to certain temperatures, a controllable cooling system was used to accelerate the cooling process of the heated particles to reduce the influence of high temperature holding time on the phase composition of the samples. As shown in Fig 2.9, before the heating, the η-Cu_6Sn_5 phase had formed. Xue et al. had reported the formation of η-Cu_6Sn_5 IMC during the electroless plating of Sn on the Cu foil [12]. This is consistent with my results. Then, at 210 ℃ before the melting of Sn coating, the η-Cu_6Sn_5 peak became stronger while the Sn peak became weaker, indicating that the η-Cu_6Sn_5 IMC grew continuously at the expense of the Sn coating. Meanwhile, the ε-Cu_3Sn peak was detected though it was weak. At 260 ℃, the Sn peak disappeared, while a stronger ε-Cu_3Sn peak and a weakened η-Cu_6Sn_5 peak were observed, indicating that a transient liquid Sn phase had been completely

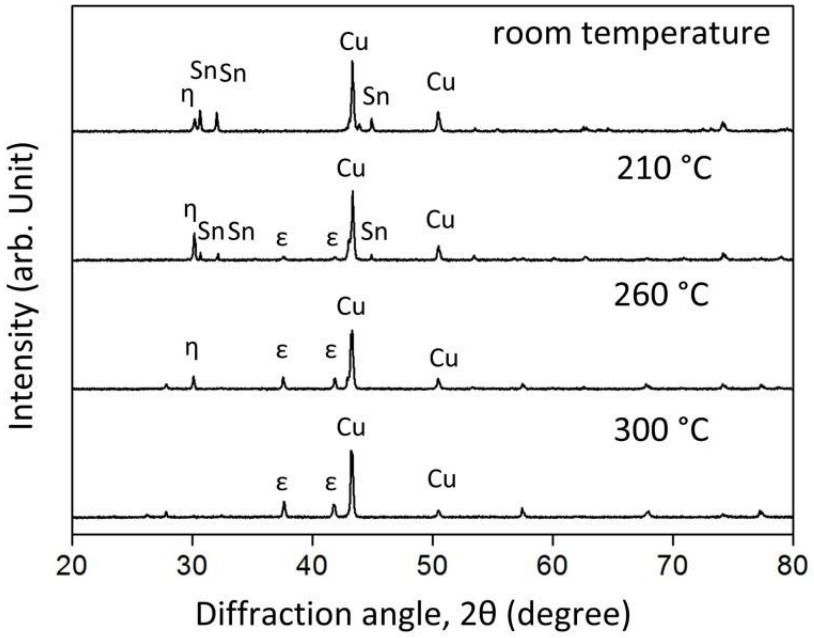

Figure 2.9 XRD analysis of consisting phases in Cu@Sn particles during the heating.

consumed during heating. Later, after bonding at 300 ℃, the η-Cu_6Sn_5 peak also disappeared, and only the ε-Cu_3Sn and Cu peaks were observed, which revealed that the transient η-Cu_6Sn_5 phase had been completely consumed. All of the η-Cu_6Sn_5 phase had completely transformed into the Cu_3Sn during the bonding process and the Cu_3Sn/Cu mixture phase was finally achieved. A Cu-Sn-based bonding joint without a Cu_6Sn_5 IMC phase is required for high-temperature usage because the Cu_6Sn_5 IMC formed during the Cu-Sn reaction is thermally unstable. It tends to transform into Cu_3Sn when the composition of the joint is at Cu-rich region of a Cu-Sn binary system. Even at the Sn-rich region, Cu_6Sn_5 phase exists in two crystal structures with an allotropic transformation from hexagonal η-Cu_6Sn_5 to monoclinic η'-Cu_6Sn_5 at temperatures lower than 186 ℃, as shown in Fig. 2.1. Cu_3Sn,

Table 2.1 Lattice type and density of three different Cu-Sn IMC phases [12, 13].

IMC phase	Lattice type	Density (g/cm^3)
η-Cu_6Sn_5	Hexagonal	8.448
η'-Cu_6Sn_5	Monoclinic	8.270
ε-Cu_3Sn	Orthorhombic	8.90
Cu	FCC	8.96

η-Cu_6Sn_5, and η'-Cu_6Sn_5 have different lattice type and density, and therefore both transformations are accompanied by a volume change, which will induce thermal stresses and affect the joint reliability during the high-temperature operation of power devices.

It is worth noting that compared to the long bonding time required to obtain a full Cu_3Sn or Cu_3Sn-Cu composite microstructure in the previously reported Cu-Sn TLP bonding [6,8], the bonding time in my study is very short. To clarify the reason for the quick formation of the Cu_3Sn-Cu two-phase mixture microstructure, we must determine the microstructure evolution of the joint during the TLP bonding. During the heating stage before the melting of Sn, the obvious evaporation of the terpineol solvent began at around 100 ℃ and reached its fastest rate at round 150 ℃, as shown in Fig. 2.3b and particles came into close contact under the applied pressure. Here, in order to avoid the excessive consumption of the Sn coating before its melting, relatively low pre-heating temperature was preferred, thus 130 ℃ was selected in the pre-heating process. Then, above 231 ℃, a liquid phase formed by the melting of the Sn coating and flowed into the gaps between the particles through capillary action, which resulted in the obvious densification of the joint layer. Thus, molten Sn can wet the Cu core without spreading over Cu core. Meanwhile, the liquid Sn was continually consumed by the growth of Cu_6Sn_5 and Cu_3Sn IMC. Once liquid Sn was fully consumed, the Cu_3Sn phase continuously grew at the expense of Cu_6Sn_5 and Cu, which is dominated by the solid-state diffusion of Sn and Cu atoms. Zeng et al. have depicted the mechanism of the growth of Cu_3Sn in a solder joint during a solid state aging [15]. The Cu atoms leave the Cu substrate and diffuse through Cu3Sn and react with Cu_6Sn_5 at the interface between Cu_6Sn_5 and Cu_3Sn, it forms more Cu_3Sn and thus pushes the Cu_6Sn_5/Cu_3Sn interface towards Cu_6Sn_5. When one formula of Cu_6Sn_5 is converted into Cu_3Sn, it releases 3 Sn atoms:

$$Cu_6Sn_5 \rightarrow 2Cu_3Sn+3Sn \qquad (2.5)$$

While the majority of the released Sn atoms will react with the in-coming Cu atoms at the Cu_6Sn_5/Cu_3Sn interface to form Cu_3Sn:

$$9Cu+3Sn \rightarrow 3Cu_3Sn \qquad (2.6)$$

Combining equation (2.5) with (2.6), we can obtain the equation to explain the growth of Cu_3Sn at the expense of Cu and Cu_6Sn_5:

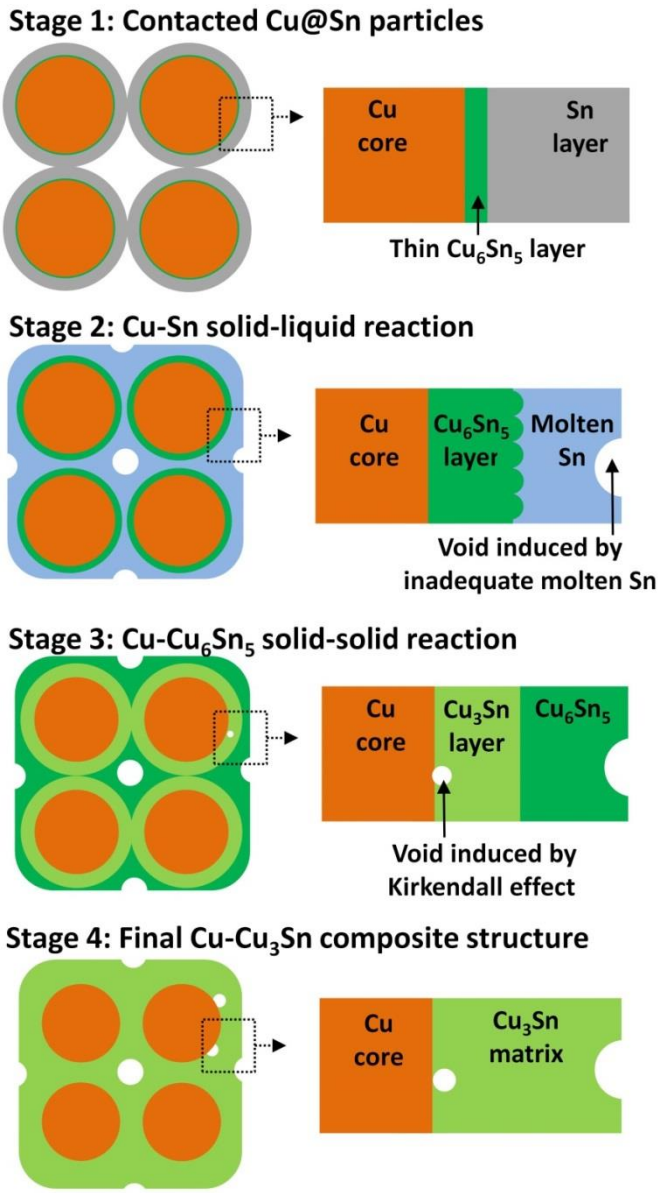

Figure 2.10 Illustration of microstructure evolution and phase transform of the bonding layer during TLP process

$$Cu_6Sn_5 + 9Cu \rightarrow 5Cu_3Sn \qquad (2.7)$$

As mentioned in section 2.2.1, the mole ratio of Cu to Sn in a particle is greater than 3:1, which means the uniformly distributed Cu particles in the joint can supply sufficient Cu flux to enable all of the Cu_6Sn_5 phase to transform into Cu_3Sn phase. Once the Cu_6Sn_5 phase was consumed completely, the solid reaction stopped. The growth kinetics of this solid reaction have been studied by many

researchers [1,3,16]. It is well known that increasing the reaction temperature can accelerate the diffusion of reacting species and thus speed up the growth of the Cu_3Sn phase. Both Cu and Sn atoms diffuse in the Cu_3Sn phase; the diffusion of Cu is approximately three times faster [1]. Therefore, it is suggested that a sufficient amount of Cu in the Cu@Sn particle (three times more than Sn) yields a Cu-rich composition in the joint and gives rise to the final Cu_3Sn/Cu two-phase microstructure. Moreover, the high bonding temperature (300 ℃) and uniformly distributed Cu core that provides the Cu flux contribute to the quick formation of this thermodynamically stable microstructure. A schematic diagram is given in Fig 2.10 to illustrate the microstructure evolution and phase transform during the TLP bonding process.

In addition, there were a few small voids in the Cu_3Sn matrix and at the interface between the Cu_3Sn matrix and the Cu particles, as shown in Fig 2.6. It was suggested that these two kinds of voids with different positions had different formation mechanism. Firstly, the formation of the void in the Cu_3Sn matrix was led by the inadequate molten Sn. It is believed that the amount of liquid Sn formed in the TLP bonding is critical for the densification and quick formation of the Cu_3Sn/Cu composite microstructure. The formation of excess liquid Sn will prolong the TLP bonding process and even change the final phase constituent of the bonding joint, and therefore a thin Sn coating layer is preferred in my study. However, the Sn coating in some particles was too thin and the formed liquid Sn did not fill the space between the particles, which result in the formation of voids in the Cu_3Sn matrix. Therefore, because only a small amount of liquid Sn phase was formed during the TLP bonding process, a certain amount of the bonding pressure is necessary to make the close contact between the particles and form the dense bonding microstructure. On the other hand, the formation of the voids at the interface between Cu_3Sn matrix and Cu particles should be caused by the Kirkendall effect. As mentioned before, Cu is the dominant diffusing species in the growth of Cu_6Sn_5 and Cu_3Sn, and consequently, the imbalance interdiffusion between Cu and Sn during the bonding process resulted in the vacancy enrichment at the interface between Cu and Cu_3Sn, leading to the formation of Kirkendall voids.

2.5 Fracture morphology observation

Many researchers had reported the fracture morphology of the TLP joint in the Cu-Sn binary system [17-19]. It was found that the fracture mostly propagated inside the Cu-Sn IMC layer of the joint and generally showed a brittle intergranular crack feature [18,19]. Moreover, in the study of Bosco et al., a layer of a two-phase microstructure comprising the δ-phase ($Cu_{41}Sn_{11}$) and a dispersion of Cu particles was formed after the bonding with Cu substrates and Sn foil at 400 ℃ for 4 h with additional treatment at 550 ℃ for 30 min [17]. And they observed that the δ-phase within the δ+(Cu) joints fractured in a brittle manner, whereas, the (Cu) particles embedded within the δ-phase exhibited significant plastic stretching. Also, they found that the addition of ductile Cu particles increased both the strength and toughness of the TLP joints and explained the property enhancements on the basis of ductile phase toughening models. However, the bonding process in their study was too long for practical application for power device packaging.

In my study, owing to the use of unique Cu@Sn particles, a similar two-phase mixture microstructure comprising the Cu_3Sn phase with a dispersion of Cu particles was obtained by bonding at 300 ℃ for 30 s. After the shear test, two types of cracks were observed in the fractured joint bonded at 300 ℃ for 30 s under the bonding pressure of 10 MPa. The first type of crack occurred at the interface between the Cu_3Sn-Cu composite bonding layer and Cu substrate, as shown in Fig. 2.11cd, and the second type of crack occurred inside the Cu_3Sn-Cu composite microstructure, as shown in Fig. 2.11 ef. In Fig. 2.11c, the fracture happened at the interface between the Cu_3Sn-Cu composite bonding layer and top Cu substrate and showed an obvious brittle behavior. Similarly, the fracture in Fig 2.11d was at the interface between the bonding layer and bottom Cu substrate, and a brittle facture morphology also can be observed on the fracture surface. In the previous discussion, it was mentioned that the inadequate amount of liquid Sn resulted in the formation of small voids. It is suggested that the amount of liquid Sn formed at the interface between the bonding layer and Cu substrate was less than that formed inside the bonding layer. At the interface, only Cu@Sn particles on one side of the interface offer Sn, whereas the pure Cu substrate on the other side did not offer any Sn. Thus, voids may be more likely to form in the region near the interface, and indeed, some voids can be observed near the interface in Fig. 2.6. In addition, it is reasonable that a thin layer of Cu_3Sn IMC without any Cu particles existed near the interface. As a result, the strength of the region near the interface is relatively weak in the TLP joint, and thus the crack tends to be initiated and

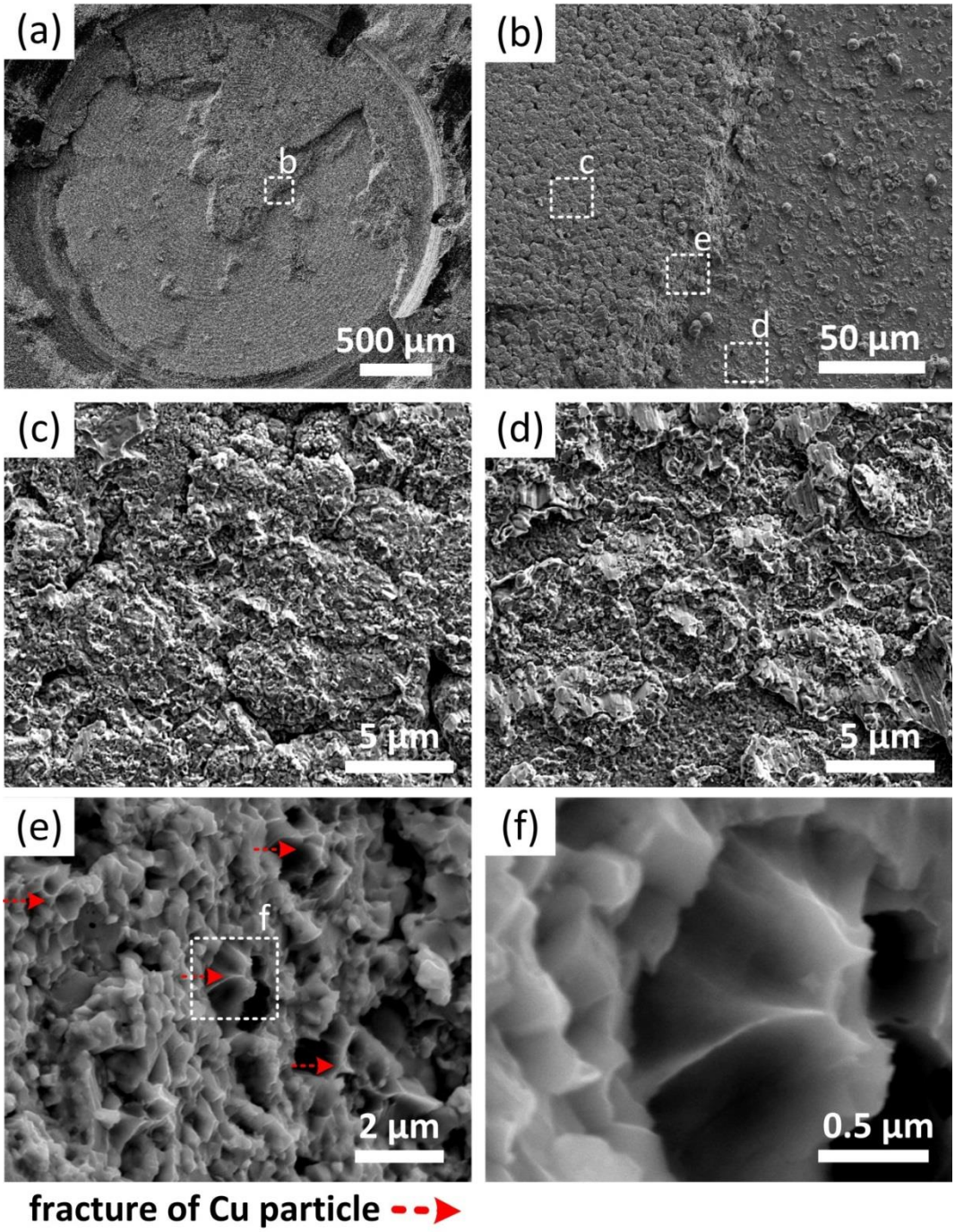

Figure 2.11 SEM images of fracture morphology of the Cu_3Sn/Cu composite joint. The magnified images of (b) denoted area in (a), (c-e) denoted area in (b) and (f) denoted area in (e).

along this region under the shear load, leading to a brittle fracture surface.

The second type of crack propagated along the Cu_3Sn-Cu composite microstructure, as shown in Fig. 2.11ef. The fracture surface exhibited a combination of brittle and ductile fractures. The Cu_3Sn

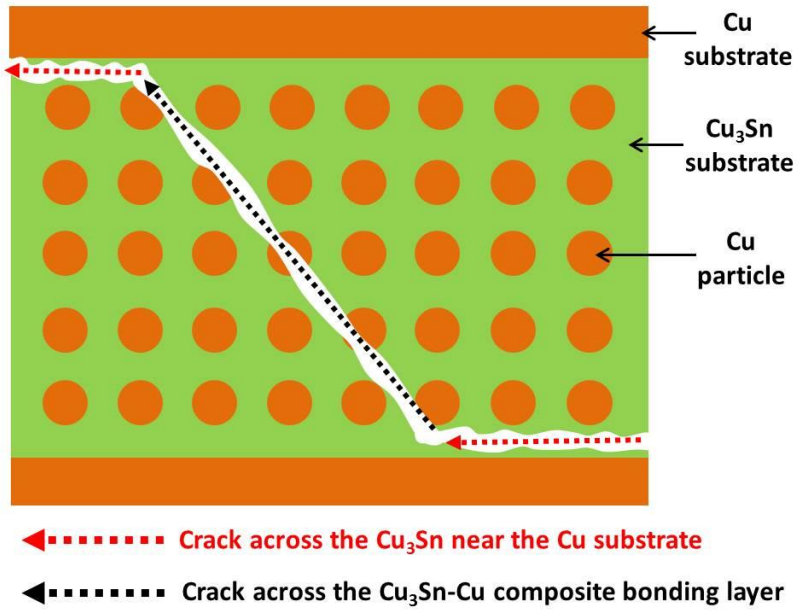

Figure 2.12 Schematic diagram of two types of crack in the Cu_3Sn-Cu composite joint under shear load.

IMC matrix show brittle intergranular fractures in most surfaces, but the embedded Cu particles show evidence of ductile fracture, which is similar to the fracture surface from Bosco. This feature exemplified the targeted ductile phase toughening associated with the two-phase microstructure [17, 20]. The observation of fractured Cu here also demonstrates that embedded Cu particles and Cu_3Sn matrix bear the shear load together, which is evidence of good bonding between Cu_3Sn matrix and embedded Cu particles. The schematic diagram of two types of crack in the Cu_3Sn-Cu composite joint is given in Figure 2.12. On the other hand, it should be noted that voids and cracks formed during the TLP bonding are likely detrimental to the strength of the joint, and the complete brittle fracture crack occupied most fracture surface.

2.6 Thermal stability of bonding joint during isothermal aging at 250 ℃

Fig. 2.13 shows the different shear strength of the TLP joints during the isothermal aging at 250 ℃ for 1000 h. It is worth noting that the shear strength of the TLP joints was increased to 30.3 MPa after the aging for 250 h. As mentioned before, the main bonding process including the densification process as well as the homogenization can be finished in a very short time (30s), and a

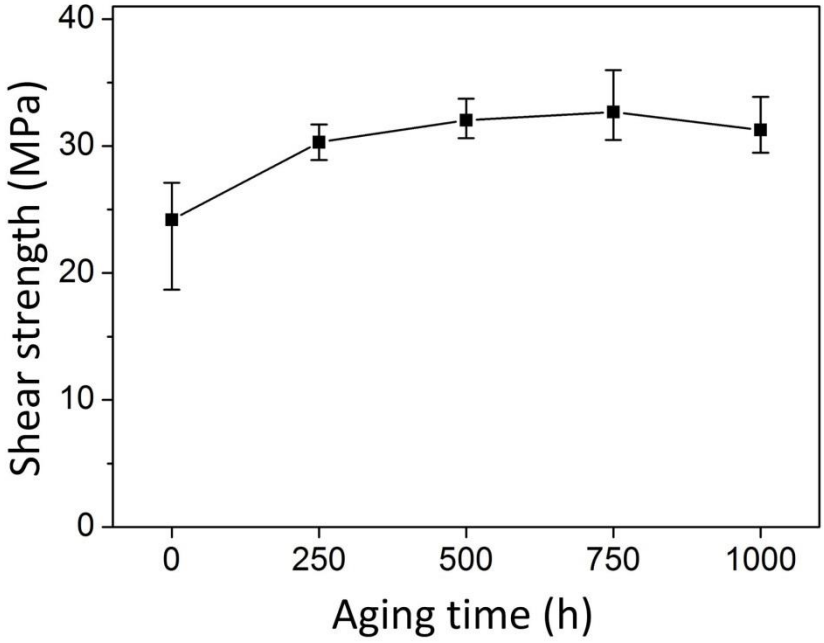

Figure 2.13 Variation of the shear strength of the TLP joints during the isothermal aging test.

sound joint strength was obtained. However, the thermal aging of first 250 h, like prolonging bonding time or an additional heat treatment, the shear strength of the joint was improved to some extent, which could be attributed to the further densification the microstructure of TLP joint during the aging. Indeed, when the bonding time was extended from 30 s to 1200 s, the joint strength shows a slight increase. After the first 250 h, the shear strength remained relatively stable with the further increase of the aging time. Finally, a shear strength of 31.3 MPa was obtained after the aging for 1000 h. This result demonstrates that the TLP joint exhibited good high-temperature reliability.

The high-temperature reliability of the die bond depends on the thermal stability of the microstructure of bonding layer during high-temperature aging. In order to clarify the mechanism responsible for the high stability of the TLP joint strength during the aging test, microstructural observation and elemental analysis of the cross-section of the joint were conducted, as shown in Fig.2.14. It can be seen that no further phase transform occurred during the thermal aging, particularly, the composite microstructure and composition of the joint remained unchanged, which confirms the thermodynamic stability of this Cu_3Sn-Cu composite microstructure. On the other hand, despite the near equilibrium state of this Cu_3Sn-Cu two-phase system, the mixture is not in its lowest energy state due to the presence of a nonzero Cu_3Sn-Cu interfacial energy. Consequently, an Ostwald

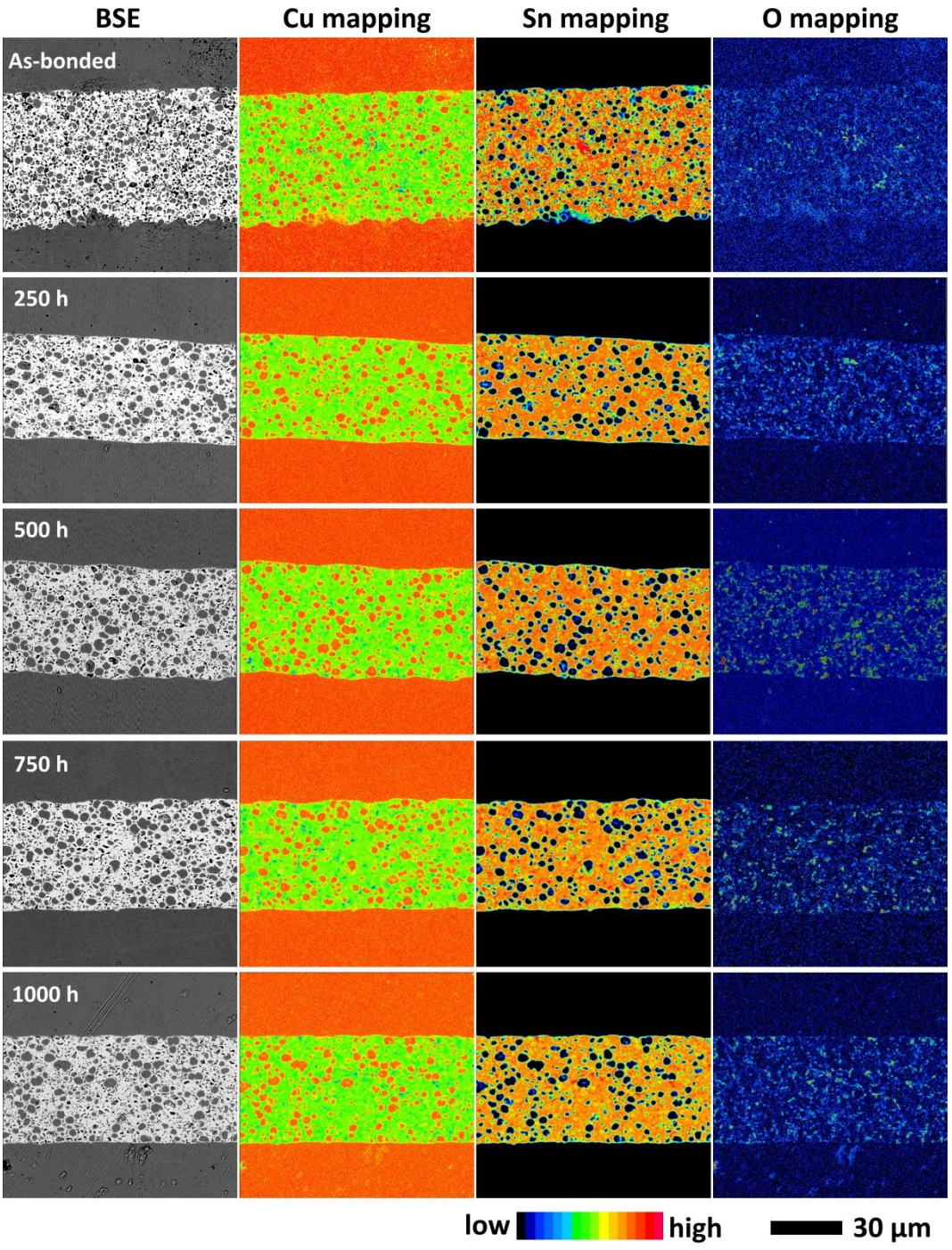

Figure 2.14 Cross-sectional back-scattered electron (BSE) images and corresponding EPMA elemental mappings of the TLP joints after the isothermal aging for different times.

ripening process may occur and affect the microstructural stability of two-phase mixture microstructure at relatively high temperature, in general, the average size of the second-phase particles could increase with time and the number of second-phase particles must decrease with time

[21]. However, in my study, it seems that the size, morphology and spatial distribution of the embedded Cu particles did not change obviously during the aging process, indicating that the Ostwald ripening process did not happen in the Cu_3Sn-Cu composite joint at 250 ℃. In addition, some sporadically distributed oxygen signals indicate the existence of small voids or cracks in the joint. And the intensity and area of the oxygen signal showed little change during the thermal aging, which reveals that the oxidation of Cu_3Sn-Cu composite was not a reliability concern since the bonding layer produced by the TLP process is dense enough and can be considered as a sealed part. Therefore, it was concluded the Cu_3Sn-Cu composite provided an excellent high-temperature microstructural stability, and which contributed to the good reliability of the TLP joint.

2.7 Conclusion

In this chapter, a Cu_3Sn-Cu composite joint was achieved through a Cu-Sn-based TLP bonding at 300 ℃ using a Cu@Sn particle paste. The influence of bonding condition on the joint strength was investigated. It was found that the bonding pressure had a great influence on the joint strength, while the influence of bonding time is insignificant. After the standard bonding condition which is at 300 ℃ for 30 s with 10 MPa under a formic acid gas atmosphere, the joint showed a thermally stable microstructure fully comprising a Cu_3Sn IMC matrix with a dispersion of ductile Cu particles, and the shear strength reached 24.2 MPa, a little higher than that of conventional Pb-5Sn alloy. Experimental results and theoretical analysis revealed that Cu_6Sn_5 transient IMCs were formed and transformed completely into Cu_3Sn IMCs in a short time. Two kinds of cracks can be found on the fracture surface of the TLP joint. The first type of crack was initiated and propagated along the Cu_3Sn near the interface between the bonding layer and Cu substrate. And the second type of crack propagated along the Cu_3Sn-Cu composite and resulted in a unique fracture surface, in which both the brittle intergranular fracture of Cu_3Sn matrix and the ductile fracture of Cu particles could be seen.

During the isothermal aging test at 250 ℃ for 1000 h, the shear strength of the joints was initially increased to 30.3 MPa after 250 h, and then, the shear strength remained almost unchanged. The EMPA results showed that the Cu_3Sn-Cu composite joint had a high microstructural stability

during the thermal aging, which was believed to contribute to the excellent high-temperature reliability of the TLP joint.

References

[1] K. N. Tu, R. D. Thompson. Kinetics of interfacial reaction in bimetallic Cu-Sn thin films, *Acta Metall.*, **30** (1982) 947-952.

[2] T. Y. Lee, W. J. Choi, K. N. Tu, J.W. Jang, S.M. Kuo, J.K. Lin, D.R. Frear, K. Zeng, J.K. Kivilahti, Morphology, kinetics, and thermodynamics of solid-state aging of eutectic SnPb and Pb-free solders (Sn-3.5Ag, Sn-3.8Ag-0.7Cu and Sn-0.7Cu) on Cu, *J. Mat. Res.* **17** (2002) 291-301.

[3] T. Laurila, V. Vuorinen, J. K. Kivilahti, Interfacial reactions between lead-free solders and common base materials, *Mate. Sci. Eng. R*, **49** (2005) 1-60.

[4] P. F. Yang, Y. S. Lai, S. R. Jian, J. Chen, R. S. Chen., Nanoindentation identifications of mechanical properties of Cu_6Sn_5, Cu_3Sn, and Ni_3Sn_4 intermetallic compounds derived by diffusion couples, *Mat. Sci. Eng. A*, **485** (2008) 305-310.

[5] H. Okamoto, *Desk Handbook Phase Diagrams for Binary Alloys*, ASM International, Ohio, 2000.

[6] J. F. Li, P. A. Agyakwa, C. M. Johnson, Interfacial reaction in Cu/Sn/Cu system during the transient liquid phase soldering process, *Acta Mater.*, **59** (2011) 1198-1211.

[7] N. S. Bosco, F. W. Zok, Critical interlayer thickness for transient liquid phase bonding in the Cu–Sn system, *Acta Mater.*, **52** (2004) 2965-2972.

[8] F. Lang, H. Yamaguchi, H. Nakagawa, H. Sato, Thermally stable bonding of SiC devices with ceramic substrates: Transient liquid phase sintering using Cu/Sn powders, *Electrochem. Soc.*, 160 (2013) 315-319.

[9] W. Lin, Y. C. Lee, Study of fluxless soldering using formic acid vapor, *IEEE Trans. Adv. Pack.*, **22** (1999) 592-601.

[10] E. Ide, A. Hirose, K. F. Kobayashi, Influence of bonding condition on bonding process using Ag metallo-organic nanoparticles for high temperature lead-free packaging, *Mater. Trans.* **47** (2006) 211-217.

[11] Y. Shi, W. Fang, Z. Xia, Y. Lei, F. Guo, X. Li, Investigation of rare earth-doped BiAg high-temperature solders, *J. Mater. Sci. Mater. Electron.* **21** (2010) 875-881.

[12] L. Xue, Z. Fu, Y. Yao, T. Huang, A. Yu, Three-dimensional porous Sn–Cu alloy anode for lithium-ion batteries, *Electrochim. Acta*, **55** (2010) 7310-7314.

[13] G. Ghosh and M. Asta, Phase stability, phase transformations, and elastic properties of Cu_6Sn_5:

Ab initio calculations and experimental results, *J. Mater. Res.*, **20** (2005) 3102-3117.

[14] H. P. R. Frederikse, R. J.Fields and A. Feldman, Thermal and electrical properties of copper-tin and nickel-tin intermetallics. J. Appl. Phys. 72 (1992) 2879-2882.

[15] K. Zeng, R. Stierman, T. C. Chiu, D. Edwards, K. Ano and K. N. Tu, Kirkendall void formation in eutectic SnPb solder joints on bare Cu and its effect on joint reliability, *J. Appl. Phys.*, **97** (2005) 4508.

[16] P. J. Shang, Z. Q. Liu, X. Y. Pang, D. X. Li, J. K. Shang, Growth mechanisms of Cu 3 Sn on polycrystalline and single crystalline Cu substrates, *Acta Mater.*, **57** (2009) 4697-4706.

[17] N. S. Bosco and F. W. Zok, Strength of joints produced by transient liquid phase bonding in the Cu–Sn system, *Acta Mater.*, **53** (2005) 2019-2027.

[18] M. Li, Z. Li, Y. Xiao, C. Wang, Rapid formation of $Cu/Cu_3Sn/Cu$ joints using ultrasonic bonding process at ambient temperature, *Appl. Phys. Lett.*, **102** (2013) 094104.

[19] K. Chu, Y. Sohn, C. Moon, A comparative study of Cn/Sn/Cu and Ni/Sn/Ni solder joints for low temperature stable transient liquid phase bonding, *Scr. Mater.*, **109** (2015) 113-117.

[20] S. L. Sigl, P. A. Mataga, B. J. Dalgleish, R. M. McMeeking, A. G. Evans, On the toughness of brittle materials reinforced with a ductile phase, *Acta Mater.*, **36** (1988) 945-953.

[21] P. W. Voorhees, Ostwald ripening of two-phase mixtures, *Annu. Rev. Mater. Sci.* **22** (1992) 197-215.

Chapter 3
Low-temperature solid-state bonding using Sn-coated Cu particles

3.1 Introduction

In *Chapter 2*, based on the Cu@Sn particles, a TLP bonding process at 300 ℃. In general was investigated, the Cu-Sn-based TLP bonding can be carried out at relatively low temperatures while resulting in Cu-Sn IMC joints with higher re-melt temperatures. For example, in my study, the processing temperature of TLP bonding was 300 ℃, lower than the reflow temperature of conventional high-lead solder, while the obtained Cu_3Sn-Cu composite had significantly higher melt temperatures than that of high lead content solder. However, Cu-Sn-based TLP bonding must be conducted above the melting point of Sn because the melting of Sn is a key step. Therefore, Cu-Sn-based TLP bonding cannot be considered as a low-temperature bonding process, many organic devices and printed circuit boards cannot withstand its processing temperature at which they are generally unstable.

On the other hand, if Cu-Sn IMCs are formed by a Cu-Sn solid-state reaction rather than liquid-solid reaction, the process temperature can be reduced. The Cu-Sn solid-state bonding at

180 ℃ for achieving Cu-Cu interconnection has been studied for 3D chip stacking applications [1]. It seems the fact that its great advantage, namely "low-temperature formation but high-temperature re-melting" is very suitable for high temperature die attach applications. However, there is little research using Cu-Sn solid-state bonding in the large area die attach instead of microbump interconnection.

In this chapter, by the use of the microscale Cu@Sn particle paste, a Cu-Sn-based low-temperature solid-state bonding process was developed for high-temperature die attach applications. It is expected that at the early stage of bonding, the Sn coating layers could facilitate the coalescence of Cu@Sn particles, and at the medium stage of bonding, the formation of Cu-Sn IMC phase between each particle can help to produce a well-sintered microstructure. In addition, the thin Sn coating layer in each particle would significantly shorten the necessary processing time for the complete consumption of Sn. Besides, the Cu-Sn IMC phase formed in the bonded joint could prevent the Cu-contained sintered microstructure from severe oxidation, and therefore the Cu@Sn joint could present a better thermal stability than the conventional Cu-sintered joint. With these in mind, the aim of this chapter is to evaluate the mechanical properties and microstructure of this solid-state bonding joint and to clarify its bonding mechanism. In addition, the thermal stability of the Cu@Sn and Cu joints at an elevated temperature aging condition up to 250 ℃ was investigated. The change of shear strength and the microstructure evolution of two kinds of sintered joint during the isothermal aging were studied.

3.2 Experimental

3.2.1 Fabrication of Sn-coated Cu particle

Microscale Cu particles were used as the starting material (1400YM, D50: 4.2 μm, Mitsui Mining & Smelting Co. Ltd), as shown in Fig. 3.1a. The Cu@Sn particles, as shown in Fig. 3.1b were fabricated through electroless plating of Sn on Cu particles by Okuno Chemical Industries Co. Ltd. The detailed Sn plating process has been described in *Chapter 2*. The cross-section view and corresponding EDX mapping of the Cu@Sn particles are presented in Fig. 3.1c. The average thickness of the coated Sn was less than 0.5 μm.

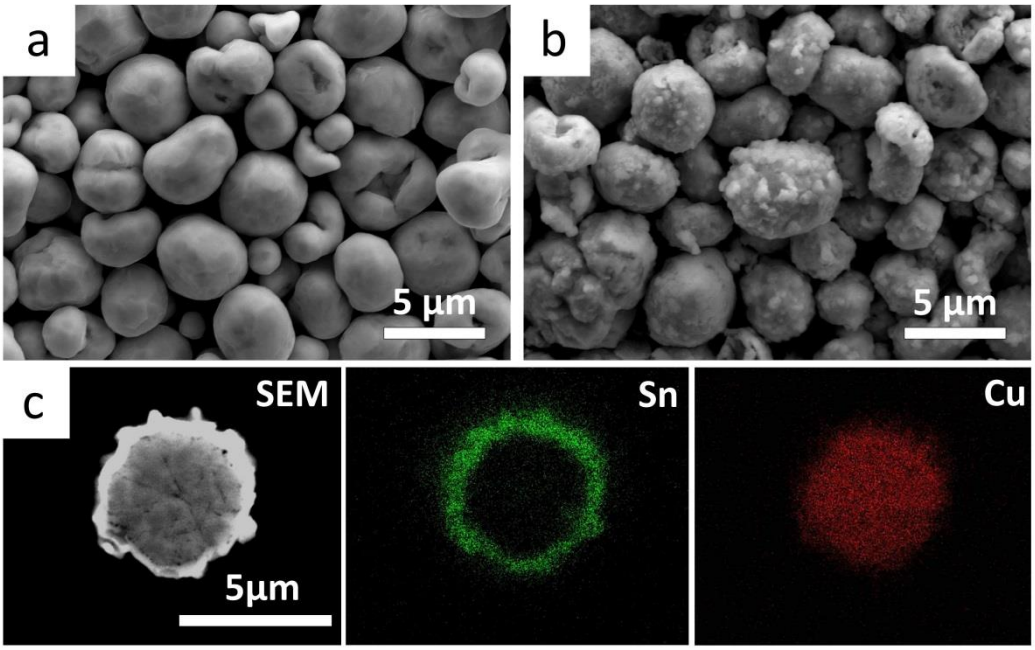

Figure 3.1 Typical SEM images of (a) original Cu particles and (b) Cu@Sn particles as well as (c) corresponding EDX mapping of Cu@Sn particles.

3.2.2 Preparation of particle paste

Cu@Sn particles paste was prepared by adding a terpineol solvent (16 wt. %) to the Cu@Sn particles (84 wt. %). Fig. 3.2 shows the thermogravimetric analysis (TGA) and the differential scanning calorimetry (DSC) curves for the paste during heating under N_2 (temperature increasing at 10.00 ℃ min -1), which revealed that the vaporization of the terpineol mostly occurred below 150 ℃. The DSC curve shows an obvious endothermic peak at approximately 230 ℃, indicating the melting of the Sn coating.

3.2.3 Low-temperature solid-state bonding process

Fig. 3.3a shows a schematic of the solid-state bonding joint with the Cu@Sn particle paste. The heating profile of the bonding process is shown in Fig. 3.3b. The prepared Cu@Sn joint specimens were first pre-heated at 110 ℃ for 5 min to evaporate the solvent, then heated to the bonding temperature of 200 ℃ at 1 ℃/s, and finally bonded at 200 ℃ with a certain bonding pressure using a

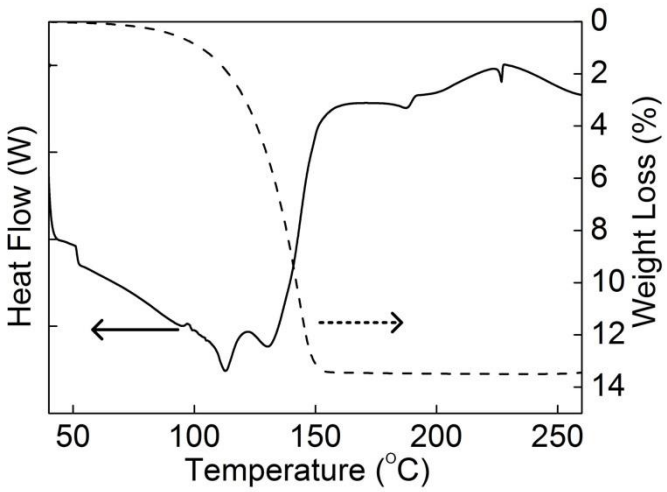

Figure 3.2 Traces of TG and DSC for Cu@Sn particle paste during heating in N_2.

thermo-compression bonding system. Two kinds of atmosphere, N_2 and formic acid vapor were used in the bonding process. In addition, to compare the thermal stability of the Cu@Sn joint and conventional Cu-sintered joints, some specimens with Cu pure paste were bonded at 200 ℃ and 250 ℃, respectively, with a bonding pressure of 10 MPa in the formic acid atmosphere. Finally, all obtained Cu@Sn joints and pure Cu joints were stored in a high-temperature oven at 250 ℃ for the isothermal aging test.

3.2.4 Characterization methods

The shear strength of the bonded joints was evaluated by using a shear tester (STR-1000, Rhesca) at a head speed of 1mm/min, where the fly height was 200 μm from the bottom of the specimen. For each bonding conditions, we tested four samples for collecting the shear strength data and calculated the average value. X-ray diffraction (XRD) analysis was conducted by an X-ray diffractometer (Rigaku Ultima IV) using Cu-Kα radiation (λ = 1.5405 Å). The diffracted beam angle, 2θ was scanned in steps by 0.01 ° in the angular range from 20 to 80 °. The cross section microstructures and the fractured surfaces of the bonded joints were observed by a field emission scanning electron microscopy (FESEM, Hitachi SU-70). The composition on the fracture surface was measured with an electron probe microanalyzer (EPMA, JXA-8530F, JEOL)

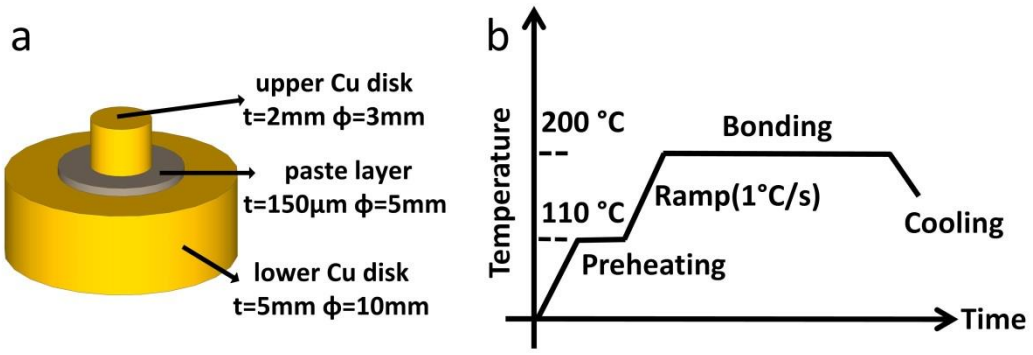

Figure 3.3 Illustration of the solid-state bonding process using Cu@Sn particle paste: (a) schematic diagram of the Cu-Cu joint and (b) the heating profile of the bonding process.

3.3 Effect of bonding conditions on microstructure and strength of bonding joint

Fig. 3.4 shows the shear strength of Cu@Sn joints bonded with various bonding times, pressures and atmospheres. When Cu@Sn joints were bonded under a pressure of 20 MPa in formic acid vapor, the value of its shear strength reached 20.4 MPa at a bonding time of 5 min, and gradually increased with increasing bonding time up to a value of 25.8 MPa at 20 min. This shear strength is higher than that of the soldered joints using conventional Pb-5Sn solder. However, after that, a longer bonding time of 40 min can only create a slight increase of 0.7 MPa. A similar trend of increasing bonding strengths can also be observed in the Cu@Sn joints bonded with 5 MPa. Its shear strength increased from 9.4 MPa to 18.2 MPa when the bonding time was prolonged from 5 min to 20 min. After 20 min, the effect of bonding time on the shear strength became negligible. Thus, it is suggested that at the low temperature of 200 ℃, effective Cu@Sn joints can be obtained within 20 min, while extending the bonding time further cannot improve the shear strength anymore. Besides, the Cu@Sn joints bonded with 20 MPa always exhibited higher shear strengths than the that with 5 MPa, indicating the bonding properties of the Cu@Sn joints were affected by the applied pressure. Moreover, it was found that the bonding atmosphere had a significant influence on the shear strength. When the Cu@Sn joints were bonded in N_2, the shear strength was always lower than 5 MPa, much weaker than that of the joints bonded in the formic acid atmosphere. As mentioned before, the formic acid atmosphere can remove the oxide layers on the coated Sn, demonstrating that a clean surface without any oxides is critical for the efficient solid-state bonding using Cu@Sn particles.

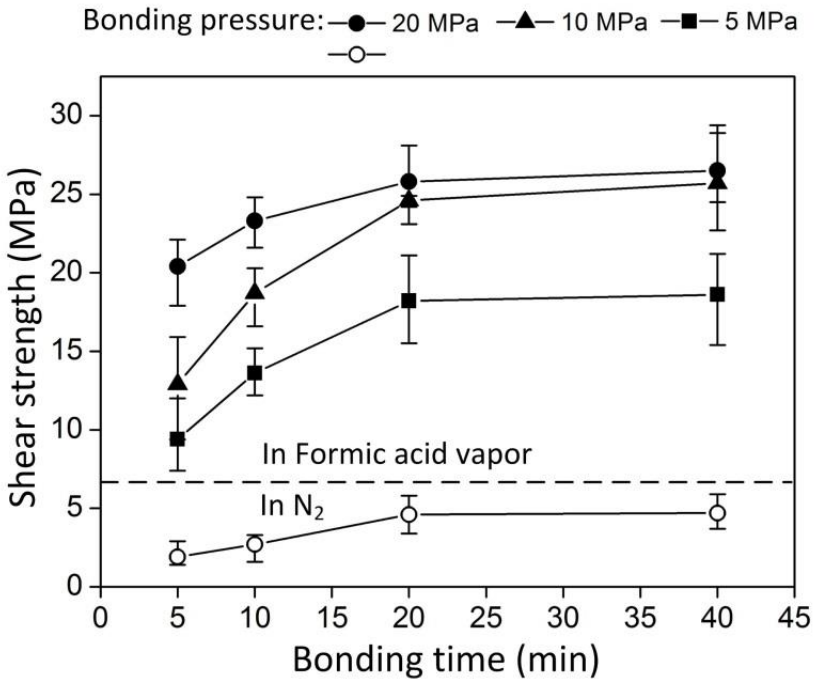

Figure 3.4 Shear strength of Cu@Sn joints after bonding at 200 ℃ for 5-40 min with a pressure of 5 and 20 MPa in the formic acid atmosphere and a the pressure of 20 MPa in N_2, respectively.

The microstructures of the Cu@Sn joints bonded for 20 min with different pressure are given in Fig. 3.5. The joint with applied pressure of 20 MPa exhibited a noticeable two-phase mixture microstructure, which is shown by a light grey color matrix with dark color embedded particles. Quantitative energy dispersive X-ray (EDX) point analysis showed a Cu-Sn mixed composition(mole ratio of Cu to Sn is 3:1) in the grey matrix and a pure Cu composition in the dark particles uniformly distributed in the matrix. It indicated that the joint consisted of a Cu_3Sn IMC matrix with a uniform dispersion of Cu particles. It should be noticed that according to the Cu-Sn phase diagram, this Cu_3Sn-Cu binary composition reached the thermodynamic equilibrium below 350 ℃ at the Cu-rich corner. Moreover, though there were some pores in the bonding layer, no individual Cu_3Cu@Sn particles could be distinguished in the bonding layer, which revealed an effective densification process during the solid-state bonding. On the other hand, the joints with applied pressure of 5 MPa showed a relatively loose bonding layer. The applied external pressure can promote the densification process of powders by an intrinsic contribution to the driving force for sintering [4]. Therefore, it is believed that higher bonding pressure induced denser bonded microstructure, thus leading to higher bonding strength.

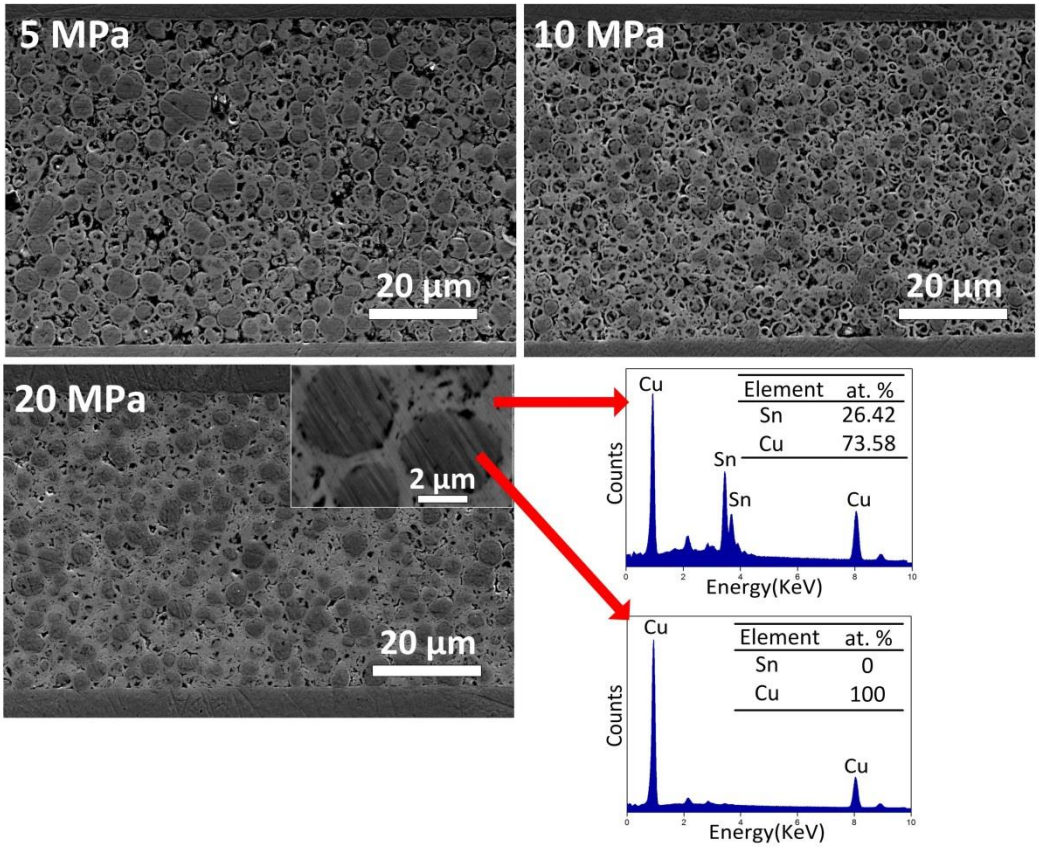

Figure 3.5 Cross-sectional SEM images of the joint after bonding at 200 ℃ for 20 min in the formic acid atmosphere with the pressure of 5 MPa, 10 MPa and 20 MPa, respectively, and the point EDX spectra of in the bonded joint.

The microstructures of the Cu@Sn joints bonded in different atmospheres are shown in Fig. 3.6. It has been mentioned that when samples were bonded in N_2, the obtained shear strength was much lower than that bonded in the formic acid atmosphere. It can be seen in Fig. 3.6, although the joints bonded in N_2 also exhibited a two-phase mixture feature, the microstructure was very loose. The particles were just closely packed together and no coalescence of particles can be observed. It indicated that these particles were merely physically contacted, and this poor bonding caused the low shear strength of the joints. It is well known that removing the oxide film on Sn-based powders is necessary for a soldering process because oxide films can lead to degradation of the coalescence of solder powders during reflow [5]. Apparently, in my solid-state bonding process, the removal of oxide films on the Sn coating is also indispensable because the coalescence of the solid-state Sn coating is more difficult than that of the molten Sn. Instead of a flux, formic acid atmosphere was

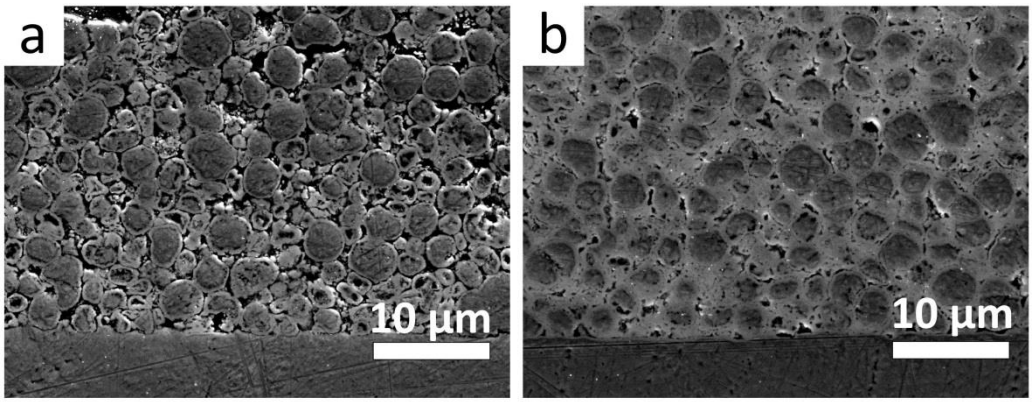

Figure 3.6 Cross-sectional SEM images of the joints after bonding at 200 ℃ for 20 min under the pressure of 20 MPa in (a) N_2 and (b) formic acid atmosphere.

used in this study. The removal of oxide layers on the coated Sn is attributed to the reducing reaction [6],

$$SnO + 2HCOOH(g) \rightarrow Sn(HCOO)_2 + H_2O(g) \quad (3.1)$$

$$SnO_2 + 2HCOOH(g) \rightarrow Sn(HCOO)_2 + H_2(g) + 2CO_2(g) \quad (3.2)$$

At temperatures higher than 150 ℃,

$$Sn(HCOO)_2 \rightarrow Sn + H_2(g) + 2CO_2(g) \quad (3.3)$$

3.4 Phase transformation and bonding mechanism

Both Cu_3Sn-Cu two-phase and Cu_3Sn single-phase microstructures have been reported in literature regarding Cu-Sn TLP bonding and soldering processes [7,8]. However, it is the first time to obtain this thermally stable microstructure by the solid-state process. Moreover, the entire time of the bonding process was reduced to 20 min. To clarify the bonding mechanism, the microstructural evolution, as well as the phase evolution during the bonding, were investigated. First, X-ray diffraction (XRD) analysis was conducted to understand the phase transformation of the Cu@Sn particles at 200 ℃, as shown in Fig. 3.7. It was found that, even before heating, the diffraction peaks of Cu_6Sn_5 phase existed, indicating the Cu_6Sn_5 phase was formed during the electroless plating process. When the Cu@Sn particles were heated at 200 ℃ for 30 s, the Cu_6Sn_5 peak became stronger while the Sn peak was weakened, revealing the Cu_6Sn_5 phase grew continuously by the solid reaction

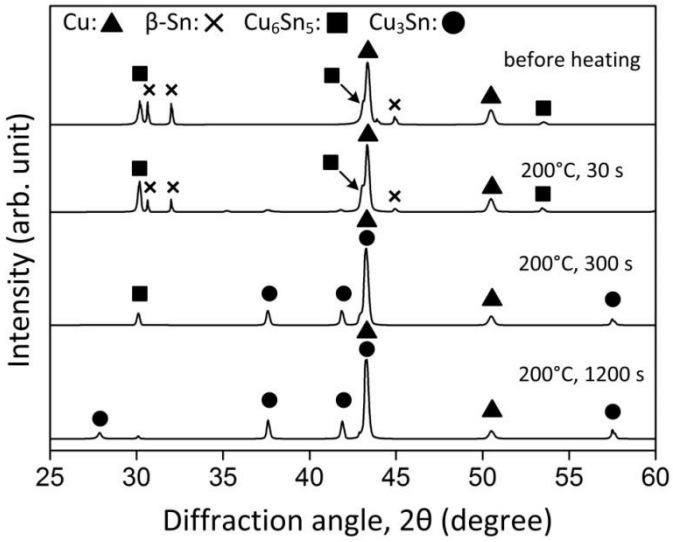

Figure 3.7 XRD analysis of the consisting phases in the Cu@Sn particles during heating at 200 ℃.

between the Cu core and the coated Sn. Then, after 5 min, the Cu_6Sn_5 peak showed a reduced intensity and the Sn peak disappeared. Meanwhile, strong Cu_3Sn peaks emerged. It indicated a phase transformation from Cu_6Sn_5 to Cu_3Sn. Finally, after heating for 20 min, the peak of Cu_6Sn_5 also disappeared, and only the peaks of Cu_3Sn and Cu were observed, which reveals that the phase transformation from Cu_6Sn_5 to Cu_3Sn had ended and Cu_6Sn_5 was completely consumed as a transient IMC phase. At that time, the Cu_3Sn-Cu mixture composition was achieved in the bonding layer. Cu_3Sn-Cu binary phase is a thermally stable composition in Cu-Sn-based joints for high-temperature use. Cu_6Sn_5 tends to transform to Cu_3Sn if the total composition of the joint is a Cu-rich region.

Moreover, it was found that the phase transformation in the bonding layer seemed related to the change of the shear strength of the joint at various bonding times. After the thermally stable Cu_3Sn-Cu mixture phase was obtained after 20 min, the increase of shear strength also stopped. Herein, to explain the reason of this relation, the microstructural evolution in the bonding layer was observed. Fig. 3.8 shows the SEM images of the interface between the Cu@Sn particle bonding layer and Cu substrate after bonding at 200 ℃ with a pressure of 20 MPa for 30 s, 300 s, and 1200 s.It is worth noting that necks were formed between the coating layers of particles after only 30 s. The XRD result shows a weakened Sn peak existed. It reveals that a certain amount of Sn coating still remained on the outlayer of Cu particles at 30 s because the Sn coating was continuously consumed from inside at the interface between Sn and Cu. Consequently, it is believed that the Sn coating

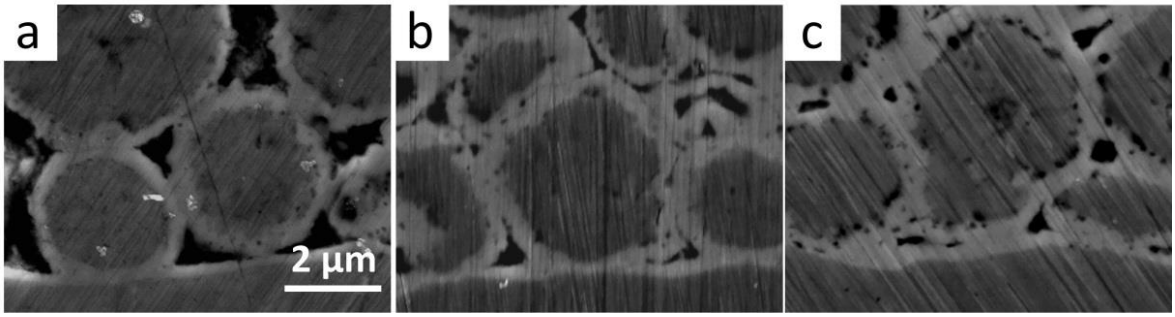

Figure 3.8 Cross-sectional SEM images of sintered Cu@Sn particles during the bonding process. (a) 30 s, (b) 300 s, (b) 1200 s.

played a key role in the formation of necks between particles at the early stage of solid-state bonding. It is well known that the formation of a neck is dependent on the mass transport in particles, and surface diffusion is the dominant mechanism for mass transport in fine particles at low sintering temperatures. Because of the low melting point of Sn, the homologous temperature of the Sn coating had reached 0.9 even at 200 ℃. Hence, the activation energy of Sn atom diffusion can be significantly reduced and the necks between Sn coatings were rapidly formed by easy surface diffusion, which was a considerable advantage of the Sn coating in the solid-state bonding. At 300 s, the obvious densification process had obviously taken place in the bonding layer, where the size of the pores and gaps between particles was significantly reduced. As a consequence, a bonding strength of 20.4 MPa was obtained at this time. Meanwhile, the Cu-Sn IMC layers of the particles became thicker due to the transformation of the layer from Sn/Cu_6Sn_5 to Cu_6Sn_5/Cu_3Sn by solid-state reaction. However, the initial shape of the coating layer can still be distinguished, and the pores among the particles presented irregular shapes, revealing that the coalescence of the particles was still insufficient. Finally, at 1200 s, the Cu_3Sn IMC layers of the Cu particles have further coalesced and evolved into a network among the Cu particles. After this further densification, the joint strength showed an increase up to 25.8 MPa. Moreover, the shape of the pores in the Cu_3Sn phase changed from an irregular shape to a more thermally stable round shape, indicating that there was a driving force for pores to attain a shape with minimum interfacial energy. These pores may have an influence on the mechanical property of the joint. Thus, the shear strength of SSB joint was lower than the conventional Cu-Sn-based TLP joint in the literature [8,15], in which a bonding layer without any pores was formed due to the existence of a large amount of liquid Sn. In addition to the pores inside

the IMC matrix, some small voids were also formed at the interface between Cu_3Sn and Cu particle. The possible mechanism for this void formation is Kirkendall effect. Compared to the Cu@Sn particles-based TLP joint in *Chapter 2*, more Kirkendall voids were found in the Cu@Sn particles-based SSB joint, which should be caused by longer solid state reaction between Cu and Cu_6Sn_5 in the SSB process. Nevertheless, it is suggested that these Kirkendall voids had an insignificant effect on the joint strength in this study because they are much smaller than the pores insides the IMC matrix. In other words, the densification degree determined the bonding

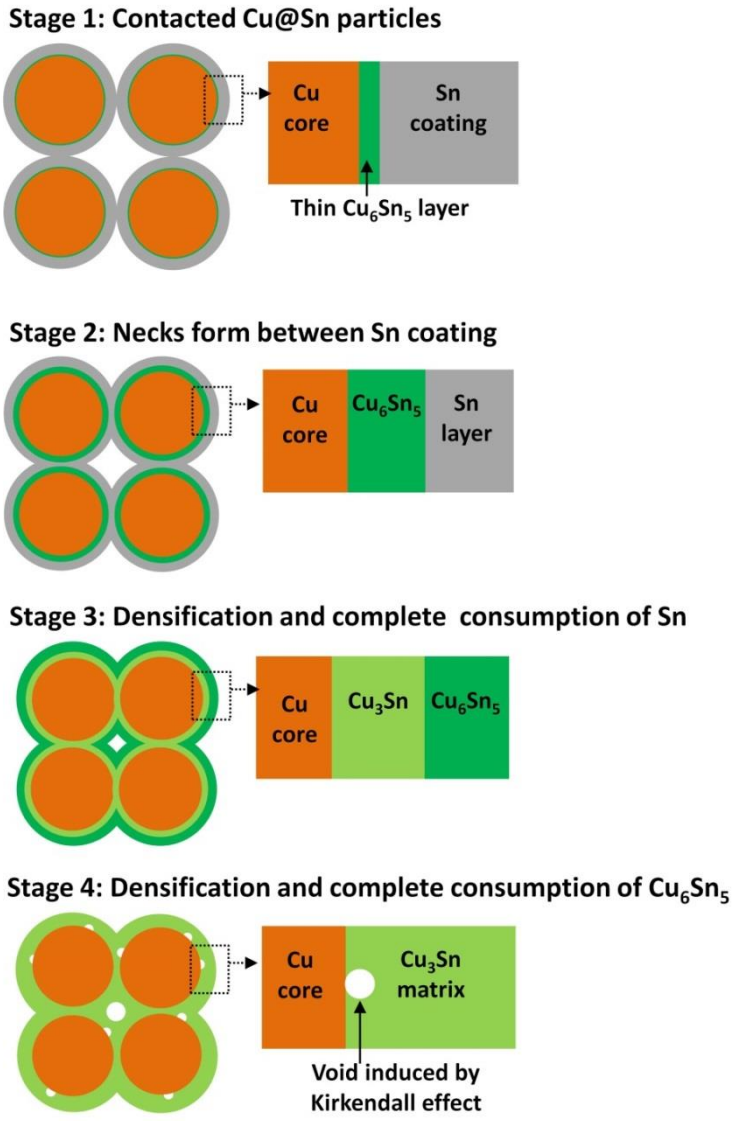

Figure 3.9 Illustration of microstructure evolution and phase transform of the bonding layer during the SSB process.

strength of the SSB joints. Therefore, when the densification and the phase transformation had already finished after bonding for 20 min, the extending of bonding time can hardly affect the bonding strength. A schematic diagram is given in Fig 3.9 to illustrate the microstructure evolution and phase transform during the solid-state bonding process using Cu@Sn particles.

It is well known that creep is a major densification mechanism in pressure-assisted sintering [9], and the IMC phase generally shows a high creep resistance. However, the Cu_6Sn_5 and Cu_3Sn IMCs that cover the Cu particles are apparently involved in the densification process during the solid-state bonding process. Of course, the formation of necks between particles facilitated by the Sn coating made the following densification process possible. Moreover, diffusional creeps such as Nabarro-Herring creep and Coble creep, controlled by lattice diffusion and grain boundary diffusion, respectively, could have dominated this densification process of Cu-Sn IMC phase [10-12]. The densification rate dρ/dt in the case of lattice diffusion and grain boundary diffusion can be expressed as:

by lattice diffusion: $$\frac{\mathrm{d}\rho}{\mathrm{dt}} \propto \frac{D_l V_m P}{RTa^2} \quad (3.4)$$

by grain boundary diffusion: $$\frac{\mathrm{d}\rho}{\mathrm{dt}} \propto \frac{D_b \delta_b V_m P}{RTa^3} \quad (3.5)$$

where D_l, D_b and δ_b are the lattice diffusion coefficient, grain boundary diffusion coefficient and diffusion thickness of the grain boundary diffusion, respectively. V_m and P are the molar volume of the solid and effective pressure, respectively. R, T and a are the ideal gas constant, temperature and grain radius, respectively. From these expressions, it is deduced that a fine grain size can greatly accelerate the densification process of the IMC phase due to the enhanced diffusional creep. It had been reported that very fine equiaxed Cu_3Sn grains without preferred orientation nucleated and grew between Cu and Cu_6Sn_5 after reflow [13,14]. During the subsequent aging of tens of hours, the Cu_6Sn_5 was converted into Cu_3Sn grains, which merged with each other, displaying a ripening process. In the bonding process, owing to the thin reaction layer (<1μm), the duration of the solid-state reaction was limited. Therefore, it is suggested that the formed IMC phase can maintain a fine grain size, thereby improving the diffusional creep and resulting in a densification process.

3.5 Fracture morphology observation

Fig. 3.10 shows fracture surface of Cu@Sn joints bonded for 20 min with a pressure of 5 MPa and 20 MPa in the formic acid atmosphere, respectively. Fig. 3.10ab give the fracture surface of the joint boned with 5 MPa. As shown in Fig. 3.10a, the sintered particles did not coalesce well, and thus the facture surface presented a feature of deformed particles. This loose fracture surface was confirmed by the high magnitude SEM image, in which the individually deformed particles could be recognized. On the other hand, as shown in Fig. 3.10cd, the fracture surface of the joint boned with 20 MPa seems quite different. Owing to the dense sintered microstructure, the particle shape had disappeared and the deformation caused by shear load was very clear at the fracture surface. Apparently, the difference in the fracture morphology was attributed to the aforementioned difference in sintered microstructures and was correlated to the obtained shear strengths.

Fig. 3.11 shows representative EPMA elemental mapping results on the fracture surface of Cu@Sn joints bonded for 20 min with a pressure of 20 MPa in the formic acid atmosphere. The fracture surfaces of the lower sample and the upper sample were presented in Fig. 3.11a and b,

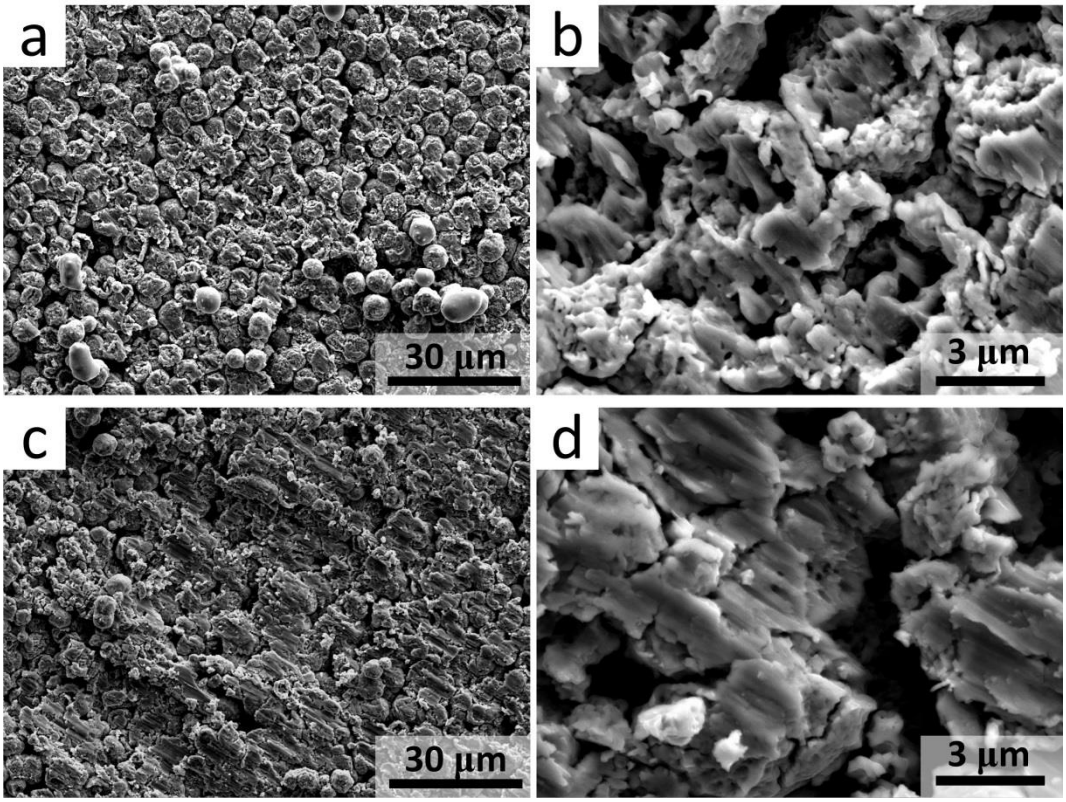

Figure 3.10 SEM images of fracture surface of low-temperature bonded joint with (a, b) 5 MPa and with (c, d) 20 MPa.

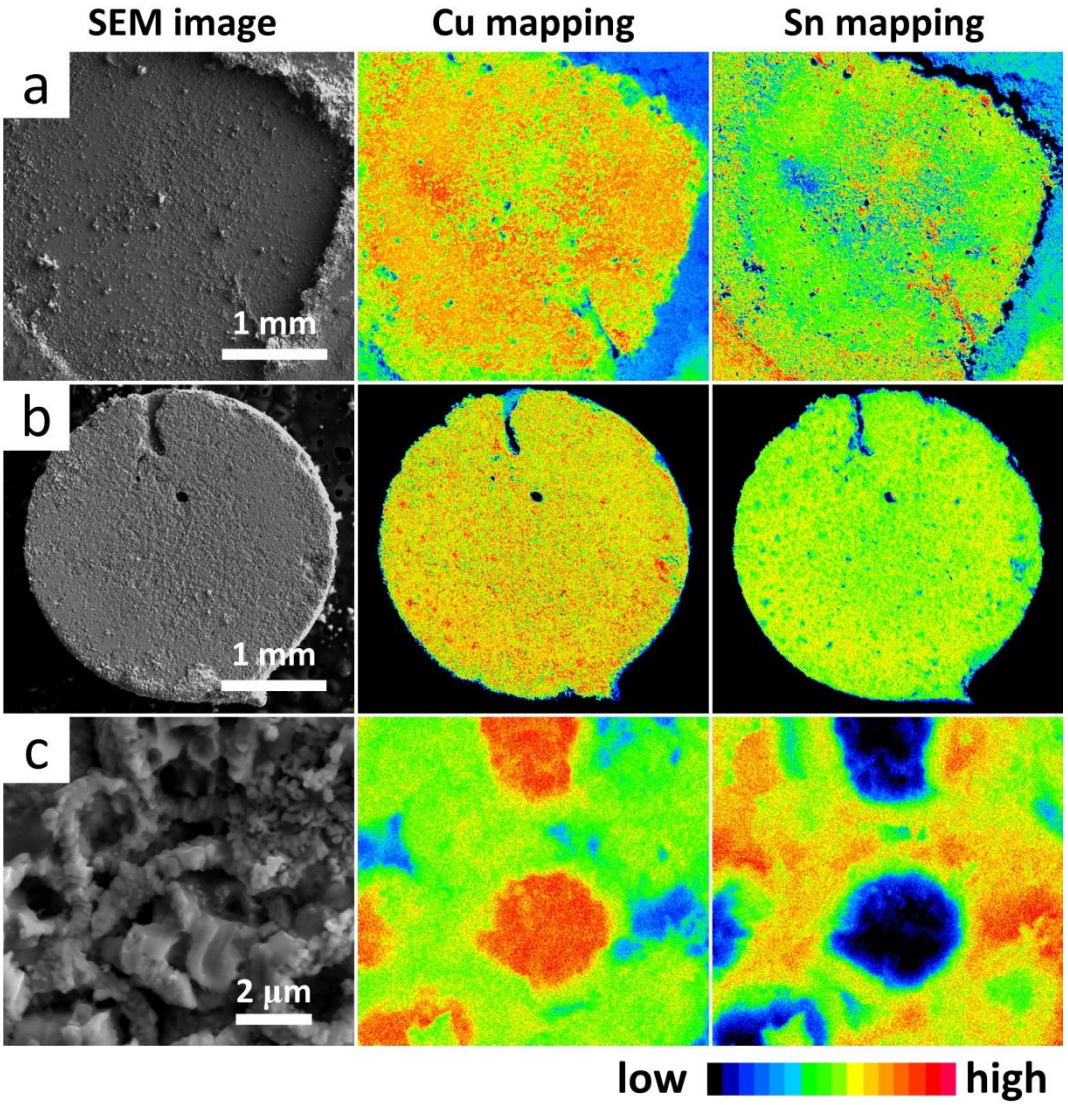

Figure 3.11 SEM images and corresponding EPMA elemental mapping of the fracture surface of Cu@Sn joint bonded with 20 MPa. (a) lower sample, (b) upper sample, (c) high magnitude on the lower sample.

respectively. They presented the similar uniform Sn and Cu signal region on the fracture surface, which indicates that fracture mainly occurred in the bonding layer composed of a mixture phase of Cu_3Sn and Cu. Moreover, as shown in Fig. 3.11c, the EPMA elemental mapping results of high magnitude image help to reveal both fractured Cu-Sn IMC matrix and deformed Cu particles existed at the fracture surface. This unique fracture morphology was attributed to the Cu_3Sn-Cu mixture microstructure in the bonding layer. Researchers had reported similar two-phase mixture microstructures that comprise the $Cu_{41}Sn_{11}$ IMC phase and a dispersion of Cu particles in

Cu-Sn-based TLP joints bonded at 400 ℃ [15]. It was reported that the $Cu_{41}Sn_{11}$ IMC within the joint fractured in a brittle manner while the Cu particles embedded within the $Cu_{41}Sn_{11}$ IMC exhibited a plastic stretch, which was similar to my observations. In addition, they found that the addition of ductile Cu particles could increase the strength and toughness of the TLP bonding joints due to a toughening effect of the ductile phase. In the present work, owing to the use of Cu@Sn particles, a similar two-phase microstructure comprising Cu_3Sn IMC with a dispersion of Cu particles can be obtained by a solid-state bonding at 200 ℃. Moreover, the fracture morphology gives clear evidence to support that the brittle Cu_3Sn IMC and ductile Cu particles simultaneously bear the shear load.

3.6 Thermal stability of bonding joint during isothermal aging at 250 ℃

3.6.1 Variation of shear strength and microstructural evolution during isothermal aging

The Cu@Sn joint that bonded with 10 MPa for 20 min was selected for the isothermal aging teat. It is because this Cu@Sn joint exhibited the obvious porous microstructure, and thus is suitable for the study of oxidation behavior of Cu_3Sn-Cu composite structure as well as the influence of oxidation on the joint strength during the isothermal aging. Fig. 3.12a gives a comparison of the shear strength between the Cu@Sn joints and Cu joints. The Cu joints were bonded at 200 ℃ and 250 ℃ for 20 min, respectively. The shear strength of the Cu@Sn joint reached 25.4 MPa, however, the Cu joint only showed a low shear strength of 15 MPa with the same bonding temperature. It demonstrates that the bonding temperature of 200 ℃ is too low to obtain a sound joint using microscale Cu particles. In order to achieve a Cu joint with the competitive shear strength to the Cu@Sn joint for the isothermal aging test, the bonding temperature was needed to elevate to 250 ℃, and by which the Cu joint achieved an enhanced shear strength of 31 MPa.

The microstructure of three kinds of joint is also given in Fig. 3.12bcd. It is observed that the thickness of the bonding layer in the Cu@Sn joint is larger than that in the Cu joints. Since the surface condition of the Cu particles and the Cu@Sn particles is different, their corresponding pastes perform different viscosity, and which caused the different thickness of the paste layer under the applied pressure. As mentioned before, the Cu@Sn joint exhibited a noticeable two-phase mixture

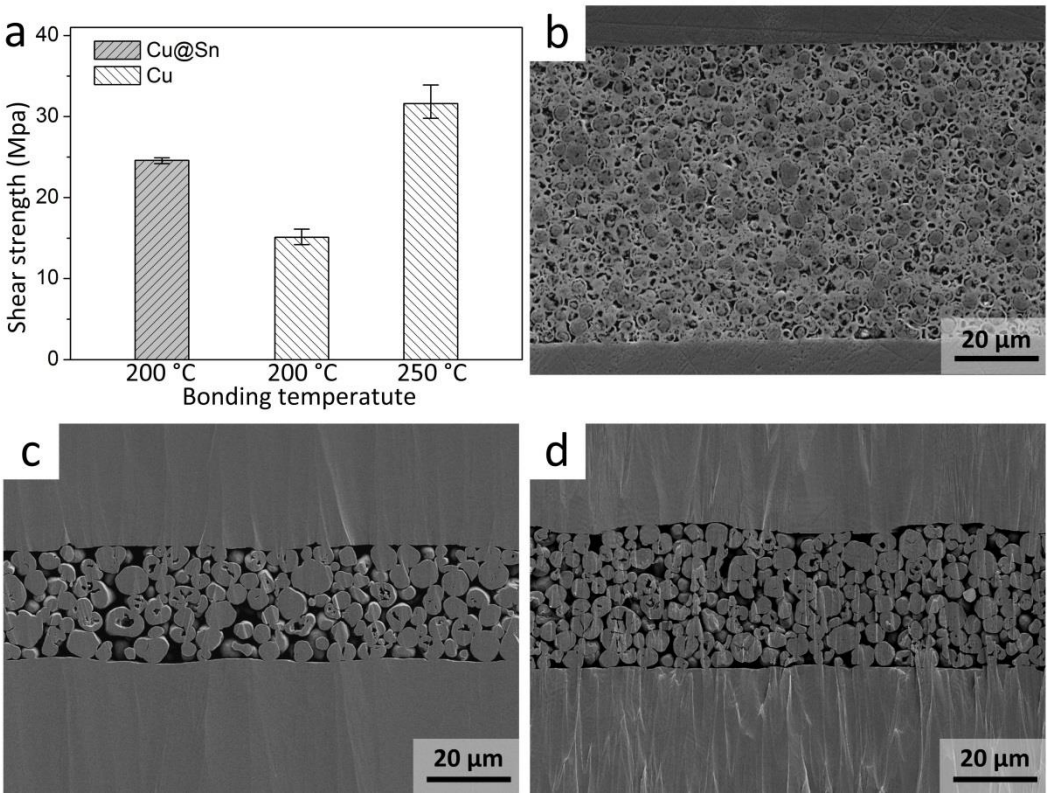

Figure 3.12 Shear strength and cross-sectional images of different sintered joints: (b) Cu@Sn joint bonded at 200 ℃, (c) Cu joint bonded at 200 ℃, and (d) Cu joint bonded at 250 ℃.

porous microstructure with a light grey-color Cu_3Sn network, dark-color embedded Cu particles, and many pores. On the other hand, as show in Fig. 3.12cd, the Cu joint showed single-phase microstructure, however, the change of initial particle shape, as well as the densification of the sintered microstructure, are not obvious. It seems that although a certain value of joint strengths was obtained, the sintering behavior of the microscale Cu particles was insufficient. Moreover, it can be seen that the joint bonded at 250 ℃ showed a similar sintered structure with the joint bonded at 200 ℃, although it presented higher shear strength. Therefore, it is suggested that the bonding temperatures used in this study, either 200 ℃ or 250 ℃, was too low to induce an obvious densification process for only Cu particles and the relatively higher temperature can only promote the formation of neck between particles rather than the reducing of porosity, and thereby the Cu joint bonded at 250 ℃ had similar porosity but different shear strength with the Cu joint bonded at 200 ℃.

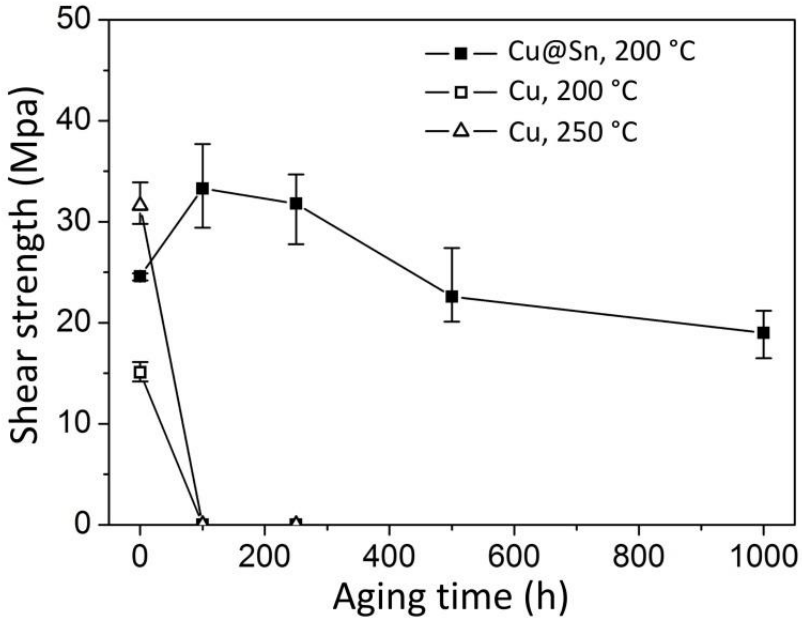

Figure 3.13 Variation of the shear strength of the Cu@Sn joints and the Cu joints during the isothermal aging test.

Fig. 3.13 shows the shear strengths of the Cu@Sn joints and two kinds of Cu joints during the isothermal aging at 250℃ for 1000 h. It can be seen that the shear strength of the Cu@Sn joints increased to 33.3 MPa initially after the first 100 h. Then, the shear strength gradually decreased with the further increase of the aging time. Finally, a shear strength of 19.5 MPa was obtained after the aging for 1000 h. On the other hand, either the bonding was performed at 200 ℃ or at 250 ℃, the obtained Cu sintered joints failed after the first 100 h. Those joints were immediately debonded after cooling down to the room temperature from aging temperature at 250 ℃, thus no shear strength was recorded. This result demonstrates that the Cu joint cannot bear the isothermal aging at 250 ℃ in air.

3.6.2 Oxidation behavior of Cu_3Sn-Cu composite structure

Fig. 3.14 shows the cross-sectional SEM images and the corresponding EDX analysis results of the Cu joints bonded at 250 ℃ after the isothermal aging for 100 h. It can be seen that the initial sintered microstructure disappeared and new dark-color phase formed in the joint. Quantitative EDX point analysis in Fig. 3.14 shows the mole ratio of Cu to O is near 2:1 in the dark-color phase, indicating the new phase is Cu_2O. The Cu_2O formed around the Cu particles and on the Cu substrate,

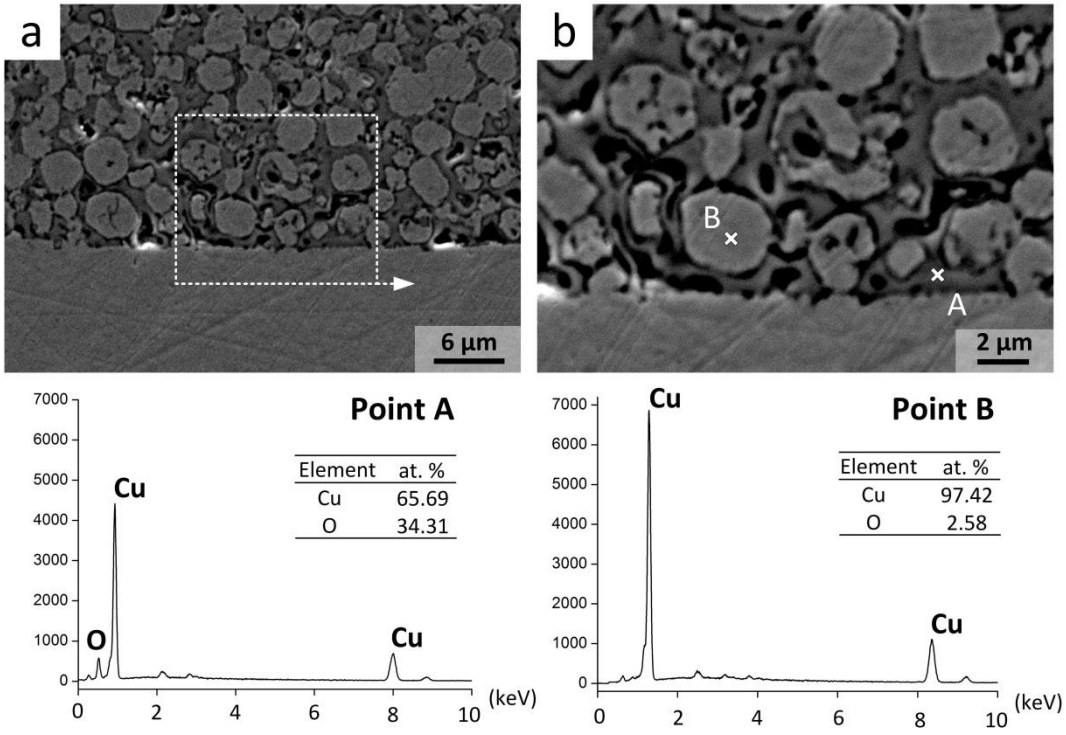

Figure 3.14 Cross-sectional SEM images of the Cu joint after the isothermal aging for 100 h and the point EDX spectra of point A and point B.

consequently, it separated the Cu particles and even formed a network in the bonding layer. Many researchers have reported that the oxidation of Cu substrate will degrade the bonding strength of silver sintered joints during a thermal aging test in air [16, 17]. Researchers even found that after the thermal aging at 300 ℃ for only 24 h, obvious Cu oxide layer was formed between the Cu substrate and the Ag plating layer. Apparently, ambient oxygen permeated through the Ag sintered layer and the Ag plating layer to oxidize the Cu substrate [16]. In my study, it is clear that the serious oxidation happened not only on the Cu substrate but also on the Cu sintered particles, and those Cu even form a network in the joint. Particularly, the initial Cu-Cu metallic bond between the sintered Cu particles and Cu substrate was replaced by the weak Cu-Cu_2O bond due to the formation of Cu_2O layer at the interface. The Cu_2O formation could have a negative effect on the shear strength of Cu joint, as shown in Fig. 3.13. A schematic diagram is given in Fig. 3.15 to explain the failure of Cu joint. During the aging, since these brittle Cu oxides have larger molar volume than Cu, a compressive stress was generated in the oxidation layer during the isothermal aging. Then, after the aging, as the sample cooled down, Cu exhibited a greater shrinkage than Cu_2O due to the larger CTE, thus a

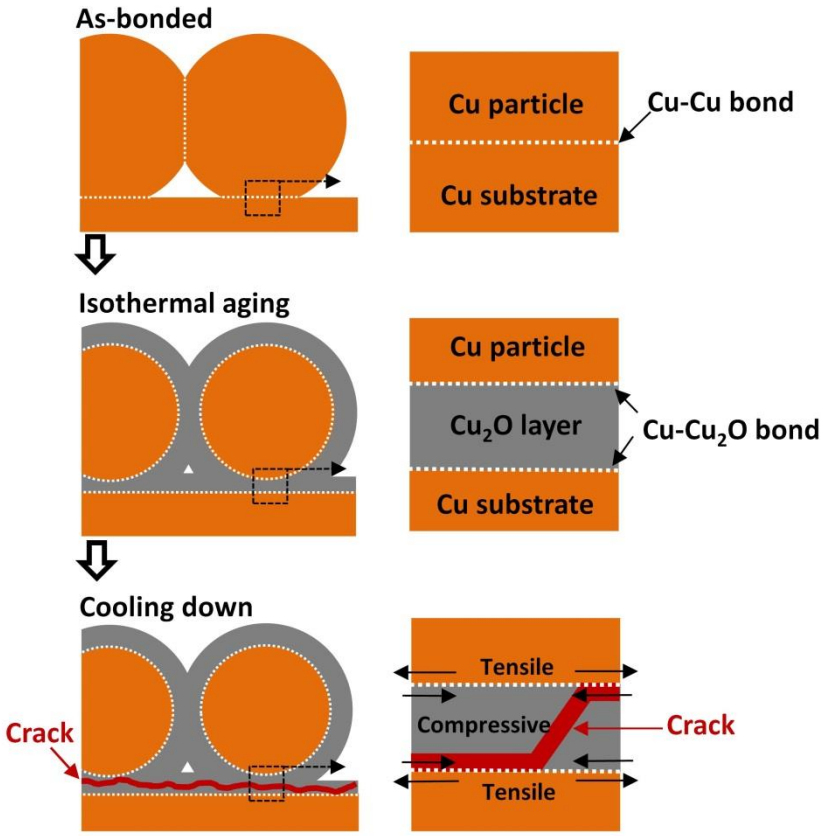

Figure 3.15 Schematic diagram of failure of Cu joint caused by the thermal oxidation.

thermal compressive stress was also produced in the oxidation layer. As the result, the substantial stress induced by the different mole volumes and CTEs for Cu oxides and Cu caused the fracture between the sintered particles and Cu substrate, thereby destroying the Cu joint. On the other hand, it should be noted that the die attach layer in practical power devices does not directly expose to air. In instead, it is generally protected by an epoxy mold compound (EMC) materials. Even so, it is suggested that the oxidation issue of a Cu-sintered layer cannot be neglected because the porous structure of the sintered layer enables the oxygen that crosses the EMC barrier to penetrate into the entire die attach layer..

Fig. 3.16 shows the cross-sectional SEM images and corresponding EDX analysis results of the Cu@Sn joints after the isothermal aging for 1000 h, in which the composition of Cu, Sn, and O in the selected point is given. It was observed that the initial two-phase mixture microstructure of the Cu@Sn joint also changed a lot. The oxides were formed in the pores among the Cu_3Sn IMC matrix

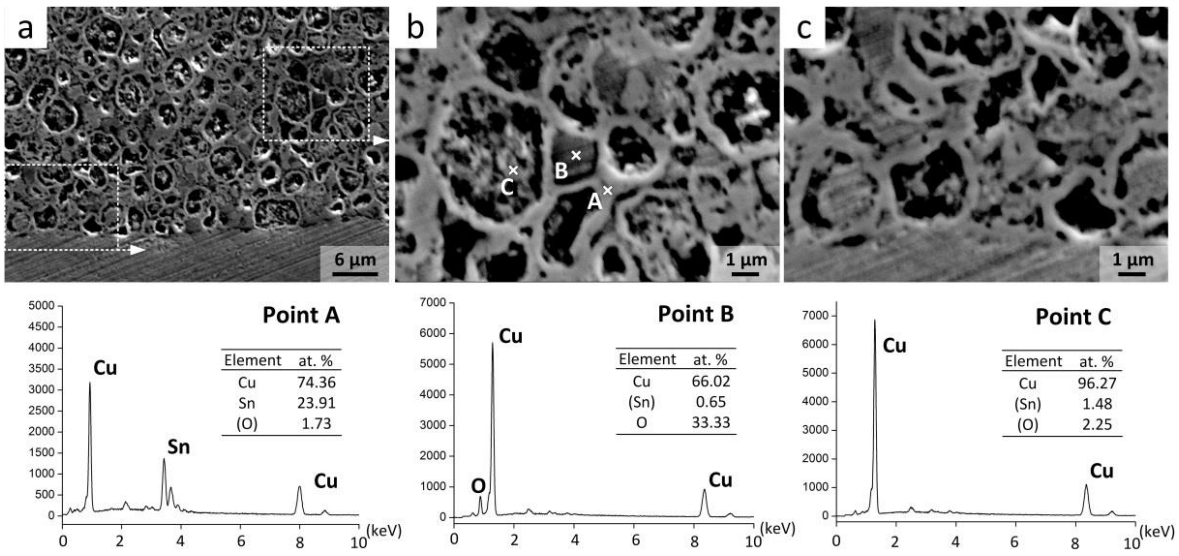

Figure 3.16 Cross-sectional SEM images of the Cu@Sn joint after the isothermal aging for 1000 h and the point EDX spectra of point A, B, and C.

while the embedded Cu particles were consumed. As shown in the Fig. 3.16b, the bright-color Cu_3Sn IMC network (the composition was confirmed by the corresponding quantitative EDX point analysis, see point A) remained, and the morphology of dark-color Cu_2O oxides (the composition was confirmed by the corresponding quantitative EDX point analysis, see point B) were like "isolated island" inside the pores. Moreover, the initial embedded Cu particles were replaced by the voids in the Cu_3Sn IMC matrix. Although some Cu still remained in the voids, the initial spherical shape of the embedded Cu had disappeared and the reduction of their volume is obvious. It is suggested that the formation of these voids led to the decrease of the joint strength after the isothermal aging for 1000 h. On the other hand, the Cu3Sn network remained and the oxide of Sn was not detected, confirming the anti-oxidation behavior of Cu_3Sn IMC. Fig. 3.16c presents the microstructure near the Cu substrate. It can be seen that the Cu_3Sn network was still connected to the Cu substrate and no continuous oxides layer were found on the Cu substrate. Therefore, it is suggested that owing to the formation of Cu_3Sn network, the Cu@Sn joint can maintain a modest shear strength after the isothermal aging for 1000 h. The oxidation of Cu-Sn IMC was never identified as a reliability concern since the Cu-Sn IMCs layer in a soldered joint can be considered as a sealed part, and thus is isolation with oxygen.

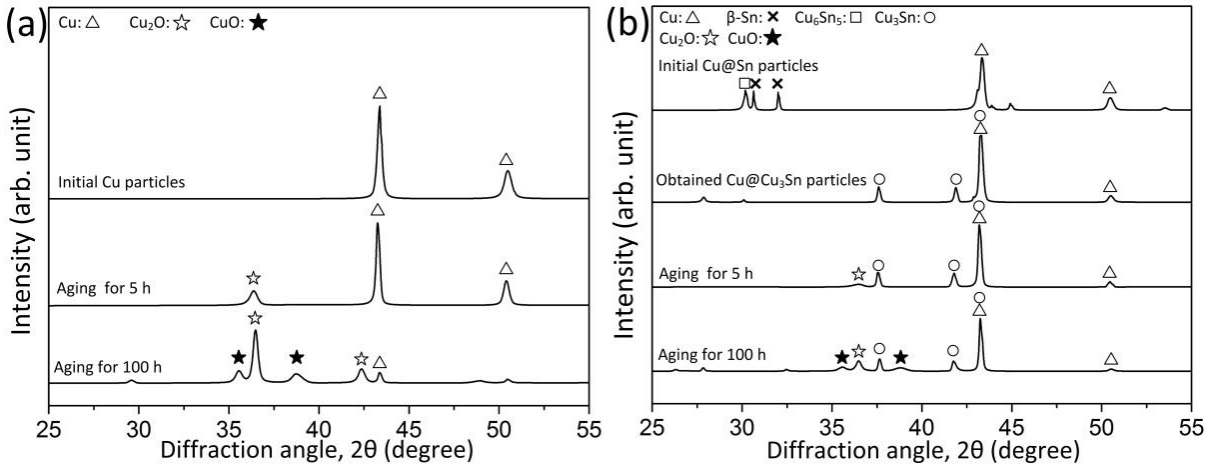

Figure 3.17 (a) XRD analysis of the Cu particles during the isothermal aging at 250 ℃ in air. (b) XRD analysis of the initial Cu@Sn particles, and that of the Cu-Cu_3Sn core-shell particles during the isothermal aging at 250 ℃ in air.

However, in the particles-based sintered joint, the ambient air can permeate into the entire joint through the porous structure, and therefore, the oxidation behavior of the Cu_3Sn-Cu binary phase had a significant influence on the joint strength in my study. In order to understand the oxidation behavior of the structure comprising the Cu_3Sn network and the embedded Cu core during the thermal aging, the XRD analysis of the oxidized Cu particles and the oxidized Cu-Cu_3Sn core-shell particles was conducted. It should be noted that the powders must have higher oxidation rate than that of their sintered layer because the dispersed powders were immediately exposed to the air and had larger specific area than the sintered layer between the Cu substrates. However, the oxidation behaviors of the Cu particles and the Cu-Cu_3Sn core-shell particles can help to understand the oxidation behaviors of their sintered counterpart. Fig. 3.17a presents the XRD profiles of pure Cu particles during the aging at 250 ℃ in air. After only 5 h, an obvious Cu_2O peak appeared. Then, after 100 h, the Cu_2O peak became very strong and obvious CuO peaks also appeared, meantime the intensity of the Cu peak was significantly reduced to lower than that of the CuO peaks. This demonstrates that the Cu particles underwent severe oxidation after the aging for only 100 h, and most Cu was consumed by the oxidation reaction. On the other hand, the XRD profiles of the Cu-Cu_3Sn core-shell particles during the thermal oxidation are shown in Fig. 3.17b. The Cu-Cu_3Sn core-shell particles were obtained by heating the Cu@Sn particle at 200 ℃ for 20 min in the formic acid atmosphere, same to

the heating profile of my bonding process. After the aging for 5 h, a weak Cu_2O peak emerged. Then, after the aging for 100 h, the peak of Cu_2O became sharper with the emerging of weak CuO peaks, and they were obviously weaker than the Cu_3Sn peak. In addition, the peak of Sn oxides was not found in the profile. Apparently, compared to the pure Cu particles, the Cu-Cu_3Sn core-shell particles presented a significantly slower oxidation rate. Moreover, in the oxidized Cu-Cu_3Sn core-shell particles, the Cu phase was consumed by the oxidation reaction, whereas the Cu_3Sn IMC was retained, which is consistent with the aforementioned SEM observation. Therefore, based on the SEM observation of the aged Cu@Sn joint and the XRD profile of the oxidized Cu-Cu_3Sn core-shell particles, it is assumed that the consumption of Cu core and the formation of voids in the Cu_3Sn matrix are caused by Kirkendall effect. A schematic diagram is given to illustrate the oxidation

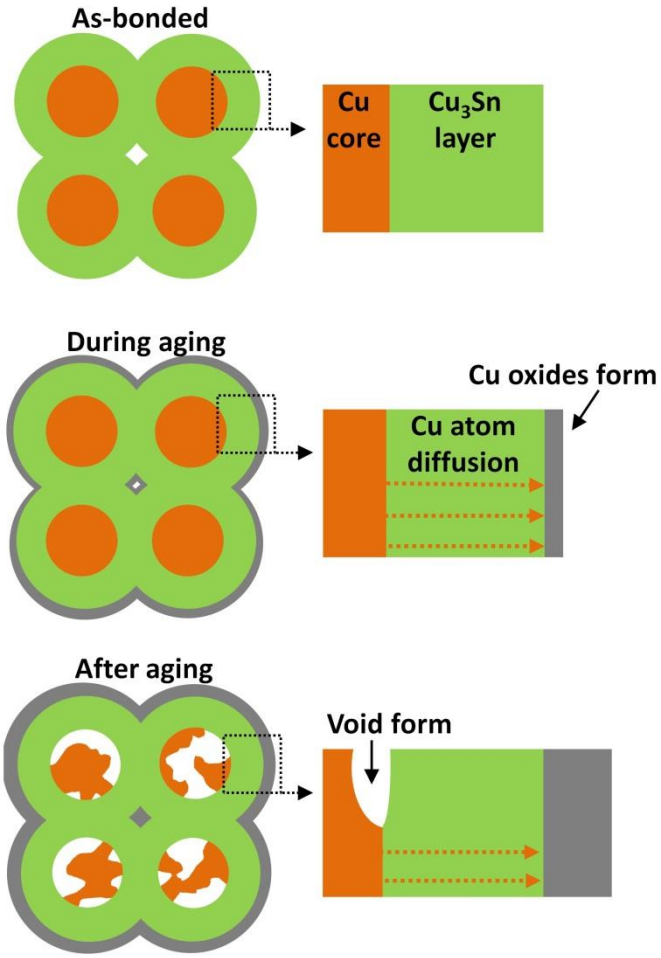

Figure 3.18 Schematic diagram of the oxidation behavior of the Cu_3Sn-Cu composite sintered microstructure.

process of Cu_3Sn-Cu composite sintered microstructure, as shown in Fig. 3.18. The formation of Cu oxides outside the Cu_3Sn layer induced the outward diffusion of Cu atom from the Cu core to the surface of Cu_3Sn that is in contact with oxygen, and as a result, this outward diffusion of copper led to the consumption of Cu core and the formation of Kirkendall void.

As mentioned before, owing to the existence of Cu_3Sn network, Cu oxides did not form a network in the Cu@Sn joint during the isothermal aging. In other words, the growth of Cu oxides was suppressed by the Cu_3Sn network. Two main reasons caused that smaller amount of Cu oxides were produced in the Cu@Sn joint than that in the Cu joint. One is the slow growth kinetic of Cu_2O in the pores that was covered by the Cu3Sn network since the Cu_3Sn network can serve as a diffusion barrier to Cu atom that participates in the oxidation reaction. Another is that the space for the growth of Cu oxides in the Cu@Sn joint is smaller than that in Cu joint. Particularly, the Cu oxides mainly formed in the empty space or the pores that the ambient air can permeate, and therefore the Cu3Sn network could limit the maximum volume of Cu oxides to the volume of pores since the Cu3Sn phase does not directly participate in oxidation the reaction. On the other hand, the Cu network was directly oxidized and consumed, thus providing larger space for the oxide growth in Cu joint. A schematic diagram to show this difference is given in Fig. 3.19, where the cross-section of the pores

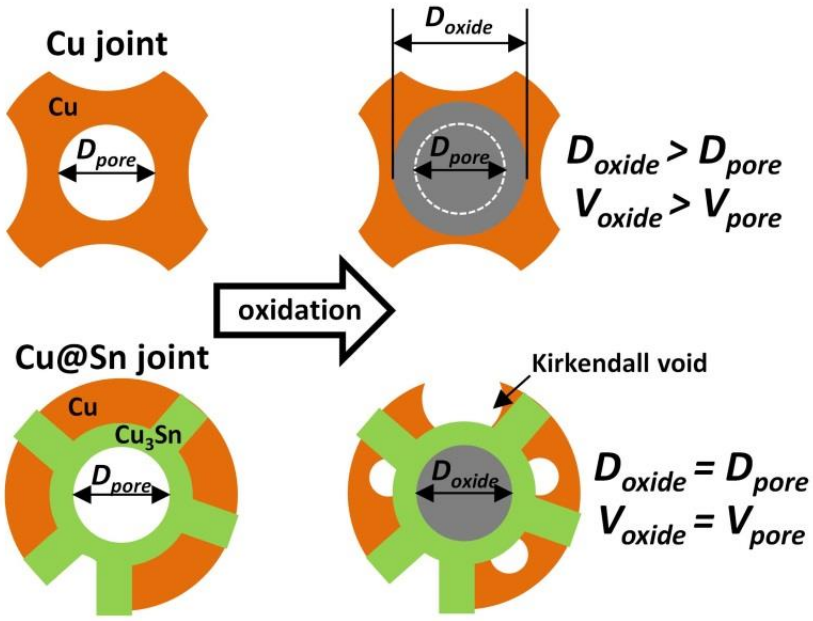

Figure 3.19 Comparison of the volume of oxides formed in the pores of Cu joint and Cu@Sn joint.

is simplified as round shape. Here, an attempt was made to estimate the volume of Cu oxides formed in the Cu@Sn joint and Cu joint after a thermal oxidation, and before that two assumptions need to be clarified. Firstly, the predominant oxidation product Cu2O is assumed to be the only oxidation product. Thus, two molar Cu is consumed to produce one molar Cu oxide. Secondly, it is assumed that the oxidation rate will become very limited once the pore is fully filled by the oxides. As the pore is fully filled, the entire bonding layer will be isolated from the ambient air, after that, further oxidation inside the joint become more difficult and complicated and thereby is neglected in the following estimate. Then, the relation among the volume of Cu oxides, initial pores, and consumed Cu in the Cu joint and Cu@Sn joint can be expressed as follows, respectively:

$$\text{Cu joint: } \begin{cases} V_{oxide} \le V_{Cu} + V_{pore} \\ V_{oxide} = \dfrac{M_{oxide}}{\rho_{oxide}} n_{oxide} \\ V_{Cu} = \dfrac{M_{Cu}}{\rho_{Cu}} n_{Cu} \\ 2n_{oxide} = n_{Cu} \end{cases} \quad (3.6)$$

$$\text{Cu@Sn joint: } \begin{cases} V_{oxide} \le V_{pore} \\ V_{\mathrm{Cu}} = V_{\mathrm{void}} \\ V_{oxide} = \dfrac{M_{oxide}}{\rho_{oxide}} n_{oxide} \\ V_{Cu} = \dfrac{M_{Cu}}{\rho_{Cu}} n_{Cu} \\ n_{oxide} = 2n_{Cu} \end{cases} \quad (3.7)$$

where n, ρ, M, and V with subscripts representing Cu and oxide are the corresponding molar quantities, densities, molar mass, and the total volume of the formed Cu_2O and consumed Cu, respectively. Correspondingly, V_{pore} and V_{void} are the total volume of pore and Kirkendall void, respectively. The densities of Cu_2O were taken as 6.0 g/cm3. And it is derived that, during the isothermal aging, the amount of Cu oxides formed in the joint should satisfy the following relation:

$$\begin{cases} V_{oxide} \le 2.47 V_{pore} & \text{------ in Cu joint} \\ V_{oxide} = 1.68 V_{\mathrm{void}} = 1.68 V_{\mathrm{Cu}} \le V_{pore} & \text{------ in Cu@Sn joint} \end{cases}$$

The result demonstrates that even both joints with the same porosity are severely oxidized, the

amount of Cu oxides formed in the Cu@Sn joint is still much less than that in Cu joint. In the real case, compare to the Cu joint, the Cu@Sn joint exhibited a lower porosity and slower oxidation rate, and therefore much fewer Cu oxides was formed in the aged Cu@Sn joint. On the other hand, the Cu joint underwent a rapid thermal oxidation at 250 ℃, and the high porosity indirectly led to the high volume ratio of Cu oxides in the aged joint and thereby contributed to the formation oxide network.

EPMA elemental mapping of the bonding layer was used to show the evolution of oxidation in the Cu joint and the Cu@Sn joint during the isothermal aging, as shown in Fig. 3.20. In Fig. 3.20a, it is very clear that the oxides occupied the most area and formed a network in the bonding layer, thereby separating the remained Cu particle. Such microstructure inevitably led to a weak bonding strength. Fig. 3.20b-e give the distribution of Cu oxides in the Cu@Sn joint after the aging of a different time. After 100 h aging, only trace amounts of oxygen was detected in the Cu@Sn joint, demonstrating that only a limited oxidation happened in the Cu@Sn joint during the first 100 h aging. After 250 h aging, the oxygen became more obvious, particularly, many isolated oxides were formed in the bonding layers. These oxides were mainly formed in the pores of the sintered structure and were separated by the Cu_3Sn network. Therefore, the growing isolated oxides cannot connect each other to form the oxides network in the bonding layer as long as the Cu_3Sn network remained. From 250 h to 1000 h, the area occupied by oxygen in the bonding layer increased with the increase of aging time, however, the existence of Cu_3Sn network inhibited the formation of oxides network, thus avoiding the failure of the bonded joint.

Fig. 3.21 presents representative SEM images and corresponding EPMA elemental mappings on the fracture surface of the Cu joint after 100 h aging and the Cu@Sn sintered joint after 1000 h aging. The flat fracture can be observed on the fracture surface of both joints, showing a brittle property. As shown in Fig. 3.21a, the EPMA mapping presented strong oxygen signal region on the fracture surface, confirming that serious oxidation happened in the bonding layer of Cu joint during the aging. Some regions, such as the periphery of the fracture surface, exhibited a weaker oxygen signal than other regions. It is suggested that the fracture occurred between the Cu substrate and thin oxide layer in those regions, thus leaving a bare Cu surface. On the other hand, the oxygen signals were relatively weak on the fracture surface of the Cu@Sn sintered joint after the aging of 100 h and the longer aging of 1000 h, as shown in Fig. 3.21bc, indicating that oxidation degree in the Cu@Sn joint

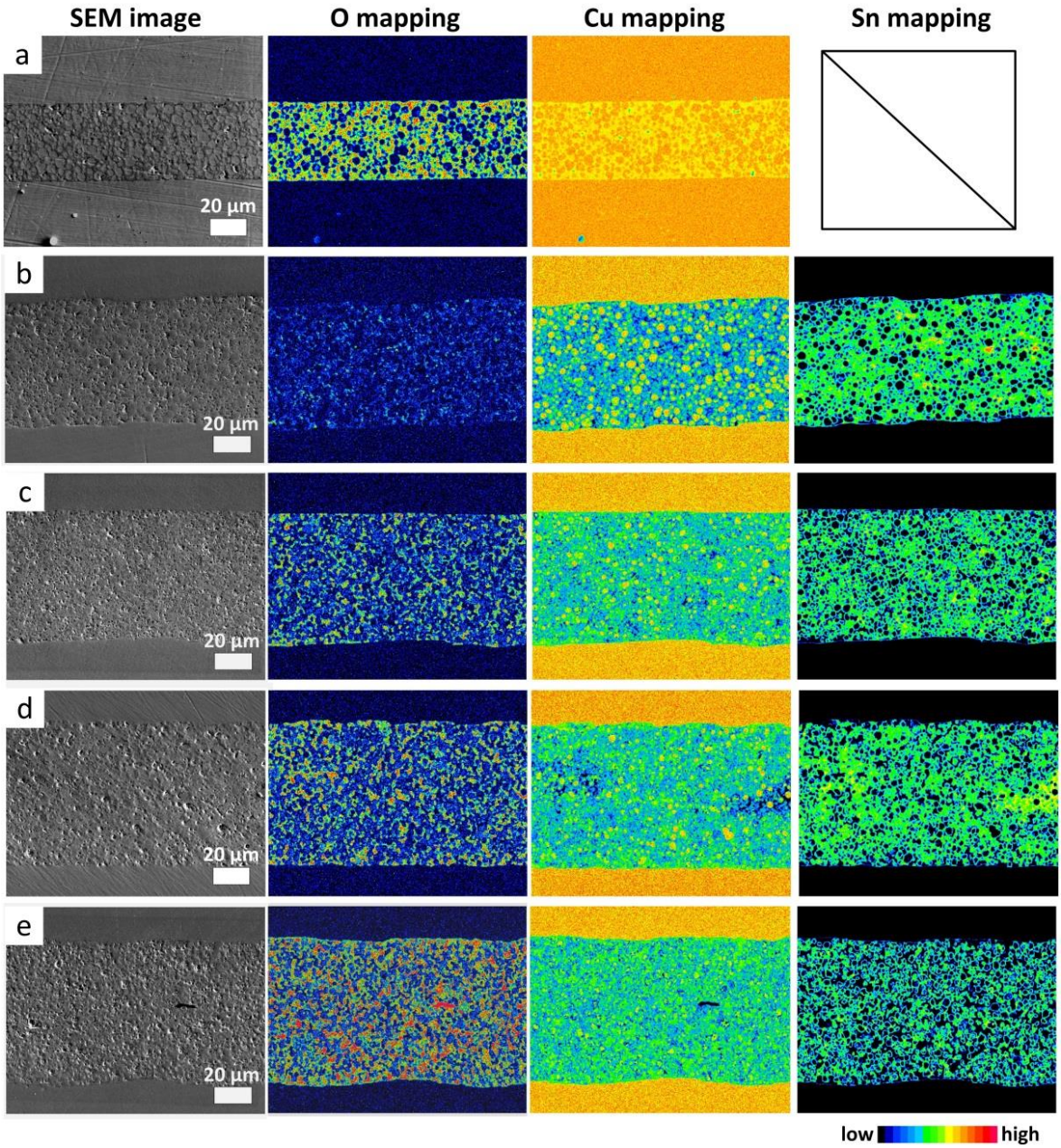

Figure 3.20 Cross-sectional SEM images and corresponding EPMA elemental mappings of the Cu joint and the Cu@Sn joints after the isothermal aging for a different time: (a) and (b) after 100 h, (c) after 250 h, (d) after 500 h, and (e) after 1000 h.

was much lower than that in the Cu joint, and which was consistent with the observation in Fig. 3.20. It is suggested that the formation of Cu_3Sn network avoided the over-oxidation in the Cu@Sn joint, and thereby ensuring the integration of the microstructure and the bonding strength. In addition, the oxygen and copper signal in some regions show a higher level than that at other regions, whereas the

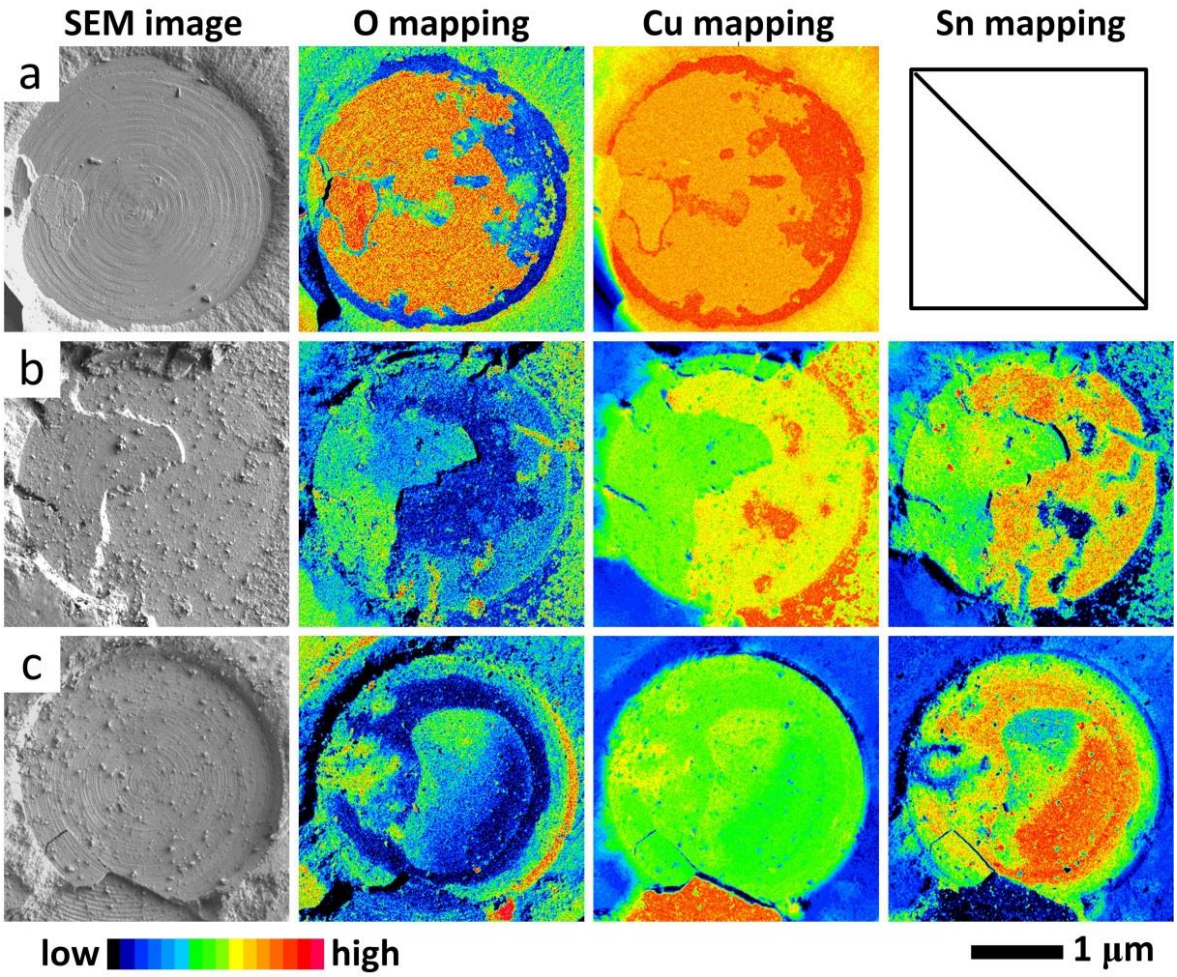

Figure 3.21 SEM images and corresponding EPMA elemental mapping of the fracture surface of (a) the Cu joint after the isothermal aging for 100 h, (b) the Cu@Sn joint after the isothermal aging for 100 h, (c) the Cu@Sn joint after the isothermal aging for 1000 h.

Sn signal exhibits a lower level at these regions, indicating that there are some Cu oxide-rich regions on the fracture surface. The existence of these oxide-rich fracture regions reveals that the degree of oxidation was not uniform in the bonding layer, and which could be due to the uneven porosity in the bonding layer. As mentioned before, the degree of oxidation is related to the porosity in the Cu3Sn-Cu composite microstructure. More oxides could be produced in the regions with a higher porosity, and also more Cu cores were consumed and larger Kirkendall voids were formed in those regions. Consequently, the oxide-rich region is likely to exhibit a weak bond and lead to the joint failure as the crack initiation under the shear load.

3.7 Comparison of transient liquid phase bonding and solid-state bonding Sn-coated Cu particles

In *Chapter 2* and *Chapter 3*, using the same Cu@Sn particle but different processing temperature, the TLP process and the SSB process were respectively developed. The primary difference between them was that molten Sn formed and participated the bonding during the TLP process, whereas, the SSB process was a complete solid-state process with a very low processing temperature. Although similar Cu_3Sn-Cu composite microstructures can be obtained by both processes, as shown in Fig. 2.8 and Fig. 3.5, the processing time of TLP is significantly shorter than that of SSB, which was attributed to the faster rate of the liquid-solid reaction. Moreover, owing to the formation of molten Sn that can flow into the gaps between the particles through capillary action, the bonding layer produced by the TLP process was very dense and can be considered as a sealed part, thus exhibiting better high-temperature microstructural stability than the SSB joint during the isothermal aging test. Particularly, after the isothermal aging for 1000 h, the TLP joint exhibited a sound shear strength with a limited oxidation degree in the bonding layer, as shown in Fig. 2.14, However, the shear strength of the SSB joint was decreased due to the obvious oxidation in the bonding layer, as shown in Fig 3.20. Table 3.1 gives a comparison of the process conditions, obtained microstructures, and performances between the Cu@Sn particle-based TLP process and SSB process.

Table 3.1 Comparison of TLP process and SSB process.

Bonding process	Temperature	Time	Microstructure	Strength	After isothermal aging at 250 ℃ for 1000 h	
					Shear strength	Oxidation degree
TLP	300 ℃	30 s	Cu_3Sn-Cu composite	24.2 MPa	31.2 MPa	Limited
SSB	200 ℃	1200 s	Cu_3Sn-Cu composite	24.6 MPa	19 MPa	Obvious

Note: A bonding pressure of 10 MPa was used in both processes.

3.8 Conclusion

In this chapter, we developed a solid-state bonding process using microscale Cu@Sn particles for high-temperature die attach applications. Compared to the Cu-Sn TLP bonding, a lower bonding temperature of 200 ℃ was used in this bonding process.

After the bonding in the formic acid atmosphere with the pressure of 20 MPa, the shear strength of Cu@Sn joint reached 20.4 MPa at a bonding time of 5 min and gradually increased with increasing bonding time. The shear strength was 25.8 MPa at a bonding time of 20 min. After 20 min, extending the bonding time further shows a limited effect on the bonding strength. The atmosphere also had an influence on the bonding strength. In the case of N_2 atmosphere, the Cu@Sn joints exhibited a very limited shear strength lower than 5 MPa.

The Cu@Sn joint exhibited a composite porous microstructure comprising a Cu_3Sn IMC matrix with a dispersion of pure Cu particles. The formation of a two-phase mixture microstructure is attributed to the unique structure of the Cu@Sn particles used in the solid-state bonding process. During the bonding, the phase transformation and densification process in the joint occurred simultaneously. Finally, the fracture morphology of the Cu@Sn joints showed a combination of IMC matrix and deformed Cu particles.

Moreover, the thermal stability of the joints bonded with Cu particles and Cu@Sn particles during the isothermal aging at 250 ℃ was also investigated. Debonding of the Cu joint happened after the aging for only 100 h, due to the severe oxidation of sintered Cu structure. On the other hand, the Cu@Sn joint presented nearly 20 MPa shear strength after the aging for 1000 h. The Cu_3Sn IMC network was remained and significantly inhibited the oxidation of Cu substrate, thereby maintaining the bonding strength of the Cu@Sn joint. The results demonstrate that compared to the pure Cu sintered structure, the Cu_3Sn-Cu composite structure obtained by the low-temperature bonding using microscale Cu@Sn particles provided the enhanced thermal stability during the isothermal aging at 250 ℃, and it has the potential to fulfill the requirements of high temperature application for power device packaging.

Reference

[1] R. Agarwal, W. Zhang, P. Limaye, R. Labie, B. Dimcic, A. Phommahaxay and P. Soussan, Cu/Sn microbumps interconnect for 3D TSV chip stacking, *Proceedings of the IEEE Electron. Compon. Technol. Conf. (ECTC)*, (2010) 858-863.

[2] R. Labie, W. Ruythooren, J. Van Humbeeck, Solid state diffusion in Cu–Sn and Ni–Sn diffusion couples with flip-chip scale dimensions, *Intermetallics*, **15** (2007) 396-403.

[3] H. Liu, K. Wang, K. Aasmundtveit, N. Hoivik, Intermetallic Cu_3Sn as oxidation barrier for fluxless Cu-Sn bonding, *Proceedings of the IEEE Electron. Compon. Technol. Conf.*, (2010) 853-857

[4] A. S. Helle, K. E. Easterling, M. F. Ashby, Hot-isostatic pressing diagrams: new developments, *Acta Metall.*, **33** (1985) 2163-2174.

[5] S. Zhang, Y. Zhang, H. Wang, Effect of oxide thickness of solder powders on the coalescence of SnAgCu lead-free solder paste, *J. Alloys Compd.*, **487** (2009) 682-686.

[6] W. Lin, Y. C. Lee, Study of fluxless soldering using formic acid vapor, *IEEE Trans. Adv. Pack.*, **22** (1999) 592-601.

[7] J. F. Li, P. A. Agyakwa, C. M. Johnson, Interfacial reaction in Cu/Sn/Cu system during the transient liquid phase soldering process, *Acta Mater.*, **59** (2011) 1198-1211.

[8] F. Lang, H. Yamaguchi, H. Nakagawa, H. Sato, Thermally stable bonding of SiC devices with ceramic substrates: Transient liquid phase sintering using Cu/Sn powders, *Electrochem. Soc.*, **160** (2013) 315-319.

[9] S. J. L. Kang, *Sintering: densification, grain growth and microstructure*, Butterworth-Heinemann, 2004.

[10] F. R. N. Nabarro, Deformation of crystals by the motion of single ions, *Report of a Conference on Strength of Solids*, (1948) 75-90.

[11] C. Herring, Diffusional viscosity of a polycrystalline solid, *J. Appl. Phys.*, **21** (1950) 437-445.

[12] R. L. Coble, Diffusion models for hot pressing with surface energy and pressure effects as driving forces, *J. Appl. Phys.*, **41** (1970) 4798-4807.

[13] P. J. Shang, Z. Q. Liu, X. Y. Pang, D. X. Li, J. K. Shang, Growth mechanisms of Cu_3Sn on polycrystalline and single crystalline Cu substrates, *Acta Mater.*, **57** (2009) 4697-4706.

[14] S. J. Wang, L. H. Hsu, N. K. Wang, C. E. Ho, EBSD investigation of Cu-Sn IMC microstructural evolution in Cu/Sn-Ag/Cu microbumps during isothermal annealing, *J. Electron. Mater.*, **43** (2014) 219-228.

[15] N. S. Bosco, F. W. Zok, Strength of joints produced by transient liquid phase bonding in the Cu-Sn system, *Acta Mater.*, **53** (2005) 2019-20

[16] S. T. Chua, K. S. Siow, Microstructural studies and bonding strength of pressureless sintered nano-silver joints on silver, direct bond copper (DBC) and copper substrates aged at 300 °C, *J. Alloys Compd.*, **687** (2016) 486-498.

[17] H. Zhang, S. Nagao, K. Suganuma, H. J. Albrecht, K. Wilke, Thermostable Ag die-attach structure for high-temperature power device, *J. Mater. Sci. Mater. Electron.*, 27 (2016) 1337-1344

Chapter 4
Surface modification of Cu particles by oxidation-reaction process

4.1 Introduction

In *Chapter 2 and Chapter 3*, we utilized microscale Cu@Sn particles to realize transient liquid phase bonding and solid-state bonding, respectively. Owing to the use of Sn surface coating, the bonding processes exhibited good manufacturability and the obtained bonded joints showed excellent thermal stability. As mentioned in *Chapter 1*, it is the great negative formation enthalpies of Cu-Sn IMC that contributes to the improvement of the driving force of low-temperature bonding.

However, on the other hand, the formation of Cu-Sn IMC also brings about some compromise in the joint performance; in particular, both fracture toughness and thermal conductivity of Cu-Sn IMC are not as good as that of pure Cu [1, 2]. In addition, a relatively high bonding pressure is needed for the bonding process using Cu@Sn particles, and which is not expected for the die attachment of brittle WBG chip. Therefore, in order to achieve a pure Cu joint with low-pressure or pressureless sintering bonding process, we proposed a unique surface modification method to Cu particles by an oxidation-reduction process. During the process, the formation of Cu_2O takes place on

the surface of Cu particles by a thermal oxidation in an air, followed by a transformation to Cu nanotextured surface during a reduction process in a formic acid atmosphere. By a switch of bonding atmosphere from air to formic acid vapor, Cu particles can be in-situ surface modified and sintered in the chamber. In this Chapter, the surface morphological evolution and phase transform of Cu particles during the oxidation-reduction process was clarified. Moreover, the inherent mechanism for this surface modification was discussed.

4.2 Experimental

4.2.1 Microscale Cu particles

Flake-shaped microscale Cu particle was used in this study as starting materials. It had an average diameter 6.9 μm, an average thickness of 1μm, and a specific area of 0.13 m^2/g. (1400YP , MITSUI MINING & SMELTING CO. LTD). These flake-shaped Cu particles are hereafter referred to as “Cu flakes”. SEM images of the Cu flakes is shown in Fig. 4.1.

4.2.2 Oxidation-reduction process

Firstly, the Cu flakes were mixed with a terpineol solvent to make the Cu paste, which consisted of 85 mass % Cu flakes and 15 mass % terpineol solvent. Then, the Cu paste was printed on a Cu

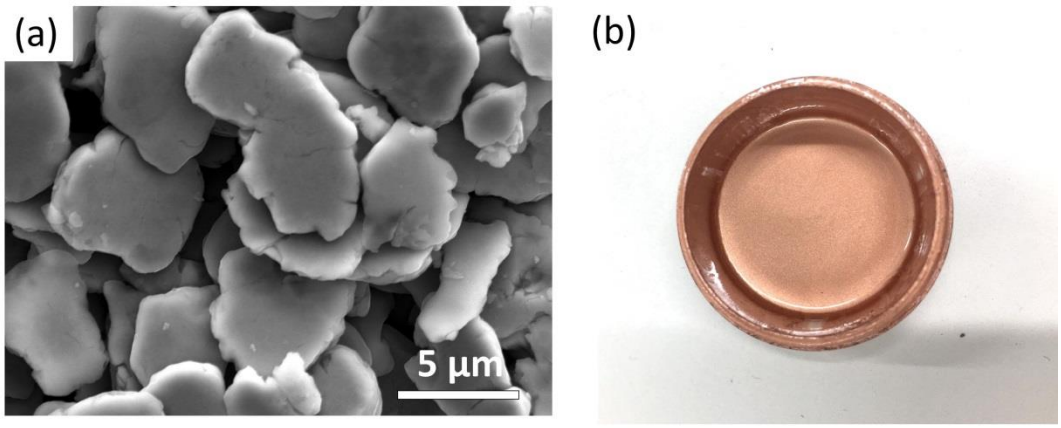

Figure 4.1 (a) SEM image of flake-shaped Cu particles and (b) optical image of Cu particle paste used in this study.

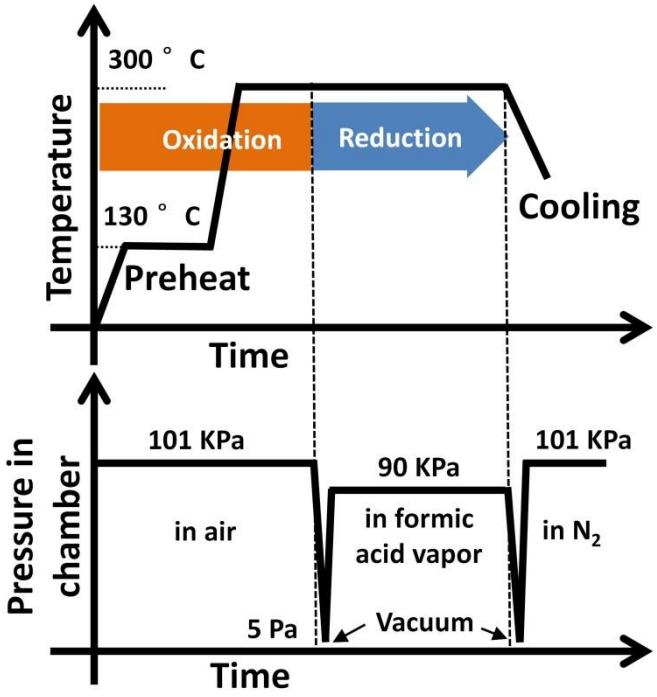

Figure 4.2 Illustration of temperature and pressure profile of oxidation-reduction process.

plate, as the sample for the oxidation-reduction process. As the name suggests, the oxidation-reduction process includes two stages: thermal oxidation in the ambient air and subsequent reduction in the formic acid atmosphere. The detailed process is as follows: The sample was first pre-heated at 130 ℃ for 5 min in the air to completely evaporate the solvent, after which it was heated up to 300 ℃ at 0.5 ℃/s and held at 300 ℃ for different times for thermal oxidation. After the thermal oxidation, the chamber was vacuumed (<5 Pa), and then formic acid vapor was introduced into the chamber until the pressure in chamber was up to 90 KPa. Then, the sample was continued to be heated at 300 ℃ in formic acid atmosphere to reduce Cu oxides. After a reduction process for different times, the oxidation-reduction process was finished. During the cooling, the chamber was vacuumed again and filled with N_2 to clean the formic acid vapor. Finally, the chamber with the sample was cooled down to room temperature. The corresponding heating profile, as well as the pressure profile is illustrated in Fig. 4.2.

4.2.3 Characterization methods

TG-DTA traces for the Cu paste were measured during heating in the air and N_2, respectively (temperature increasing at 0.5 ℃/s). In addition, the TG-DTA measurement of pure Cu flakes during heating in the air was also performed with the same heating rate. X-ray diffraction (XRD) analysis of initial Cu flakes, oxidized Cu flakes, and reduced Cu flakes were conducted by an X-ray diffractometer (Rigaku Ultima IV) using Cu-Kα radiation (λ = 1.5405 Å). The diffracted beam was scanned in steps by 0.01 ° in an angular range from 20 to 80 °, 2θ. A field emission scanning electron microscopy (FE-SEM, Hitachi SU-70) was used for surface microstructural observation. Moreover, cross-sectional sample of oxidized Cu flakes was prepared by focus ion beam (FIB, Hitachi) for transmission electron microscopy (TEM) observation. The TEM observation was conducted using a JEOL microscope equipped with an EDX device.

4.3 Thermal oxidation process

4.3.1 Thermal behavior of Cu paste and Cu flakes during heating in air

Fig. 4.3 shows the TG-DTA trace of the Cu paste during heating in the air and in N_2, respectively. In the curves, exothermic peaks and rapid weight loss occurred at approximately 125 ℃, regardless of the atmosphere, indicating the thermal decomposition and combustion of terpineol solvent occurred at around 125 ℃. In addition, the exothermic peak in air was higher than that in N_2, indicating the combustion of terpineol was improved in an air. Then, the weight losses of the paste in both atmospheres were similar and near their highest value at around 200 ℃. It demonstrates that, at around 200 ℃, the solvent was mostly evaporated, and moreover the thermal oxidation of Cu flakes in the air was still insignificant. After that, the sample heated in the air showed different trace with that heated in N_2. It presented an obvious exothermic peak at approximately 250 ℃, accompanied with the start of weight increase. On the other hand, there is no exothermic peak in the DTA curve of the sample heated in N_2, and the corresponding TG curve remained level. It is suggested that the emerging of exothermic peak and the start of weight increase were caused by the thermal oxidation of Cu flake in the air, and this thermal oxidation did not become obvious until 250 ℃.

Fig. 4.4 gives the TG-DTA trace of pure Cu flake during heating in air. The sample was heated to 300 ℃ from room temperature at the rate of 0.5 ℃/s, and then isothermally oxidized at 300 ℃ for

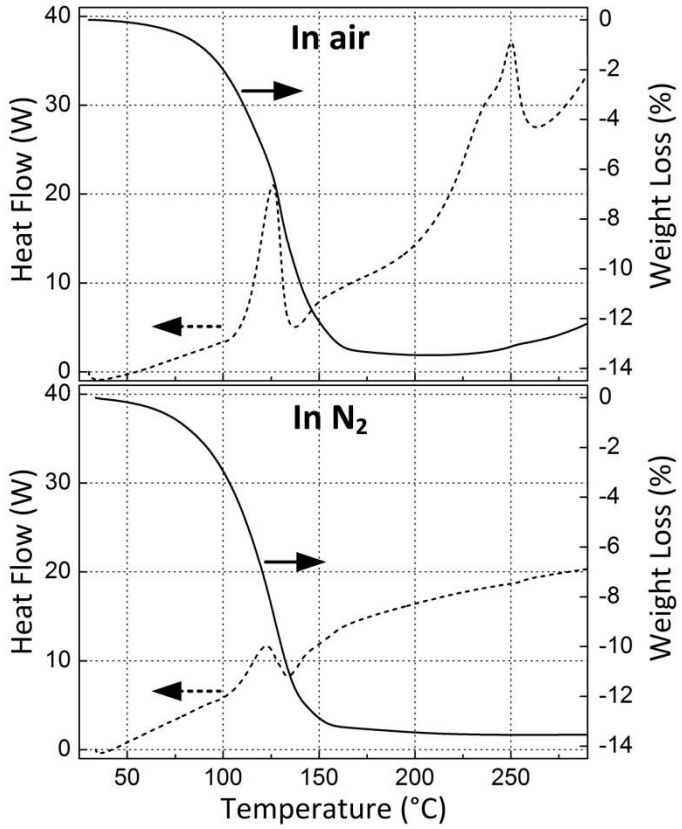

Figure 4.3 Traces of TG-DTA for Cu paste during heating in air and in N_2 (temperature increasing at 30 ℃ min^{-1}).

50 min. It can be seen that the oxidation occurred exothermically, beginning from the period of temperature rising and continuing at the period of isothermal holding, and two adjacent exothermic peaks existed on the curve. The first exothermic peak occurred at around 242 ℃ and was accompanied by a rapid increase of sample weight, corresponding to the thermal oxidation of Cu flakes during the period stage of temperature rising. It is same to the TG-DTA curve of Cu paste heated in air, as shown in Fig. 4.3. Afterward, when the sample was heated to around 296 ℃, a widening and increasing exothermic peak emerged. After that, no other peaks can be seen during the period isothermal holding and the corresponding TG curve gradually became flat.

It is reasonable that the exothermal peak occurs at the initial stage of exothermal oxidation process because the growth of surface oxide was reaction-controlled at that time [3]. As mentioned in *Chapter 3*, it has been shown univocally that the growth of Cu oxide is controlled by the outward

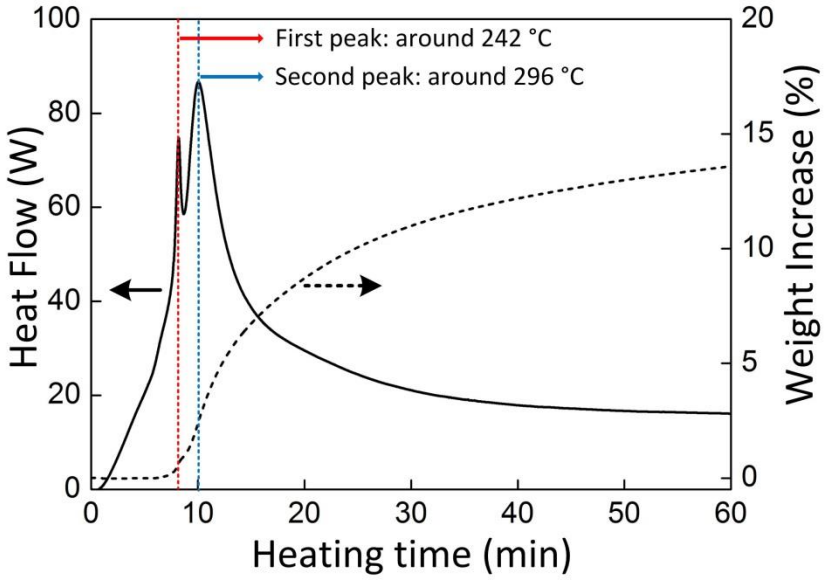

Figure 4.4 Traces of TG-DTA for Cu flakes during heating in air (temperature increasing to 300 ℃ at 30 ℃ min^{-1} and holding at 300 ℃ for 50 min).

diffusion of copper cation during the oxidation of Cu [4-7]. However, at the initial period of oxidation, the surface oxide was very thin, the reactivity of the oxidation was realized to the full extent because the supply of the Cu atoms was almost instantaneous due to the negligibly short diffusion path. Thus, chemical reaction took place at an almost constant rate and the oxide layer grew at the highest rate [8]. Meantime, the reaction heat was quickly released, resulting in the appearing of exothermic peak. After that, the growth of oxide layer was converted to diffusion-controlled, and as the oxide layer thickens, the transport of the Cu atom across the bulk Cu oxide from the Cu flake to the reaction interface became increasingly slow. During the period of diffusion-controlled, the reaction heat was slowly released, thus the exothermic peak cannot appear. According to the above discussion, it is suggested that the first exothermal peak corresponds to the period of reaction-controlled and indeed it occurred in the initial oxidation reaction. On the other hand, it is very interesting that another exothermal peak appeared next to the first one. One possible reason is that two different oxidation reactions produced two kinds of oxidation products, Cu_2O and CuO, as shown below:

$$4Cu + O_2(g) \rightarrow 2Cu_2O \qquad (4.1)$$

$$2Cu_2O + O_2(g) \rightarrow 4CuO \qquad (4.2)$$

And two close exothermal peaks corresponds the initial period of each oxidation reaction respectively. However, the XRD result in Fig. 4.5 shows that during the thermal oxidation at 300 ℃, Cu_2O peaks appeared and significantly increased, whereas emerged CuO peak were always very weak. It demonstrates that reaction (1) was the predominant oxidation reaction when Cu flakes were thermally oxidized at 300 ℃. Indeed, many researchers have reported that when Cu is oxidized in the air at low temperatures (below 400 ℃), Cu_2O is the major product, whereas the formation CuO is very limited [9, 10]. Thus, the second exothermic peak that was even stronger than the first one cannot be caused by the production of CuO. Another possible reason for the formation of separated peaks is that the initial growth of the Cu_2O on the surface of Cu flake can be subdivided into two

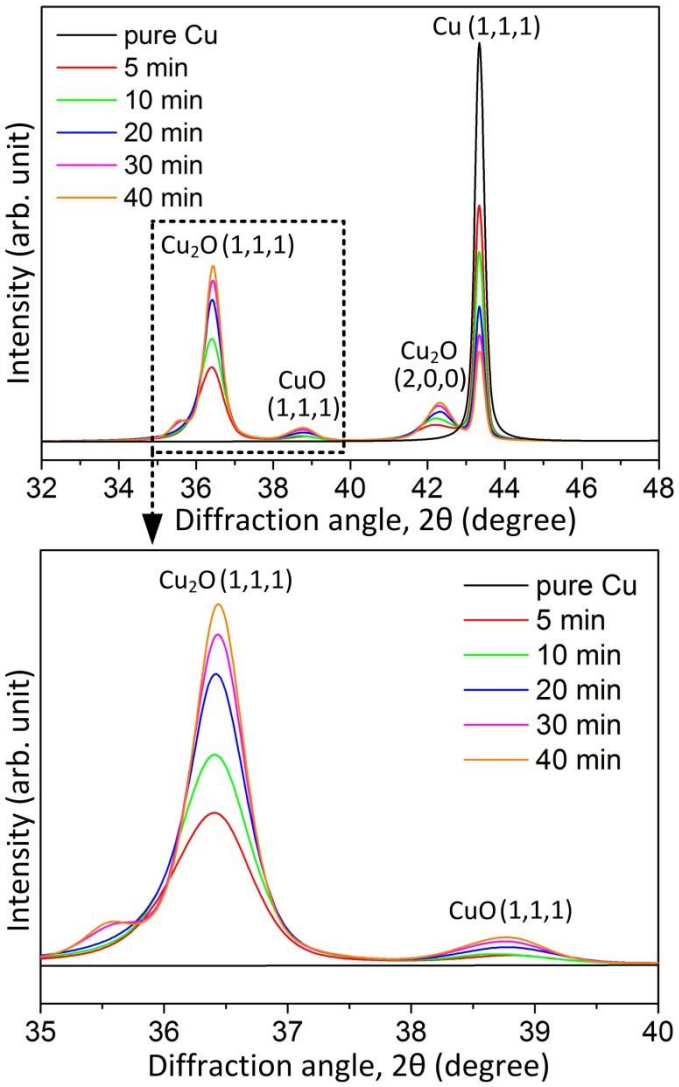

Figure 4.5 XRD profiles of Cu flakes as well as oxidized Cu flakes at 300 ℃ with different times.

stages, and each stage induced each exothermic peak respectively. In the following part, based on the SEM observation, we will verify this assumption and clarify the correlation of oxide growth with the surface morphological evolution on the Cu flake during the thermal oxidation at 300 ℃.

4.3.2 Formation of Cu_2O nanoparticles

Fig. 4.6 shows the SEM images of Cu flakes thermally oxidized at 300 ℃ in air for different times. And Table 4.1 gives the corresponding EDX point analysis of points A-F in Fig. 4.6. As shown in Fig. 4.6, Cu oxide nanoparticles formed and gradually covered the entire surface of Cu flakes during the thermal oxidation. Based on the XRD results in Fig. 4.5, it is suggested that these nanoparticles were Cu_2O nanoparticles. In Fig. 6ab, when the Cu flake was just heated to 300 ℃, a few Cu_2O nanoparticles emerged on the surface of Cu flake, although they were not obvious in the low magnitude image. In the high magnitude image, it is more clear that Cu_2O nanoparticles that have a diameter less than 50 nm formed on the flake surface, while relatively flat surface still existed in many areas. The EDX analysis shows that not only the nanoparticles but also the flat surface had a certain content of oxygen, indicating the relatively flat surface may be actually a thin Cu_2O layer that grew on the flake surface. It is should be noted that both the layer of Cu_2O nanoparticles and the flat Cu_2O layer in Fig. 4.6ab were too thin, thus the composition of Cu_2O cannot be accurately measured by EDX. In addition, the content of oxygen in the “nanoparticle-formed” region (point A) was higher than that in the “flat surface” region (point B), and which could be caused by the thicker surface oxides in the “nanoparticle-formed” region. After the Cu flake was thermally oxidized at 300 ℃ for 1 min, as shown in Fig. 4.6cd, the layer of Cu_2O nanoparticles became more obvious in the low magnitude image, the most surface of Cu flake had been covered by Cu_2O nanoparticles. Moreover, in the high magnitude image, it can be seen that both the size and the number of Cu_2O nanoparticles were increased. The nanoparticle shows a larger diameter around 100 nm, and also the feature of scattered individual nanoparticles was replaced by a layer of densely packed nanoparticles. The EDX analysis shows that the flat surface (point C) in Fig. 4.6d had similar oxygen content with the flat surface (point A) in Fig. 4.6b, thus it seems that the flat Cu_2O layer did not grow during one minute’s thermal oxidation. On the other hand, its area was obviously reduced by the massive propagation

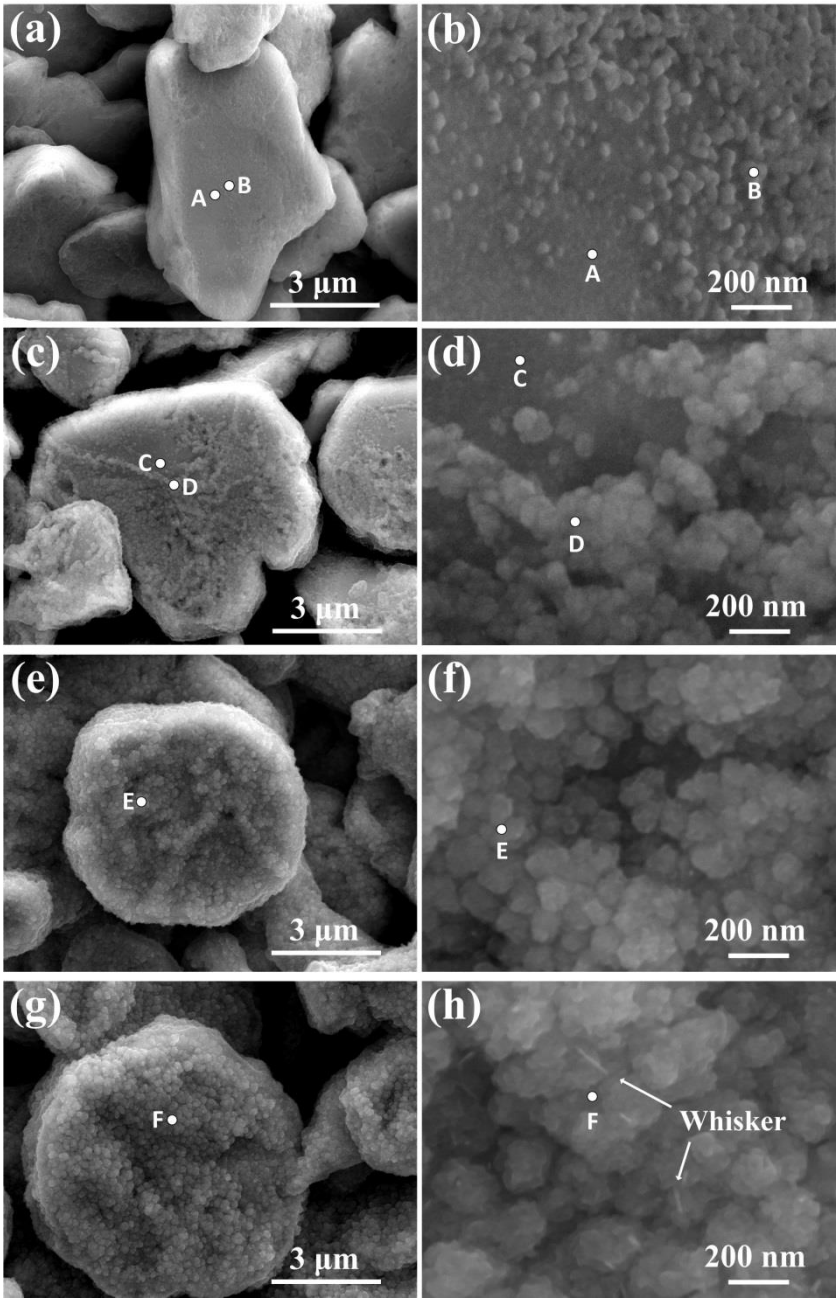

Figure 4.6 SEM images of the Cu flakes thermally oxidized at 300 ℃ for different times. (a,b): just heated to 300 ℃, (c,d): 1 min, (e,f): 20 min, (g,h): 40 min.

Table 4. 1 EDX point analysis of points A-F in Figure 4.6.

Element	**Composition (at. %)**					
	A	**B**	**C**	**D**	**E**	**F**
Cu	94.15	90.80	94.43	84.55	70.17	67.34
O	5.85	9.20	5.57	15.45	29.83	32.66

of nanoparticles during one minute's thermal oxidation. Moreover, the oxygen content in the "nanoparticle-formed" region (point D) became higher, indicating the thickness of nanoparticle layer was increased. Therefore, it is suggested that at the initial period of thermal oxidation at 300 ℃, thin Cu_2O layer firstly formed, and then Cu_2O nanoparticles formed and massively propagated on the thin Cu_2O layer.

As mentioned before, both two exothermic peaks in Fig. 4.4 were caused by the oxidation reaction (1), and the formation of two separated exothermic peak suggests that the initial growth of Cu_2O can be subdivided into two stages. Here, based on above SEM observation and EDX analysis, it can be deduced that these two stages are: (1) formation of thin Cu_2O film. (2) formation of Cu_2O nanoparticles on the thin Cu_2O film. Two stages are shown schematically in Fig. 4.7. The first exothermic peak that occurred at around 242 ℃, corresponds to the initial nucleation of Cu_2O grains as well as the lateral growth of Cu_2O grains to form thin Cu_2O layer before heating to 300 ℃. The duration of Stage 1 was very short because the formation of thin Cu_2O layer was very fast and its further growth was suppressed, consequently, the corresponding exothermic peak was quite sharp, as shown in Fig. 4.4. The second exothermal peak that occurred at around 296 ℃, corresponds to the massive propagation of Cu_2O nanoparticles on the thin Cu_2O film. According to the SEM observation in Fig. 4.6, the propagation of Cu_2O nanoparticles (Stage 2) can be identified as starting from the formation of individual Cu_2O particles on the flat Cu_2O film and finishing when the entire surface of Cu flake was covered by a layer of densely packed nanoparticles, and which released more heat and lasted for longer time than that in the formation of thin Cu_2O film. Consequently, the second exothermal peak was stronger and broader than the first one.

As shown in Fig. 4.6ef, after the Cu flake was thermally oxidized at 300 ℃ for 20 min, the surface of Cu flake had been completely covered by the Cu_2O nanoparticles. Moreover, the EDX analysis shows that the atomic ratio of Cu to O on the flake surface was near to 2:1, which confirms that the formed Cu oxides were Cu_2O and demonstrates that the layer of Cu_2O nanoparticles had grown to a thickness that is adequate for the EDX quantitative analysis. Then, after the Cu flake was thermally oxidized at 300 ℃ for 40 min, as shown in Fig. 4.6gh, the coarsening of Cu_2O nanoparticles is obvious. In addition, several fine whiskers can be observed on the Cu_2O nanoparticles. Some researchers have reported the formation of CuO nanowires or whisker on Cu_2O

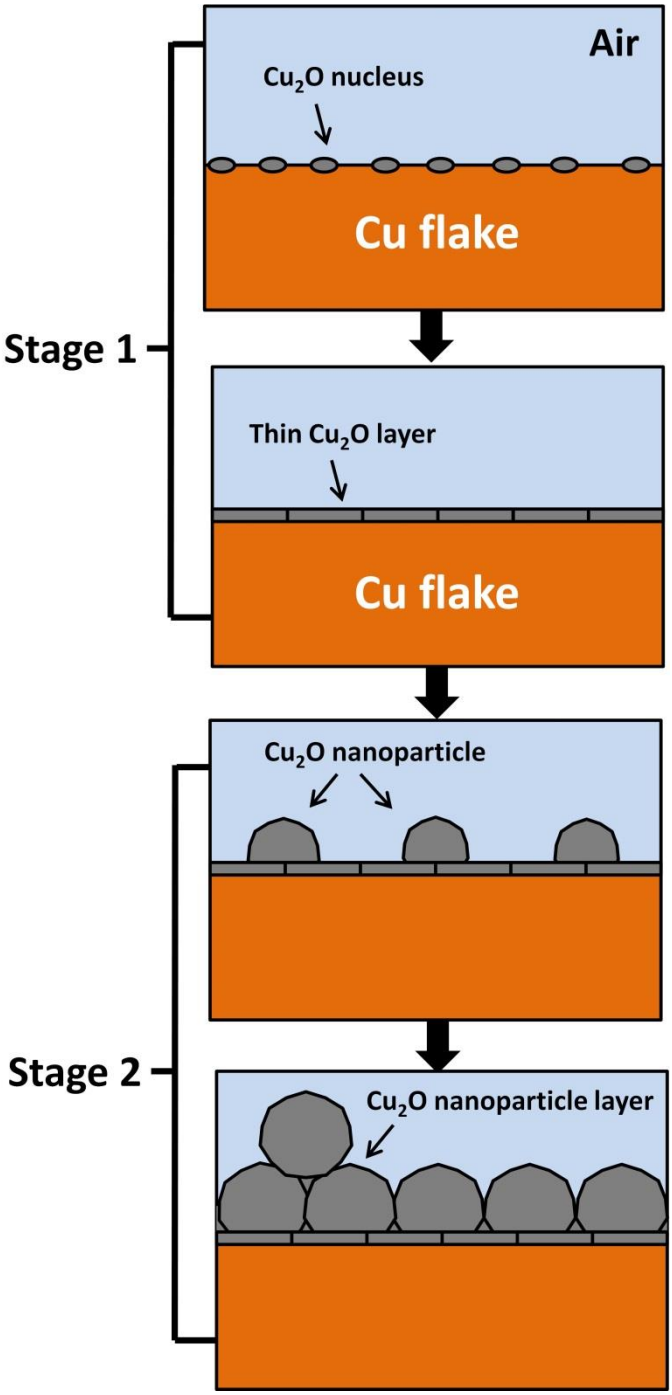

Figure 4.7 A schematic drawing of Stage 1 and Stage 2 at initial period of thermal oxidation at 300 ℃.

layer by thermal oxidation in the temperature range of 400 to 700 ℃, and they proposed that Cu_2O played an important role as a seed for the growth of CuO nanowires [7, 9-12]. In our study, the Cu_2O is the only predominant oxidation product due to relative low oxidation temperature, thus the

formation of CuO whisker is insignificant. Besides, the EDX analysis shows the atomic ratio of Cu to O on the flake surface was near to 2:1, similar to that oxidized for 20 min.

4.3.3 Driving force and mechanism for Cu_2O nanoparticle formation

In the surface morphological evolution on Cu flakes by thermal oxidation, the formation of Cu_2O nanoparticles at the surface is most concerning part. Also, it can be seen as the most critical phenomenon during the entire oxidation-reduction process because it directly determines the surface microstructure of the Cu flake after the subsequent reduction process, which will be described in detail in section 4.4.1. Therefore, it is paramount to identify the driving force leading to Cu_2O nanoparticle formation in stage 2 and the mass transport mechanism governing the massive propagation of Cu_2O nanoparticles. On the other hand, before the formation of Cu_2O nanoparticles (Stage 2), the thin Cu_2O layer was initially formed on the Cu surface (Stage 1). A number of experiments on reactive diffusion in multilayer films, including Nb/Al, Ti/Al, Al/O_2, and Cu/O_2, have shown that the intermediate phase formation has two steps: (i) rapid formation of thin intermediate phase layer, including nucleation and lateral growth, and (ii) classical diffusion controlled growth of intermediate phase layer [13-16]. Although we are not focused on the formation of the thin Cu_2O layer, the layer is very important because it is believed that a compressive stress existed in the thin Cu_2O layer near the Cu_2O/Cu interface and the driving force for Cu_2O nanoparticle formation is related to this compressive stress. The existence of a stress accompanying the growth of oxides on metal has been known for many years, and also it has been widely accepted that the role of stress during isothermal oxidation process could affect the structure of the oxide scales [17, 18]. In the following part, we will firstly explain the origins of stress generation in the thin Cu_2O layer, and then clarify the mechanism for Cu_2O nanoparticle formation in term of the correlation of the stress field and the kinetics of Cu oxide growth.

It has been concluded that three main origins can induce growth stress: 1) epitaxy; 2) incompatibility of the mole volumes; 3) the oxide growth in the oxide grain boundaries (GBs) leads to a compression stress state [18]. The cubic Cu_2O lattice aligns epitaxially with the Cu lattice. The natural lattice misfit between Cu and Cu_2O exists. The misfit is defined by $f = (a_{Cu}-a_{Cu2O})/a_{Cu2O}$ is

-15.4%, where the lattice constants of bulk Cu_2O and Cu are 4.269 and 3.61 Å, respectively. Cammarata and etc. have analyzed the critical thickness of epitaxial film dependence on misfit for epitaxy [19]. They concluded that, for f <0, at large film thickness, all of the misfit will be taken up by interface dislocations and the effect of epitaxial stress can be negligible. As the film thickness is decreased, the film will begin to elastically compress in order to accommodate the misfit. For an oxide film, the effect of epitaxial stress is generally limited to the first ~50 nm of oxide [20], thus it cannot be negligible in our study because the initial Cu_2O layer was quite thin. Fig.8 gives the TEM images of the Cu flake thermally oxidized at 300 ℃ for 1 min, in which the Cu_2O on the flake surface were confirmed by the high-resolution TEM (HRTEM) image. It can be seen that the thickness of total oxide that includes initial Cu_2O film and Cu_2O nanoparticle layer was around 100 nm. Therefore, a residual strain with associated stress can be generated in the initial Cu_2O film to accommodate the lattice mismatch at the Cu_2O/Cu interface. Moreover, the difference of molar

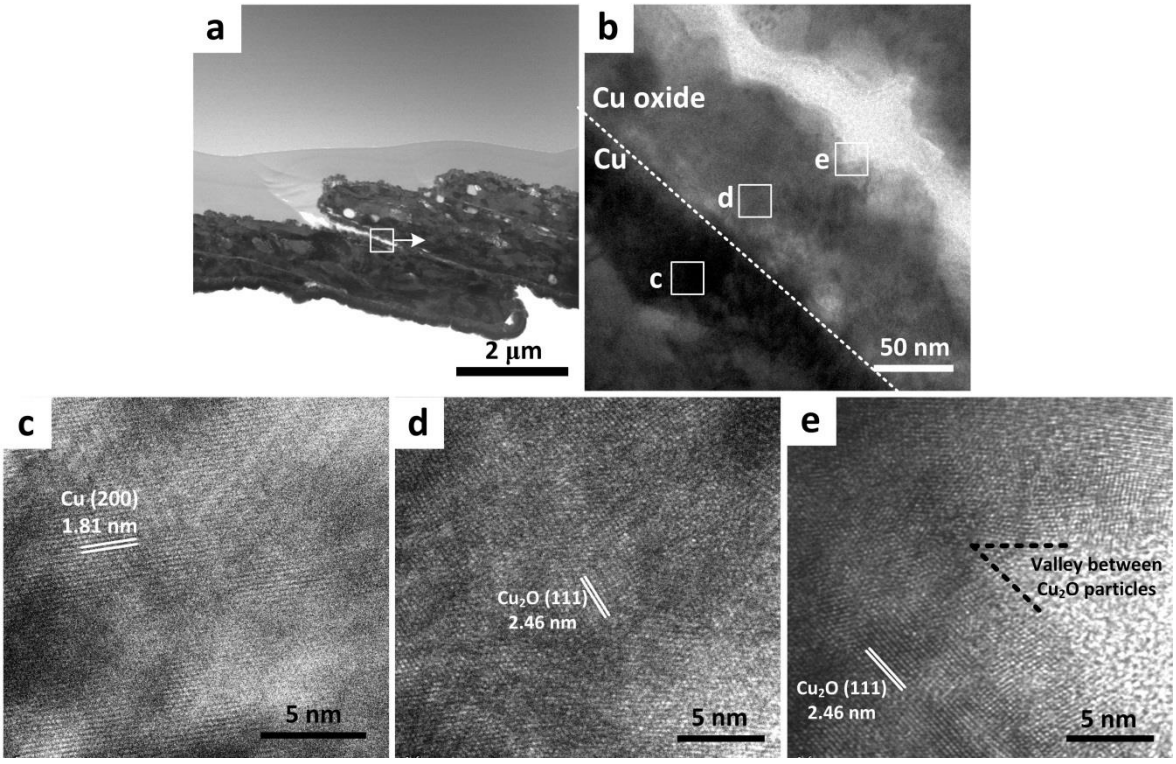

Figure 4.8 Transmission electron microscopy (TEM) bright field (BF) images of cross section of Cu flake thermally oxidized at 300 ℃ for 1 min and corresponding high-resolution TEM (HRTEM) image of selected areas.

volume V_M between Cu_2O film and Cu substrate also induced a growth strain ε [21], which is given by

$$\varepsilon = \sqrt[3]{\frac{V_{M(Cu_2O)}}{V_{M(Cu\ )}}} - 1 = \varepsilon_{xx} = \varepsilon_{yy} = \varepsilon_{zz} \qquad (4.3)$$

Since the molar volume of Cu_2O is larger than that of Cu, the associated stress in the oxide layer is compressive. In addition to the stress caused by incompatibilities of lattice parameter or molar volume between oxide and metal, stress with a microstructural origin also could exist. Many researchers have suggested that the oxidation can take place via the short circuits of diffusion in the grain boundaries (GBs), and which generate a compressive stress in the GBs [22, 23]. However, in their proposed models, a considerable inward flux should exist in the GBs, in order to form the oxide. Thus, the effect of this microstructural stress can be negligible in our study because the growth of Cu_2O is controlled via outward diffusion of Cu atoms [7].

For the low range of the oxidation temperature (< 400 ℃) and the small size of Cu_2O grains, the mass flux comes primarily along Cu_2O GBs. During Stage 2 of the initial thermal oxidation, a normal Cu atoms diffusion flux along the GBs in Cu_2O was driven by the chemical potential difference in oxygen partial pressure between the Cu_2O-atmosphere and Cu_2O-Cu interfaces. Moreover, Cu atoms also prefers to diffuse along GBs from the region in compression (near the Cu_2O-Cu interface) to the outer surface of the Cu_2O layer, where is stress-free [12]. In other words, The Cu diffusion is also driven by the gradient of the chemical potential induced by the stress field. The chemical potential along the GB is associated with the stress σ by the relation $\mu=\mu_0+E$, $E=\sigma\cdot\Omega$, where μ_0 is the chemical potential of an atom in a stress-free system, E is the strain energy, and Ω is the atomic volume. And the diffusive flux J_B along a given GB depending on the strain energy gradient can be expressed as follows [12]:

$$J_B = D_B \cdot \frac{\partial C}{\partial x} + \frac{D_B C}{RT}\frac{\partial E}{\partial x} \qquad (4.4)$$

Here D_B is the GB diffusion coefficient, C_B the concentration of Cu atom along the diffusion path, x the local spatial coordinate along the diffusion path, R Boltzmann's constant, and T is the absolute temperature. Cu atoms diffusing along the GBs are concentrated at the GB junctions on the Cu_2O surface, and also deposited on the top of Cu_2O layer via surface diffusion that was driven by the

concentration gradients of Cu atoms between the GB junction area and the other area on the top of Cu_2O layer, And the diffusive flux J_S along the surface can be expressed as follows [12]:

$$J_S = D_S \cdot \frac{\partial C}{\partial x} \qquad (4.5)$$

Here D_S is the surface diffusion coefficient, C the concentration of Cu atom along the diffusion path, x the local spatial coordinate along the diffusion path.

The formation process of Cu_2O particles (Stage 2) is schematically shown in Fig. 4.9. At the GB junction areas on the surface of thin Cu_2O film, the local Cu-rich composition naturally existed since the Cu diffusion along the surface depends on the concentration gradients of Cu atoms on the surface. Moreover, owing to the contribution of the strain field, the inwards Cu diffusion along the GBs was greatly improved, as shown in Equation 4.4, and therefore, the enhanced local Cu enrichment could break the equilibrium state and led to the nucleation of new Cu_2O grains. It is suggested that a process of forming new Cu_2O nuclei at the GB junction areas on the surface of Cu_2O thin film was kinetically more favorable than incorporating Cu atoms onto existing Cu_2O grain in the thin Cu_2O film, although it has to overcome a nucleation barrier. It is mainly attributed to the substantial energy and composition fluctuations on the surface of Cu_2O film. Firstly, those GB junctions are the high energy areas on the surface where the energy barrier for nucleation was reduced. Moreover, the huge imbalance between the GB diffusion and the surface diffusion of Cu made a significant Cu enrichment at the GB junctions on the surface, which led to the metastable state at those areas and greatly increased the nucleation probability of Cu_2O. With the nucleation of new Cu_2O grains, the Cu_2O nanoparticles or nanograins formed by the equiaxial growth of Cu_2O nuclei and finally covered the entire surface of Cu flake. Due to the massive new nucleation of Cu_2O, this process is accompanied by a rapid heat release, as shown in Fig. 4.4 (second exothermic peak).

After Stage 2, the interface between the Cu_2O nanoparticles can be seen as new fast diffusion path. Consequently, Cu diffusion was still promoted by the strain gradient and Cu atom was concentrated at the valley bottom between Cu_2O nanoparticles, as shown in Fig. 4.8e, thus Cu_2O nanoparticles continued to form but in a slower rate due to the longer diffusion path of Cu. In this period, the surface oxide was thickened mainly by the formation of Cu_2O nanoparticles in the direction which is perpendicular to the flake surface. Once the surface oxide reached to a critical

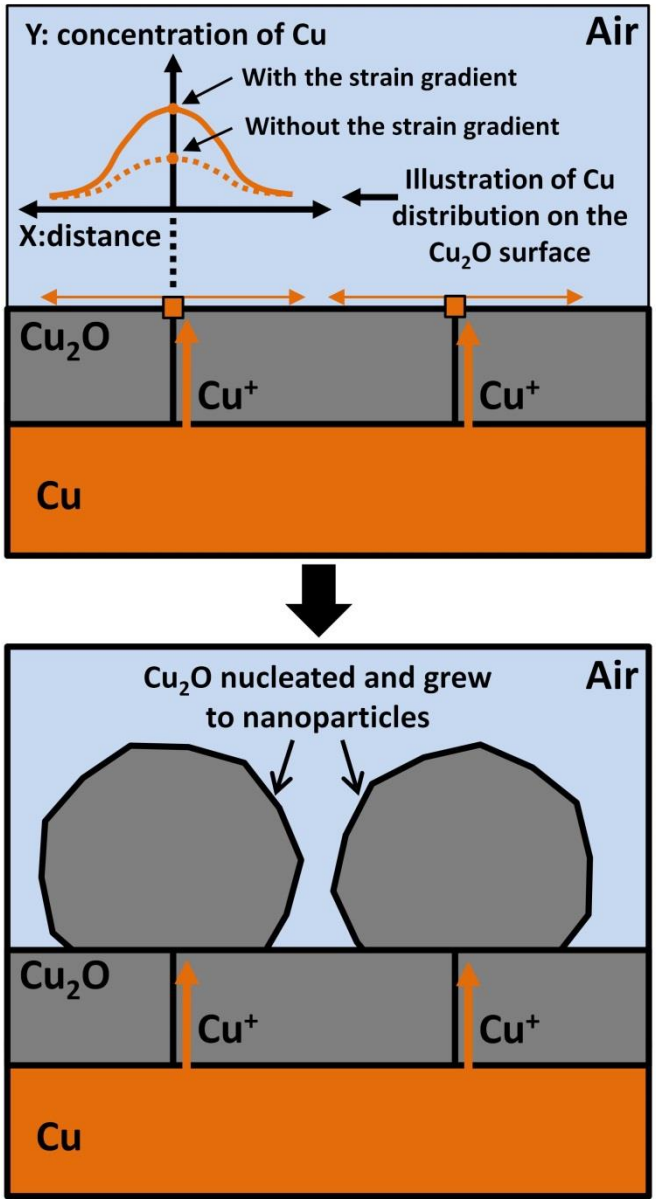

Figure 4.9 Mass transport and mechanism for Cu_2O nanoparticle formation: Cu atom diffuse outward from Cu/Cu_2O interface to free surface via GB diffusion, followed by surface diffusion from GB junction areas to entire surface of Cu_2O film. Imbalance between GB diffusion and surface diffusion give rise to Cu enrichment at GB junction areas where Cu_2O nanoparticles form.

thickness at which the effect of stress gradient can be ignored and a balance between the stress-driven diffusion and the surface diffusion was built, the formation of new Cu_2O nanoparticles stopped, replacing by the growth or coarsening of the existing Cu_2O grains, as shown in Fig. 4.6gh.

4.4 Reduction process

4.4.1 Formation of nanotextured Cu surface

Fig. 4.10 shows the SEM images of Cu flakes after the oxidation-reduction process. The Cu flakes were firstly thermally oxidized at 300 ℃ in the air for different times and then reduced by formic acid vapor at 300 ℃ for 2 min. As shown in Fig. 4.10ab, the reduced Cu flake exhibited a similar surface morphology to the oxidized flake in Fig. 4.6ab. Some individual nanoparticles were formed on the surface of Cu flake, while the flat surface still existed in the most area. Table 4.2 gives the corresponding EDX point analysis of point A-F in Fig. 4.10, which indicates both the flat Cu_2O layer and Cu_2O nanoparticles in Fig. 4.6ab had been reduced to Cu surface (point A) and Cu nanoparticles (point B). Moreover, the XRD patterns in Fig. 4.11 show the absence of both Cu_2O and CuO peaks in reduced flakes, confirming that 2 min is enough to achieve the complete reduction of the Cu_2O that formed in the thermal oxidation by the formic acid atmosphere at 300 ℃. On the other hand, if the oxidized flakes were covered by the layer of Cu_2O nanoparticles, as shown in Fig. 4.6c-h, the corresponding reduced flakes showed a Cu nanotextured surface. The fact that nearly 100 at.% Cu was detected in the corresponding EDX spectrum (point C-F) demonstrates that the layer of Cu_2O nanoparticles was completely reduced to the Cu nanotextured surface. Moreover, the trend of surface morphological evolution of the Cu flakes during the thermal oxidation with increasing time remained in the reduced flakes. In Fig. 4.10cd, the most surface of the Cu flake was covered by the nanotextured structure, while the flat surface still existed. And in Fig. 4.10e-h, it can be seen that the Cu nanotextured surface became coarse.

Apparently, the formation of this Cu nanotextured surface is caused by the reduction of Cu_2O nanoparticles and the simultaneous coalescence of the reduced Cu nanoparticles on the surface of Cu flake. Soininen had reported the reduction of Cu_2O films to elemental Cu with formic acid gas [24]. The following equation represents this reduction reaction:

$$Cu_2O + HCOOH(g) \rightarrow 2Cu + H_2O(g) + CO_2(g) \qquad (4.6)$$

The result demonstrates that after the oxidation-reduction process, the chemical composition of the

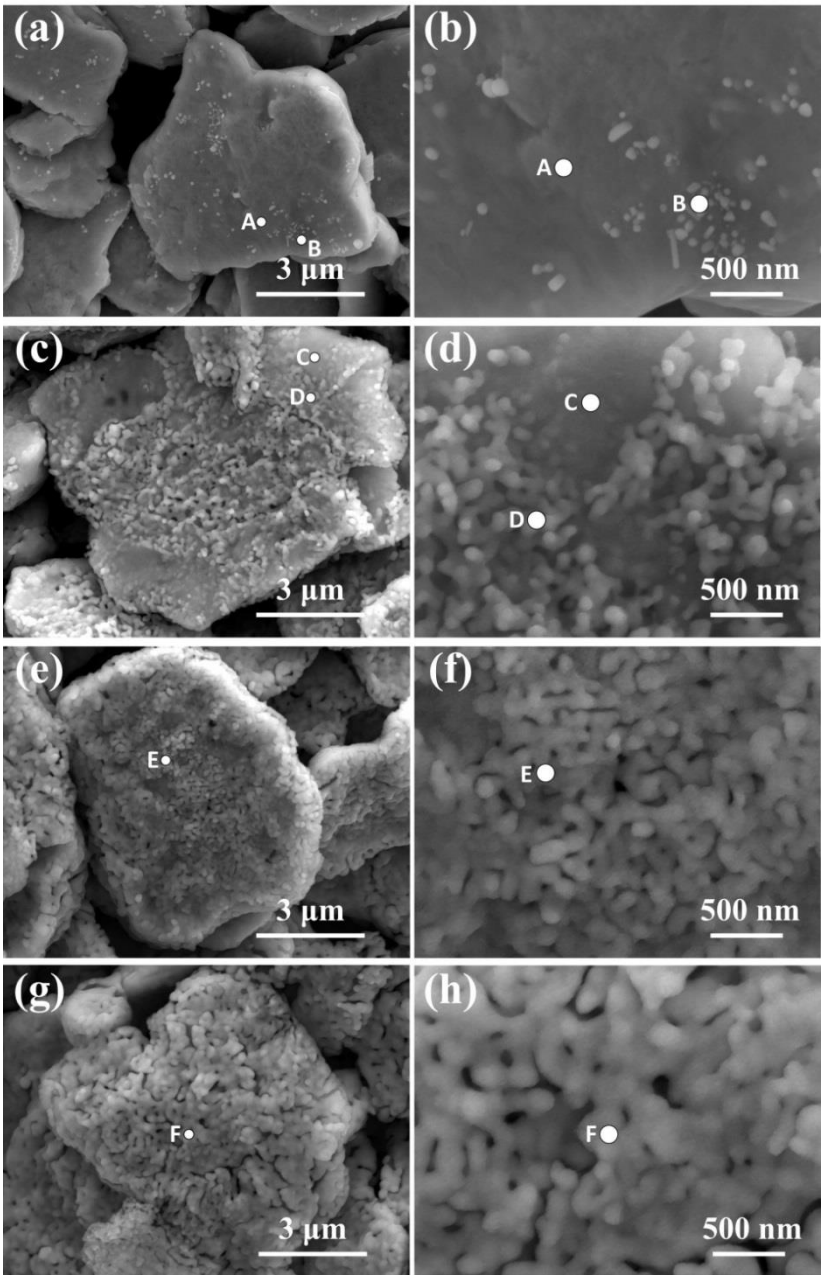

Figure 4.10 SEM images of oxidized Cu flakes after reduction by formic acid vapor at 300 ℃ for 2 min. Oxidation time: (a, b) just heated to 300 ℃. (c, d) 1 min. (e, f) 20 min. (g, h) 40 min.

Table 4.2 EDX point analysis of points A-F in Figure 4.10.

Element	Composition (at. %)					
	A	**B**	**C**	**D**	**E**	**F**
Cu	99.65	99.80	99.43	99.55	99.47	99.54
O	0.35	0.20	0.57	0.45	0.53	0.46

Note: the trace content of oxygen could be caused by measurement errors.

microscale flake (pure Cu) was retained, and only the surface morphology was modified. In other words, in-situ surface modification of the microscale Cu particles was achieved during the oxidation-reduction process.

4.4.2 Flattening of nanotextured surface during thermal annealing

In order to improve the surface activity of Cu particles for enhancing low-temperature sintering bonding process, surface-modified Cu flakes with nanotextured surface was fabricated via the oxidation-reduction process. In this part, the increased surface activity of surface-modified Cu flakes was verified through a thermal-activated flattening process.

It is well known that metallic nanostructure is thermally less stable than their bulky counterpart due to the highly active surface. Particularly, metallic nanoparticles can be easily sintered at relatively low sintering temperature [25-28], and also many researchers have reported that Au or Pt nanoporous can be coarsened to microscale porous structure by a thermal annealing [29-32]. In our study, the obtained Cu nanotextured surface can be seen as a nanostructure between the nanoparticles and the nanoporous: it is constituted by partially sintered Cu nanoparticles, while no regular pores can be identified on the surface. Therefore, it is expected that this nanotextured surface also presents

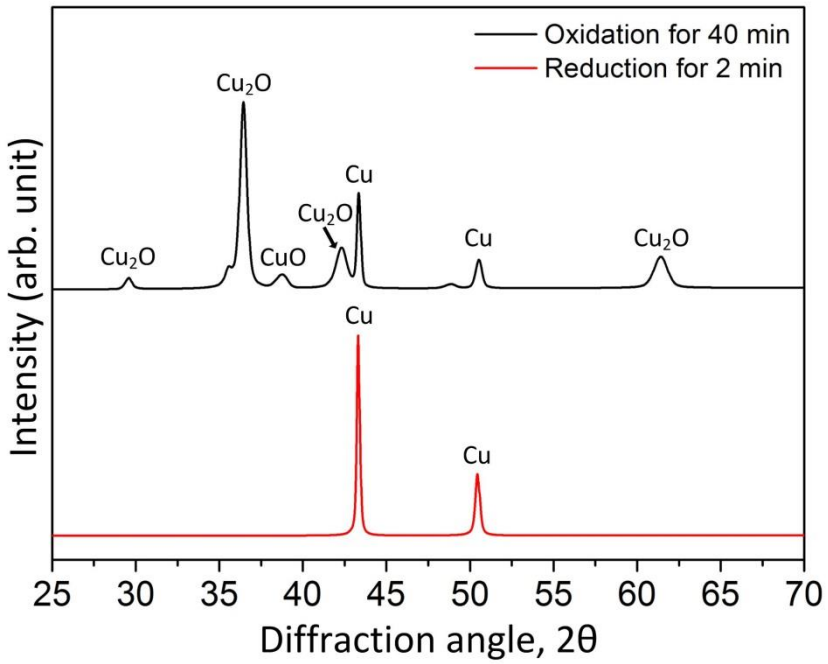

Figure 4.11 XRD profile of oxidized Cu flakes and reduced Cu flakes.

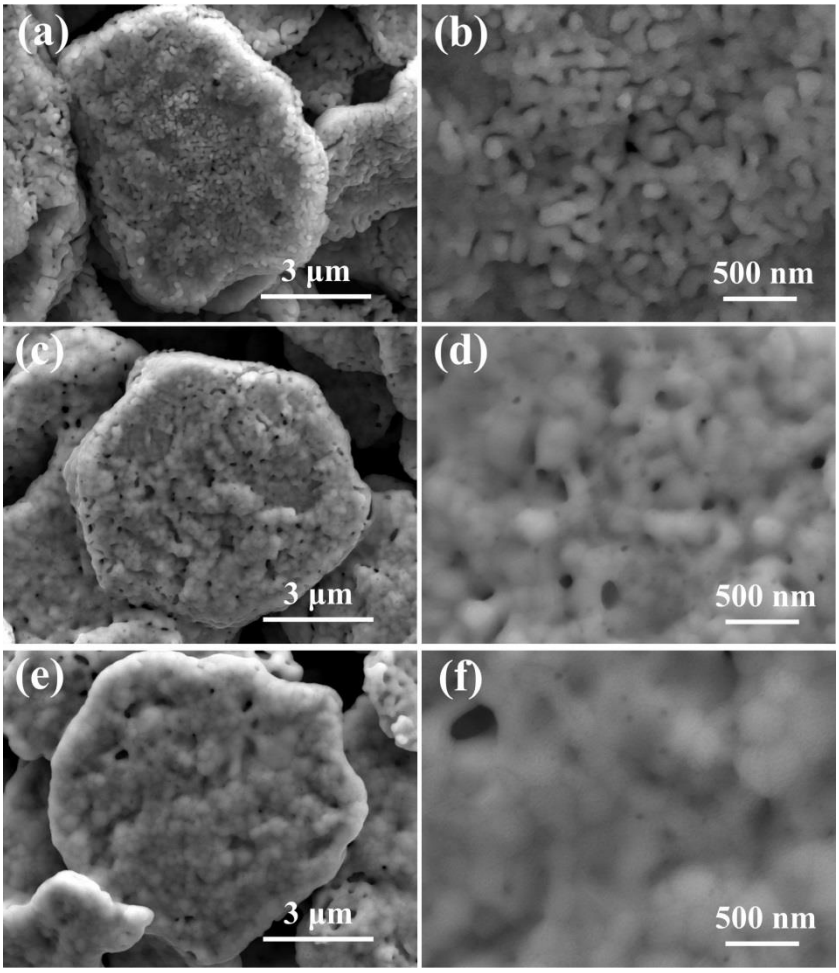

Figure 4.12 SEM images of surface-modified Cu flakes with different reducing times (reduction was at 300 ℃ in formic acid atmosphere): (a, b) 2 min, (c, d) 5 min; (e, f) 20min.

a high surface activity, and if so, a thermal flattening or coarsening process can be observed during the thermal annealing.

Fig. 4.12 shows the nanotextured surface of Cu flakes after oxidation-reduction process and its evolution with a thermal annealing at 300 ℃ in formic acid atmosphere. The surface-modified Cu flake was obtained by 20 min oxidation and 2 min reduction at 300 ℃. It can be seen that partially sintered Cu nanoparticles tended to further coalesce together, and thereby the nanotextured surface gradually transformed to a relatively flat surface. After the annealing for 5 min, any individual nanoparticles had been hardly recognized, and a number of nanoscale pores appeared on the flake surface, apparently, induced by the coalescence of contacted Cu nanoparticles. Then, after the annealing for 20 min, the feature of the nanotextured surface had completely disappeared, replaced

by a relatively flat surface with very fine roughness. Moreover, the number of those small pores was reduced, while the size of pores was increased, thus it can be identified as a thermal coarsening process. This microstructural evolution induced by the thermal annealing demonstrates that the surface-modified Cu flakes had a highly active surface, and thus suitable for the low-temperature sintering bonding.

4.5 Conclusion

In this chapter, thermal oxidation and formic acid atmosphere reduction were applied on the microscale Cu flake to create a nanotextured surface that exhibited a significantly increased surface activity. During the thermal oxidation, the thin Cu_2O layer was initially formed on the flake surface, accompanied with a quick release of reaction heat. Afterward, the Cu_2O nanoparticles quickly formed on the initial Cu_2O layer and covered the entire flake, during which the heat of oxidation reaction was massively released again. Then, the Cu_2O nanoparticle continued to propagate and the nanoparticle layer became thicker, meantime the Cu_2O nanoparticles were also grown. Finally, this Cu_2O nanoparticle layer was subsequently reduced to Cu nanotextured surface in the formic acid atmosphere, and the surface-modified Cu particle was obtained. In addition, the increased surface activity of the surface-modified Cu flake was verified by a thermal-activated flattening process.

References

[1] H. P. R. Frederikse, R. J. Fields, and A. Feldman, Thermal and electrical properties of copper-tin and nickel-tin intermetallics, *J. Appl. Phys.*, **72** (1992) 2879-2882.

[2] G. Ghosh, Elastic properties, hardness, and indentation fracture toughness of intermetallics relevant to electronic packaging, *J. Mater. Res.*, **19** ((2004) 1439-1454.

[3] N. Birks, G. H. Meier, F. S. Pettit, *Introduction to the high-temperature oxidation of metals 2nd edn*, Cambridge University Press, 2006

[4] R. A. Rapp, The high-temperature oxidation of metals forming cation-diffusing scales, *Metall. Mater. Trans. A*, **15** (1984), 765-782.

[5] G. M. Raynaud and R. A. Rapp, In situ observation of whiskers, pyramids and pits during the high-temperature oxidation of metals, *Oxid. Met.*, **21** (1984) 89-102.

[6] Y. Zhu, K. Mimura, and M. Isshiki,. Oxidation Mechanism of Copper at 623-1073 K, *Mater. Trans.*, **43** (2002) 2173-2176.

[7] K. Mimura, J. W. Lim, M. Isshiki, Y. Zhu, and Q. Jiang, Brief review of oxidation kinetics of copper at 350 ℃ to 1050 ℃, *Metall. Mater. Trans. A*, **37** (2006) 1231-1237.

[8] F. S. Pettit and J. B. Wagner. Transition from the linear to the parabolic rate law during the oxidation of iron to wüstite in CO-CO_2 mixtures, *Acta Metal.*, **12** (1964) 35-40.

[9] X. Jiang, T. Herricks, and Y. Xia, CuO nanowires can be synthesized by heating copper substrates in air, *Nano Lett.*, **2** (2002) 1333-1338.

[10] C. J. Love, J. D. Smith, Y. Cui, and K. K. Varanasi, Size-dependent thermal oxidation of copper: single-step synthesis of hierarchical nanostructures, *Nanoscale*, **3** (2011) 4972-4976.

[11] A. M. B.Gonçalves, L. C. Campos, A. S. Ferlauto, and R. G. Lacerda, On the growth and electrical characterization of CuO nanowires by thermal oxidation, *J. Appl. Phys.*, **106** (2009) 034303.

[12] L. Yuan, Y. Wang, R. Mema, and G. Zhou, Driving force and growth mechanism for spontaneous oxide nanowire formation during the thermal oxidation of metals, *Acta Mater.*, **59** (2011) 2491-2500.

[13] L. Klinger, Y. Brechet, G. Purdy, On the kinetics of interface-diffusion-controlled peritectoid reactions, *Acta Mater.*, **46** (1998) 2617-2621.

[14] C. Michaelsen, K. Barmak, and T. P. Weihs, Investigating the thermodynamics and kinetics of thin film reactions by differential scanning calorimetry, *J. Phys. D: Appl. Phys.*, **30** (1997) 3167.

[15] L. P. H. Jeurgens, W. G. Sloof, F. D. Tichelaar, and E. J. Mittemeijer, Growth kinetics and mechanisms of aluminum-oxide films formed by thermal oxidation of aluminum. *J. Appl. Phys.*, **92** (2002) 1649-1656.

[16] J. C. Yang, B. Kolasa, J. M. Gibson, and M. Yeadon, Self-limiting oxidation of copper, *Appl. Phys. Lett.*, **73** (1998) 2841-2843.

[17] M. Schütze, *Protective oxide scales and their breakdown*, Wiley,1997

[18] B. Panicaud, J. L. Grosseau-Poussard, J. F. Dinhut, On the growth strain origin and stress evolution prediction during oxidation of metals, *Appl. Surf. Sci.*, **252** (2006) 5700-5713.

[19] R. C. Cammarata and K. Sieradzki, Surface stress effects on the critical film thickness for epitaxy, *Appl. Phys. Lett.*, **55** (1989) 1197-1198.

[20] H. E. Evans, Stress effects in high temperature oxidation of metals, *Int. Mater. Rev.*, **40** (1995) 1-40.

[21] R. E. Bedworth and N. B. Pilling, The oxidation of metals at high temperatures, *J. Inst. Met.*, **29** (1923) 529-582.

[22] V. K. Tolpygo, J. R. Dryden, and D. R. Clarke, Determination of the growth stress and strain in α-Al_2O_3 scales during the oxidation of Fe-22Cr-4.8Al-0.3Y alloy, *Acta Mater.*, **46** (1998) 927-937.

[23] D. R. Clarke, The lateral growth strain accompanying the formation of a thermally grown oxide, *Acta Mater.*, **51** (2003) 1393-1407.

[24] P. J. Soininen, K. E. Elers, V. Saanila, S. Kaipio, T. Sajavaara, and S. Haukka, Reduction of copper oxide film to elemental copper, *J. Electrochem. Soc.*, **152** (2005) 122-125.

[25] L. J. Lewis, P. Jensen, and J. L. Barrat, Melting, freezing, and coalescence of gold nanoclusters, *Phys. Rev. B*, **56** (1997) 2248.

[26] K. S. Moon, H. Dong, R. Maric, S. Pothukuchi, A. Hunt, Y. Li, and C. P. Wong, Thermal behavior of silver nanoparticles for low-temperature interconnect applications, *J. Electron. Mater.*, **34** (2005), 168-175.

[27] K. K. Nanda, A. Maisels, F. E. Kruis, H. Fissan, and S. Stappert, Higher surface energy of free nanoparticles, *Phys. Rev. Lett.*, **91** (2003) 106102.

[28] E. Ide, S. Angata, A. Hirose, and K. F. Kobayashi, Metal–metal bonding process using Ag metallo-organic nanoparticles, *Acta Mater.*, **53** (2005) 2385-2393.

[29] M. Hakamada and M. Mabuchi, Thermal coarsening of nanoporous gold: Melting or recrystallization, *J. Mater. Res.*, **24** (2009) 301-304.

[30] M. Hakamada, and M. Mabuchi, Fabrication of nanoporous palladium by dealloying and its thermal coarsening, *J. Alloys Comp.*, **479** (2009) 326-329.

[31] Y. C. K. Chen-Wiegart, S. Wang, Y. S. Chu, W. Liu, I. McNulty, P. W. Voorhees, and D. C. Dunand, Structural evolution of nanoporous gold during thermal coarsening. *Acta Mater.*, **60** (2012) 4972-4981.

[32] P. Gao, X. Ye, Z. Zhu, Y. Wu, A. A. Volinsky, L. Qiao, and Y. Su, Defects evolution of nanoporous AuAg (Pt) during thermal coarsening, *Scr. Mater.*, **119** (2016) 51-54.

Chapter 5
Oxidation-reduction bonding using in-situ surface-modified Cu particles

5.1 Introduction

In *Chapter 4*, the unique surface modification method of microscale Cu particle using oxidation-reduction process was proposed. The Cu_2O nanoparticles formed on the surface of the flake-shaped Cu particles during a thermal oxidation process in an air, followed by a transformation to Cu nanotextured surface during the subsequent reduction process in the formic acid atmosphere, and moreover, the inherent mechanism for the surface morphological evolution was clarified. Also, the thermal-activated flattening process at 300 ℃ was presented to verify that the Cu nanotextured surface possess a high surface activity. Therefore, it is expected that this unique oxidation-reduction process can significantly improve the low-temperature sinterability of microscale Cu particles.

In this chapter, we applied this oxidation-reduction process in low-temperature sintering bonding process by switching the bonding atmosphere from air to a formic acid vapor in the bonding process, and presented how this in-situ surface modification method improved the bonding properties of the sintered Cu joint. Moreover, the mechanism for this improvement was discussed. The nanotextured surface that formed during the oxidation-reduction process played a key role in the

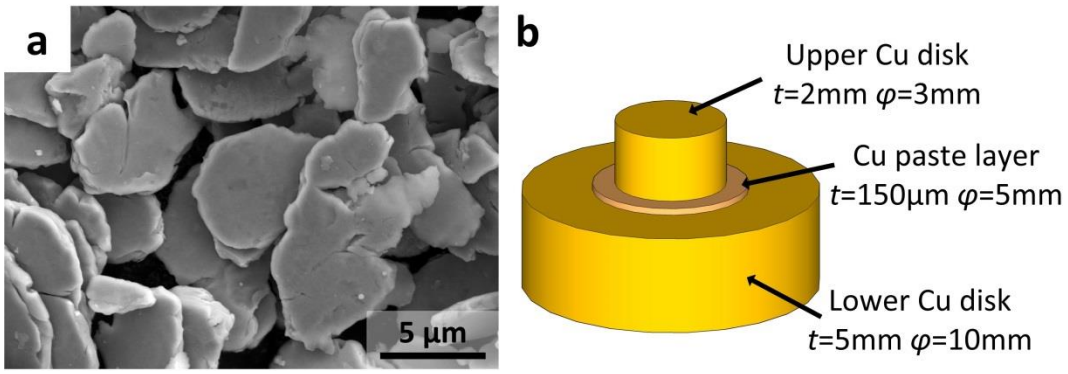

Figure 5.1 (a) SEM image of flake-shaped microscale Cu particles used in the study, (b) schematic diagram of Cu-Cu bonded joint.

enhanced coalescence of the sintered particles. Moreover, we investigated the thermal stability of the joints at an elevated temperature aging condition up to 250 ℃. The change of shear strength and the microstructure evolution of two kinds of sintered joint during the isothermal aging were provided. Finally, the compatibility of this oxidation-reduction bonding (ORB) process with differently shaped Cu particles and the effect of substrate on the bonding properties of the ORB process was also studied.

5.2 Experimental

5.2.1 Microscale Cu particle paste

Microscale flake-shaped Cu particle was used as starting materials. The flake-shaped particles had an average diameter 6.9 μm, an average thickness of 1μm, and a specific area of 0.13 m^2/g (1400YP, MITSUI MINING & SMELTING CO. LTD). SEM images of the Cu particles are shown in Fig. 5.1a. Terpineol, boiling point 220.8 ℃, was used as a solvent to prepare the Cu flake paste and Cu sphere paste, which consisted of 85 mass % Cu particles and 15 mass % terpineol solvent.

5.2.2 Oxidation-reduction bonding process

The schematic diagram of the bonded joint is shown in Fig. 5.1b. A pure Cu disc was used to fabricate the Cu-Cu joint. The pure Cu disc was cleaned with a diluted hydrochloric acid to remove

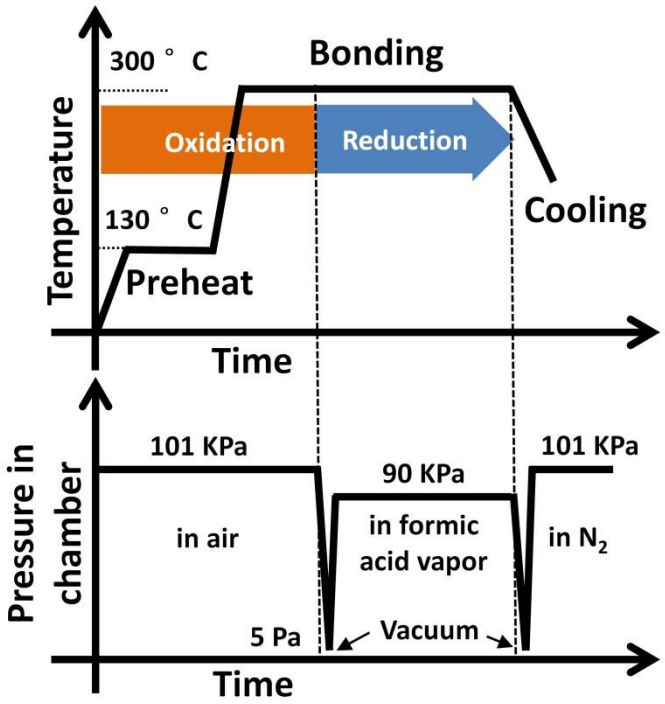

Figure 5.2 Illustration of temperature and pressure profile of ORB process.

the initial copper oxides before bonding. The oxidation-reduction bonding (ORB) process is as follows. The prepared Cu-Cu joints were first pre-heated at 130 ℃ for 5 min in an air to completely evaporate and decompose the terpineol solvent, after which they were heated to the bonding temperature of 300 ℃ at 0.5 ℃/s and held at 300 ℃ for various times. After evacuation to reduce the air pressure to < 5 Pa, formic acid vapor was introduced into the chamber. Then, the bonding was continued by maintaining the samples at 300 ℃ for various times in the formic acid atmosphere. In addition, the bonding that conducted only in the air was also carried out to verify the effect of oxidation process in the ORB process, and this process was labeled as oxidation bonding (OB) process. In contrast, some Cu-Cu joint specimens were bonded at 300 ℃ for various times in formic acid atmosphere and this process was labeled as a non-oxidation bonding (NOB) process. The heating profile and the atmosphere switching in ORB process is illustrated in Fig. 5.2. Both pressureless and pressure-assisted conditions were utilized to create NOB joint and ORB joint, respectively. For the pressure-assisted bonding, 0.5 MPa was applied during the reduction period of the bonding process. In addition, thermal aging test of pressureless ORB and NOB joint was conducted at 250 ℃ in the convection oven for the storage time up to 1000 h under an air atmosphere.

5.2.3 Characterization methods

Thermogravimetric analysis (TGA) of the Cu particles was carried out to examine their oxidation behavior during the thermal oxidation. X-ray diffraction (XRD) analysis of the Cu particles was conducted by an X-ray diffractometer (Rigaku Ultima IV) using Cu-Kα radiation (λ = 1.5405 Å). A field-emission scanning electron microscope (FE-SEM, Hitachi SU-70) was used for microstructure observation, including the surface morphology of the Cu particles, cross-sectional microstructures, and the fracture surface of the bonded joints. Also, the composition of the microstructure was measured with an electron probe microanalyzer (EPMA, JXA-8530F, JEOL). The shear strength of the bonded joints was evaluated by using a shear tester (STR-1000, Rhesca) at a head speed of 1mm/min, where the fly height was 200 μm from the bottom of the specimen.

5.3 Comparison of bonding properties of oxidation-reduction bonding and non-oxidation bonding

In order to evaluate the influence of different bonding process on the bonding properties of the Cu-Cu joint, the surface morphology of the treated Cu flakes with different bonding process was first identified. Fig. 5.3 shows the SEM images and the corresponding XRD patterns of the Cu flakes after different heating processes. After the NOB process for 60 min, the Cu flake still exhibited a flat and smooth surface, same to those initial Cu flakes (in Fig. 5.1a), and no peaks due to copper oxides were detected. This result demonstrates that owing to the efficient reducing effect of the formic acid atmosphere, no oxidation happened and the surface morphology of the Cu flake had no change during the NOB process. On the other hand, after the OB process for 20 min, the Cu flakes were completely covered by a layer of densely packed nanoparticles of ~100 nm diameter. The XRD results show that strong Cu_2O peaks appeared, indicating that these uniform nanoparticles are Cu_2O nanoparticles. In *Chapter 4*, the driving force and mechanism for the Cu_2O nanoparticle formation on Cu flakes surface during the thermal oxidation has been clarified. After the subsequent reduction process, as shown in Fig. 5.3ef, uniformly distributed Cu_2O nanoparticles feature were replaced by a nanotextured surface feature. The XRD patterns show the absence of both Cu_2O and CuO peaks, indicating the complete reduction of Cu_2O by the formic acid atmosphere at 300 ℃. The following

equation represents this reduction reaction [1]:

$$Cu_2O + HCOOH(g) \rightarrow 2Cu + H_2O(g) + CO_2(g) \qquad (5.1)$$

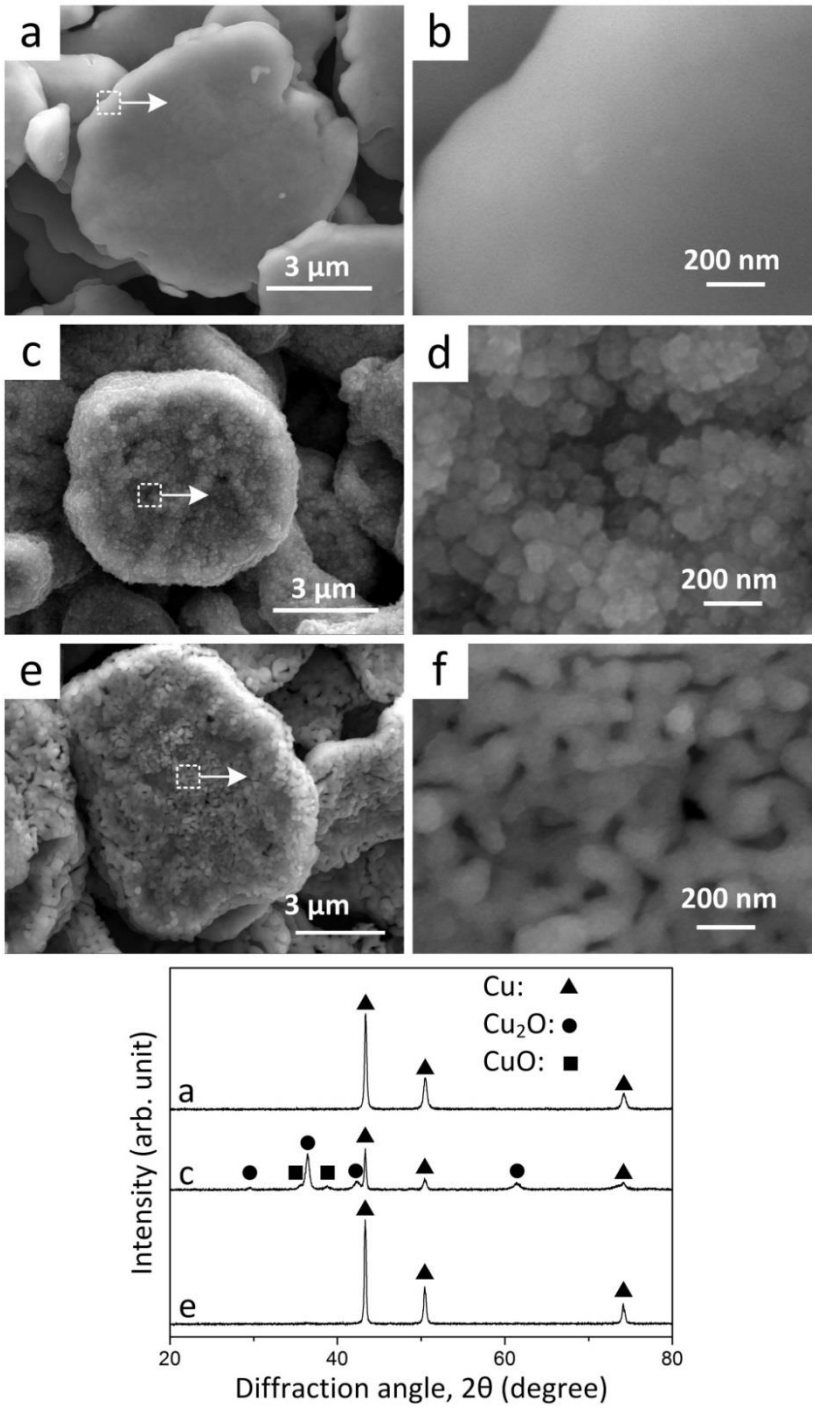

Figure 5.3 SEM images and XRD patterns of Cu flakes. (a, b) after heating at 300 ℃ for 60 min in formic acid atmosphere, (c, d) after heating at 300 ℃ for 20 min in air, (e, f) after heating at 300 ℃ for 20 min in air followed by heating at 300 ℃ for 2 min in formic acid atmosphere.

The formation of Cu nanotextured surface is caused by the reduction of Cu_2O nanoparticles and the simultaneous coalescence of the reduced Cu nanoparticles. And this in-situ surface-modified microscale Cu flake is expected to exhibit a significantly higher sinterability than the initial Cu flake.

We applied three kinds of bonding process for Cu-Cu bonding using pure Cu disc. The shear strengths of the Cu-Cu joints bonded with the different process were shown in Fig. 5.4. Within, Fig. 5.4a presents the shear strengths of the bonding joints fabricated with the pressureless NOB process. Different bonding temperature and bonding time were selected to investigate the effect of bonding conditions on the shear strength. It is clear that all samples showed very limited shear strength (<5MPa), regardless of the bonding temperature and time. Apparently, this result demonstrates that the microscale Cu flake has a very poor sinterability; without any applied pressure, a well-sintered Cu joint cannot be obtained even in the reducing atmosphere. On the other hand, as shown in Fig.

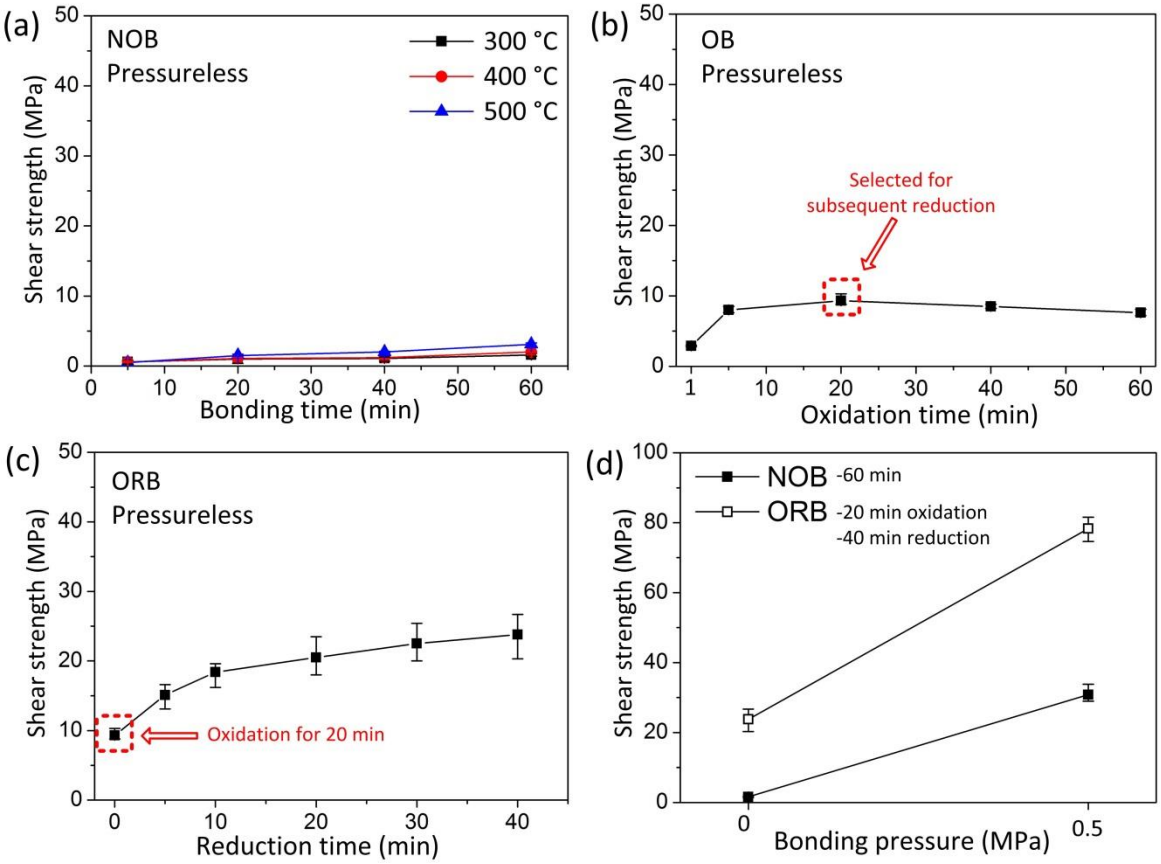

Figure 5.4 Shear strength of Cu-Cu joint bonded with increasing bonding time: (a) pressureless NOB process, (b) pressureless OB process, (c) pressureless ORB process. (d): Comparison of shear strength between OBR and NOB joint bonded with pressure or without pressure, respectively.

5.4b, it is interesting that the joints fabricated with the pressureless OB process can obtain a shear strength that was a little higher than those prepared by the pressureless NOB process although the Cu flakes were oxidized. After the oxidation for 5 min, a bonding strength of 8 MPa was obtained. When the oxidation time was extended from 5 min to 60 min, the bonding strength was relatively stable at around 9 MPa, which demonstrates that the joint strength was still weak, and cannot be enhanced by increasing the oxidation time. It has been known that the surface nanostructure of the Cu flake was originally generated by the formation of Cu_2O nanoparticles, however, Cu_2O is a brittle semiconductor and its formation is deleterious to the mechanical property of Cu-Cu interconnection, as well as its thermal and electrical conductivity. Therefore, for producing a pure Cu joint, the subsequent reduction process is required to transform those Cu_2O nanoparticles to Cu nanotextured surface. Here, the samples that oxidized for 20 min were selected for the subsequent reduction process. According to the XRD result in Fig. 5.3g, it is known that the oxidized Cu flakes had been reduced to pure Cu flakes after the reduction for 2 min. Thus, the further reduction process after 2 min can be seen as a simple bonding process in the formic acid atmosphere. Fig. 5.4c shows the shear strengths of the pressureless ORB joints bonded with an increasing bonding time in the formic acid atmosphere. It can be seen that the bonding strength of the ORB joint was gradually improved with the increasing bonding time, corresponding to a diffusion-controlled sintering process. After the bonding for 40 min, the joints showed a shear strength of 23.8 MPa, significantly higher than that fabricated with the pressureless NOB process. The greatly enhanced bonding strength should be attributed to the in-situ formation of the nanotextured surface of Cu particles. These nanostructures can more easily coalesce than the microscale flakes themselves, due to the highly reactive surface resulting from the nanoscale effect [2-4]. Therefore, during the pressureless ORB process, the facile coalescence of the in-situ formed nanotextured surface between the adjacent Cu flakes greatly increased the sintered bonding strength of these microscale particles. The bonding strength reach a value similar to that of joints fabricated with high Pb-containing solders [5]. Moreover, Fig. 5.4d gives the comparison of the shear strength between the ORB joint and the NOB joint both that were bonded with a pressure of 0.5 MPa. With the bonding pressure, the bonding strength of the NOB joint was obviously increased from nearly 0 to 30.8 MPa; however the ORB joint was significantly stronger than the NOB joint, it exhibits a very high shear strength near to 80 MPa.

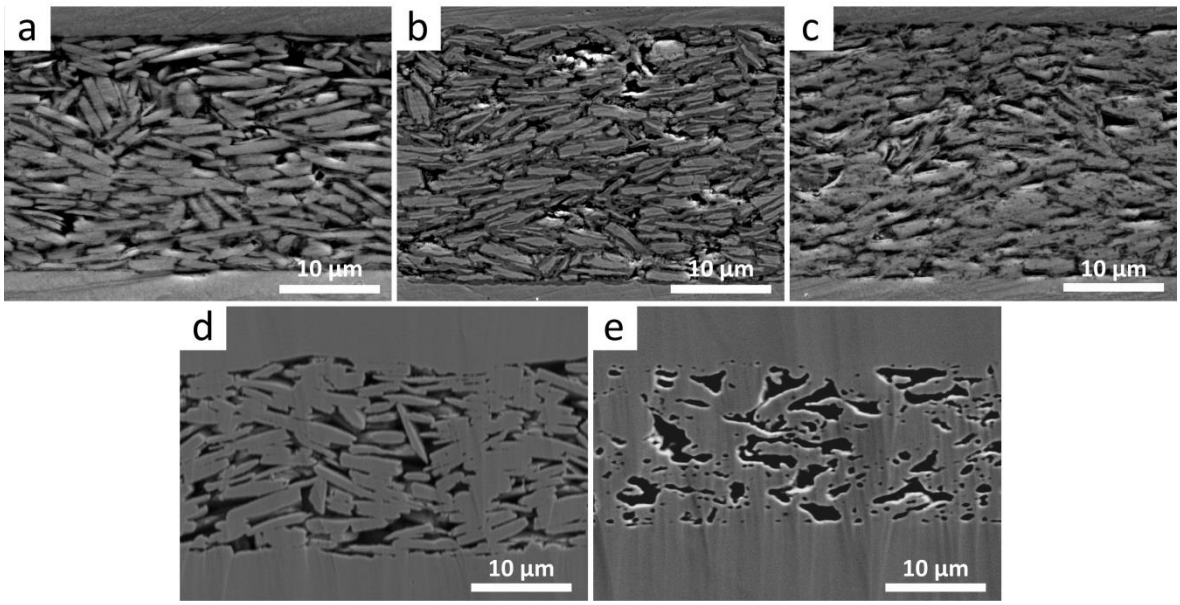

Figure 5.5 Cross-sectioned SEM images of Cu-Cu joints fabricated with different bonding process: (a) pressureless NOB process, (b) pressureless OB process, (c) pressureless ORB process, (d) pressure-assisted NOB process, (e) pressure-assisted ORB process.

Figs. 5.5 show the cross-section microstructure of the NOB and ORB joints bonded with or without pressure, respectively. After the pressureless NOB process, as shown in Fig. 5.5a, though the Cu flakes were closely packed, neither shape change nor coalescence of the particles can be observed, showing the poor sinterability of microscale Cu flakes at 300 ℃. It is well known that sintering is dependent on the mass transport in particles; surface diffusion is the dominant mechanism for mass transport in Cu particles below 10 μm diameter at temperatures < 600 ℃ [6]. Obviously, in a pressure bonding condition, the applied heating temperature (300℃) is too low to obtain a well-sintered microstructure due to the inherent low surface activity of the microscale Cu flakes. Consequently, this loose microstructure directly resulted in the negligible bonding strength of the joint. After the pressureless OB process, as shown in Fig. 5.5b, the Cu flakes were covered by a thin layer of Cu oxide. Though the particles were separated by the oxide layers, the shape of Cu flakes appeared a little change due to the formation of surface oxides, leading to an increase of the packing density in the bonding layer, and which could attribute to the slightly higher shear strength than that of the NOB joints. However, similar to that in the pressureless NOB joints, these oxidized Cu flakes were just closely packed, no sintering between the flakes can be observed. Indeed, generally, the Cu

powders with oxides layers are more difficult for sintering than those with a clean surface.

In contrast, when the pressureless ORB process was used (Fig. 5.5c), the loosely packed structures were replaced by a partially sintered structure, indicating the mass transport occurred during the ORB process. It is clear that the initial particle shapes and some interfaces between the flakes had disappeared, apparently, caused by the coalescence of the formed Cu nanotextured surface during the ORB process. On the other hand, when the bonding pressure of 0.5 MPa was applied, the NOB joint also exhibited a partially sintered microstructure, as shown in Fig, 5.5d. The external pressure can provide an intrinsic contribution to the driving force for sintering [7], therefore, the partial coalescence between the adjacent Cu flakes occurred in the joint. However, the initial shape of those flakes still remained, and a number of individual flakes can be recognized. Thus, overall the bonding layer exhibited a feature of closely packed and partially sintered flakes, indicating that the sintering of the Cu flakes is still insufficient. The Fig. 5.5e shows the bonding layer of the pressure-assisted ORB joint. As shown in Fig. 5.4d, it presented the highest joint strength, so it is no surprise that the joint exhibited a well-sintered microstructure with some long-shaped pores. The initial shape and interface between the flakes had completely disappeared, and clear Cu porous structure was formed by the coalescence of individual Cu flakes. Compared to a fully dense Cu layer, this sintered structure with many pores is preferred. Because the presence of pores can help reduce the elastic module of bonding layer and consequently promote to relieve the thermo-mechanical stresses generated from mismatched coefficients of thermal expansion between the semiconductor and the substrate, thus leading to better reliability [8]. This experimental evidence suggests that the surface-modified flakes are very suitable to the pressure-assisted bonding process, the change in the surface morphology of the microscale Cu flakes contribute to obtaining a well-sintered microstructure and resulting in a considerably high bonding strength.

The low magnification SEM images of the fractured NOB and ORB joints bonded with pressure or without pressure are shown in Fig. 5.6. The pressureless NOB joint exhibited a smooth surface on both side, no evidence of rupture and deformation can be found. On the other hand, varying degrees of rupture can be observed on both sides of other three fractured joints. In these three ORB joints that show sound joint strengths, the fracture happen partially in the Cu sintered layer and partially near the interface between Cu substrate and Cu sintered layer. More details on the fracture

surface of joints ware given in the high magnification SEM images of the selected area, as shown in Fig. 5.7. Firstly, on the fracture surface of the pressureless NOB joint, the Cu flakes were retained

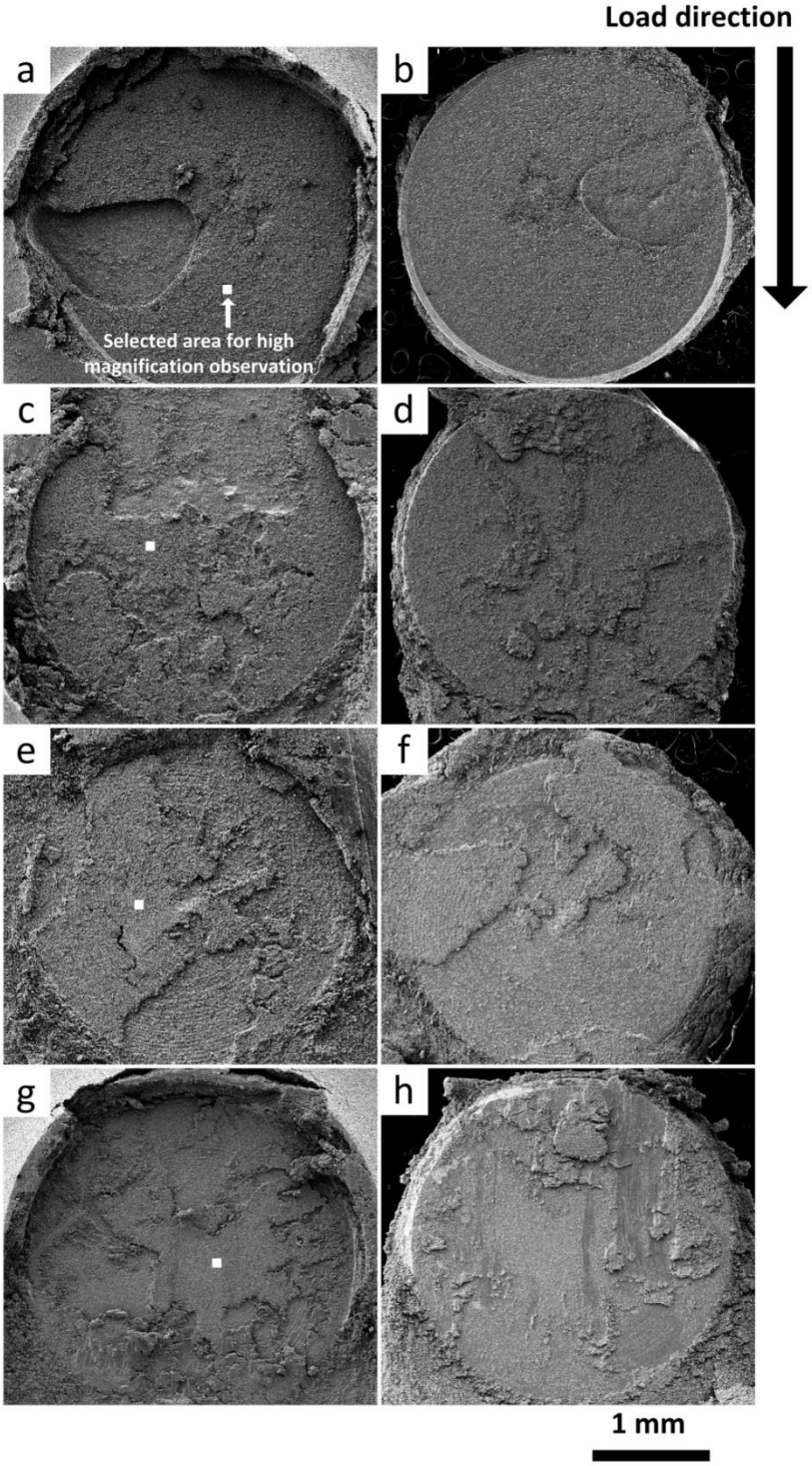

Figure 5.6 Low magnification SEM images of fracture morphology of Cu-Cu joints fabricated with different bonding process: (a, b) pressureless NOB process, (c, d) pressureless ORB process, (e. f) pressure-assisted NOB process, (g, h) pressure-assisted ORB process

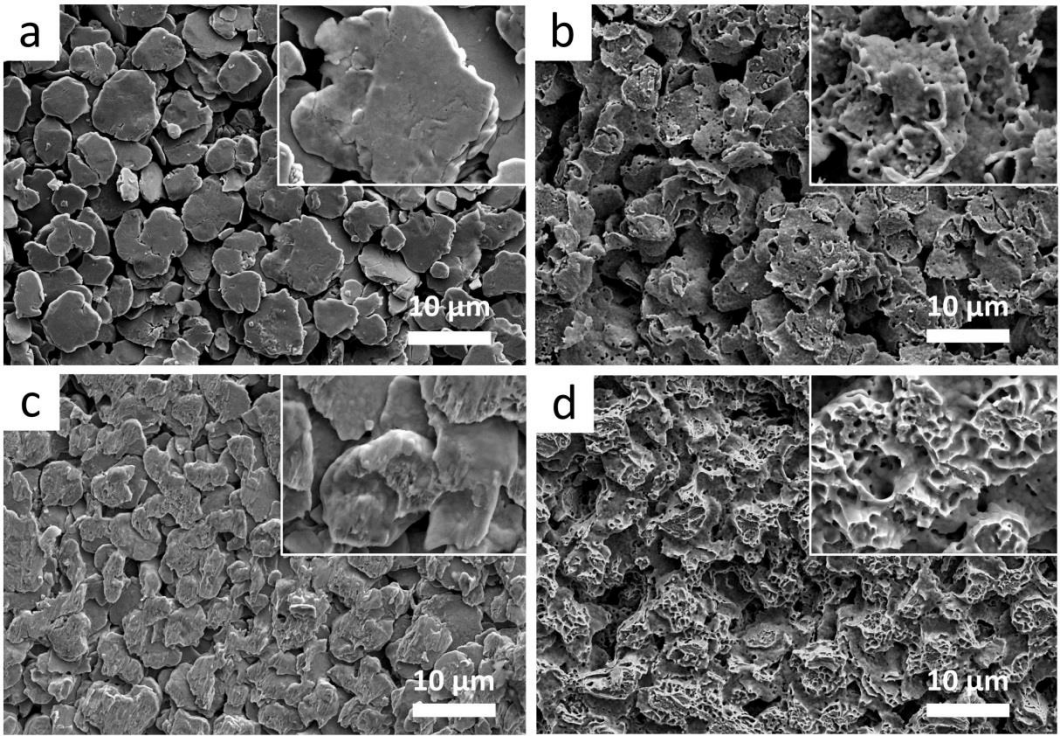

Figure 5.7 High magnification SEM images of selected area on fracture morphology of Cu-Cu joints fabricated with different bonding process: (a) pressureless NOB process, (b) pressureless ORB process, (c) pressure-assisted NOB process, (d) pressure-assisted ORB process.

well, even no fracture or deformation can be observed on the surface of Cu flakes, confirming that the sintering of Cu flakes did not happen. In contrast, the Cu flakes partially coalesced in the pressureless ORB joint, thereby the fractured flakes can be observed on the surface of the fractured joint, as shown in Fig. 5.7b. The pressure-assisted NOB joint exhibits a relatively flat fracture morphology, where the Cu flakes remaining the initial shape laid on the surface, as shown in Fig. 5.7c. However, some local fracture can be seen on the surface of flake, confirming the partial coalescence of the Cu flakes. Finally, as shown in Fig. 5.7d, the fracture morphology of the pressure-assisted ORB joint seems quite different. It exhibited evidence of ductile deformation on the entire surface, moreover, no individual fractured flake can be recognized, which is consistent to the aforementioned well-sintered microstructure and also give evidence to support the effective sintering by the pressure-assisted ORB process.

5.4 Relation of oxidation time with bonding properties of ORB process

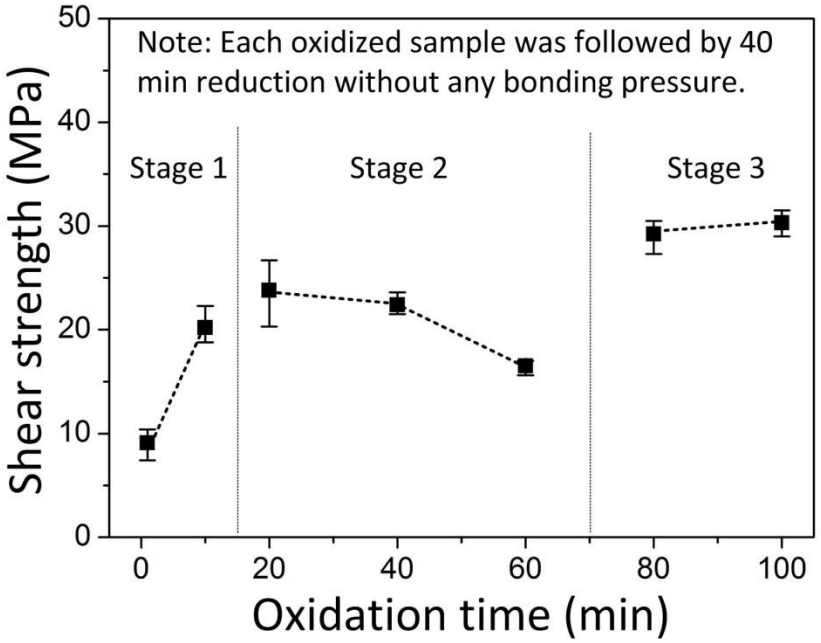

Figure 5.8 Relation between the shear strength of ORB joint and the oxidation time at 300 ℃.

As mentioned before, during the reduction process, the transformation from Cu_2O nanoparticles layer to Cu nanotextured surface only took 2 min, so the following process can be considered as a sintering process with modified Cu flakes. Indeed, the reduction time show a parabola relation with the ORB joint strength, a typical relation for diffusion-controlled bonding process. On the other hand, although the oxidation process did not provide a sintering behavior, it is even more important than the reduction process because it created the Cu_2O nanoparticle layer, and thereby controlling the surface morphologyof Cu flakes and affecting the sintering bonding during the reduction process. Fig. 5.8 gives a curve that indicates the relation between the bonding strength of ORB joint and the duration of oxidation process. It should be noted that, after the oxidation of selected times, shear test sample undertook 40 min reduction to complete the ORB process. It can be seen the curve shows a interesting three-stage trend. Stage One is from 1 min to 20 min, during which the bonding strength increased from lower than 10 MPa to higher than 20 MPa. Stage Two is from 20 min to 60 min, during which the bonding strength gradually decreased with the further extension of the oxidation time. Stage Three is after 60 min, the bonding strength exhibited a great improvement from 60 min to 80 min, and then it maintained a high value around 30 MPa at 100 min.

To explain the this three-stage trend, we need to firstly clarlify the effect of oxidation time on the surface morphology of modifed Cu flakes. Fig. 5.9 shows the surface morphplogy of the oxidized

Cu flakes with increasing oxidaion time, and Fig. 5.10 shows the surface morphplogy of corresponding reduced Cu flakes. As mentioned *in Chapter 4*, after 1 min oxidation, the Cu_2O nanoparticles had massively propagated on the flake surface while some flat surface still remained. After 10 min, the Cu_2O nanoparticles had covered the entire flake surface. From 10 min to 20 min, the change of surface morphology was insignificant. However, from 20 min to 60 min, the

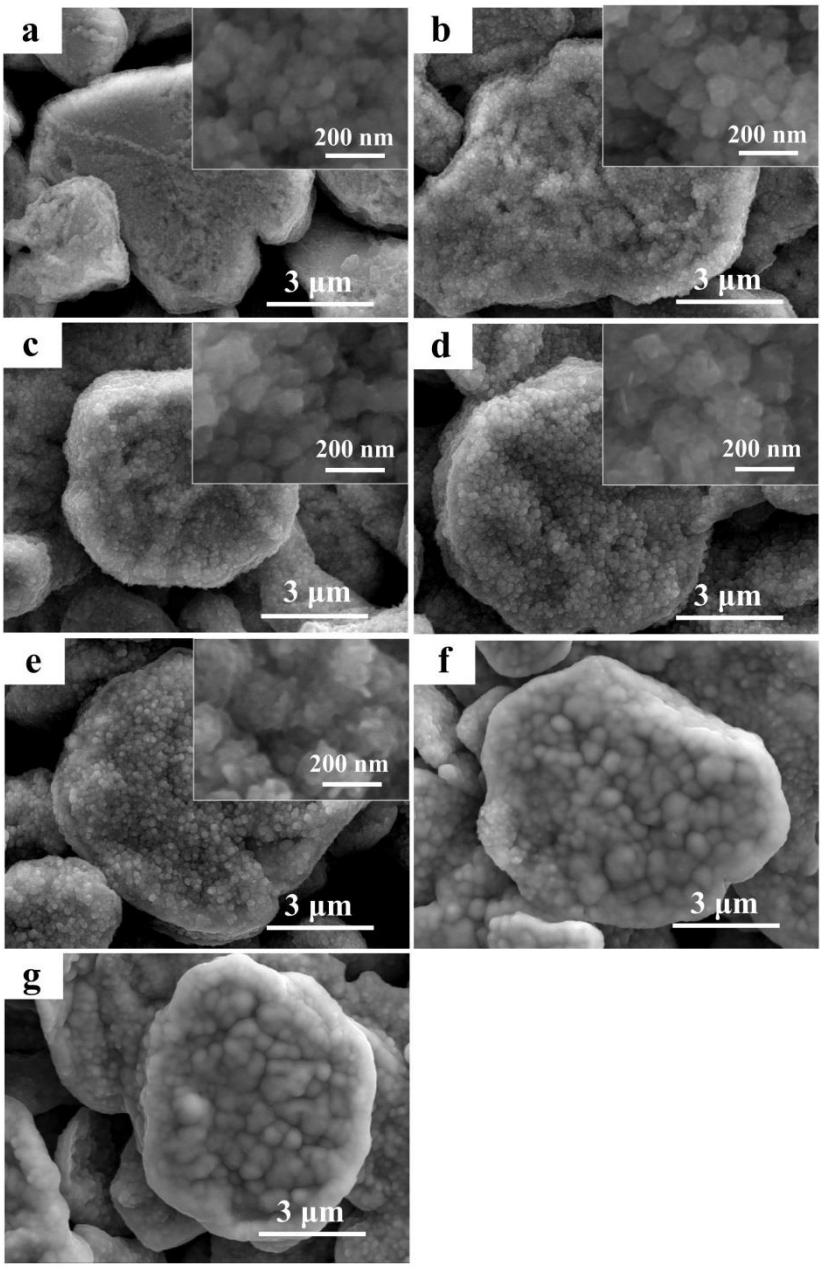

Figure 5.9 SEM images of Cu flakes oxidized at 300 ℃ for (a) 1 min, (b) 10 min, (c) 20 min, (d) 40 min, (e) 60 min, (f) 80 min, (g) 100 min.

nanoparticles exhibited a coarsening process. Finally, for 80 min and 100 min, the feature of uniform nanoparticles disappeared, and instead, irregular oxide bulges formed on the surface of oxidized Cu flakes. It can be seen in Fig 5.9 f and g that the size of oxide bulge is not uniform, some are very fine but some are quite coarse. It is suggested that this morphology is result from the coarsening process

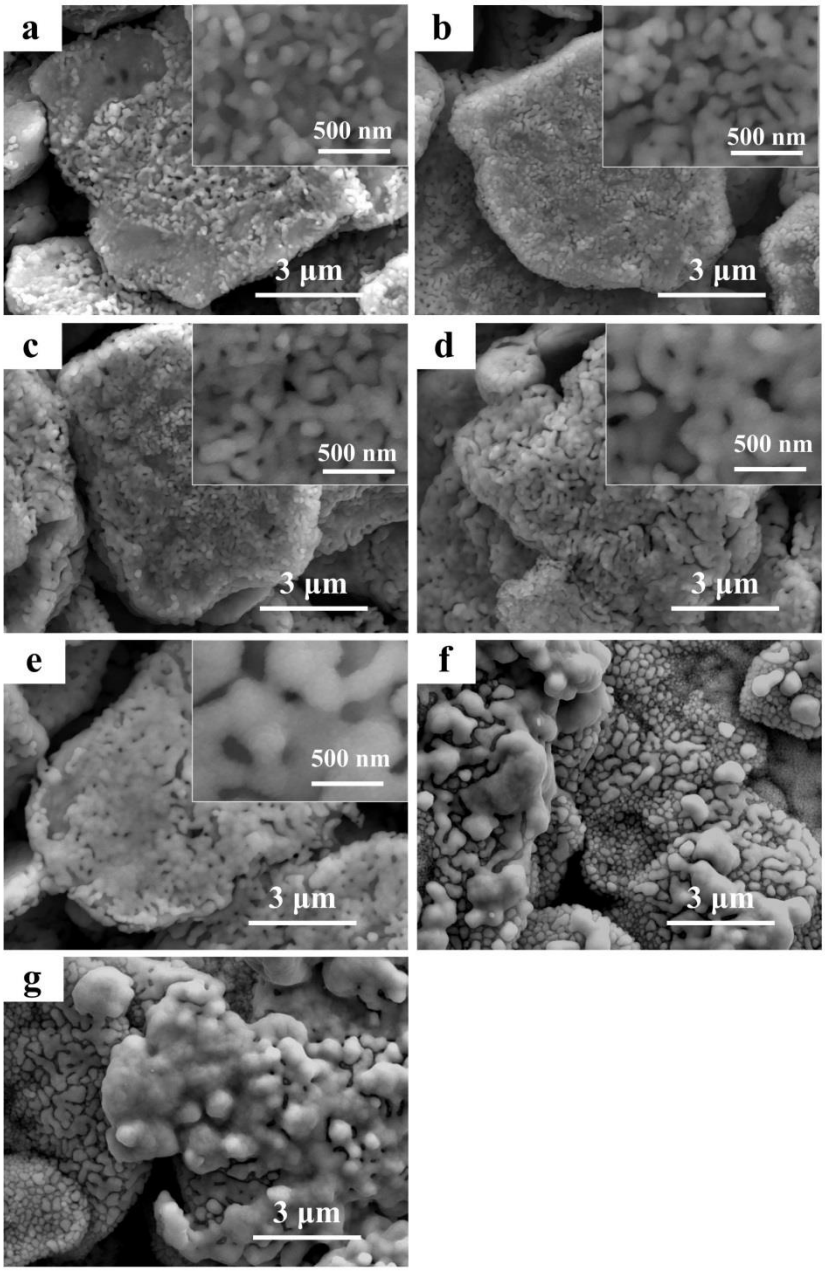

Figure 5.10 SEM images of the Cu flakes that were oxidized for different times and followed by a reduction for 2 min.: (a) oxidation for 1 min, (b) oxidation for 10 min, (c) oxidation for 20 min, (d) oxidation for 40 min, (e) oxidation for 60 min, (f) oxidation for 80 min, (g) oxidation for 100 min.

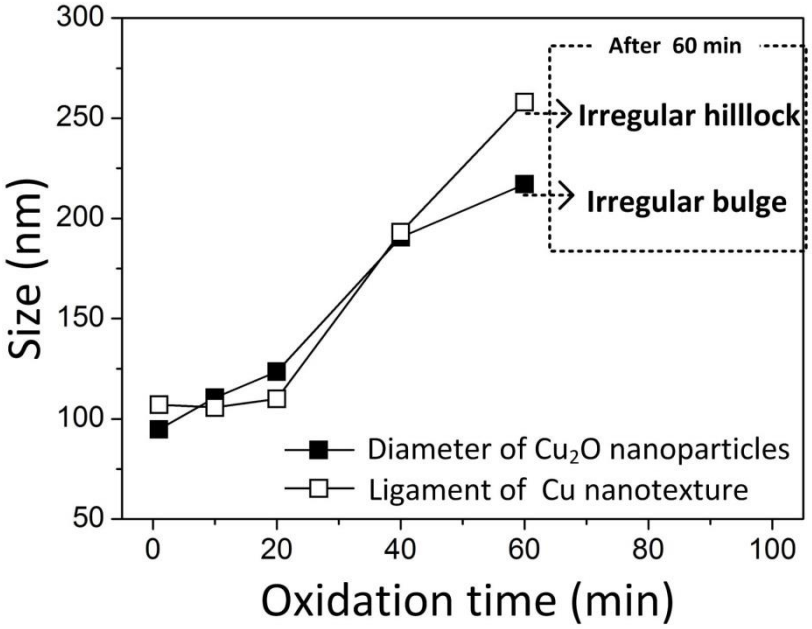

Figure 5.11 Diameters of Cu_2O nanoparticles on the oxidized Cu flakes and ligament sizes of Cu nanotextured structure on reduced Cu flakes with increasing oxidation time at 300 ℃.

of the Cu_2O nanoparticle layer. Apparently, the surface with irregular bulges is more thermodynamic favorable flat than the surface covered by fine nanoparticles. On the other hand, after the reduction for 2 min, the cover area and the structure size of Cu_2O nanoparticle layer can be inherited to some extent. Some flat surface can be observed in Fig. 5.10a, demonstrating a insufficient cover area of nanotextured surface. In contrast, as shown in Fig. 5.10 b and c, the nanotextured surface had covered entire Cu flakes, indicating a sufficient surface modification. Therefore, it is suggested that when oxidation time was extended from 1 min to 20 min (Stage One), the cover area of surface modification increased, and as a result the bonding strength of ORB joint also impoved.

Fig. 5.10 gives the diameters of Cu_2O nanoparticles and ligament sizes of Cu nanotextured structure under increasing oxidation times. And it clearly shows that Cu_2O nanoparticles underwent obvious coarsening from 20 min to 60 min, and consequently the corresponding Cu nanotextured surface also exhibited a coarsening process. Therefore, it is suggested that when oxidation time was extended from 20 min to 60 min, the Cu_2O nanoparticles were gradually coarsened, leading to the coarsening of nanotextured surface. Since the coarse nanotextured surface should exhibit lower surface activity the bonding strength of the ORB joints gradually decreased during Stage Two.

However, as mentioned before, when the oxidation time was further extended from 60 min to 80 min and 100 min, this decreasing trend stopped and a rapid increase of bonding strength happened. Fig 5.9 e and f have shown a transform of oxide morphology from uniform nanoparticles to irregular bulge during this period. And Fig 5.10 f and g present the surface morphology of Cu flakes after the reduction of irregular oxide bulge. It is found those irregular oxide bulges was transformed to a layer of irregular hillock. Apparently, the surface with irregular hillocks shows a different morphology with the nanotextured surface, and it is suggested their formation mechanisms are different. As mentioned in *Chapter 4*, the formation of Cu nanotextured surface is caused by the reduction of Cu_2O nanoparticles and the simultaneous coalescence of the reduced Cu nanoparticles. On the other hand, it is thought the reduction of irregular oxide bugle caused a volume shrink on the particle surface due to the different molar volume of Cu_2O and Cu, and thus leading to the formation of irregular hillock. This volume shrink also happened in the transform from Cu_2O nanoparticles to Cu nanotextured surface, but this shrink did not change the shape of spherical nanoparticles, and the simultaneous coalescence Cu nanoparticles generated the nanotextured structure, a feature of partially sintered Cu nanoparticles. For the surface with irregular bugles, it can be considered as a relatively flat surface compared to the nanoparticles surface. The volume shrink of this flat surface can lead to an entirely different surface morphology. As shown in Fig 5.10 f and g, the irregular hillock formed, like the cracked ground caused by drought, and moreover, the size of hillock is not uniform, varying from nanoscale to microscale. Due to the existence of many nanoscale hillocks, it is suggested these irregular hillocks can be seen as a nanostructure, and therefore, the increase of bonding strength should be attributed to the formation of this new surface nanostructure, and its surface activity could be higher than that of the coarsened nanotextured surface.

5.5 Thermal stability of bonding joint during isothermal aging at 250 ℃

Fig. 5.8 shows the shear strength of the pressureless and pressure-assisted ORB joints during the isothermal aging at 250 ℃ for 1000 h, respectively. It can be seen that the shear strength of both kinds of ORB joint was decreased initially after 250 h. After that, their shear strengths remained relatively stable with the further increase of the aging time. Finally, after the aging for 1000 h, the

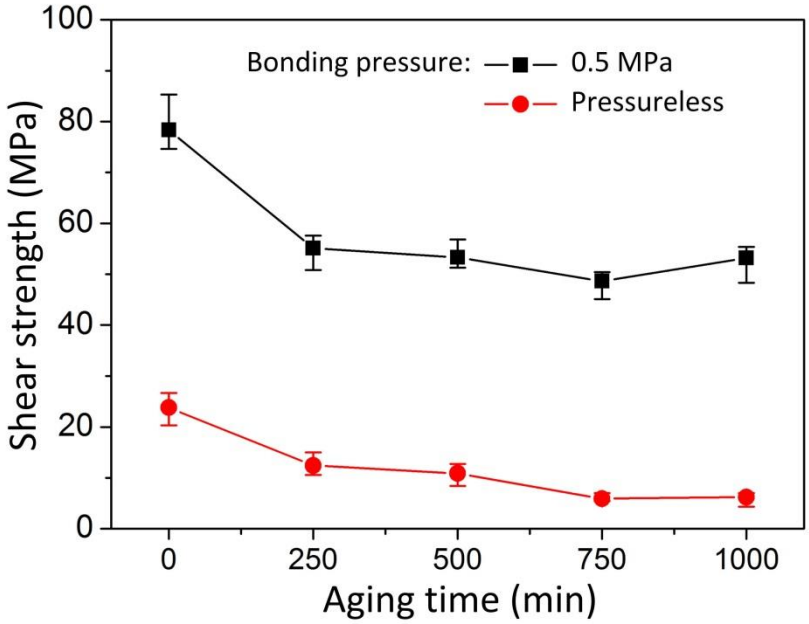

Figure 5.12 Variation of shear strength of ORB joints during isothermal aging test at 250 ℃.

shear strength of the pressureless ORB joint was decreased down to 10 MPa, while the pressure-assisted ORB joint showed a high shear strength above 50 MPa. This result demonstrates that the pressure-assisted ORB joint exhibited better high-temperature reliability than the pressureless ORB joint.

The high-temperature reliability of the die bonding layer depends on the thermal stability of the microstructure during high-temperature aging, therefore the microstructural observation and elemental analysis of the bonding layer of both joints after the thermal aging were conducted, as shown in Fig. 5.9 and Fig. 5.10, respectively. In the Fig. 5.9, new dark-color phase formed in the

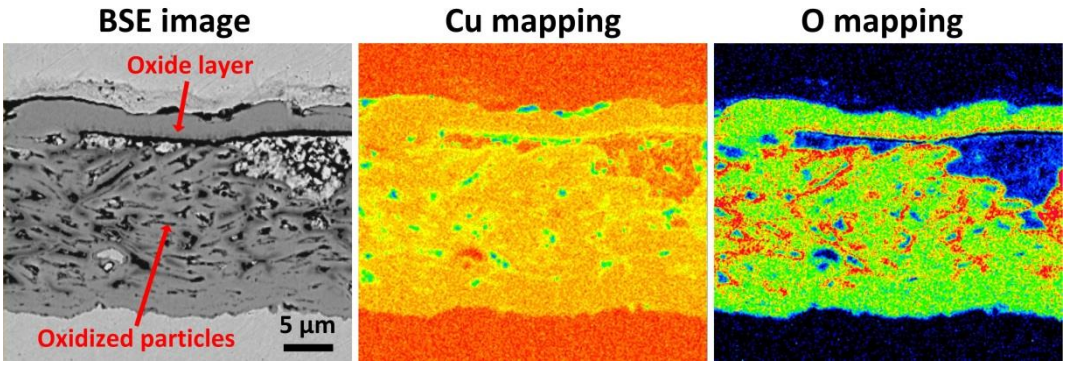

Figure 5.13 Cross-sectional BSE images and corresponding EPMA elemental mappings of (a) the pressureless ORB joint after the isothermal aging at 250 ℃ for 250 h

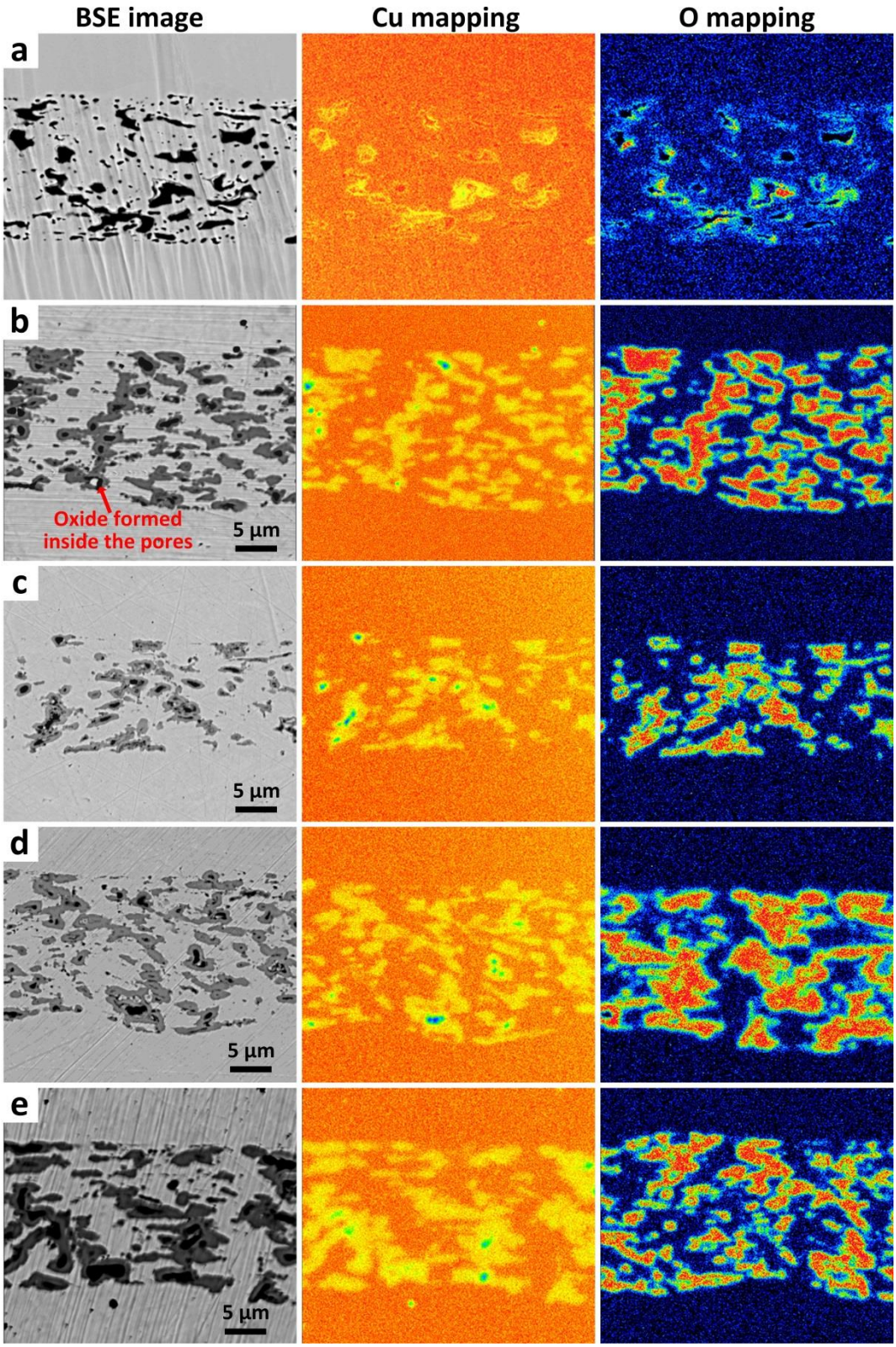

Figure 5.14 Cross-sectional BSE images and corresponding EPMA elemental mappings of (a) as bonded pressure-assisted ORB joint, and (b-e) pressure-assisted ORB joint after the isothermal aging at 250 ℃ for 250 h, 500h, 750h, 1000h, respectively.

bonding layer of the pressureless ORB joint after the aging for 250 h. The corresponding O mapping demonstrates that the new phase was Cu oxide, and it had occupied nearly the entire bonding layer of the joint. The oxidation of Cu is a big reliability issue in the Cu-Cu interconnection. Many researchers have reported that the oxidation of Cu substrate will degrade the bonding strength of Ag sintered joints during an isothermal aging test in the air [9, 10]. It has been found that even the Cu substrate was plated by Ag layer, that the ambient oxygen can easily permeate through the Ag sintered layer and the Ag plating layer to oxidize the Cu substrate during the thermal aging test [8]. In our study, not only the substrate but also the sintered particles were made of Cu, moreover, the partially sintered Cu structure provided a large specific surface area that beneficial to the oxidation, thereby the pressurelss ORB joint was severely oxidized during the thermal aging. Consequently, the joint strength was reduced to lower than 10 MPa.

On the other hand, Fig. 5.10 shows the microstructural and composition evolution of pressure-assisted ORB joint during the thermal aging. Compared to the composition in the as-bonded pressure-assisted ORB joint, an obvious oxidation can be observed after the aging for 250 h. However, these Cu oxides were formed around the pores of the bonding layer and were separated by the Cu network. Therefore, it is suggested that, the formation of Cu oxidation can be limited around the pores that were exposed to the air as long as the sintering is effective and the Cu particles can coalesce to the bulk Cu network. Moreover, from 250 h to 1000 h, as shown in Fig. 5.9b-e, the growth of those isolated oxides was not obvious. Apparently, the existence of bulk Cu network effectively avoided the complete oxidation of the Cu joint, thus ensuring the integration of the microstructure and the high bonding strength of the joint. Therefore, it can be concluded that the well-sintered Cu joint that bonded with the pressure-assisted ORB process exhibited an excellent high-temperature microstructural stability, and which contributed to the excellent high-temperature reliability.

5.6 Conclusion

In this Chapter, the bonding properties of the Cu-Cu joint prepared with the oxidation-reduction bonding process were verified. For the pressureless and pressure-assisted conditions, the ORB joints

exhibited shear strength of 23.8 MPa and 78.3 MPa, respectively, significantly higher than the corresponding NOB joints. The observation of the cross-section and the fracture surface of the ORB and NOB joints suggest that the in-situ modified surface can significantly improve the low-temperature sinterability of the Cu particles, thus contributing to the increased bonding strength. Moreover, during the isothermal aging test at 250 ℃ for 1000 h, the shear strengths of both the pressureless and the pressure-assisted ORB joints were initially decreased after first 250 h. However, the pressureless ORB joint had been completely oxidized after first 250 h, whereas the pressure assisted ORB joint was only partially oxidized after entire 1000 h aging, thus still remaining a high shear strength that above 50 MPa.

References

[1] P. J. Soininen, K. E. Elers, V. Saanila, S. Kaipio, T. Sajavaara, and S. Haukka, Reduction of copper oxide film to elemental copper, *J. Electrochem. Soc.*, **152** (2005) 122-125.

[2] J. W. M. Frenken, J.F. Vanderveen, Observation of surface melting, *Phys. Rev. Lett.*, **54** (1985) 134.

[3] L. J. Lewis, P. Jensen, J. L. Barrat, Melting, freezing, and coalescence of gold nanoclusters, *Phys. Rev. B*, **56** (1997) 2248.

[4] K.S. Moon, H. Dong, R. Maric, S. Pothukuchi, A. Hunt, Y. Li, C. P. Wong, Thermal behavior of silver nanoparticles for low-temperature interconnect applications, *J. Electron. Mater.*, **34** (2005) 168-175.

[5] E. Ide, A. Hirose, K. F. Kobayashi, Influence of bonding condition on bonding process using Ag metallo-organic nanoparticles for high-temperature lead-free packaging, *Mater. Trans.*, **47** (2006) 211-217.

[6] M. Yeadon, J. C. Yang, R. S. Averback, In-situ observations of classical grain growth mechanisms during sintering of copper nanoparticles on (001) copper, *Appl. Phys. Lett.*, **71** (1997) 1631-1633.

[7] A. S. Helle, K. E. Easterling, M. F. Ashby, Hot-isostatic pressing diagrams: new developments, *Acta Metall.*, **33** (1985) 2163-2174.

[8] R. Khazaka, L. Mendizabal, and D. Henry, Review on joint shear strength of nano-silver paste and its long-term high temperature reliability. J. Electron. Mater., **43** (2014) 2459-2466.

[9] S. T. Chua, K. S. Siow, Microstructural studies and bonding strength of pressureless sintered nano-silver joints on silver, direct bond copper (DBC) and copper substrates aged at 300 ℃, *J.*

Alloys Compd., **687** (2016) 486-498.

[10] H. Zhang, S. Nagao, K. Suganuma, H. J. Albrecht, K. Wilke, Thermostable Ag die-attach structure for high-temperature power devices, *J. Mater. Sci. Mater. Electron.*, **27** (2016) 1337-1344.

Chapter 6
Effect of particle shape and substrate on bonding properties of oxidation-reduction bonding

6.1 Introduction

In *Chapter 5*, we applied the oxidation-reduction process in the low-temperature sintering bonding process by switching the atmosphere during the bonding process, and presented how this in-situ surface modification method improved the bonding properties of the sintered Cu joint. The nanotextured surface that formed during the oxidation-reduction process played a key role in the enhanced coalescence of the sintered particles. However, some important aspects of this bonding method are not yet fully understood. First is the compatibility of the ORB process with differently shaped Cu particles. In addition, the effect of the substrate on the bonding properties of the ORB process is not clear. In this Chapter, we investigated the bonding properties of the ORB process with hybrid Cu particle paste, which is composed of flakes and spherical particles. Also, we studied the bonding properties of the ORB process with various substrates.

6.2 Experimental

6.2.1 Microscale Cu particle paste

Two kinds of microscale Cu particles were used in this study as starting materials. The flake-shaped particles had an average diameter 6.9 μm, an average thickness of 1μm, and a specific area of 0.13 m^2/g (1400YP, MITSUI MINING & SMELTING CO. LTD). The spherical particles had an average diameter 1.2 μm with a specific area of 0.26 m^2/g (1100Y, MITSUI MINING & SMELTING CO. LTD). These two kinds of particles are hereafter referred to as "Cu flakes" and "Cu spheres", respectively. SEM images of the two kinds of particles are shown in Fig. 6.1. Terpineol, boiling point 220.8 ℃, was used as a solvent to prepare the Cu flake paste and Cu sphere paste, which consisted of 85 mass.% Cu particles and 15 mass.% terpineol solvent. Moreover, the Cu flakes and Cu spheres were mixed in different proportions to make hybrid particle paste. Finally, the five Cu pastes produced were labeled as F_{100}, $F_{75}S_{25}$, $F_{50}S_{50}$, $F_{25}S_{75}$ and S_{100}, in which the concentration of Cu spheres are 0 mass %, 25 mass %, 50 mass %, 75 mass % and 100 mass %, respectively. The Cu flakes, Cu sphere and their hybrid particles were utilized to identify the compatibility of ORB process with differently shaped Cu particles.

6.2.2 Bonding substrate

The schematic diagram of the bonded joint is shown in Fig. 6.2. Cu disc was used to fabricate the joint. The pure Cu disc was cleaned with a diluted hydrochloric acid to remove the copper oxides

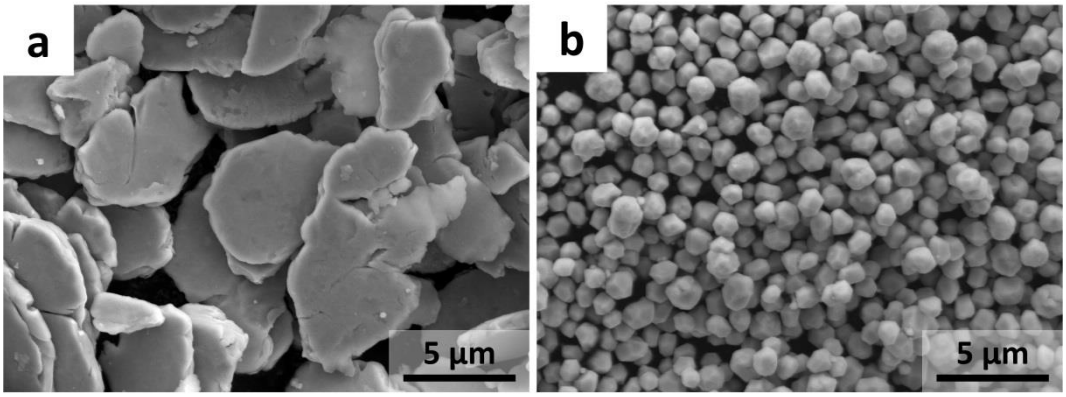

Figure 6.1 SEM images of (a) flake-shaped Cu particles and (b) spherical Cu particles used in this study.

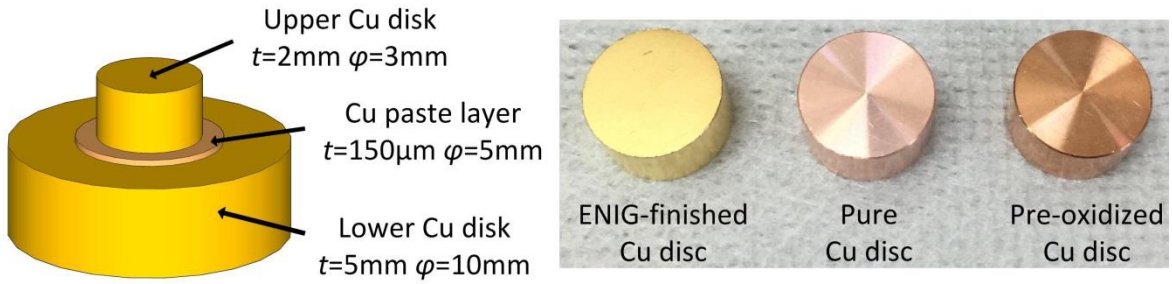

Figure 6.2 Schematic diagram of bonded joint and optical images of the ENIG-finished Cu disc, pure Cu disc and pre-oxidized Cu disc used as the lower Cu disk.

before bonding. In addition, to study the bonding performance of the ORB process with different substrates, other two kinds of Cu discs were used to create the joint. They were the electroless nickel/immersion gold (ENIG)-finished Cu disc and pre-oxidized Cu disc. The pre-oxidized Cu disc was obtained by a pre-oxidation treatment of a cleaned pure Cu disc at 200 ℃ for 5 min in air. In the ENIG-finished disc, the thickness of Ni(P) and Au were about 2 μm and 80 nm, respectively. The optical images of three kinds of substrates are shown in Fig. 6.2. Compared to the pure Cu disc, the pre-oxidized Cu disc shows a darker color because of the formation of a very thin oxide layer.

6.2.3 Oxidation-reduction bonding process

The ORB process is as follows. The prepared joints were first pre-heated at 130 ℃ for 5 min in the air to completely evaporate the solvent, after which they were heated to the bonding temperature of 300 ℃ at 0.5 ℃/s and held at 300 ℃ for 20 min. After evacuation to reduce the air pressure to < 5 Pa, formic acid vapor was introduced into the chamber. Then, the bonding was continued by maintaining the samples at 300 ℃ for 40 min in the formic acid atmosphere. In contrast, some Cu-Cu joint specimens were bonded at 300 ℃ for 60 min in the formic acid atmosphere, labeled as a non-oxidation bonding (NOB) process. The heating profiles of both process are illustrated in Fig. 6.3.

6.2.4 Characterization methods

Thermogravimetric analysis (TGA) of the Cu particles was carried out to examine their oxidation behavior during the thermal oxidation. X-ray diffraction (XRD) analysis of the Cu particles

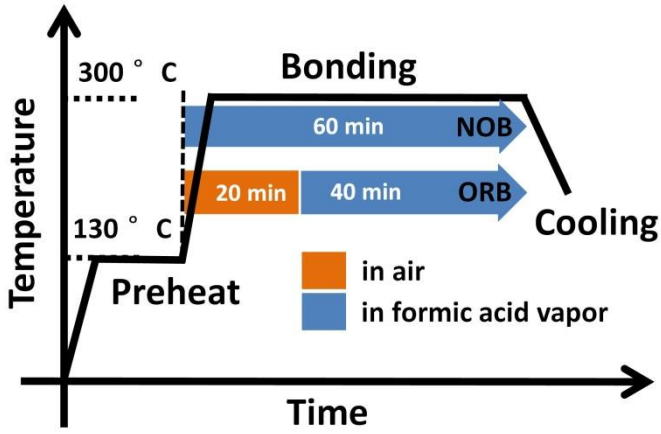

Figure 6.3 Illustration of temperature profiles of NOB and ORB process.

was conducted by an X-ray diffractometer (Rigaku Ultima IV) using Cu-Kα radiation (λ = 1.5405 Å).

The diffracted beam was scanned in steps by 0.01 °in an angular range from 20 to 80 °(2θ). A field-emission scanning electron microscope (FE-SEM, Hitachi SU-70) was used for microstructure observation, including the surface morphology of the Cu particles, cross-sectional microstructures, and the fracture surface of the bonded joints. Also, the composition of the microstructure was measured with an electron probe microanalyzer (EPMA, JXA-8530F, JEOL). The shear strength of the bonded joints was evaluated by using a shear tester (STR-1000, Rhesca) at a head speed of 1mm/min, where the fly height was 200 μm from the bottom of the specimen.

6.3 Effect of particle shape on bonding properties

6.3.1 Characteristics of Cu flakes and Cu spheres treated by oxidation-reduction process

Fig. 6.4 shows the TGA trace of Cu flakes and Cu spheres during heating in air. The weight of the samples increased with the oxidation process, and the increasing sample weight can reveal the oxidation rate of the sample. It is found that both curves increased rapidly at first, and then tended to stabilize gradually, indicating a power law relation. It is well known that the oxidation of bulk Cu is controlled by the outward diffusion of Cu cations in the oxide scale, thereby following the power law model [1]. The result reveals that the oxidation of microscale Cu particles is also a diffusion-controlled process. Moreover, it is observed that the Cu flakes underwent oxidation at a faster rate than the Cu spheres, even though they had a smaller specific surface area than the Cu

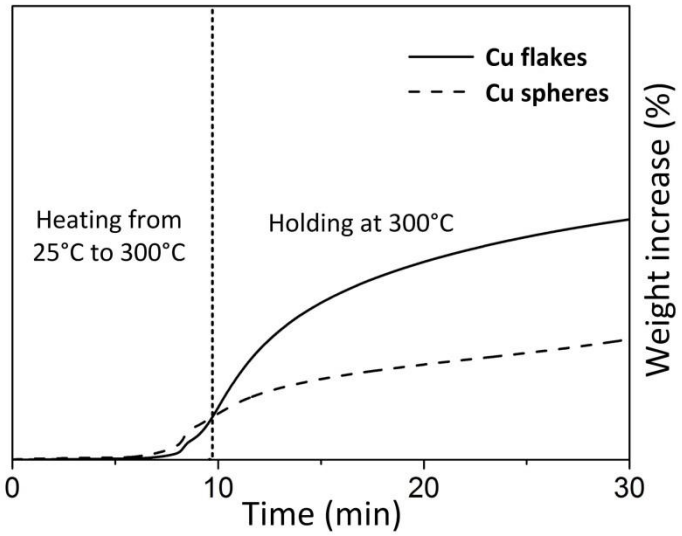

Figure 6.4 TGA traces of Cu flakes and the Cu spheres during thermal oxidation in air (temperature increasing at 30 ℃ min^{-1} to 300 ℃ and holding at 300 ℃ for 20 min)

spheres. Fig. 6.5 shows the SEM images and the corresponding XRD patterns of the two kinds of Cu particles after thermal oxidation for 20 min and after subsequent reduction for 2 min in the formic acid atmosphere. As mentioned before, the oxidized Cu flakes were covered by densely packed Cu_2O particles. And after the reduction, the densely packed Cu_2O nanoparticles were replaced by a nanotextured feature on the surface of the Cu flakes. On the other hand, as shown in Fig. 6.5c, the flat surface of the Cu spheres became very rough after the thermal oxidation. The surface morphology can be more accurately described as a nanoscale rough surface. The XRD profile shows that an obvious Cu_2O peak appeared after the oxidation, similar to that of the oxidized Cu flakes. However, the relative intensity of the Cu_2O peak to the Cu peak in the oxidized Cu spheres is obviously lower than that in the oxidized Cu flakes, indicating that the mole fraction of Cu_2O formed on the Cu spheres also is lower than that on the Cu flakes. This result is consistent with the aforementioned TGA curves of Cu flakes and Cu spheres and should be attributed to the slower oxidation rate of the Cu spheres. It is worth noting that the larger specific surface area of the Cu spheres did not bring about the faster oxidation rate; in fact, the Cu spheres actually presented a slower oxidation rate. Thus, the growth of the Cu_2O layer on the "small" Cu sphere should be much slower than that on the"big" Cu flake. It is believed that the different growth rate of Cu_2O on the two kinds Cu particles led to their different surface morphologies; the formation of a nanoscale rough surface, rather than

the nanoscale Cu_2O particles on the oxidized Cu sphere could be caused by the much slower growth rate of oxide scale on the Cu sphere. Fig. 6.5d shows the morphology of the Cu spheres after the oxidation-reduction process; it demonstrates that the nanoscale rough surface disappeared on all the

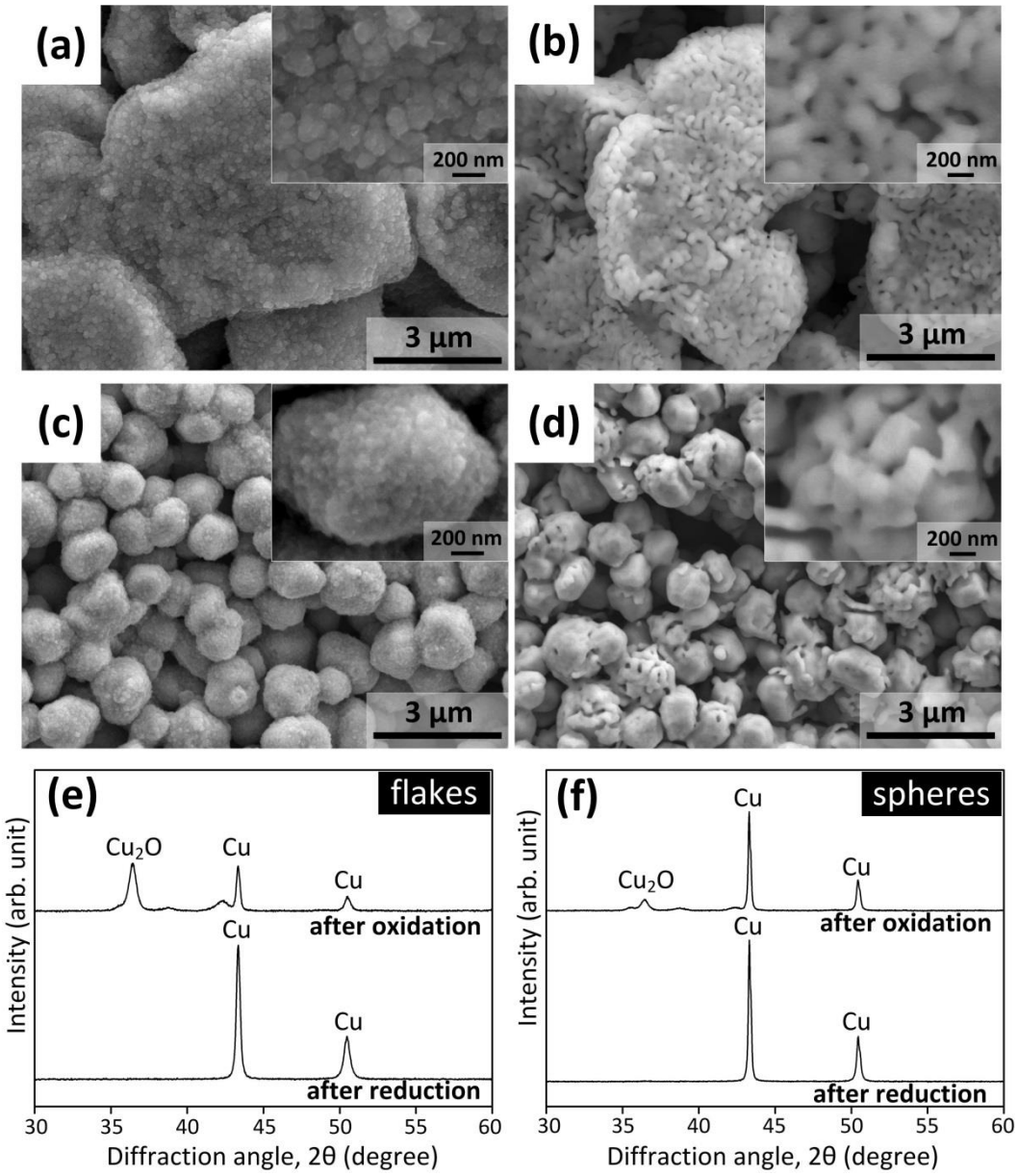

Figure 6.5 SEM images of Cu flakes: (a) after heating at 300 ℃ for 20 min in air, (b) followed by heating at 300 ℃ for 2 min in formic acid atmosphere, and SEM images of Cu spheres: (c) after heating at 300 ℃ for 20 min in air, (d) followed by heating at 300 ℃ for 2 min in formic acid atmosphere. (e) XRD patterns of Cu flakes in (a) and (b). (f) XRD patterns of Cu spheres in (c) and (d).

spheres, and some spheres had a clear nanotextured surface, as shown in the high-magnification image. On the other hand, many spheres regained the relatively flat surface. The corresponding XRD profile confirmed that these reduced spheres are pure Cu spheres. Thus, after the oxidation-reduction process, the chemical composition of the Cu spheres did not change; only thesurface morphology was modified. Moreover, through the comparison of the surface morphology of Cu flakes and Cu spheres after the oxidation-reduction process, it seems that the surface modification by the oxidation-reduction process is more complete on the Cu flakes than on the Cu spheres. It is thought the different microstructure of the oxide scale on the Cu flakes and Cu spheres led to their different surface morphologies after the reduction process. The formation of nanoscale Cu_2O particles is a precondition for the formation of the Cu nanotextured surface, which is caused by the reduction of Cu_2O nanoparticles and the simultaneous coalescence of the reduced Cu nanoparticles.

6.3.2 Bonding properties with hybrid Cu particles

Fig. 6.6 presents the shear strength of the Cu-Cu joints bonded using hybrid particle pastes by the NOB and the ORB process without bonding pressure, respectively. It is obvious that the shear strength of the joints prepared using the NOB process was very low, indicating that the Cu substrate cannot be bonded with the NOB process using microscale Cu paste. On the other hand, the joints fabricated with the ORB process showed much higher shear strength. Moreover, the ORB joints

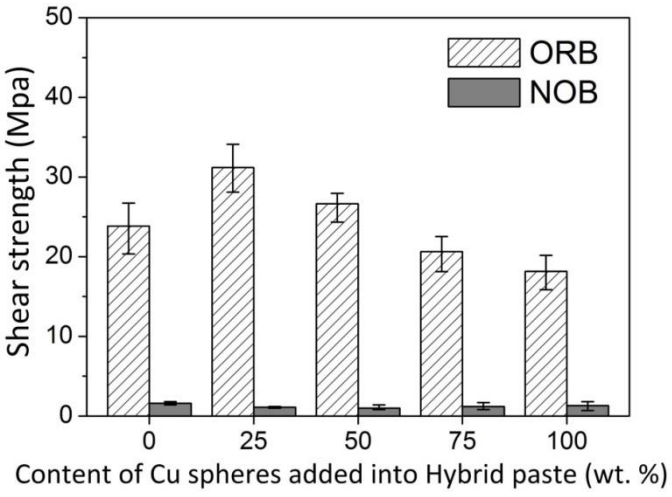

Figure 6.6 Shear strength of Cu–Cu joints bonded with different Cu pastes by NOB and ORB process, respectively.

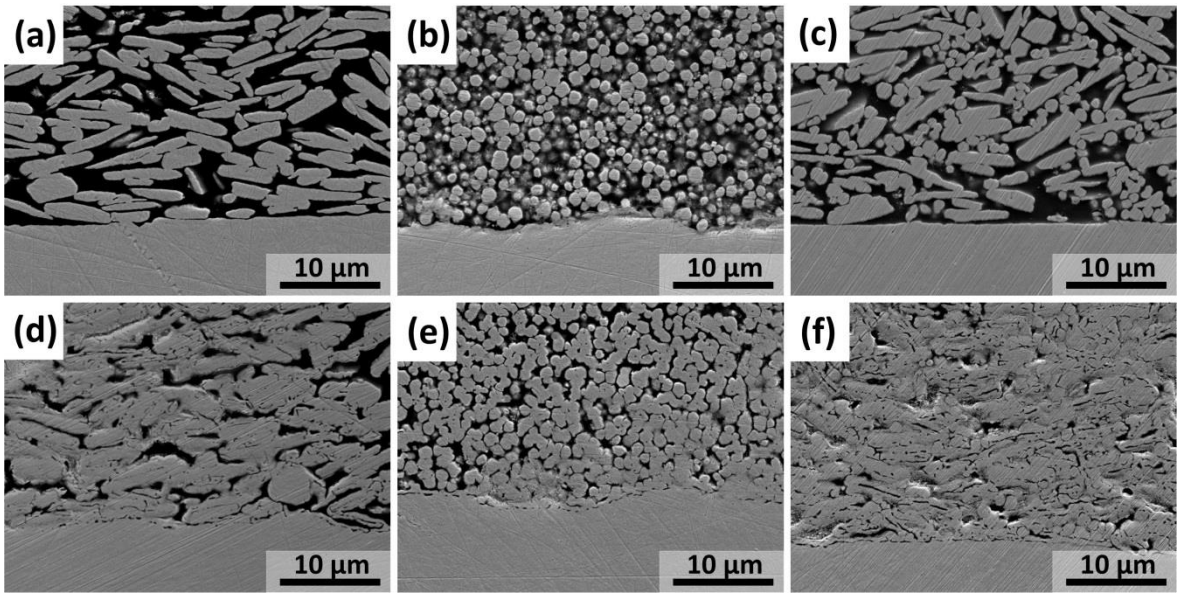

Figure 6.7 Cross-sectional SEM images of Cu-Cu joints bonded with different Cu pastes by NOB and the ORB process, respectively, a, b, c are F_{100}, S_{100} and $F_{75}S_{25}$ with NOB process, respectively, d, e, f are F_{100}, S_{100}, and $F_{75}S_{25}$ with ORB process, respectively.

bonded with different pastes show various shear strengths. The shear strength of the joint bonded with pure Cu flake paste (F_{100}) was higher than that with pure Cu sphere paste (S_{100}). The joint bonded with $F_{75}S_{25}$ paste showed the highest shear strength, 31.2 MPa. After that, the shear strength decreased with the increase of Cu sphere content. The joint bonded with S_{100} had the lowest shear strength.

Fig. 6.7 shows the cross-sectional microstructure of the ORB-based and the NOB-based Cu-Cu joints prepared with F_{100}, $F_{75}S_{25}$, and S_{100} paste, respectively. After the NOB process, as shown in Fig. 6.7a-c, the Cu particles including the Cu flakes, the Cu spheres, and their mixture were merely packed close together; no coalescence between the Cu particles was observed. In Fig. 6.7c, the use of hybrid particles led to a more dense distribution of Cu particles and reduced the porosity of packed particles; however, sintering did not occur. Apparently, when the microscale Cu particles are employed, a well-sintered microstructure cannot be obtained by conventional sintering bonding in the reducing atmosphere. It seems that not only the Cu flakes but also the smaller Cu spheres, which have an average diameter of 1.2 μm, are too “big” compared to their nanoscale counterparts; thereby inevitably exhibiting a low surface activity. This inherent low surface activity of the microscale Cu

particles cannot trigger the sintering behavior at 300 ℃, thereby leading to the failure of low-temperature sintering bonding. On the other hand, the joints bonded with the ORB process present a different interfacial microstructure. The joint bonded with F_{100} showed a partially sintered structure. It is thought that the coalescence of the Cu flake was greatly facilitated by the nanotextured surface that had formed. The partially sintered microstructure was also observed in the joint bonded with S_{100}, revealing that the sintering behavior of the Cu spheres was also promoted in the ORB process. However, the porous microstructure in both joints reveals that the densification process of the bonding layer is incomplete. It is well known that the densification of a sintered microstructure is dependent on temperature, pressure, and surface energy of the particles. For the low-temperature pressureless sintering, a highly dense microstructure is difficult to obtain, especially using the microscale particles. Therefore, we used the method of hybrid particles to decrease the porosity of the bonding layer and thereby improve the bonding properties. As shown in Fig. 6.7f, the joint bonded with $F_{75}S_{25}$ paste shows higher density than those bonded with F_{100} or S_{100}. The initial shape of the Cu flakes and the Cu spheres has disappeared, and all the Cu particles are connected together. Fig. 6.6 shows that the joint bonded with $F_{75}S_{25}$ had the highest shear strength, and the shear strength decreased with the increasing concentration of Cu spheres. This demonstrates that when the Cu flakes functioned as the basic particles and the Cu spheres were used as an additive in the hybrid mixtures, the bonding strength was the highest. Therefore, it is suggested that the Cu flakes coalesced, resulting in a porous sintered structure. The smaller Cu spheres filled in the pores between the sintered flakes, thereby decreasing the porosity of the sintered layer and enhancing the bonding strength of the joint.

The surface morphologies of the fractured NOB and ORB joints fabricated with $F_{75}S_{25}$ hybrid paste are shown in Fig. 6.8. The fractured NOB joint exhibited a very smooth surface, demonstrating a poor resistance to the shear load. On the other hand, rupture and deformation can be observed on the surface of fractured ORB joint, however, its fracture surface was also relatively flat, indicating that the most fracture occurred near the interface of Cu sintered layer and Cu substrate. More details on the fracture surface ware given in the high magnification SEM images of the selected area, as shown in Fig. 6.9. It is clear that, on the fracture surface of the NOB joint, both the Cu flakes and the Cu spheres were retained. Two kinds of particles were mixed together, however, no sintering

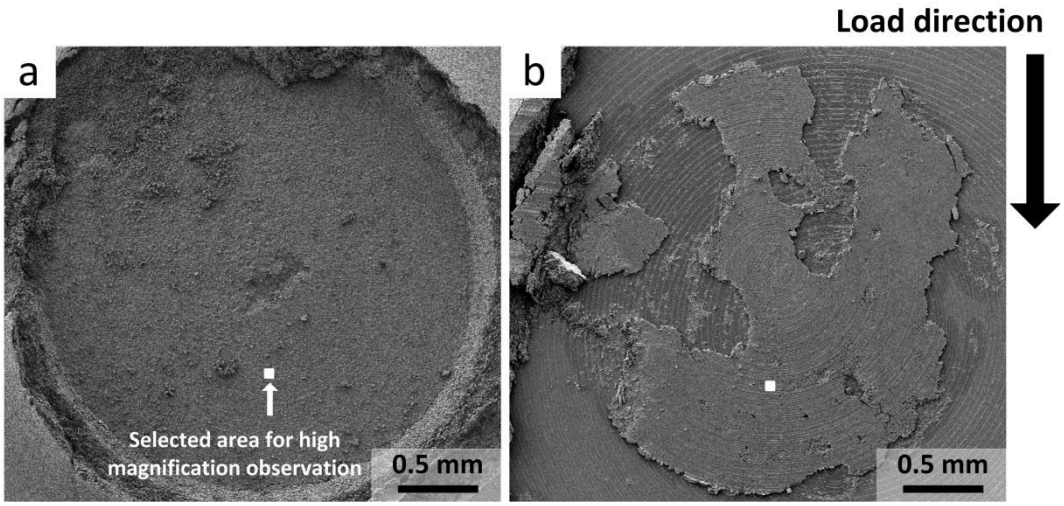

Figure 6.8 Low magnification SEM images of fracture surface of pressureless (a) NOB joint and (b) ORB joint fabricated with $F_{75}S_{25}$ hybrid particle paste.

behavior can be observed. On the other hand, the ORB joint exhibited evidence of ductile fracture; the initial flake and sphere shape of Cu particles can hardly be recognized and the deformation caused by the shear load is clear at the fracture surface. Moreover, the deformation of the fracture

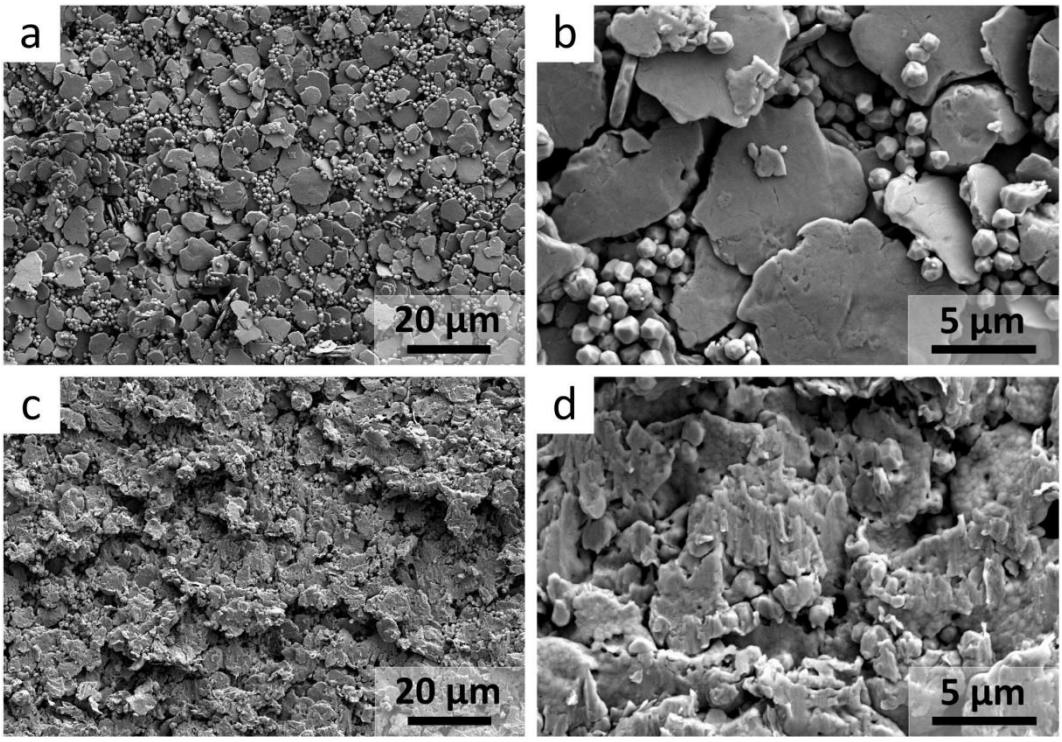

Figure 6.9 High magnification SEM images of fracture surface of pressureless (a, b) NOB joint and (c, d) ORB joint fabricated with $F_{75}S_{25}$ hybrid particle paste.

particles and ductile fracture characteristic of the ORB joint fabricated with hybrid particles is more obvious than that of the ORB joint fabricated with pure Cu flakes (see Fig 6.9b), which is attributed to the denser sintered structure with hybrid particles.

6.4 Effect of substrate on bonding properties

In a low-temperature bonding process, the native amorphous oxides on the Cu substrate can prevent the bonding between the Ag or Cu particles and the Cu substrate, leading to a greatly reduced joint strength. Consequently, in the prior literature, the cleaning of the Cu substrate with diluted acid has been deemed necessary to remove the copper oxides and thereby ensure good bonding. However, such surface preparation seems unacceptable in large-scale manufacturing. Thus, surfaces metallized with Ag or Au are generally needed to ensure good bonding in the absence of any surface preparation [2-5]. There is no doubt that a bonding technology in which both surface metallization and surface cleaning of the substrate are unnecessary is essential to achieve practical application. Therefore, in

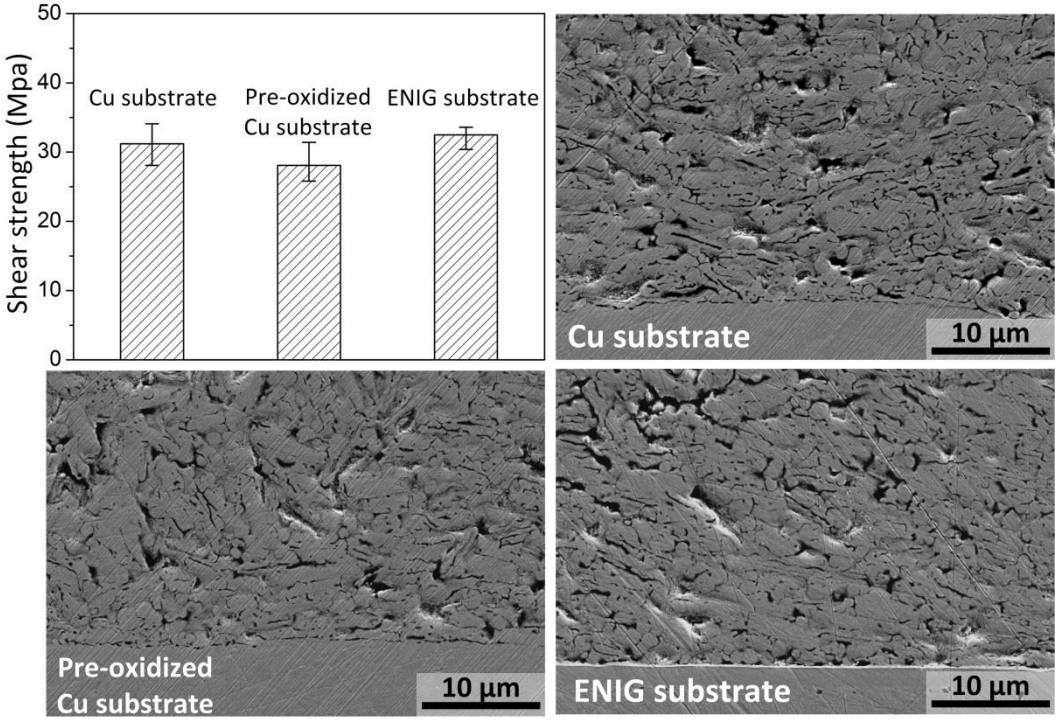

Figure 6.10 Shear strength and cross-sectional SEM images of the joint bonded with ORB process on pure Cu, pre-oxidized Cu and ENIG-finished Cu substrate, respectively.

this study, the adaptability of the ORB process to different substrates was evaluated. Fig. 6.10 shows the shear strength of joints bonded with $F_{75}S_{25}$ paste on pure Cu, pre-oxidized Cu, and ENIG-finished Cu substrates, as well as the corresponding cross-sectional images. It is worth noting that the pre-oxidized Cu joint shows a shear strength that is only slightly lower than that of the pure Cu joint. This demonstrates that the pre-formed oxide layer, which is similar to the native oxides on the uncleaned Cu substrate, has only a small influence on the shear strength of the joint when the ORB process is employed. Apparently, compared to the pre-oxidation at 200 ℃, the Cu substrate undergoes more severe oxidation in the oxidation stage of the ORB process. Thus, the pure Cu substrate and the pre-oxidized Cu substrate had similarly oxidized surfaces before the reduction stage started. Then, during the reduction stage, these oxidized substrates were reduced and bonded with the Cu particles. Therefore, the bonded pre-oxidized Cu substrate can obtain a shear strength that is similar to that of the pure Cu substrate. In addition, it should be noted that it is the unique oxidation-reduction process that gave the bonded pre-oxidized Cu substrate the sound shear strength, rather than the use of reducing atmosphere. A reducing atmosphere such as formic acid vapor and hydrogen is the commonly used atmosphere in low-temperature Cu sintering, but this is the first time that a well-sintered joint on a pre-oxidized Cu substrate has been reported. Moreover, the ENIG joint shows a very similar strength to the Cu joint, demonstrating that the ORB process was effective on both pure Cu and ENIG-finished substrates. As shown in Fig. 6.10, when the ORB process was used, all three kinds of joint clearly show the contacted interface between dense sintered particles and substrate. It is believed that the bonding properties of the ORB process are insensitive to the formation of native Cu oxides and the use of a common ENIG-finished surface.

6.5 Conclusion

In this Chapter, the adaptability of the ORB process was investigated by the use of various Cu particle pastes and different substrates. Flake-shaped Cu particles, Spherical Cu particles, and their hybrids were used to bond the pure Cu substrate by the ORB process and by the NOB process. The ORB process successfully created the bonding joints with various Cu pastes, while the NOB process failed to bond any samples. When the ORB process was applied, the highest shear strength to a

bonded Cu substrate was obtained by the use of 75 mass % Cu flake-25 mas .% Cu sphere mixed hybrid Cu paste. The bonding properties of hybrid Cu particles on pure Cu, pre-oxidized Cu, and ENIG-finished Cu substrates were also studied when the ORB process was used. It was found that the shear strength of the ORB joint was insensitive to the substrate. The bonded ENIG joint showed similar shear strength to the bonded pure Cu joint, and the shear strength of the bonded pre-oxidized Cu joint was just slightly lower than the others. These results show that the ORB process has a strong adaptability to both the native Cu oxides and the Au surface metallization.

References

[1] N. Birks, G. H. Meier, F. S. Pettit, *Introduction to the High-Temperature Oxidation of Metals*, 2nd edn. Cambridge University Press, Cambridge, 2006.

[2] S.T. Chua, K.S. Siow, Microstructural studies and bonding strength of pressureless sintered nano-silver joints on silver, direct bond copper (DBC) and copper substrates aged at 300 ℃, *J. Alloys Compd.*, **687** (2016) 486-498.

[3] S. Paknejad, G. Dumas, G. West, G. Lewis, S. Mannan, Microstructure evolution during 300 ° C storage of sintered Ag nanoparticles on Ag and Au substrates, *J. Alloy Compd.*, **617** (2014) 994-1001.

[4] Y. Fang, R.W. Johnson, M.C. Hamilton, Pressureless Sintering of Microscale Silver Paste for 300 ℃ Applications, *Proceeding of the IEEE Trans. Compon. Packag. Manuf. Technol.*, **5** (2015) 1258-1264.

[5] Q. Xu, Y. Mei, X. Li, G.Q. Lu, Correlation between interfacial microstructure and bonding strength of sintered nanosilver on ENIG and electroplated Ni/Au direct-bond-copper (DBC) substrates, *J. Alloy Compd.*, **675** (2016) 317-324.

Chapter 7
Summary and future work

7.1 Summary

In this dissertation, novel bonding process using surface-modified microscale Cu particles was applied for high-temperature die attach application as a low-cost, green, and reliable substitution of high-lead solder alloys. Objective of this research was to improve low-temperature bondability of microscale Cu particles with surface modification methods, thereby achieving robust Cu-based joint. Two different surface modification methods were used in the study, including Sn surface coating on Cu particles by an electroless plating and in-situ formation of Cu nanotextured surface by an oxidation-reduction process. Correspondingly, three different bonding process: Transient liquid phase (TLP) bonding process using Cu@Sn particles, Solid-state bonding (SSB) process Cu@Sn particles, and oxidation-reduction bonding (ORB) process using Cu particles were developed, respectively. The bonding properties, bonding mechanism and thermal stability at 250 ℃ of the joints fabricated with each bonding process were presented.

In *Chapter 1*, the emerging issues on the increasing demand of wide-band-gap semiconductor-based power device and the current technologies for high temperature electronic

packaging were summarized. The high-temperature lead-free soldering, TLP bonding, low-temperature Ag sintering had been reviewed with their bonding mechanism, development, application, and technical limits. It was shown that low-temperature Ag sintering exhibited the best performance; however it cannot be satisfactory with the need of low cost. Therefore, a purpose of low-temperature bonding process using surface-modified microscale Cu particles was suggested. Finally, two specific surface modification methods with their theoretical basis to improve the bondability of Cu particle were presented.

In *Chapter 2*, based on microscale Cu@Sn particles, the novel transient liquid phase (TLP) bonding process was present. It was shown that a thermally stable composite joint fully comprising a Cu_3Sn IMC with a dispersion of ductile Cu particles can be obtained after bonding at 300 ℃ for 30 s with 10 MPa under a formic acid gas atmosphere. The joint exhibited a shear strength of 24.2 MPa, a little higher than that of conventional Pb-5Sn alloy. The influence of bonding condition on the mechanical property the TLP joint was also studied. The bonding pressure had a great influence on the joint strength, while the influence of bonding time was insignificant. During the isothermal aging test at 250 ℃ for 1000 h, the shear strength of the joints was initially increased to 30.3 MPa after 250 h, and then, the shear strength remained almost unchanged. The EMPA results show that the Cu3Sn-Cu composite joint had a high microstructural stability during the thermal aging.

In *Chapter 3*, the solid-state bonding (SSB) process using microscale Cu@Sn particles for high-temperature die attach applications was developed. Compared to the Cu-Sn TLP bonding, the lower bonding temperature of 200 ℃ was used in this SSB process. After the bonding in formic acid atmosphere with a pressure of 20 MPa, the shear strength of Cu@Sn joint reached 20.4 MPa at a bonding time of 5 min and gradually increased with increasing bonding time up to a value of 25.8 MPa at a bonding time of 20 min. After 20 min, further extending the bonding time showed insignificant effect on the bonding strength. The SSB joint exhibited a composite porous microstructure comprising a Cu_3Sn IMC matrix with a dispersion of pure Cu particles. The formation of a two-phase mixture microstructure is attributed to the unique structure of the Cu@Sn particles used in the solid-state bonding process. During the bonding, the phase transformation and densification process in the joint occurred simultaneously. Moreover, the thermal stability of the joints bonded with Cu particles and Cu@Sn particles during the isothermal aging at 250 ℃ was also

investigated. Debonding of the joint bonded with Cu particles happened after the aging for only 100 h, due to the severe oxidation of sintered Cu structure. On the other hand, the joint bonded with Cu@Sn particles presented nearly 20 MPa shear strength after the aging for 1000 h. The Cu_3Sn IMC network was remained and significantly inhibited the oxidation of Cu substrate, thereby maintaining the bonding strength of the joint.

In *Chapter 4*, the surface morphological evolution of the Cu particles during the thermal oxidation and subsequent reduction process was presented, and the corresponding mechanism was discussed. During the thermal oxidation, thin Cu_2O layer was initially formed on the Cu flake surface, accompanied with a quick release of reaction heat. Afterward, Cu_2O nanoparticles quickly formed on the initial Cu_2O layer and covered the entire flake, during which the heat of oxidation reaction was massively released again. The compressive strain existed in the thin Cu_2O layer near the Cu_2O/Cu interface and the driving force for Cu_2O nanoparticle formation is related to this compressive strain. During the subsequent reduction process, this Cu_2O nanoparticle layer was reduced to Cu nanotextured surface in the formic acid atmosphere, and the surface-modified Cu particle was obtained. In addition, the improved surface activity of the surface-modified Cu flake was verified by the thermal-activated flattening process of the nanotextured surface.

In *Chapter 5*, the bonding properties of the Cu-Cu joint using the oxidation-reduction bonding (ORB) process were verified. This oxidation-reduction bonding process was realized by switching the atmosphere from air to formic acid vapor in the bonding process. The pressureless and pressure-assisted ORB joint exhibited a shear strength of 23.8MPa and 78.3 MPa, respectively, both were significantly higher than that of their corresponding non-oxidation bonding (NOB) joint. It was found that the nanotextured surface that formed during the oxidation-reduction process played a key role in the enhanced coalescence of the sintered particles. Here, to show the excellent performance of the ORB process, a comparison of this process and current Ag and Cu-based bonding process is given in Fig.7.1. It can be seen that the excellent bonding strength were reported for the first time when using the microscale Cu particles for die attach materials. Moreover, after the thermal aging at 250 ℃ for 1000 h, the shear strength of the pressureless ORB joint was decreased down to 10 MPa, while the pressure-assisted ORB joint remained a high shear strength above 50 MPa.

In *Chapter 6*, the compatibility of the ORB process with differently shaped Cu particles and

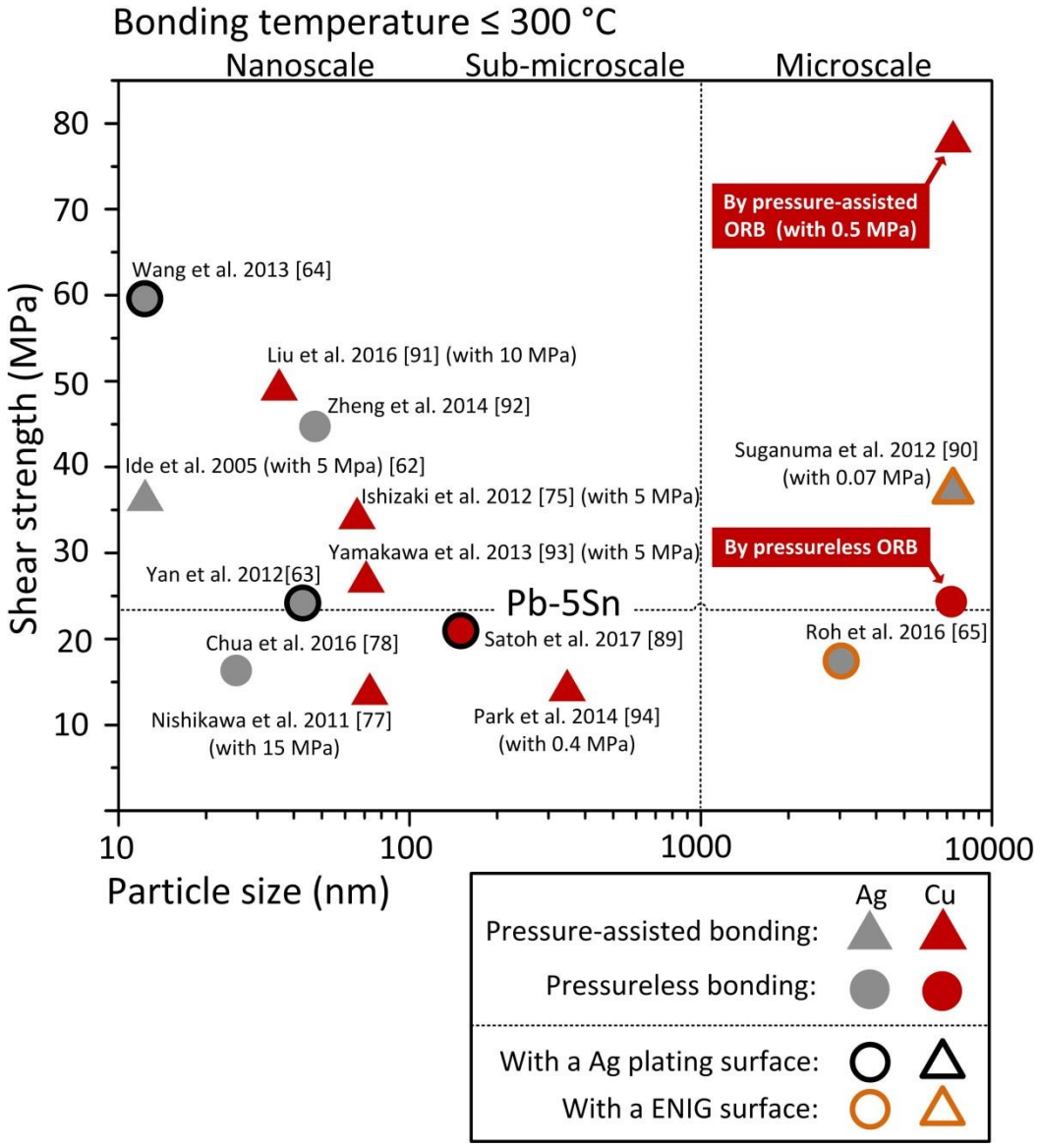

Figure 7.1 Comparison of ORB process and other Ag and Cu bonding process. [62-65, 75, 78, 90-94]

different substrates was studied. The Cu-Cu joints were bonded with the pressureless ORB process, and the highest shear strength 31.2 MPa was achieved by using the hybrid particle paste comprising 75 mass % flake-shaped Cu particles and 25 mass % spherical Cu particles. Moreover, ORB joints were also fabricated with pre-oxidized Cu and electroless nickel/immersion gold (ENIG)-finished Cu substrates. The bonded ENIG-finished Cu joint has a shear strength that is similar to that of the bonded pure Cu joint. On the other hand, the bonded pre-oxidized Cu joint shows a shear strength of 28.1 MPa, only 10 % less than the shear strength of the bonded pure Cu joint.

7.2 Environmental assessment on various die attach materials as well as bonding processes

As mentioned above, the bonding process with surface-modified microscale Cu particles is proven a promising low-cost lead-free die attach method for high-temperature power device packaging. In addition to the performance of the bonded joint, environmental aspect should be also evaluated for the practical use. In this section, an environmental assessment on the selected die attach materials and bonding processes were performed.

7.2.1 Materials

The selected materials includes Pb-5Sn solder paste, Cu nanoparticle paste, microscale Cu particle paste, and microscale Cu@Sn particle paste. Particularly, waste fluid produced in the materials manufacturing, toxicity of materials itself, and additives to make the paste were considered as critical criterion to compare the environmental impact of each materials, as shown in Table 7.1.

Pb-5Sn solder powders and microscale Cu particles are fabricated by gas-atomization from the molten Pb-Sn alloy and Cu metal, respectively, and thereby do not produce any waste fluid. However, usage of Pb should be forbidden due to environmental regulation. Although Cu is non-toxic, strong reducing agents, such as hydrazine and sodium borohydride, are generally used to synthesize Cu nanoparticles. Hydrazine is extremely toxic and dangerous and sodium borohydride produces impurities, such as boron and sodium salts, which are hard to remove by solvent washing. Moreover, the potential toxicity of metallic nanoparticles is also an issue [1, 2]. Thus, in term of the environmental perspective, it is still doubtful that the Cu nanoparticles can be used for large-scale application. On the other hand, the manufacture of microscale Cu particle paste is quite simple, and materials toxicity is not an issue for microscale Cu particles. As for the Cu@Sn particles, the fabrication needs an electroless Sn plating process. Owing to the wide application in the electronics industry, this plating process has been a well-matured technology, and non-toxic (fluoride-free) electroless Sn plating solution have been developed. Therefore, in terms of environmental perspective, the microscale Cu particle paste is an excellent material, while the usage of microscale Cu@Sn particle paste is also acceptable.

Table 7.1 Comparison of various die attach materials in term of the environmental perspective

Items	Pb-5Sn solder paste	Cu nanoparticle paste	Microscale Cu particle paste	Microscale Cu@Sn particle paste
Waste fluid	-	Strong reducing agents, such as hydrazine and sodium borohydride.	-	Electroless Sn plating solution
Toxicity of materials	Toxic ban from ROHS	Toxicity of nanoparticles	-	-
Additives to make the paste	Flux	Polymers, such as PVP and gelatin	Terpineol	Terpineol
Summary	Forbidden	Doubtful	Excellent	Acceptable

7.2.2 Bonding process

In addition to the die attach materials, the environmental assessment of various bonding process was also conducted, in term of the energy consumption and possible pollution release of each process, as shown in Table 7.2. The performance of soldering process using Pb-5Sn solders or high-temperature lead-free solders is excellent for the sake of energy saving. The entire reflow process only lasts for several minutes and no external pressure is needed. On the other hand, although the Cu-Sn TLP bonding, Ag sintering, and Cu sintering can be identified as low-temperature bonding process for high-temperature die attach application, they could be time-consumed process. Thus, the energy consumption may be an issue for emerging TLP bonding and Cu sintering bonding process. Moreover, a reducing atmosphere such as H_2 or formic acid vapor is generally needed in the Cu sintering to avoid the formation of thin Cu oxides layer on the Cu particles because these oxides layer will strongly inhibit the sintering behavior of Cu particles. Indeed, in my study, the formic acid vapor is needed as a reducing atmosphere, and the usage of formic acid vapor may bring about an environmental impact. Currently, as a promising alternative of flux in soldering process, formic acid atmosphere is attracting more and more attention in industry. Therefore, it can be expected that its potential environmental impact will be minimized with the improvement of the treatment technology

Table 7.2 Comparison of various bonding process in term of the environmental perspective

Items	Soldering (Pb-5Sn)	Cu-Sn TLP	Ag sintering	Cu sintering
Energy consumption (Temperature and Time)	around 350 ℃	250-300 ℃	200-300 ℃	300-400 ℃
	< 10 minutes	10-60 min	10-60 min	10-60 min
Pollution release (Processing atmosphere)	N_2	N_2 (with a flux)	N_2 or Air	Reducing atmosphere
Summary	Excellent	Acceptable	Acceptable	Acceptable

to the formic acid vapor.

7.3 Future work

7.3.1 Optimization of the structure of Sn-coated Cu particle for low-pressure bonding

In *Chapter 2* and *Chapter 3*, when the microscale Cu@Sn particles were used as the bonding materials, relatively high bonding pressure (10-20MPa) was adopted for both the transient liquid phase bonding and the solid-state bonding. However, an excessive bonding pressure is not expected in a die attaching process. It could lead to the fracture and damage of brittle semiconductor chip and electric circuit on the top of chip. Thus, the bonding pressure applied in the die attaching process should be lowered as low as possible.

One possible solution is to increase the mole ratio of Sn to Cu in the Cu@Sn particle. The purpose for applying high pressure in both bonding is to densify the microstructure in the bonding layer. As the highly reactive component with the low melting point, Sn coating layer play a key role in the coalescence of particles and the formation of Cu_3Sn matrix in both bonding. Thus, it is suggested the densification process of the Cu@Sn particles can be enhanced by increasing the mole ratio of Sn to Cu in the Cu@Sn particle, in particular, thickening the Sn coating layer. On the other hand, too thick Sn coating layer will prolong the reaction duration between Sn and Cu, and even

change the final phase constituent of the bonding joint. Therefore, more experiments are needed to confirm the optimal thickness of the Sn coating layer.

7.3.1 Improvement of the manufacturability of oxidation-reduction bonding

In *Chapter 4*, the oxidation-reduction bonding (ORB) was realized by switching the atmosphere from air to formic acid vapor during the sintering bonding process. To show the excellent bonding propertiesof this process, a stantard processing condition was untilized, including 20 min thermal oxidation at 300 ℃ and 40 min reduction at 300 ℃. Although well-sintered Cu joint was achieved, this process may exhibit a poor manufacturability in the view of production. As shown in Table 7.2, compared to the soldering process, this ORB process need much longer processing time. Therefore, the processing conditions of ORB need to be modified. In particular, processing temperature and processing time should be reduced to save the energy consumption.

For the thermal oxidation, the necessary temperature and time for the formation of Cu_2O nanoparticle layer on the entire flake surface should be found, and these temperature and time are suggested as the minimum oxidation condition. And it should be noted that this minimum oxidation condition is dependent on the size and shape of the Cu particles used in the ORB process. On the other hand, as mentioned before, the reduction process can be simplified as a sintering bonding process. Therefore, the improvement of reduction process can refer to the studies of low-temperature Ag sintering process. According to those studies, the sintering temperature can be reduced by applying a sintering pressure. And the sintering time generally presented a parabola relation with the strength, as shown in Fig.5.4c. Thus, it is suggested the selection of proper sintering time should depends on the requirements of real die attach application. In addition, if the surface-modified Cu particles with nanotextured surface can be manufactured beforehand by an oxidation-reduction processs, the duration of the bonding process with these pre-modified Cu particles will be much shorter than that of the ORB process.

7.3.2 Mechanism of surface morphological evolution on sphere-shaped Cu particles for oxidation-reduction bonding

In *Chapter 6*, it was presented that the Cu flake and the Cu sphere exhibited different surface morphology after the thermal oxidation at 300 ℃ for 20 min. The oxidized Cu flake was covered by densely packed Cu_2O particles, the oxidized Cu sphere only showed a nanoscale rough surface. The different morphology of surface oxide on two kinds of particles also led to the different surface morphologies of their reduced particles. As a result, when the ORB process was applied, the Cu flakes exhibited a higher sinterability than the Cu sphere; even the latter had a smaller particle size. In addition to the Cu flake and Cu sphere, two other kinds of microscale Cu particles were also selected to undergo a thermal oxidation process at 300 ℃, the detailed information can be seen in *Appendix 1*. It was found only the Cu spheres that mentioned in *Chapter 6* showed different surface morphological evolution and thermal behavior during the thermal oxidation at 300 ℃.

The driving force and mechanism of the surface morphological evolution on Cu flake during the thermal oxidation had been presented in *Chapter 4*. Here, it is believed that a deep understanding of the mechanism for the surface morphological evolution on Cu sphere is also necessary. Firstly, this understanding can help to find a method to produce Cu_2O nanoparticle layer on the surface of oxidized Cu sphere, thereby obtaining a completely surface-modified Cu sphere with a nanotextured surface after the reduction process. This surface-modified Cu sphere has the potential to perform higher sinterability than their flake-shaped counterpart, since it has a much smaller particle size.

Moreover, this research can help to improve the proposed theory that explains the formation of Cu_2O nanoparticles on the Cu particles during the thermal oxidation. In *Chapter 4*, it was proposed that the driving force for Cu_2O nanoparticle formation is related to the compressive stress in the Cu_2O layer near the Cu_2O/Cu interface. Particularly, an imbalance between the stress-driven Cu diffusion along the Cu_2O grain boundary and the surface Cu diffusion on the top of Cu_2O layer gave rise to the local Cu-rich composition at GB junction area, and thereby leading to the formation of Cu_2O nanoparticles. The absence of Cu_2O nanoparticle layer on the surface of oxidized Cu sphere does not necessarily weaken the proposed mechanism. In contrast, more direct or indirect evidences could be provided to improve the mechanism as long as the reason that leads to the different surface morphology of Cu flake and Cu sphere after the thermal oxidation can be figured out.

Fig 7.1 gives a comparison of TG-DTA curve between Cu flake and Cu sphere during thermal oxidation. The curve of Cu flake has been analyzed in *Chapter 4*, and it was proposed that the second

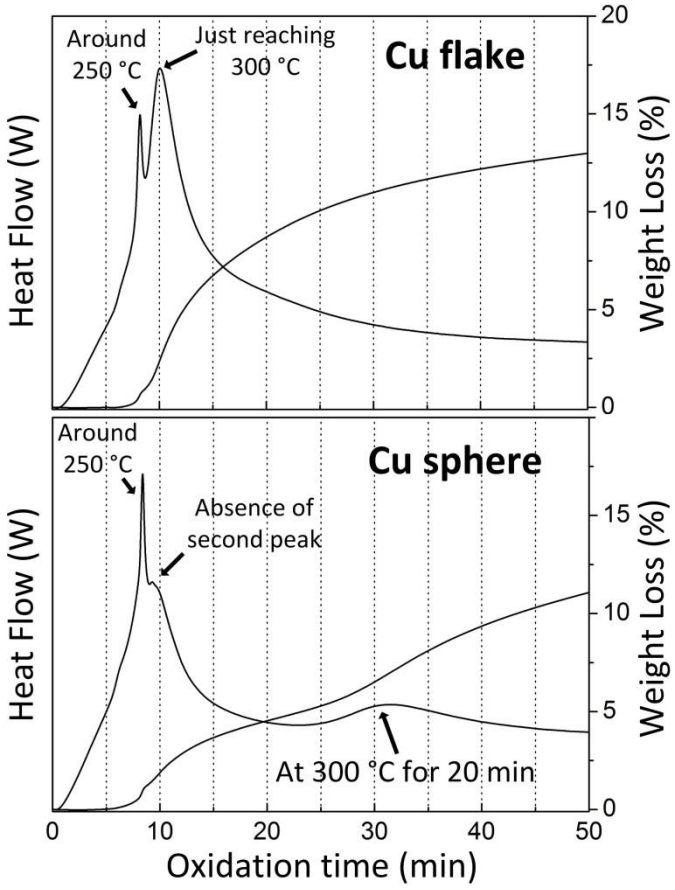

Figure 7.2 Traces of TG-DTA for Cu flakes and Cu spheres during heating in air (temperature increasing to 300 ℃ at 30 ℃ min^{-1} and holding at 300 ℃ for 50 min).

exothermic peak was induced by the rapid formation of Cu_2O nanoparticles on the initial thin Cu_2O film. Therefore, it is no surprising that the similar second exothermic peak cannot observed on the DTA curve of Cu sphere, since it is consistent with the fact that Cu_2O nanoparticles did not form on the surface of oxidized Cu sphere. Moreover, during the period of isothermal oxidation at 300 ℃, the TG-DTA curve of Cu sphere also show different trend from that of Cu flake. Therefore, it is assumed that surface morphological evolution of Cu flake and Cu sphere actually obey the same mechanism, but being different due to some factors. So far, it is suggested the curvature of reactive interface is one key factor. It can affect both the epitaxial stress and the stress induced by the incompatibility of molar volume [3, 4], thereby altering the mass transport mode of Cu ion during the thermal oxidation. Thus, the small Cu sphere that presents a significantly smaller surface curvature than that of the Cu flake will exhibit a different surface morphology after the thermal oxidation for 20 min.

7.3.3 Other applications of Cu-Cu interconnection using oxidation-reduction method

In the thesis, it was shown this facile ORB process has the potential to overcome the limitation of microscale Cu particles for low-temperature, low-pressure or even pressureless bonding and enable the sintering of the microscale Cu particles in view of a practical bonding technology for power device packaging. Moreover, this study also provides a new insight into the Cu-Cu interconnection technology for other applications, such as Cu ink sintering for printed electronics and Cu-Cu direct bonding for 3D IC.

Ag particle inks have been widely used recently for printed electronics; however, Cu inks have become a promising candidate for future conductive inks due to much lower cost and higher electromigration resistance [5, 6]. In order to achieve high conductivity of copper films prepared from the copper inks, ORB process also can be used to facilitate the sintering of Cu particles. In addition, copper wafer bonding is one of the most promising approaches for 3D IC applications because it provides low costs and high throughput for advanced CMOS integration when compared to other bonding approaches [7]. Currently, thermal-compression Cu bonding, also known as diffusion Cu bonding, is one basic bonding method that achieves good wafer bonding results. Although its design scheme is simple and costs less, thermal-compression Cu bonding does require high temperature and pressure. Therefore, it is expected that the surface modification by the oxidation-reduction process will enable two Cu surfaces to bond at lower temperature and pressure.

7.3.4 Reliability assessment of proposed bonding methods for real application.

Although the bonding properties and thermal stability of three bonding methods had been verified in the dissertation, there are still several issues needed to address for the real applications, such as the reliability and manufacturability. As a researcher in academia, I am mainly focused on the reliability issue.

In the thesis, the pure Cu disc was selected to fabricate the joint. It is because direct bonding Cu (DBC) with Cu surface is the common used substrate for high temperature die attach. Moreover, compared to the Ni- or Au-finished substrate, Cu substrate generally shows a modest bondability in current die attaching process, thus making it suitable as dummy chip. For the practical use of the

bonding processes presented in the thesis, it is necessary to extend the Cu-Cu joint to more realistic power semiconductor interfaces, e.g. DBC substrate and either Au or Ni terminated SiC.

In *Chapter 2*, *Chapter 3* and *Chapter 5*, the reliability of the Cu-Cu joint was only investigated by the isothermal aging test at 250 ℃. Isothermal aging test of the sintered die attach layer are attracting lots of interests in recent years [8, 9]. Since the junction temperature of the WGB-based power device may exceed 200 ℃, the date about the performance of die attach exposed in air at 250 ℃ is basic and valuable. In addition to the isothermal aging test , the temperature cycling is very suitable for studying die-attach degradation at high and low temperatures and it can be implemented using dummy devices in order to purely study mechanical degradation mechanisms. In the test, temperature is varied by temperature-controlled chamber, namely external heating and cooling. There are several standards concerning the temperature cycling of electronic parts, such as MIL-STD-883H and MIL-STD-750E. On the other hand, of course, using working devices assembled on practical packages, power cycling must also be performed, since it can offer the similar temperature swing with the practical application. In the test, the power device is heated by the power loss of power semiconductor and is cooled with heat sink, namely internal heating and cooling [10]. Therefore, for the practical application, the reliability of more realistic joint fabricated with the proposed bonding methods should be further verified by the temperature cycling and power cycling test.

References

[1] P. V. AshaRani, G. Low Kah Mun, M. P. Hande, and S. Valiyaveettil, Cytotoxicity and genotoxicity of silver nanoparticles in human cells, *ACS nano*, **3** (2008) 279-290.

[2] M. Ahamed, M. S. AlSalhi, and M. K. J. Siddiqui, Silver nanoparticle applications and human health, *Clin. Chim. acta*, **411** (2012) 1841-1848.

[3] M. I. Manning, Geometrical effects on oxide scale integrity. Corros. Sci., **21** (1981) 301-316.

[4] F. J. Von Preissig, Applicability of the classical curvature-stress relation for thin films on plate substrates, *J. Appl. Phys.* 66 (1989) 4262-4268.

[5] S. Jeong, K. Woo, D. Kim, S. Lim, J. S. Kim, H. Shin, and J. Moon, Controlling the thickness of the surface oxide layer on Cu nanoparticles for the fabrication of conductive structures by ink-jet printing, *Adv. Func. Mater.*, **18** (2008) 679-686.

[6] Y. Yong, T. Yonezawa, M. Matsubara, and H. Tsukamoto, The mechanism of

alkylamine-stabilized copper fine particles towards improving the electrical conductivity of copper films at low sintering temperature, *J. Mater. Chem. C*, **3** (2015) 5890-5895.

[7] Y. S. Tang, Y. J. Chang, and K. N. Chen, Wafer-level Cu-Cu bonding technology, *Microelectron. Relia.*, **52** (2012) 312-320.

[8] H. S. Chin, K. Y. Cheong, and A. B. Ismail, A review on die attach materials for SiC-based high-temperature power devices. *Metall. Mater. Trans. B*, **41** (2010) 824-832.

[9] S. T. Chua and K. S. Siow, Microstructural studies and bonding strength of pressureless sintered nano-silver joints on silver, direct bond copper (DBC) and copper substrates aged at 300 °C. *J. Alloy Comp.*, **687** (2016) 486-498.

[10] J. Lutz, H. Schlangenotto, U. Scheuermann, R. de Doncker, Semiconductor power devices, Heidelberg, Germany, 2011.

Appendix 1
Oxidation-reduction process to different microscale Cu particles

A1.1 Characteristics of different microscale Cu particles

In *Chapter 4* and *Chapter* 5, flake-shaped microscale Cu particles were used as basic materials for the studying of in-situ surface modification of Cu particles and corresponding bonding properties. Although an effective ORB process using flake-shaped microscale Cu particles had been proven, it is also needed to clarify whether other kinds of microscale Cu particles can be used in this unique ORB process. As mentioned before, the formation of surface Cu_2O nanoparticles after the thermal oxidation at 300 ℃ is the most critical phenomenon during the in-situ surface modification process. Therefore, in order to show the compatibility of this in-situ surface modification method with different Cu particles, the surface morphologies of four different kinds of microscale Cu particles after the thermal oxidation at 300 ℃ were characterized. ORB

Two flake-shaped particles and two spherical particles were used, including the big flake-shaped particles with an average diameter of 6.9 μm (1400YP, MITSUI MINING & SMELTING CO. LTD), the small flake-shaped particles with an average diameter of 1.2μm (1100YP, MITSUI MINING &

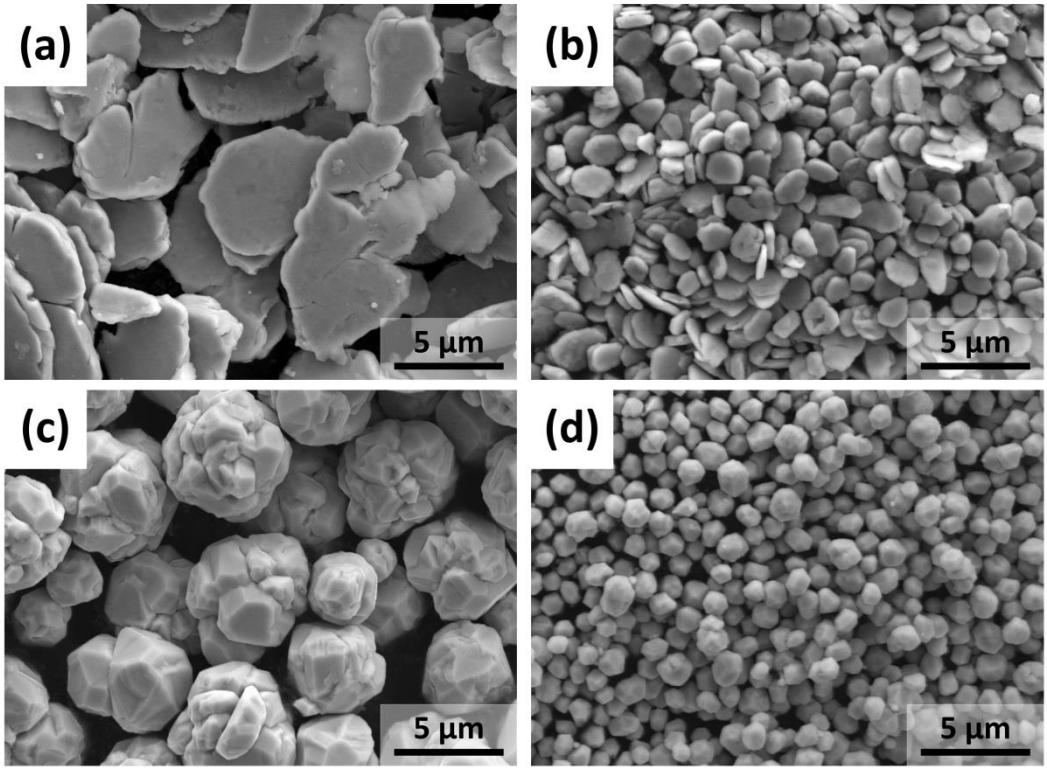

Figure A1.1 SEM images of four kinds of microscale Cu particles: (a) big Cu fakes, (b) small Cu flakes, (c) big Cu spheres, and (d) small Cu spheres

SMELTING CO. LTD), the big spherical particles with an average diameter 5.5 μm (1400Y, MITSUI MINING & SMELTING CO. LTD), and small spherical particles with an average diameter 1.2 μm (1100Y, MITSUI MINING & SMELTING CO. LTD). These four kinds of particles are hereafter referred to as "big flakes", "small flakes", "big spheres", and "small spheres", respectively. SEM images of the four kinds of particles are shown in Fig. A1.1 and selected properties of each are listed in Table. A1.1.

Table A1.1 Selected properties of microscale Cu particles.

Type	Big flake	Small flake	Big sphere	Small sphere
Diameter D50 (μm)	6.9	1.2	5.5	1.2
Specific surface area (m^2/g)	0.26	1.3	0.13	0.86

A1.2 Surface morphology after thermal oxidation

Fig. A1.2 shows the SEM images of four kinds of Cu particles after thermal oxidation for 20 min. It can be seen that big flakes, small flakes, and big spheres showed similar surface morphology. The oxidized particles were covered by densely packed oxide nanoparticles. Within, the formation of nanoparticles on the big flake was more obvious than that on the other two particles. In contrast, it can be seen that the flat surface of the small Cu spheres became very rough after the oxidation. However no nanoscale oxide particles can be identified on the surface of the Cu spheres; instead,

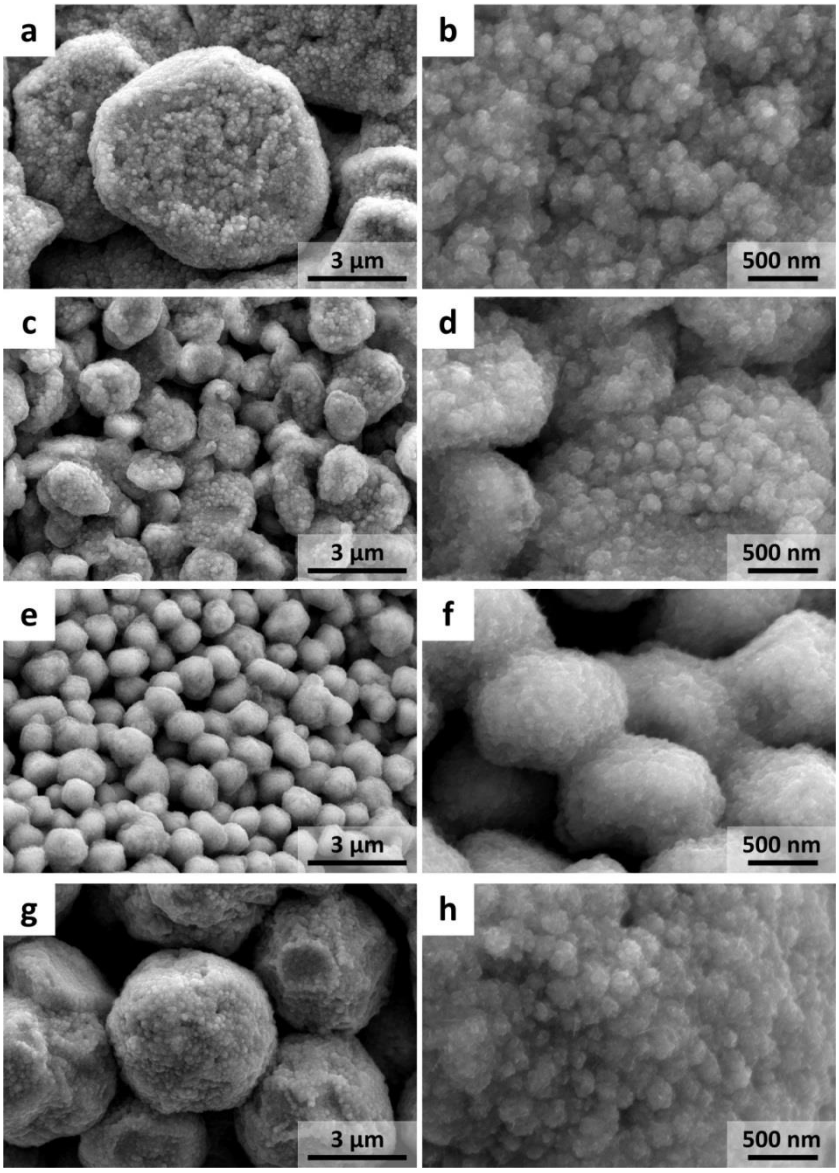

Figure A1.2 SEM images of four kinds of microscale Cu particles after thermal oxidation for 20 min: (a, b) big Cu fakes, (c, d) small Cu flakes, (e, f) big Cu spheres, and (g, h) small Cu spheres.

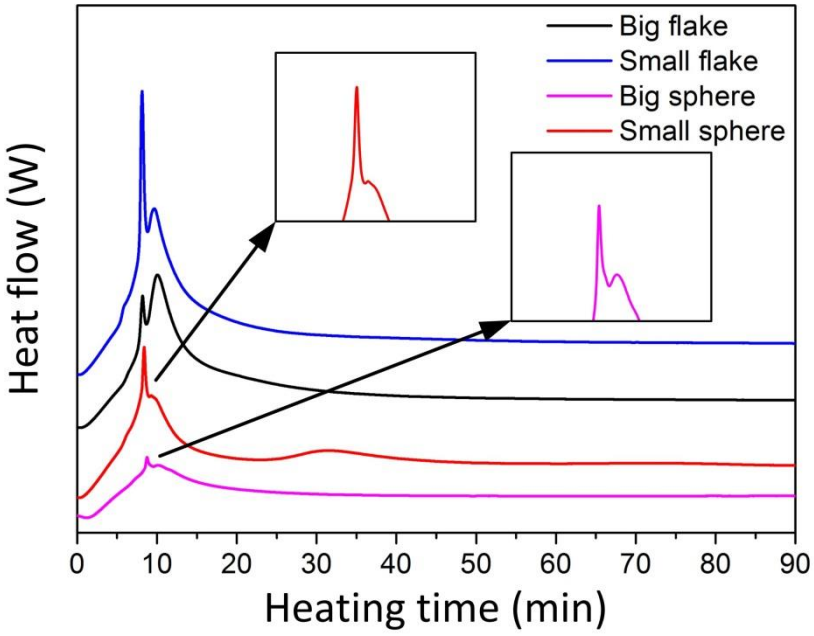

Figure A1.3 Trace of DTA for four kinds of Cu particles during heating in air (temperature increasing to 300 ℃ at 30 ℃ min^{-1} and holding at 300 ℃ for 80 min). The embedded graphs show the magnified peaks on the curve of big sphere and small sphere.

the surface morphology can be more accurately described as a nanoscale rough surface. These results demonstrate that the formation of surface Cu_2O nanoparticles during the thermal oxidation at 300 ℃ should be a general phenomenon for microscale Cu particles, regardless of particle shape. On the other hand, the absence of nanoparticles on the surface of small spheres is a special case.

Moreover, Fig. A1.3 gives the DTA trace of four kinds of Cu particles during heating in air. The sample was heated to 300 ℃ from room temperature at the rate of 0.5 ℃° , and then isothermally oxidized at 300 ℃ for 90 min. As mentioned in *Chapter 4*, two adjacent exothermic peaks appeared on the curve of big flake, and the second exothermal peak corresponds to the heat release in the formation of Cu_2O nanoparticles, thus can be seen as a sign of nanoparticle formation. The similar two-peak feature also can be seen on the curves of small flake and big sphere, but absence on the curve of small sphere. This result is consistent with the aforementioned SEM observation of oxidized Cu particles. The formation of Cu_2O nanoparticles on the small spheres is not clear in SEM images. Correspondingly, the second exothermal peak also cannot be identified on the DTA curve of small spheres.

A1.3 Surface morphology after reduction

Fig. A1.4 shows the SEM images of four kinds of Cu particles after subsequent reduction for 2 min. The nanotextured surface can be observed on the big flakes, small flakes, and big spheres. In *Chapter 4*, it had been mentioned that the formation of Cu nanotextured surface is caused by the reduction of Cu_2O nanoparticles and the simultaneous coalescence of the reduced Cu nanoparticles on the surface of Cu particles. On the other hand, similar with the absence of Cu_2O nanoparticles after thermal oxidation, this unique surface morphology is not obvious on the small sphere. After the

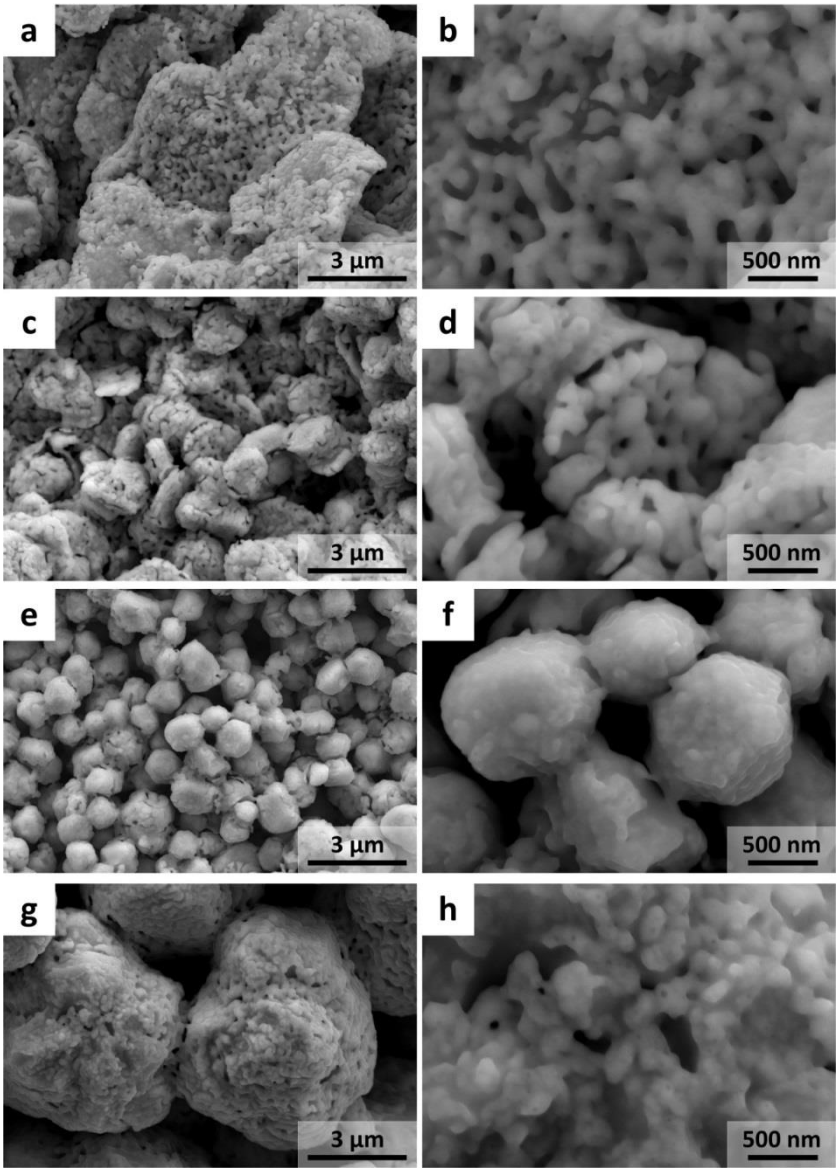

Figure A1.4 SEM images of four kinds of microscale Cu particles after subsequent reduction for 2 min: (a, b) big Cu fakes, (c, d) small Cu flakes, (e, f) small Cu spheres, and (g, h) big Cu spheres.

reduction, the nanoscale rough surface that obtained by the thermal oxidation was retained on most small spheres, as shown in Fig. A1.4f. Only a small amount of small spheres exhibited a nanotextured surface (please see Fig. 6.5d).

Research achievements

I List of publications

Peer-reviewed journal articles

1. Hiroshi Nishikawa, **Xiangdong Liu**, Xianfan Wang, Akira Fujita, Nobuo Kamada, Mutsuo Saito, Microscale Ag particle paste for sintered joints in high-power devices, *Materials Letters*, **161** (2015) 231-233.
2. **Xiangdong Liu**, Siliang He, Hiroshi Nishikawa, Thermally stable Cu_3Sn/Cu composite joint for high-temperature power device, *Scripta Materialia*, **110** (2016) 101-104.
3. **Xiangdong Liu**, Hiroshi Nishikawa, Low-pressure Cu-Cu bonding using in-situ surface-modified microscale Cu particles for power device packaging, *Scripta Materialia*, **120** (2016) 80-84.
4. **Xiangdong Liu**, Siliang He, Hiroshi Nishikawa, Low temperature solid-state bonding using Sn-coated Cu particles for high temperature die attach, *Journal of Alloys and Compounds*, **695** (2016) 2165-2172.
5. **Xiangdong Liu**, Hiroshi Nishikawa, Pressureless sintering bonding using hybrid microscale Cu particle paste on ENIG, pure Cu and pre-oxidized Cu substrate by an oxidation–reduction process, *Journal of Materials Science: Materials in Electronics*, **28** (2017) 5554–5561
6. **Xiangdong Liu**, Qishi Zhou, Hiroshi Nishikawa, Thermal stability of low-temperature sintered joint using Sn-coated Cu particles during isothermal aging at 250 ℃, *Journal of Materials Science: Materials in Electronics*, accepted.
7. **Xiangdong Liu**, Hiroshi Nishikawa, Transient liquid phase bonding using Sn-coated Cu particles for high-temperature electronic packaging, in preparation.
8. **Xiangdong Liu,** Hiroshi Nishikawa, Mechanism and bonding property of in-situ surface

modified microscale Cu particles by an oxidation-reduction process, in preparation.

Conference proceedings

1. Hiroshi Nishikawa, **Xiangdong Liu**, Xianfan Wang, Akira Fujita, Nobuo Kamada, Mutsuo Saito, Bonding strength of Cu/Cu joints using micro-sized Ag particle paste for high-temperature application, *Proceeding of International Conference on High temperature Electronics (HiTEC 2015)*, pp. 68-72, 2015
2. **Xiangdong Liu**, Hiroshi Nishikawa, Microstructure of Transient Liquid Phase Sintering Joint by Sn-Coated Cu Particles for High Temperature Packaging, *Proceeding of International Symposium on Microelectronics (IMAPS 2015)*, pp. 449-452, 2015.
3. **Xiangdong Liu**, Siliang He, Hiroshi Nishikawa, Low temperature bonding using microscale Cu particles coated with thin Sn layers at 200 °C, *Proceeding of International Conference on Electronics Packaging (ICEP 2016)*, pp. 306-309, 2016.
4. **Xiangdong Liu**, Hiroshi Nishikawa, Improved Joint Strength with Sintering Bonding Using Microscale Cu Particles by an Oxidation-Reduction Process, *Proceeding of Electronic Components and Technology Conference (ECTC 2016)*, pp. 455-460, 2016

II List of presentations

1. Hiroshi Nishikawa, **Xiangdong Liu**, Xianfan Wang, Akira Fujita, Nobuo Kamada, Mutsuo Saito, Bonding strength of Cu/Cu joints using micro-sized Ag particle paste for high-temperature application, *International Conference on High temperature Electronics (HiTEC 2015)*, Cambridge, United Kingdom, July 6-8, 2015.
2. **Xiangdong Liu**, Hiroshi Nishikawa, Microstructure of Transient Liquid Phase Sintering Joint by Sn-Coated Cu Particles for High Temperature Packaging, *48th International Symposium on Microelectronics (IMAPS 2015)*, Orlando, USA, October 27-29, 2015.
3. **Xiangdong Liu**, Siliang He, Hiroshi Nishikawa, Low temperature bonding using microscale Cu particles coated with thin Sn layers at 200 °C, *16th International Conference on Electronics Packaging (ICEP 2016)*, Sapporo, Japan, April 27-29, 2016.
4. **Xiangdong Liu**, Hiroshi Nishikawa, Improved Joint Strength with Sintering Bonding Using Microscale Cu Particles by an Oxidation-Reduction Process, *66th Electronic Components and Technology Conference (ECTC 2016)*, Las Vegas, USA, May 31-Jun 03, 2016.

Acknowledgement

Firstly, I would like to express my sincere gratitude to my advisor Assoc. Prof. Hiroshi Nishikawa for his insightful advices and support to my Ph. D. study and related research, for his motivation and immense knowledge. His guidance helped me in all the time of research and writing of this thesis.

Besides my advisor, I would like to thank the rest of my thesis committee: Prof. Michihiko Ike, Prof. Akio Hirose, and Prof. Soshu Kirihara, for their insightful comments and encouragement, but also for the hard question which incented me to widen my research from various perspectives. My thanks also goes to staff of Joining and Welding Research Institute, Mr. Kenji Asano, Mr. Takuya Ogura, for technical supports.

I thank members and alumni of Nishikawa Laboratory, Ms. Satomi Takahashi, Dr. Omid Mokhtari, Dr. Myonghoon Roh, Dr. Min-Su Kim, Mr. Siliang He, Mr Sanghun Jin, Mr. Shiqi Zhou, Mr. Jun Tajima, Mr. Ryo Matsunobu, Mr. Yujian Zhang, Mr. Shunichi Koga, Dr. Li-Ngee Ho, Mr. Xiaofan Wang, Mr. Shinya Kubota, Mr. Makoto Ujimo, Mr. Shinya Ojima, Ms. Kaori Matsunaga, and Ms. Kimiko Ikkai, Without their encouragement and support it would not be possible to conduct this research.

Also I thank my friends and colleagues in Osaka University. Dr. Xiao Yang, Dr. Zhonghao Heng, Dr. Zhengquan Tan, Dr. Qinglong Pan, Dr. Biao Chen, Dr. Jianghua Shen, Dr. Xiaoxin Ye, Dr. Zhang Hao, Dr. Chuantong Chen, Mr. Hao Zhang, and Mr. Wanli Li. In particular, I am grateful to Dr. Ziqin Chen for her invaluable support and patience.

Last but not the least, I would like to thank my parents for inspiring me to realize my own potential, for supporting me spiritually throughout my life. All the encouragement, support, and love they have provided me over the years is the reason why I can do it.